The Pennsylvania State University

The Graduate School

College of Earth and Mineral Sciences

NANOSTRUCTURED ELASTOMERS: FROM SMECTIC

LIQUID CRYSTALS TO NOBLE METAL NANOCOMPOSITES

A Dissertation in

Materials Science and Engineering

by

Daniel M. Lentz

Submitted in Partial Fulfillment
of the Requirements
for the Degree of

Doctor of Philosophy

August 2010

The dissertation of Daniel M. Lentz was reviewed and approved* by the following:

Ronald C. Hedden
Associate Professor of Chemical Engineering, Texas Tech University
Dissertation Co-Adviser
Co-Chair of Committee
Special Member

Evangelos Manias
Associate Professor of Materials Science and Engineering
Dissertation Co-Adviser
Co-Chair of Committee

Ralph H. Colby
Professor of Materials Science and Engineering

Thomas E. Mallouk
Dupont Professor of Materials Chemistry and Physics

Gary L. Messing
Distinguished Professor of Ceramic Science and Engineering
Head of the Department of Materials Science and Engineering

*Signatures are on file in the Graduate School

# ABSTRACT

Noble metal/polymer nanocomposites are a desirable and useful class of material due to their combination of the beneficial processibility and mechanical properties of polymers with the optical, electrical, barrier, and other engineering properties of metal nanoparticles. Potential applications of such materials include non-linear optical materials with gold nanoparticles or conductive polymer substrates with percolated silver nanoparticles. A processing approach has been developed whereby metal nanoparticles, especially silver and gold, can be infused into the surface of a thermoplastic elastomer following the melt processing operation. This reaction-diffusion approach (nanoinfusion) allows metal nanoparticles to be introduced at relatively low cost while avoiding the issues of thermal degradation, microphase separation, or agglomeration that can occur at elevated temperatures in the melt state. The nanoinfusion process involves immersion of a molded, cast, or extruded plastic article in an aqueous plasticizer solution (Bayer MaterialScience AURA® Infusion Technology) containing a metal salt such as $HAuCl_4$ or $AgNO_3$. Infusion of the metal salt into the plastic surface is achieved well below the melt-processing temperature due to plasticization of a thin surface layer of 10-500 μm. The metal salt is subsequently reduced to produce zero-valent metal nanoparticles by a second infusion of a reducing agent or a thermal or photochemical reduction process. The growth and agglomeration of the nanoparticles is arrested by the high viscosity of the polymer matrix, producing a stable nanocomposite.

In order to examine how nanoparticle size distribution and concentration are affected by soak times in the salt and reducing agent solutions, combinatorial, high-throughput screening methods have been applied. Particle size distributions are characterized rapidly by small-angle x-ray scattering (SAXS) using a "dual gradient" nanoinfusion matrix. In addition, an improved method of the nanoinfusion process has been demonstrated that displays significant enhancements to nanoparticle concentration (volume fraction) in thermoplastic polyurethane elastomers (TPUs), as well as decreased average particle size. This latter method involves the creation of an interpenetrating layer of a functionalized monomer via an infusion-polymerization approach. Said functional group is subsequently used to reduce the metal precursor as it is infused using the same processing step as the above method. TEM images show significantly higher volume fraction of nanoparticles using this method, providing the potential for more drastic improvements in optical and other properties.

Another material of interest for synthesis of nanocomposites are liquid crystalline elastomers. Liquid crystalline elastomers have received attention for their unique mechanical properties, which underlie their potential for use in applications such as artificial muscles (due to the electroclinic effect) and constrained vibration damping applications (due to their broad peak in tan δ versus either temperature or frequency). An interesting feature observed in the liquid crystalline elastomers produced in our groups is the formation of a neck in the sample under uniaxial tension. The mechanical response of these smectic main-chain liquid crystalline elastomers (MCLCE) has been characterized at a variety of strain rates and temperatures in order to understand the cause of the observed neck formation. A well-defined yield stress is observed at a critical strain that is essentially independent of strain rate, followed by necking and cold-drawing. Cold-drawing is rarely observed in liquid crystalline elastomers, but we believe that it is observed in MCLCE due to the unfolding of hairpin chains at the start of the polydomain to monodomain transition. A neck forms as the hairpins straighten out, resulting in a decreased cross-sectional area that promotes yielding. Infusions of both metal nanoparticles and dichroic dyes were attempted.

# TABLE OF CONTENTS

# LIST OF FIGURES

# LIST OF TABLES

# ACKNOWLEDGEMENTS

# Chapter 1

# Introduction

The term "elastomer" encompasses a wide variety of polymer materials, both thermosetting and thermoplastic, which are characterized by their elasticity. Due to their rubbery nature, this class of materials has achieved a great deal of commercial success in applications such as seals, adhesives, and molded flexible parts. Herein, two primary elastomer systems are considered: thermoplastic polyurethane elastomers (TPUs) and smectic main chain liquid crystalline elastomers (MCLCE). This dissertation deals with nanocomposites of these elastomers with both organic dyes and noble metal nanoparticles. These systems are interesting due to the addition of features on the size scale of the polymer chains, resulting in changes to the observed macroscopic properties of the samples. In the polymer/metal nanocomposites, the addition of nanoparticles imparts characteristics of the filler, such as conductivity or useful optical properties, to the flexible elastomer sample. In the latter case, liquid crystalline elastomers exhibit unusual mechanical behavior due to the coupling of the order inherent in the polymer chains with that of the rigid liquid crystal mesogens. Processing methods for synthesizing nanocomposites within these elastomers via diffusion-based techniques are investigated herein. The following sections introduce the key techniques used, such as AURA[®] Infusion Technology and combinatorial sample preparation, as well as the properties of the TPUs and LCEs tested.

## 1.1 AURA[®] Infusion Processing

AURA[®] Infusion Technology (hereafter simply referred to as AURA) refers to a collection of patented processing technologies developed at Bayer MaterialScience as a means of coloration for polymer articles that have already been molded or extruded.[1-8] The color is infused via immersion of a plastic article in a proprietary solvent mixture containing an added dye to produce a color change in a short time, usually less than 10 minutes. The infused dye penetrates the surface of the polymer and thus will not rub off with use. Infusion is usually done at a

temperature greater than room temperature to expedite the diffusion of solvent and dye into the plastic. AURA processing can be performed on opaque and translucent parts made from a variety of materials, including polycarbonate (PC), acrylic, and thermoplastic polyurethane elastomers (TPUs), with no significant change to the mechanical properties or surface characteristics of the article. Spray coating methods can be employed which recycle dye from the bottom of the spray apparatus.[6] Spray coating also improves uniformity, requires less solution heating, and eliminates transport problems to a water rinse step, when compared to dip-dying at an industrial level.[6] At the end of processing, remaining dye solution can be collected and separated into unused dye and solvent using activated carbon.[7] The processing system is considered to be relatively sustainable due to the ability to reuse this recovered solvent. Most recently, AURA has been extended as a means of infusing various property-enhancing agents, such as ultraviolet (UV) stabilizers, optical brighteners, mold release agents, antistatic agents, thermal stabilizers, infrared (IR) absorbers, and antimicrobial agents.[7,8]

One of the key advantages of AURA is the frugal amount of solvent and dye used. Traditionally, dyes or pigments have been directly incorporated into a polymer, for instance via compounding of the dye into the molten polymer.[7] Slightly colored or tinted articles are difficult to create via such direct incorporation methods.[7] In such instances, a large quantity of dye is used, and it is difficult to sufficiently reduce the amount of dye while still achieving an even coloration. Methods of introducing dyes using a solution in contact with the article surface allow for control of the amount of dye entering the article, via dye concentration and time and temperature of infusion, and are thus better suited to slightly colored and tinted applications.[7] In AURA, the article is processed as long as needed to achieve the desired color, after which immersion or spraying is stopped. This flexibility is useful in applications such as sunglass lenses, where tinting via an immersion step in a dye solution can reduce light transmission and mitigate glare.[4,5] The amount of solvent and dye consumed can be further decreased via process improvements.

### 1.1.1 Solvent Composition and Infusion Conditions

AURA uses a ternary solvent system, consisting of 70 % water, 20 % butyl cellosolve (BCS), and 10 % diethylene glycol (DEG) (see Fig. 1-1).[2,3] Each component has a specific purpose in the process. Both BCS and DEG serve as plasticizing agents for the polymer in the surface layer of

the article being treated, increasing the free volume of the system. DEG has an additional function as a surface leveling agent.[3] It allows for the even coloration of the article, without patchiness. Instead of BCS and DEG, a variety of alternative plasticizing agents may be used, such as propylene glycol propylether or tripropylene glycol propylether;[3] however, the present work will be concerned only with the DEG formulation. Water is a poor solvent for the polymer article and, as such, is present in order to prevent complete dissolution of the polymer in the BCS and DEG. Water may also enhance the solubility of certain hydrophilic dyes and compounds with the polymer. The dye amount sufficient for coloration is generally 0.1 to 15 % w/w and is most commonly about 0.4 to 2 % w/w.[2,3]
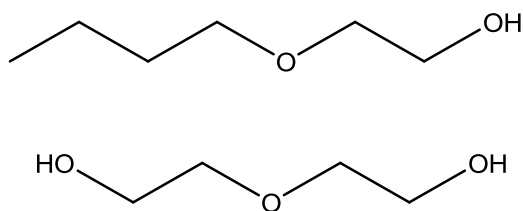
Figure 1-1. Chemical structures of the non-aqueous components of the infusion solvent: 2-butoxyethanol (BCS, top) and 2-hydroxyethyl ether (DEG, bottom).

The dyeing takes place at a time and temperature suitable to allow a sufficient amount of dye enter the polymer article. Time is kept to a minimum, and thus temperature of the solution is increased to speed up the infusion wherever possible. Both higher dye concentrations and higher temperatures can be used to increase the rate of dyeing.[5] As such, 90 to 99 °C is typically used for infusions such that temperature is as high as possible without boiling.[1,5,7] However, lower temperatures can be used where appropriate. For instance, a TPU sample with much lower glass transition temperature than polycarbonate can be sufficiently dyed in less than ten minutes at 50 °C to 60 °C. Processing temperatures are generally at or above room temperature.[7]

## 1.1.2 Relevant Dyes and Polymers

AURA can be applied to both thermosetting and thermoplastic polymers, as well as blends and copolymers of two or more of the relevant polymers. Such relevant polymers include polyesters, polycarbonates (including both aromatic and aliphatic polycarbonates), polyesterpolycarbonate copolymers, acrylonitrile-butadiene-styrene (ABS), copolymers of polymethylmethacrylate (PMMA) and styrenic polymers, polyalkyl(meth)acrylate, polyamide, and polyurethane.[1,2,4,5,7] Note that although styrene copolymers are included in this list,

particularly ABS, AURA is not applicable to homopolystyrene.[5]   The focus of the patent literature is on polycarbonates, and more specifically on thermoplastic aromatic polycarbonates.[1,2,4]   AURA can be applied to articles produced via a variety of methods, including compression molding, injection molding, rotational molding, extrusion, injection and extrusion blow molding, and casting.[2,7]   Furthermore, the articles to be processed may contain a wide variety of fillers and property-enhancing moieties, such as metal flakes, flame retardant agents, opacifying agents (such as titania particles), light-diffusing agents (such as cross-linked PMMA minispheres), UV stabilizers, hydrolytic stabilizers, and thermal stabilizers.[1,7]

Numerous organic dyes are suitable for AURA infusion into plastics (see Fig. 1-2). The prerequisite for successful use of a given dyes is its solubility within the plastic.   For diffusion into a plane sheet, permeability can be described by the equation

$$P = DS \tag{1-1}$$

where P is the permeability constant, D is the diffusion coefficient, and S is solubility coefficient.[9]   As such, adequate solubility is absolutely required for successful infusion.   Broadly, the dye is chosen from static dyes, photochromic dyes, and combinations of the two.[7]   Static dyes are those which do not substantially change color upon exposure to UV light, while photochromic dyes are those that do change color upon exposure to UV light.[7]   The latter functions via reversibly converting into an open or active form, which is colored, when exposed to a particular wavelength of UV light.   The most successful dyes are disperse static dyes, such as disperse blue 3, disperse red 13, and disperse yellow 3.[2,3,7]   More generally, static dyes of the classes of azo, diphenylamine, or anthraquinone compounds infuse readily into plastics of interest to Bayer MaterialScience.[1-4,7]   Dyes known as solvent dyes, such as solvent blue 35 and acridine orange base, are found to be viable with AURA, but their color is noticeably less intense than that of the disperse dyes.[2,4]   A class of static dyes known as direct dyes and dyes referred to as acid dyes do not provide a suitable level of color and are generally not used, though acid dyes work well when used with nylon.[2,7]   Of the photochromic dyes, spiro(indoline)naphthoxazines, spiro(indoline)benzoxazines, and benzopyrans are examples of dyes that infuse readily into TPUs and PCs.[7]   However, it is interesting to note that the photochromic nature of these dyes is lost upon infusion into thermoplastics, likely due to their conformation becoming trapped upon infusion into the polymer matrix.[7]   Polymers with sufficient free volume to allow the dye to make conformational changes do not exhibit this suppression of photochromic properties.
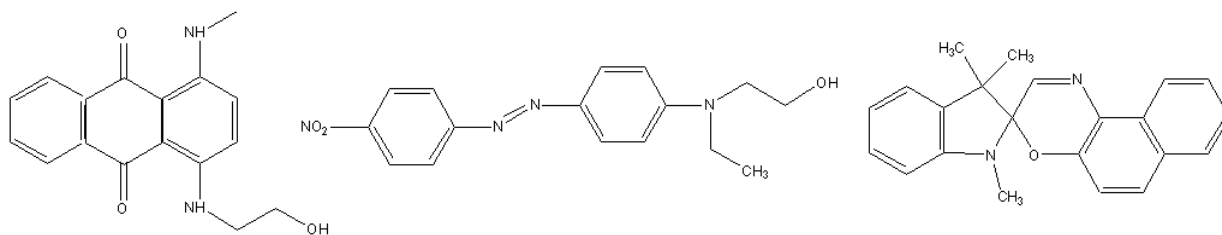
Figure 1-2. Static dyes containing anthraquinone groups (e.g. disperse blue 3, left) or azo groups (e.g. disperse red 1, middle), and certain photochromic dyes (e.g. spiro(indoline)naphthoxazine, right) have all been infused using AURA.

## 1.2 Polymer Nanocomposites

Polymer-inorganic nanocomposites are an interesting and potentially useful class of materials which combine the ease of processing of a polymer with the optical, barrier, and electrical properties of an inorganic nanofiller. Examples of nanofillers include carbon-based (carbon nanotubes, carbon black, nanographite, nanodiamond), oxides (clay, zirconium phosphate, silica), and metals/intermetallics (gold, silver, platinum, palladium).[10] Herein, we will primarily discuss the nanocomposites of polymers with clays, carbon nanotubes, and, most particularly, metal nanoparticles.

The term nanocomposite was first used in the polymer field in a paper in 1990.[11] "Polymer nanocomposite" has evolved to refer to a multi-component system that is primarily polymer with some minor constituent (or constituents) with a dimension less than 100 nm.[12,13] These systems have received a great deal of research attention since polymer/layered silicate clay nanocomposites were first demonstrated in a nylon-6/clay system synthesized at Toyota Central R&D Labs Inc. in 1985.[10,11,14] This first demonstration generated tremendous interest due to the large increase observed in elastic modulus, strength, heat resistance, and gas barrier properties, in addition to a decrease in flammability. These properties were largely due to the quality of the exfoliation of the clay, which was separated into almost singular platelets.[10,14] Automobiles which made use of the nylon-6/clay system were first released in 1989, and the field has grown significantly since. For example, in 2005 alone, polymer nanocomposites were the topic of some 500 papers in major journals.[11]

It is worth noting that "nanotechnology" was not a new invention with the work at Toyota in the 1980's. Carbon black reinforcement of elastomers, naturally occurring fibers, phase

separated polymer blends, and organic-inorganic composites from sol-gel chemistry have all existed with the potential for features on a nanometer scale before the recent blossoming of the polymer nanocomposite field.[15] Larger scale composites, such as those with glass fiber, talc, calcium carbonate, carbon black, and many other fillers have all been used to confer property improvements to polymers for some time.[11] Generally between 20-40 % w/w of these fillers are incorporated, resulting in a phase separated composite.[11] By moving to a smaller nanofiller content a more uniform distribution can be created, such that the interfacial area between nanofiller is greatly increased as is the interaction between the polymer and the filler. For instance, compared to glass-fiber composites, polymer/clay nanocomposites are lighter, have a longer useful life, are much smoother and paintable, are more transparent, and more recylable.[11]

In addition to structural, barrier, and flame retardance applications, nanocomposites hold potential in a variety of other areas, such as polymer blend compatibilizers, biomedical materials (such as nanofiber scaffolds and drug delivery applications), fuel cell membranes and electrode binders, photovoltaic anodes, hole injection layers, light emitting layers, and sensor applications.[15] One nascent field of research is in the production of bionanocomposites, which use naturally occurring polymers. These materials possess the same property enhancements seen in synthetic polymers, but also possess biocompatibility, biodegradability, and, depending on the biological or inorganic moiety employed, functional properties.[16] In addition to their synthesis, characterization, and applications, the rise of nanocomposites as an oft-studied material has catalyzed a large effort in toxicity studies of such materials, specifically investigating the effects that they have on biological tissues as a function of size, morphology, mass, composition, crystallinity, surface area, surface chemistry, reactivity, and thermal response.[17]

Successes on the level of the nylon-clay system are rare, possibly due to a lack of a complete understanding of the changes in polymer behavior due to the interaction of the polymer with such a large surface area of filler material as is seen in a nanocomposite.[10] Polymer nanocomposites are distinguished by the similarity of the dominant length scales of the radius of gyration of the polymer chains, a dimension of the nanoparticle (diameter of nanospheres or tubes, thickness of nanoplates), and the mean distance between the particles.[10] With the dimensions of polymer, particle, and morphology all on the same length scale, interfacial interactions between polymer and particle, as well as cooperativity between particles, dominate the macroscopic properties of the composite.[13] Notably, nanofillers alter the crystallinity and glass transition temperature of the polymer matrix, among other effects.[15] For example, it can be argued that the favorable interactions between the polymer and a surface-modified nanoparticle in

a stable nanocomposite will cause the glass transition temperature ($T_g$) of the polymer to increase (Fig. 1-3). Conversely, processing techniques which disperse unmodified particles, such that there is not a favorable interaction between filler and polymer, may see a decrease in $T_g$ for the polymer.[10] Early nanocomposite research tended to focus on understanding the underlying synthetic and physical chemistry aspects of colloidal particle physics, and mechanical, thermal, and physical properties of such nanocomposites. More recently, research has begun to move away from synthesis and characterization towards an improved understanding of the physics of the polymer in such materials, such that better nanocomposites may be engineered for specific applications.[10] In order for polymer nanocomposites to transition to truly engineered, designed, functional systems, a better understanding of the structure-property-processing relationship is needed.[10] Additionally, our understanding and control must be extended beyond the interfacial interactions of the particles to the extent, spatial arrangement, and ordering of the fillers within the polymer.[13]
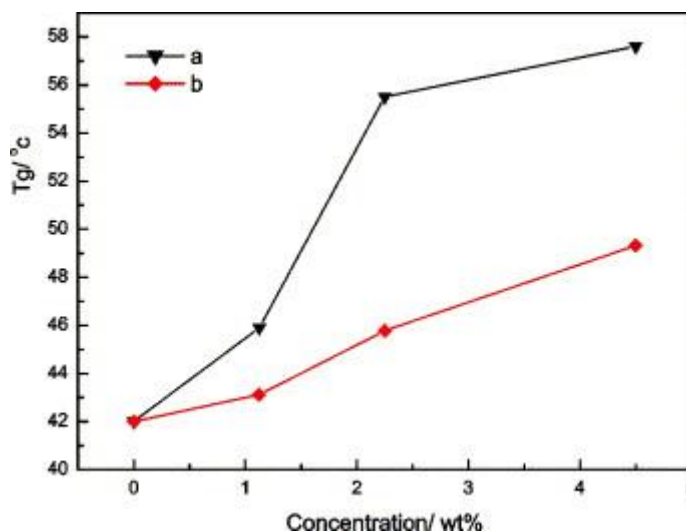


Figure 1-3. An example of the increase of glass transition of a polyurethane sample as silica particles, synthesized via addition of tetraethyl orthosilicate (TEOS) monomer to the matrix. The functionalized silica interacts favorably with the polyester segments. A larger $T_g$ increase is seen for in situ polymerization (a.) than for melt blending (b.) due to the increased opportunity for this interaction to take place. [Source: Chen, *J Col Int Sci* 2004]

Below is an introduction to three primary classes of polymer nanocomposites. Though by no means a complete review of the vast amount of literature on each, the chief synthesis methods, challenges, and applications of each are addressed.

**1.2.1 Clay/Polymer Nanocomposites**

Clay/polymer nanocomposites are one of the most widely studied polymer nanocomposite systems, certainly owing in no small part to the success seen in the nylon-6/clay system discussed above. Nanocomposites of layered inorganic crystals and polymers generally refer to fillers in the form of sheets of a few (1-3) nm thick and hundreds to several thousand nanometers long.[18] The clay portion of these nanocomposites can be any of a wide range of inorganic fillers. Chief among them are the layered silicates due to availability and ease of surface treatment. These include mica, fluoromica, hectorite, fluorohectorite, saponite, and montmorillonite (MMT), the latter of which is the most commonly used (Fig. 1-4).[18,19] Layered silicates have a crystal structure defined by layers of two tetrahedrally coordinated silicon atoms fused to an edge-shared octahedral sheet of either aluminum or magnesium hydroxide. Substitutions can be made within the layers (such as $Al^{3+}$ by $Mg^{2+}$ or $Fe^{2+}$, or $Mg^{2+}$ by $Li^+$), generating negative charges that are counterbalanced by alkali and alkaline earth cations. Thus, such layered silicates have a moderate surface charge.[18] One key feature of these nanocomposites is the low fraction of filler needed to impact a useful change of properties. For instance, addition of as little as 1-5 % of MMT into a polymer matrix can produce a significant improvement to mechanical strength due to the dimensions and high aspect ratio of the clay sheets.[12,19] For example, addition of 4 % w/w Na-MMT to poly(vinyl alcohol) results in a three times increase in Young's modulus compared to the unmodified bulk value.[20]
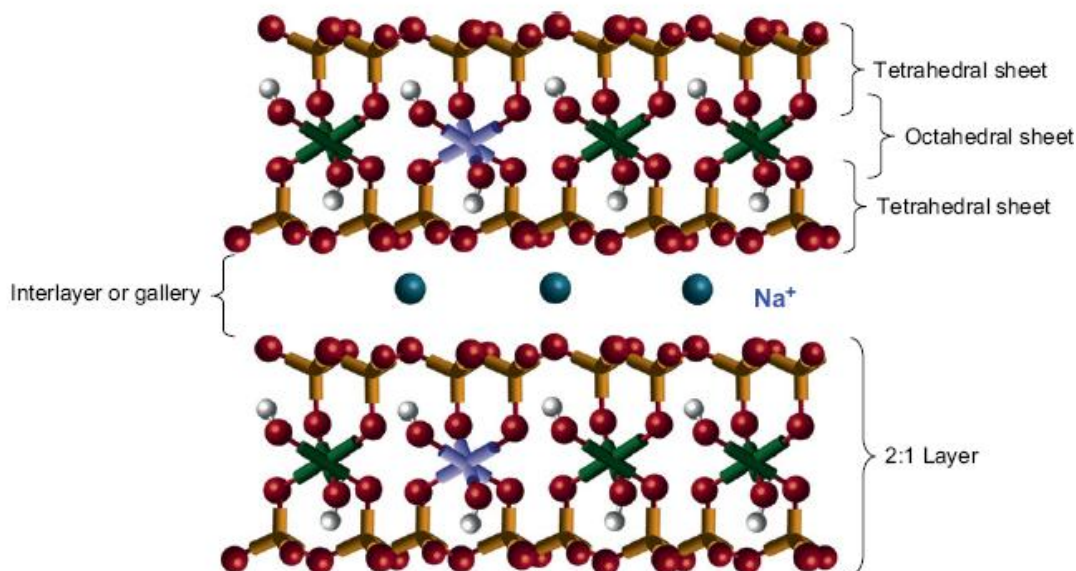
Figure 1-4. Schematic of the layered structure of montmorillonite. Orange tetrahedra represent silicon atoms, red spheres represent oxygen atoms, white spheres represent hydrogen atoms, green octahedra represent aluminum, purple octahedra represent magnesium atoms, and blue spheres represent sodium ions. [Source: Paul, *Polymer* 2008]

The applications of clay/polymer nanocomposites are numerous. Of the various forms of polymer nanocomposites, nanodisperse clays are the most convenient for partial improvement of thermal stability and elastic modulus, as well as gas permeability.[18] In addition to these properties, addition of small amounts of clay nanofillers to a polymer imparts increased tensile strength and modulus, large increase in heat distortion temperature, increase in smoothness and paintability, increase in transparency, and similar recyclability.[11] However, care must be taken, as adding too much of the clay nanofiller actually harms these characteristics.[11] Due to these property enhancements, clay/polymer nanocomposites have seen use as coating, structural, and packaging materials.[14] Improvements to the polymer all depend on both the degree of nanodispersion of the layered inorganic filler and the interfacial interaction of the clay with the polymer.[18,19]

Pristine layered inorganic materials are hydrophilic, and only miscible with hydrophilic polymer such as poly(ethylene oxide) (PEO) and poly(vinyl alcohol) (PVA). As such, ion exchange modification with cationic or anionic surfactants bearing long alkyl chains is generally used to make intercalation with the polymer more viable. For example, ammonium cations with long ($C_{14}$-$C_{18}$) alkyl chains may be used to obtain the hydrophobic character necessary for dispersal.[18] Four primary methods exist to prepare clay/polymer nanocomposites: in situ

polymerization, intercalation from a polymer solution, direct intercalation by molten polymer, and sol-gel methods.[19] It is important to note that all methods of clay/polymer nanocomposite preparation involve high temperatures at some point, thus necessitating a knowledge of both the thermal stability and degradation behavior of the polymer.[19]

## 1.2.2 Carbon Nanotube/Polymer Nanocomposites

Carbon nanotubes (CNTs) were first synthesized in 1991 by Iijima.[18,21,22] CNTs possess high flexibility, low mass density, and large aspect ratios, as well as other useful engineering properties, such as high thermal conductivity along the tube and the ability to be synthesized with conductivities in either the semiconducting or metal-like range.[22] Due to these remarkable properties, they are a logical dispersant in polymer nanocomposites for improvement of thermal, electrical, and mechanical performance.[18,21,22] CNT/polymer composites were first synthesized by Ajayan et al. in 1994.[18,22] The properties of CNT/polymer nanocomposites depend on a number of factors related to both the synthesis of the CNT and its dispersion within the polymer, including the type of nanotube, chirality, purity, defect density, nanotube dimensions, nanotube loading, dispersion state, alignment of nanotubes, and interfacial adhesion between polymer and nanotube.[22] Two primary varieties of CNT exist. Single-walled CNTs (SWNTs) are a single graphene sheet wrapped into cylindrical tubes with diameters of 0.7 to 2 nm, with lengths generally in the micrometer range, while multi-walled CNTs (MWNTs) are formed from concentric SWNTs, and thus have larger diameters (Fig. 1-5).[18] In addition to tubes, nanographene sheets with thicknesses of 0.34 nm to 100 nm have also been investigated as useful nanofillers.[23] Although CNTs are more expensive and difficult to handle relative to other nanofillers, the improvements that they offer to the mechanical and electrical properties of a polymer are significant enough to motivate widespread consideration as a commercial product.[18] One drawback to CNTs is their negative health effects, particularly due to inhalation.[17]

SWNT                    MWNT
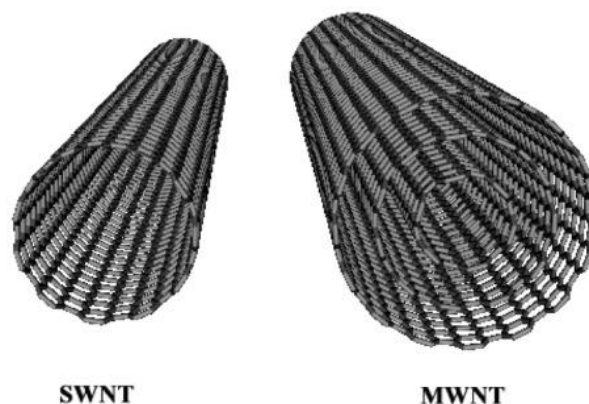
Figure 1-5. Schematic structures of single- and multi-walled carbon nanotubes.    [Source: itech.dickinson.edu/chemistry/?p=422 02/12/10]

The major challenge of dispersing CNTs within a polymer is the strong $\pi$-$\pi$ interaction between tubes, in addition to entanglements, which results in a strong tendency to form aggregates of 100-500 CNTs packed together.[18,21]   It is very difficult to achieve homogenous distribution of CNTs using melt blending processes.[21]   While several strategies have been developed to disperse CNTs reasonably well within the polymer, such as solution blending, melt blending, and in situ polymerization methods, the most pursued strategy is the surface modification of the CNTs to improve polymer-CNT interaction while deterring CNT-CNT interactions.[18]  Two main approaches are prevalent.[21,22]  In the first, select functional groups are grafted onto the CNT sidewalls to improve the interaction with the polymer matrix or to serve as a bonding point for polymer chains.  Though this approach would be an excellent approach for mechanical property enhancement due to an improved load transfer between polymer and CNT, the current methods of achieving grafted functional groups, such as ball milling and chemical reaction in solvent, only functionalize a fraction of the nanoparticles.[21]  In addition, these methods may disturb the delocalized electronic system of the CNT, which is largely responsible for its electrical and mechanical properties.[21]   A second strategy aims to non-covalently modify the CNT, such as through surfactant-assisted dispersion, polymer wrapping, and plasma polymerization.[21]  While such processing does not perturb the electronic nature of the CNT, it also does not optimize the CNT/polymer surface interaction as well as the first method.[21]

Much effort has been put into producing strong, lightweight CNT nanocomposites for a variety of applications, including electrochemical, field emission and nanometer-size electronic devices, sensors, and functional materials for space and air technologies.[18]  Increased electrical conductivity and a low percolation threshold have been achieved in a variety of materials

including PMMA and PC, as well as, to a lesser extent, polyolefins.[18]  There is also interest in mechanical applications, as CNTs can improve tensile modulus and strength.  However, strain at break, and thus polymer ductility, is generally decreased by the presence of CNTs.[18]

### 1.2.3 Noble Metal/Polymer Nanocomposites

Metal nanoparticles have been utilized for catalytic properties for several decades and are more recently becoming interesting for nanocomposite synthesis, particularly for applications that leverage their catalytic and optical properties.[18]  Noble metal nanoparticles in particular have a dramatic effect on the optical properties of a polymer, most obviously due to the real, natural color imparted to the article by the addition of the nanofiller.[18]  For this reason, gold nanoparticles have been used for centuries as pigments, such as in stained glass.[24]  Contemporarily, inorganic materials, both ionic precursors and elemental nanoparticles, have been recognized as desirable for dispersal throughout a polymer matrix for their physical properties, particularly their high electrical conductivity and catalytic capability.[25]  Metal nanoparticles are also industrially useful when embedded in a polymer as a means of increasing the adhesion of metal layers deposited via electroless deposition, which is very often employed to metallize polymer surfaces due to its ability to uniformly coat complicated shapes.[26]  Gold and silver nanoparticles, in particular, have applications in many fields, including catalysis, sensing, recording media, surface enhanced Raman spectroscopy substrates,  microwave absorption, biotechnology, and optics.[27-30]

The bright colors of metal nanoparticles result when an electromagnetic field induces the coherent oscillation of the conduction band electrons.  This resonance is referred to as a surface plasmon and is a phenomenon observed only in small particles, not individual atoms or bulk materials.[24,31]  As nanoparticles increase in size, the surface plasmon absorbance is seen to broaden and red-shift.[24,31]  In order to understand this broadening and red-shifting, the Mie theory of scattering must be considered.  Mie solved Maxwell's equations with the appropriate boundary conditions for spherical particles, resulting in an expression for the total extinction coefficient cross section due to absorption and scattering as a summation over all electric and magnetic multipole oscillations.[24,31]  The result of this analysis are two regimes for small spherical particles.  For particles much smaller than the wavelength of the exciting light and with diameter (2r) less than 25 nm, Mie theory reduces to:[24,31]

$$\sigma_{ext} = \frac{9V\varepsilon_m^{3/2}}{c} \cdot \frac{\omega\varepsilon_2(\omega)}{[\varepsilon_1(\omega)+2\,\varepsilon_m]^2+\varepsilon_2(\omega 2)^2} \tag{1-2}$$

where $\sigma_{ext}$ is the extinction cross section (in units of $nm^2$), V is the spherical particle volume, c is the speed of light, $\omega$ is the angular frequency of the exciting radiation, $\varepsilon_m$ is the dielectric constant of the surrounding medium (assumed to be frequency independent), and $\varepsilon_1(\omega)$ and $\varepsilon_2(\omega)$ are the real and imaginary part of the dielectric function of the particle material, respectively. Resonance occurs when $\varepsilon_1(\omega) = -2\,\varepsilon_2$, if $\varepsilon_2$ is small and weakly depends on $\omega$. Particle size only scales $\sigma_{ext}$ intensity through V in this equation, but experimentally the plasmon bandwidth is seen to vary strongly with diameter.[18,24] To reflect this size dependence in equation 1-2, the dielectric function is assumed to be size dependent for these small particles ($\varepsilon_1(\omega,r)$ and $\varepsilon_2(\omega,r)$).[24,31] Because of this assumed size dependence, changes in the optical absorption spectra in this size regime are referred to as "intrinsic size effects."[24,31] For particles with $2r > 25$ nm, the extinction coefficient explicitly depends on the nanoparticle size because higher order terms, which depend directly on particle radius, begin to contribute.[24,31] With increasing size, the plasmon absorption maximum is shifted to longer wavelength and the absorption bandwidth increases as the size becomes closer to the wavelength of the incident light. The changes in the absorption spectra with particle size in this larger size regime are termed "extrinsic size effects" because the size dependence enters in through the full Mie equation, with no assumptions about the complex dielectric function.[24,31]

Due to the surface plasmon resonance, gold nanoparticles could simply be applied as a method of coloring polymers such that the color will not photobleach in the way that organic dyes will, but it also provides access to non-linear optical properties when combined with shaped (i.e. non-spherical) particles and/or anisotropic distributions of particles.[18] Interest in metal nanoparticles is due not only to the bright colors that they exhibit, but also to the ability to tune the electronic and optical properties by fine control of parameters including: particle size and shape, aggregation state, and the nature of the nanoparticle matrix.[31,32] Furthermore, gold nanoparticles are useful as a model system for metal nanoparticles in general, due to their chemical stability as elemental nanoparticles and their easy reduction to said state.[33]

It can be difficult to achieve well-dispersed noble metal nanoparticles within a plastic article, due in part to the fact that the nanoparticles are too small to be effectively mixed. That is to say, the shear forces generated by most mechanical mixing means are insufficient to break the agglomerates. The result is that adequate dispersion is not achieved, thus melt mixing is rarely employed.[18,34] If nanoparticles can be successfully introduced to a polymer without aggregation, then suspension in a polymer is advantageous, as the polymer matrix serves to prevent further

agglomeration of the embedded particles.[35] As such, other strategies must be pursued in order to achieve a quality dispersion of metal nanoparticles within the polymer matrix. The two primary classes of methods involve the use of either pre-synthesized metal nanoparticles or the in situ synthesis of the nanoparticles within the polymer.

Whether in situ or in solution, the synthesis of metal nanoparticles is frequently accomplished through the reduction of an ionic metal precursor to elemental nanoparticles (Fig. 1-6). Thermal decomposition methods may also be used, such as the heating of $Fe(CO)_5$ to 200 °C in the presence of the proper stabilizing agents, but purely thermal methods tend to involve precursors that are both expensive and toxic.[36,37] Chemical reduction is more economical, as well as employing temperatures viable for in situ reaction in polymers. Reducing agents such as sodium borohydride, sodium hydroxide, sodium citrate, N,N-dimethylformamide, or formamide can be used to reduce metal precursors such as $HAuCl_4$ to elemental nanoparticles in solution.[33,38-44] Sodium borohydride is one of the most often used reducing agents, found to be successful with a number of metal precursors.[45] Reduction of $HAuCl_4$ with $Na_2S$ has also been shown to be viable.[46] Silver ions (often in the form of $AgNO_3$) can be reduced with sodium hydroxide, sodium carbonate, sodium borohydride, sodium citrate, N,N-dimethylformamide, formamide triethylamine, pyridine, and formaldehyde.[42,43,47] Because sodium in ionic reducing agents may contaminate the metal nanoparticles, use of organic reducing agents is preferable when possible. Along these lines, $HAuCl_4$ is reducable to gold nanoparticles by a variety of amines, including 4-aminophenol, triethylamine, and glycine.[40] A thorough study has been done in order to ascertain the reduction potential range required for various amines to be successful reducing agents for $HAuCl_4$.[40] Generally, these reductions are of the form:[40]

$$HAuCl_4 + 3\ NR_3 \rightarrow Au^0 + 3\ NR_3\bullet^+ + H^+ + 4Cl^- \tag{1-3}$$
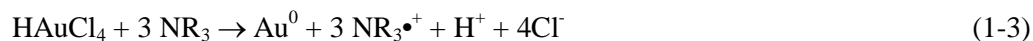
$AgClO_4$ is also a successful metal precursor, which can be reduced with sodium borohydride.[48,49] Platinum has also been studied, with $H_2PtCl_6$ being reducible to nanoparticles with sodium borohydride.[43] Some more interesting systems involve the use of reduction triggered by thermal or photochemical means. Irgacure® 2959 (1-[4-(2-hydroxyethoxy)phenyl]-2-hydroxy-2-methyl-1-propane-1-one) is a radical initiator that produces ketyl radicals upon irradiation by 350 nm light.[50] These radicals can reduce HAuCl to $Au^0$ via a two-step reaction, providing a means for photochemical reduction.
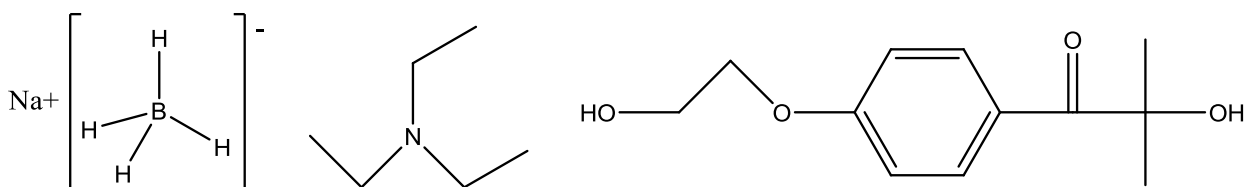
Figure 1-6. Sodium borohydride (left) and triethylamine (middle) are two common reducing agents for the formation of metal nanoparticles. Radical initiators such as Irgacure® 2959 (right) are also useful as UV-initiated reducing agents.

Nickel, copper, and iron nanoparticles are more difficult to synthesize than gold, silver, and platinum nanoparticles, as they are more easily oxidized. Nonetheless, successful reduction methods have been developed for these metals. Copper nanoparticles can be produced via reduction of CuCl$_2$ with sodium borohydride.[51] FeCl$_2$ can be reduced to iron nanoparticles with sodium borohydride, while FeCl$_3$ is reducible by sodium borohydride, hydrazine, and lithium borohydride.[36,37,52] NiCl$_2$ has been successfully reduced to elemental nanoparticles with either hydrazine or sodium hydroxide to produce nanoparticles.[53] Due to the lower standard reduction potential of metals such as iron, nickel, and cobalt relative to noble metals, the addition of a small amount of noble metal ion can help promote nucleation when using both the thermal decomposition and chemical reduction synthesis methods.[36] Notably, the addition of palladium to the reduction of FeCl$_3$ with sodium borohydride resulted in particles of noticeably smaller diameter.[36]

It is important to note that, although the metal salts and reducing agents have been concentrated on in the above discussion of reduction methods, the pH, solvent, and stabilizers used are also very important in determining both the viability of the nanoparticle synthesis and the quality (shape, size, etc.) of the nanoparticles produced. Aqueous reduction methods are generally desirable, and such instances make use of hydrated forms of the metal salts, such as Ni(NO$_3$)$_2$·6H$_2$O or HAuCl$_4$·3H$_2$O. With respect to polymer/metal nanocomposites, it is often noted that the relative amounts of polymer, reducing agent, and metal precursor used in the in situ nanoparticle synthesis methods play a part in the final particle size, shape, and distribution.[54]

Use of pre-synthesized metal nanoparticles allows for the leveraging of the many nanoparticle synthesis methods available to produce nanoparticles with controllable size and shape, as may be desirable for optical and other applications. However, surface modification is required in order to ensure compatibility of the nanoparticle to the polymer matrix.[32] Due to this requirement, these methods may be undesirable for an industrial setting due to time and cost constraints.[55] Two primary methods of dispersing the surface-modified nanoparticles are the

polymerization of a monomer around the surface modified particles or via solution casting of a mixture of dissolved polymer and nanoparticles.[29] Interestingly, the use of pre-synthesized metal nanoparticles with appropriate surface functionalization has been shown useful in controlling the dispersion of particles within the polymer matrix. A prime example involves the capping of gold nanoparticles with a PS and poly(ethylene glycol) (PEG) block copolymer.[56] These particles are dispersed in a PS-block-PMMA, where the outer PEG layer compatibilized the nanoparticles with the PMMA segment. Upon thermal treatment to break the PS-PEG linkage, the nanoparticles, now coated in PS, migrated to the PS segments of the block copolymer matrix.

In situ formation of metal nanoparticles within the polymer matrix is a relatively simple process that usually involves the heating and/or UV irradiation of the metal precursor, resulting in the formation of elemental nanoparticles that are stabilized and size-restricted by the polymer matrix.[29,57,58] Reduction can also be accomplished via chemical means, such as the exposure of a polymer article containing a metal precursor to hydrazine gas.[29] Despite its simplicity, the rigorous control of the particle shape and size is greatly compromised compared to pre-synthesized nanoparticle methods. In situ methods can be further broken down into the simultaneous synthesis of polymer and metal nanoparticles or the production of nanoparticles from a precursor that is embedded within the polymer.[29,32] In the latter case, the precursor is often added to the polymer in solution, allowing it to be cast into a film prior to the reduction step. Addition of the precursor to the dissolved polymer creates a more homogeneous distribution of metal precursor, and thus of metal nanoparticles following reduction, throughout the film than methods which introduce the precursor to the solid polymer.[29] However, methods which introduce the precursor to a finished polymer article allow for the creation of a metal nanocomposite in geometries other than thin films. It is worth noting that conversion of precursors to nanoparticles within the polymer can generate unwanted byproducts, such as gases that may remain in the article.[29] Fortunately, careful choice of chemistry can avoid such situations.

A variety of examples of "in situ reduction" methods exist. Reduction via heat treatment works by either decomposing the precursor or causing some change to the polymer, leading to the matrix itself becoming the reducing agent.[29] For instance, $HAuCl_4$ added to polystyrene-block-poly(2-vinylpyridine) (PS-b-PVP) and subsequently heated to 200 °C results in octahedral gold nanoparticles.[29] Similar heating works for films of PMMA containing (1,1,1,5,5,5-hexafluoroacetylacetonato)Ag(I) to form silver nanoparticles following casting and irradiation.[29] An example of UV irradiation is found in the system containing $HAuCl_4$ and ethylene glycol,

added to solutions of PVA, allowing for production of gold nanocomposites.[29]   Porel et al. also produced gold nanoplates within PVA.[59]   Aqueous solutions of $HAuCl_4$ and PVA were spin-coated onto glass or quartz and heated to 100-170 °C for between 5 and 60 minutes.  The PVA served to both reduce and stabilize the synthesized nanoparticles.    The shape and size of the resulting gold nanoplates was found to depend on the $HAuCl_4$/PVA ratio, the heating time, and the heating temperature.  PVA is often used as a polymer matrix for metal nanocomposites due to the ability of the hydroxyl groups on the polymer to reduce the metal salt under mild thermal treatment.[29]

Another "in situ reduction" strategy is the use of a polymer matrix which, when irradiated with UV light, forms free radicals that will reduce the metal precursor.  An example is the use of methoxypolyethylene glycol with $HAuCl_4$ to form gold nanoparticles or with $AgNO_3$ for silver nanoparticles.[60,61]   Such methods have some potentially interesting applications.  Films of gold nanoparticles in PVA, formed by casting and UV irradiation of solutions of $HAuCl_4$ and PVA, were found to remain colorless while at 0 °C, but turned purple as the temperature increased to room temperature.[62]   Due to this transition, the films were demonstrated to be useful as a freeze indicator, such as for the prevention of spoilage of frozen foods.  Examples of these commonly used methods extend beyond gold.  Photoreduction of $AgNO_3$ infused into blends of PVA and poly(acrylic acid) (PAA) from a methanol solution has been demonstrated to form silver nanoparticles,[62,63] and $AgNO_3$ in solution with PVA can be cast and heated to form silver nanocomposites, via reduction of the silver nitrate by the polymer.[35]

It is also possible to use the structure of a block copolymer as a nanoreactor to produce metal nanoparticles.[64]   PS-block-PVP films immersed successively in 1 % w/w solutions of $HAuCl_4$ in ethanol and sodium borohydride in ethanol yielded metal nanoparticles within the PVP portion of the system, due to the coordination of the $HAuCl_4$ with the pyridine unit of the PVP.[64]   Another unique system involves polymer blends of PVA and sulfonated poly(ether-ether ketone) (SPEEK).[65]   When irradiated with 350 nm light, the benzophenone groups of SPEEK abstract hydrogen atoms from the PVA.    The resulting benzophenone ketyl radicals reduce $AgNO_3$ to silver nanoparticles.  As with many UV methods,  photopatterning is possible via masking during the cure step, which has utility in a variety of applications.[65]

Recently, another class of "in situ reduction" method has received attention.  Super critical $CO_2$ (sc$CO_2$) methods for producing nanocomposites allow for the in situ formation of nanoparticles after the polymer has been processed into its final form.[30,66,67]   Sc$CO_2$ is used as a solvent    for    an    organometallic    precursor,    such    as    (1,5-cyclooctadiene)(1,1,1,5,5,5-

hexafluoroacetylactonate)Ag(I). Following infusion of the metal precursor, subsequent reduction can be accomplished via heating in an autoclave filled with hydrogen.[30,66] Many polymers are known to swell in $scCO_2$, which is why it facilitates rapid infusion of the metal precursor into a polymer, such as polycarbonate.[30,66,68] Swelling of a polymer with a penetrant dissolved in $scCO_2$ was demonstrated in 1986, while the first demonstration of this technique to produce nanoparticles was achieved in 1995 using dimethyl(1,5-cyclooctadiene)Pt(II).[67,69,70] By changing the pressure (while remaining above the critical point of $CO_2$) and time of infusion, both the size and the depth of penetration of the particles can be controlled.[30,66] $ScCO_2$, in addition to being an environmentally benign solvent, also has the advantages of controlling solubility of many precursors via tuning pressure, uniform dispersion due to low viscosity, surface tension, and high diffusivity, and ease of removal from the polymer once the system is returned to ambient temperature.[26,67] Other examples of $scCO_2$ infusion involve the use of (1,5-cyclooctadiene)dimethylPt(II) or Pd(II)hexafluoroacetylacetonate as metal precursors.[26,68] Gas phase infusion techniques have also been accomplished, where gaseous metal precursors are used to introduce the metal to the free volume of a polymer to allow the synthesis of a nanoparticle.[34] An example is the introduction of palladium nanoparticles via exposure to bis(acetylacetonato)Pd(II) with subsequent heat treatment.[29]

The shape and size of metal nanoparticles is dependent on a large number of variables, including the relative concentrations of precursor and polymer stabilizer and the chemical structure of the polymer used.[29,71] As the optical, mechanical, and electrical properties of these particles are largely determined by size and shape, tunable methods are needed to predictably control these variables. For instance, silver nanoparticles in solution have been synthesized using irradiation from a fluorescent tube. Significantly, it was found that when filters were used to expose the solution (containing borohydrate as a reducing agent and silver nitrate as the metal precursor), size and shape could be controlled to a degree via the wavelength of light used.[72] Another more recent study demonstrated the use of light emitting diodes which produced different wavelengths of light as a means of irradiation to produce silver nanoparticles of different sizes and shapes.[73] Such methods, when coupled with the steric limitations of synthesis within a polymer matrix, may be an avenue for enhanced particle control via "in situ reduction" synthesis methods.

As an example of the application of shape control of metal nanoparticles, metal nanorods are potentially useful as polarizers in optical materials, due to their larger absorption coefficients and higher photostability relative to organic moieties.[32] Polarizing films using silver and gold

nanorods have been synthesized by drying an aqueous solution of prefabricated particles and PVA, followed by a slight warming up and drawing of the sample in order to align the particles.[32] It was also found that laser irradiation caused a rod to sphere transition, which could be used to pattern the polarizing portions of a sample. Further, it has been noted that two-photon laser irradiation methods, when applied to films of $HAuCl_4$ and PVA, can be used to produce patterned lines of gold nanoparticles.[74] This latter work was done with an eye on using metal nanoparticles as a means of imparting electrical conductivity or increased mechanical strength to a polymer.

It has been recognized for some time that the melting point of a metal nanoparticle is affected by the particle size.[75] Decreasing the radius of metal particles decreases the melting point of the material dramatically compared to the bulk melting point.[76,77] As the radius of the particle decreases, the ratio of the number of surface atoms to volume atoms greatly increases. Because the liquid/vapor interfacial energy tends to be lower than the solid/vapor interfacial energy, the melting point temperature decreases as the particle gets smaller and the free energy makes it more favorable to be a liquid at a lower temperature.[76] Fig. 1-7 shows experimental and modeled data for the dependence of melting temperature on particle diameter for both gold and silver nanoparticles. Despite the decrease in melting point as particle radius decreases, it is pertinent to note that the melting points of gold and silver nanoparticles even as small as 2 nm in diameter are still well above the melting point of an average thermoplastic polymer.
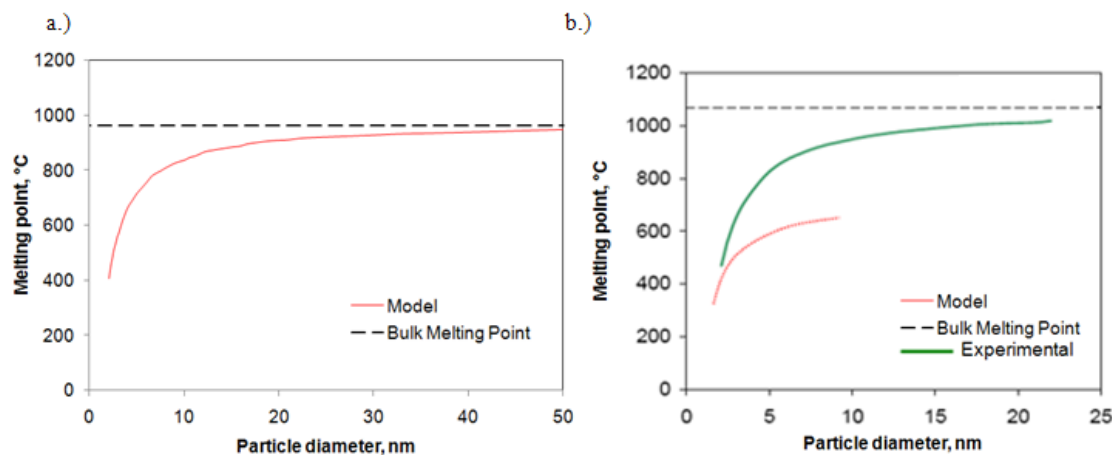


Figure 1-7. Nanoparticle size dependence of the melting temperature of a) silver and b) gold. Data is based on models developed by recent publications. Experimental results are also shown for melting of gold nanoparticles, as are the bulk melting temperatures for both silver and gold. [Adapted from: (a.) Luo, *J. Phys Chem C* 2008; (b.) Cortie, *Mat For* 2002.]

### 1.2.4 Characterization of Nanocomposites

It is important to be able to accurately characterize nanocomposite morphology, specifically particle size, shape, and spacial distribution within the polymer. A wide range of characterization techniques are commonly employed which each possess their own strengths and weaknesses. Though by no means a comprehensive list, frequently encountered techniques include AFM, SEM, EDS, TEM, SAXS, WAXS, SANS, UV-vis, FTIR, DSC, NMR, and spectroscopic ellipsometry. Atomic force microscopy (AFM) is useful as a method of producing images of fillers at or near the surface of a nanocomposite. Different sample preparation and AFM modes may be used to examine a sample. For instance, part of the polymer matrix may be removed via solution etching, and tapping mode AFM may then be used to image the topography of the nanoparticles left embedded in the new surface of the polymer.[78] Alternatively, samples may be microtomed to a smooth surface to allow for phase imaging in tapping mode.[79,80] This latter example compares the driving amplitude to the amplitude of the tip oscillation and allows for differentiation of, for instance, hard and soft regions. Harder nanoparticles within some distance from the surface may be imaged in contrast to the softer polymer matrix.

Electron microscopy methods are frequently employed to images the particles within a nanocomposite. Samples may be prepared for scanning electron microscopy (SEM) using similar methods to those used for AFM as they are both topological methods. However, it may be necessary to thinly coat the surface of the sample with gold to help dissipate charge build-up and avoid sample damage. The polymer matrix may also be completely dissolved or evaporated, leaving only the particles remaining on a substrate surface.[35] However, data pertaining to the particles' distribution through the sample is lost using such methods.[35] Thin nanocomposite films, such as those produced via spin-coating from solution, are also useful for SEM investigation.[74] Often included as an attachment to SEM instruments, energy dispersive x-ray spectroscopy (EDS) allows for elemental analysis of a sample surface. Such analysis is useful in confirmation of successful nanocomposite synthesis, particularly for "in situ reduction" methods.[60] Transmission electron microscopy (TEM), primarily in bright field mode, is very commonly used as a nanocomposite characterization tool. Though TEM is time- and labor-intensive and is often criticized for only analyzing small areas at a time,[15] the ability to create clear images of particles, particularly when the electron density contrast between filler and matrix

is good, makes the method almost indispensable in the characterization of nanocomposites. Electron diffraction patterns can also be generated using TEM for structural analysis.[62]

Scattering and diffraction methods, such as wide angle x-ray diffraction (WAXD), small angle x-ray scattering (SAXS), and small angle neutron scattering (SANS) are also applicable to nanocomposites. WAXD is widely used due to its ease and availability and is particularly suited to characterization of ordered materials, such as crystalline polymers, crystalline particles, or clays.[81] For metal particles, Scherrer's equation,

$$d = 0.9\lambda/\beta cos\theta \tag{1-4}$$

may be used to determine the mean diameter, d, of particles based on the wavelength of the x-ray source ($\lambda$), the full width at half maximum of the diffraction peak ($\beta$), and the diffraction angle ($\theta$).[62,82] In the case of clays, x-ray diffraction allows for the determination of the d-spacing of the layered structures.[83,84] However, care must be taken in interpreting results. For instance, a peak shift to larger d-spacing due to intercalation of clay within a polymer may be canceled by a shift to larger angles due to surfactant degradation.[15] Spatial distribution is information is also not provided by WAXD, thus use of complementary methods such as TEM is often desirable.[81] Small angle x-ray scattering (SAXS) provides a means of interrogating, with relative ease, the size distribution of nanoparticles in a non-invasive fashion, giving an average size taken over the population of particles in the path of the beam.[85,86] The difficulty with SAXS comes in finding an appropriate model for interpretation of the scattering data. Small angle neutron scattering (SANS) is very similar to SAXS in its uses and difficulties. The size scale accessible to each is approximately 1 nm to 20 µm (not including small angle instrumentation).[87] However, there are very important differences. To begin with, SANS facilities are much less common and accessible than SAXS instrumentation. Further, the two techniques are useful for examination of different aspects of nanocomposite samples due to their different contrast mechanisms. The x-rays used in SAXS scatter due to changes in average electron density, such as at the interface of a low electron density polymer and a high electron density metal nanoparticle.[87] The neutron beam used in SANS scatters due to contrast in the nuclear scattering cross section (also called scattering length density).[87] Similarly to the more widely used SAXS, SANS is useful in characterization of the particle dispersion in nanocomposite samples.[88-90] However, by careful choice of deuterated solvent or deuterated polymers to provide contrast, other structures which are not readily accessible to SAXS may be characterized.[90] For instance, the polymer structure in a polymer nanocomposite gel can be determined by matching the scattering length density of the solvent and the clay nanofiller, such that only the structure of the polymer chains is evaluated using SANS.[88]

Non-destructive spectral techniques such as ultraviolet-visible absorption spectroscopy (UV-vis) and Fourier transform infrared spectroscopy (FTIR) have utility in the characterization of nanocomposites as well. UV-vis is an important characterization method, particularly in the case of noble metal/polymer nanocomposites, where the surface plasmon absorbance is clearly detectable.[29] Polarized UV-vis is important for the observation of dichroic behavior in organized collections of particles, such as nanorods in a stretched sample.[18,32] FTIR may be used to probe chemical changes to both polymer and nanoparticles as a result of the combination of the two, such as changes in surfactant molecules at the particle surface or as a measure of the intercalation of clay nanofillers.[81,82,84] "In situ reduction" methods of creating gold nanoparticles have also been probed using FTIR as a means of determining how the metal precursor salt is reduced.[59] Differential scanning calorimetry (DSC) is a common method for thermal evaluation of nanocomposite materials. For instance, DSC is often used for determination of $T_g$ before and after addition of a nanofiller.[83] Spectroscopic ellipsometry is a useful alternative or complement to SAXS for monitoring the development of particles from metal precursors within polymer/metal thin films, as it allows for a rough determination of the particle size and metal content within the film.[35] Nuclear magnetic resonance spectroscopy (NMR) allows for the gathering of data about the interaction between polymer and filler that is inaccessible via methods such as TEM and SEM.[91] For clay nanocomposites, solid state NMR measurements seek to correlate the measured longitudinal relaxations of the interrogated nuclei with the quality of the clay dispersion.[81] Researchers have seen success in correlating NMR measurements to properties such as Young's modulus, degree of clay dispersion, and polymer mobility in polymer/clay nanocomposites.[81,91]

In this thesis, TEM, SAXS, and UV-vis are chosen for their suitability to characterization of polymer/metal nanocomposites. The remainder of this review will examine these techniques and their applicability to characterizing the nanocomposite morphology in such systems. SAXS has been used extensively to characterize both metal nanoparticles in solution and in polymer nanocomposites.[92] At the simplest level, SAXS may be used to determine particle size and spacing.[33,93,94] In addition, it may be used in time-resolved methods, providing insight into growth or migration of particles.[56,58] Spacial correlations between arrays of particles may also be probed, such as in the determination of the structure of colloidal crystals.[95-99] In addition to information about the particles, the change in the morphology of an ordered polymer due to the presence of nanoparticles, such as in block copolymers and liquid crystals may be observed.[27,100] Because of the large contrast in electron density between polymers and nanoparticles such as metals, nanoparticles may also be useful simply as probes or model systems.[101]

SAXS measurements are often complemented by UV-vis and TEM.[28,33,95] UV-vis is particularly useful for noble metal nanocomposites due to the surface plasmon resonance, which is observed as a distinct absorbance peak for a given metal nanoparticle. For instance, a peak is observed at approximately 550 nm for gold nanoparticles and about 410 nm for silver nanoparticles.[60,71] The surface plasmon absorbance peak changes based on the size and shape of the nanoparticles. For instance, increasing particle size cause the surface plasmon absorbance to broaden and red-shift.[60] As such, UV-vis can be utilized to monitor the in situ growth of metal nanoparticles or to detect changes in particle size or shape as a result of processing.[72,82]

TEM is an excellent way to characterize morphology, provided an adequate sampling of images is taken, as the morphology in a small region may not be indicative of the whole.[15] TEM is a very useful technique for determining particle size distribution, mean particle size, and nanoparticle shape due to the ability to directly image the particles within the polymer.[83,85,86] However, TEM is a complex technique that requires a great deal of time, skillful sample preparation, and instrument operator ability.[81] Samples must be microtomed into slices of approximately 50-100 nm thickness. In order to cut rubbery materials such as thermoplastic polyurethane elastomers, liquid nitrogen-cooled conditions must be used to lower the sample significantly below the glass transition temperature to allow cutting without deformation of the sample. In addition to the skill and patience required to perform this sample preparation, the invasive nature of the method may produce non-representative sections. Nanoparticle aggregates of greater than the thickness of the section may be damaged or pulled entirely from a section during microtoming. The invasive nature of TEM sample preparation may limit the number of particles shown per image, leading to statistical problems in calculating particle characteristics.[85] User selectivity may also be a problem. For instance, areas of a nanocomposite containing nanoparticles may be more interesting to observe and record than areas without. In order to avoid both of these problems, care must be taken to systematically view a large number of sections at both low and high magnifications in order to acquire a sufficient sampling of the nanocomposite material.[81,83]

It has been claimed that the presence of large scale aggregates is not widely acknowledged in the nanocomposites literature.[102] Aggregates are difficult to find and image with the predominant electron microscopy techniques, largely due to the sampling and user selectivity difficulties discussed above.[102] TEM is in principle more useful than SAXS for nanocomposite interrogation because an observed scattering pattern may be explained by more than one plausible structure.[102] Further, it is not possible using SAXS to reconstruct the spacial

position of every particle within a given section of a nanocomposite. However, the strength of SAXS is the characterization of a large number of particles expeditiously. By fitting to an appropriate scattering model, it may be possible to differentiate between different particle sizes, detect the presence of aggregates, and determine average particle radius and polydispersity. Thus, electron microscopy and SAXS are complementary techniques for complete characterization of a nanocomposite. TEM may, for instance, reveal particle shape and assist in selection for an appropriate scattering model for SAXS, while SAXS gives superior quantitative data that is not subject to user selectivitity.[102] Of course, the utility of SAXS is contingent on successful modeling of the scattering data, which may be difficult if, for instance, the sample contains a large number of irregular aggregates. TEM and SAXS are both well suited for characterization of polymer/metal nanocomposites due to the strong contrast between the less electron dense polymer and the more electron dense metal particles.

## 1.3 Combinatorial Process Optimization

Combinatorial high-throughput screening methodology has come to be an important tool for the expeditious investigation of new materials systems. Originally championed by the pharmaceuticals industry, high-throughput screening techniques have been applied extensively in materials science, especially in the areas of catalysis, electronic materials, and polymers.[103] Significant work has been devoted to developing high-throughput synthesis and characterization methods for discovery and optimization of polymeric materials, with applications in polymer formulations, thin film dewetting,[104-107] polymer blend phase behavior,[108] and block copolymer morphology,[109] among others.[107,109-113] Techniques have been developed to create libraries of physical property information by generating continuous gradients in film thickness,[114] temperature, and surface energy.[110,111] In addition, high-throughput techniques have more recently been applied to the synthesis of nanoparticles and for subsequent optimization of particle size and properties.[115-118]

The key feature of a combinatorial method is the creation of a composition library, in which many sample compositions are synthesized in an expeditious and systematic manner. Such composition libraries can be generated either by preparing a single piece of material using continuous property gradients or by systematic preparation of a matrix of discrete samples.[119] Fig. 1-8 shows examples of both continuous and discrete combinatorial libraries. Fig. 1-8a shows

a discrete library on a silicon wafer, created via sequential sputtering or pulsed laser deposition of a variety of rare earth and transition metal oxides through a series of progressively different masks.[120] The sample was annealed to allow phase formation in the respective layered oxides and characterized to identify composites with blue photoluminescence.[120] Fig 1-8b shows a continuous combinatorial sample with perpendicular gradients in molybdenum and cobalt thickness for an investigation of binary metal catalysts.[121] The gradients are produced via chemical vapor deposition of each separate metal through a mask with a single 2 mm wide slit 3.6 mm above the sample. Deposition through the slit results in a one dimensional gradient in deposited concentration along an axis perpendicular to the slit.[121] Combinatorial methods expedite exploration of a sample space through rapid sample preparation. One common issue with continuous gradient sample libraries is the presence of variation across the sampled area, which would not be present in a uniform sample.[108,111] However, the effects of such variation, if significant, can be eliminated by preparation of a sample of large enough size compared to the sampling size of the characterization technique used, such as the beam diameter in UV-vis or SAXS. It must be understood that results are an average over the sampled area and that statistics may be useful to help determine the appropriate sample size.
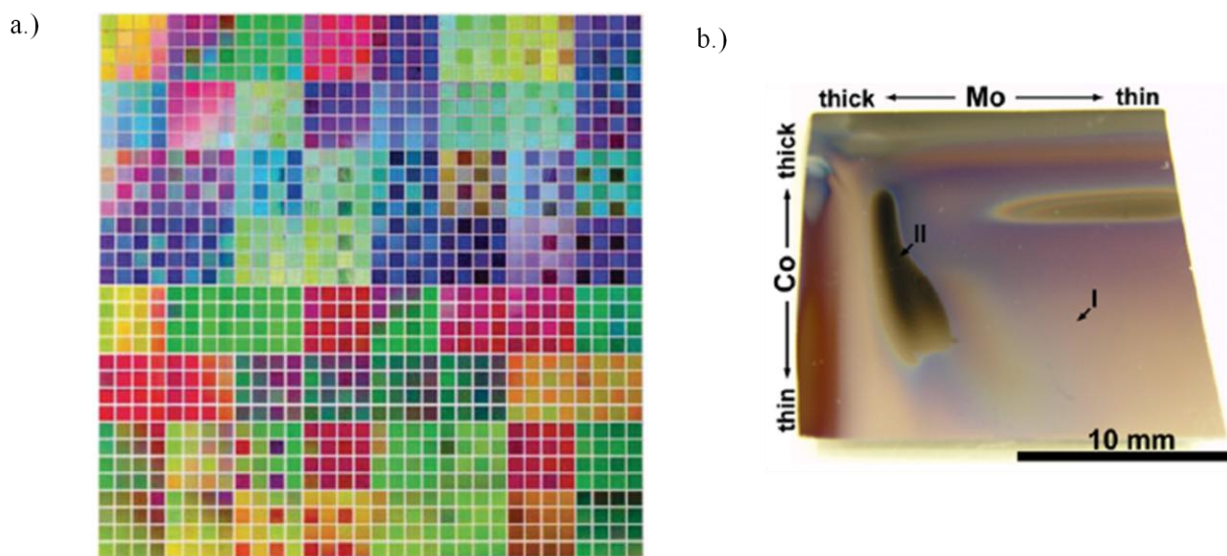


Figure 1-8. Examples of (a.) discrete and (b.) continuous combinatorial libraries. [Sources: Wang, *Science* 1998; Noda, *Carbon* 2006.]

One of the challenges of applying combinatorial methodology to polymers was the need for new techniques to create sample libraries quickly. A variety of methods were developed for producing continuous gradients in polymer samples. In a study of the thin film dewetting of a

polymer blend, Meredith et al. describe the creation of orthogonal gradients in composition and temperature on a substrate.[104]  The former was created via a deposition technique involving the use of sample syringes containing a gradient in polymer blend composition (Fig 1-9a), provided that the polymer was dispensed before molecular diffusion would be able to equalize the concentration (Fig. 1-9a).[104,122]  Temperature gradients  were created using a linear temperature gradient heating stage. [104]  Polymer thickness gradients can be created using a velocity-gradient knife-edge coating apparatus, whereby a dissolved polymer is deposited on a substrate and the knife edge is drawn at an angle at constant acceleration across the surface (Fig. 1-9b).  With a solvent that evaporates expeditiously, the result is a gradient in thickness.[105,122]  More recently, a polymer "flow coater" has been demonstrated for producing similar gradients using a stationary knife and a translated sample.[114]  Gradients are not limited to time and temperature.  For example, a gradient-etching procedure can be used in order to create substrates with surface energies that vary continuously between hydrophilic and hydrophobic.  To create this gradient, a silicon wafer passivated with an Si-H surface layer is introduced at a constant immersion rate to a Piranha solution at 80 °C.[108]  Piranha solution is a mixture of $H_2SO_4$ and $H_2O_2$.  Exposure to this solution results in etching of the Si-H surface and growth of an $SiO_x/SiOH$ oxide layer at a rate dependent on both temperature and $H_2SO_4$ volume fraction.[108]  Thus, a gradient from hydrophobic Si-H to hydrophilic $SiO_x/SiOH$ is created across the surface of the wafer.
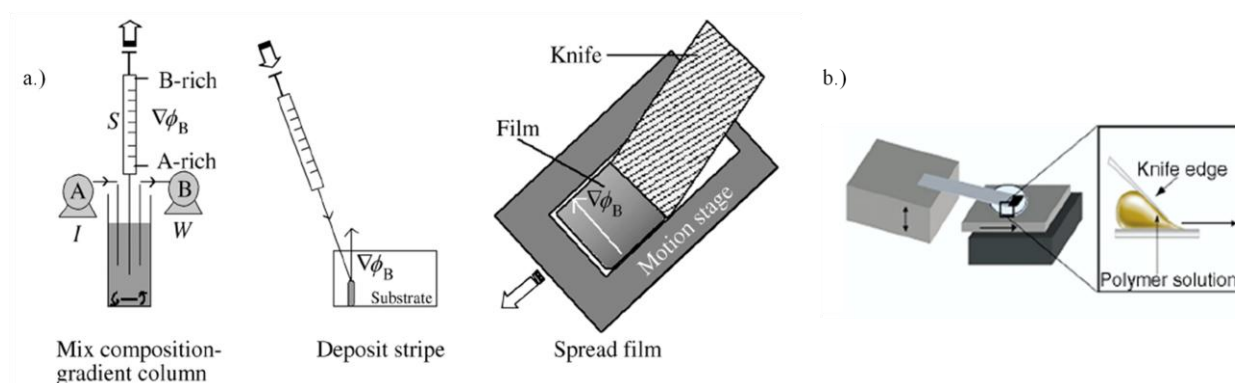


Figure 1-9. (a.) Schematic of the technique used to create a gradient in polymer blend composition within a film.  Polymer A is pumped into a mixing vial as material is continuously removed.  This mixture is deposited and spread on a substrate. (b.)  Schematic of a velocity-gradient knife coater, which moves across a polymer film at constant acceleration to create a gradient in thickness. [Source: Meredith, *MRS Bulletin* 2002]

Combinatorial methodology has also been applied to synthesis of nanoparticles and nanocrystals.  Both Šljukić et al. and Dai et al. demonstrated combinatorial screening methods for

electrode nanomaterials, using samples where pre-formed silver, gold, and palladium nanoparticles were deposited on glassy carbon microspheres both separately and in conjunction.[123,124] Combinatorial voltammetric measurements were taken to evaluate the samples as electrodes for detection of an analyte. It was found that an electrode using all three metals functioned equally well as an electrode with only silver for the detection of bromide.[123] The application of combinatorial methods has also been extended to the synthesis of nanomaterials. In order to study the effect of polymer brush molecular weight (MW) on gold nanoparticle dispersion, Bhat et al. synthesized gradients in polymer brush MW and attached pre-formed gold nanoparticles of varying dimensions.[125] UV-vis and x-ray photoelectron spectroscopy were utilized for characterization of the nanoparticle dispersion. Roth et al. employed the gradient sputtering of a gold nanoparticle layer on top of polystyrene on a silicon substrate.[126] SAXS was utilized as a nondestructive, high-throughput screening method to study the morphology of the multi-layered system as a function of nanoparticle size, along with SEM and TEM for real-space verification of the SAXS data.[126] High-throughput methodology has further been applied to the synthesis of single and multi-metallic nanoparticles for catalytic testing.[115] Baeck et al. used pulsed electrodeposition to create an array of gold nanoparticles, where the particle size was varied by changing the number of pulses used in the deposition (and thus deposition time). The electrocatalytic activity of the nanoparticles was optimized by high throughput electrochemical testing.[118]

Beam-based techniques such as UV-vis, FTIR, SAXS, SANS, and WAXS are ideal for combinatorial sample characterization, as they are nondestructive and data acquisition is rapid.[119] For example, Norman et al. used SAXS and WAXS to study the formation and stability of the vesicle phase of a water soluble diblock copolymer, investigating how it changes as a function of both the composition and temperature of the system. SANS was employed by Karim et al. to investigate the phase behavior of polystyrene/polyvinylmethylether blends containing MMT platelets.[113,122] Optical microscopy and cloud point measurements, also done via scattering, have also been employed in the investigation of polymer systems, particularly thin film dewetting investigations.[104,105,113] AFM is a useful tool in instances where the gradient produces a change in topology or separation into phases have significantly different hardnesses. An example is the work done by Smith et al., wherein the surface pattern of a diblock copolymer combinatorial sample with gradients in film thickness and molecular mass was investigated via AFM.[109,113]

## 1.4 Thermoplastic Polyurethane Elastomers

### 1.4.1 Synthesis and Processing of Thermoplastic Polyurethane Elastomers

Thermoplastic polyurethane (TPU) elastomers were the first, homogeneous, thermoplastically melt-processable thermoplastic elastomers to be commercialized.[127] Most thermoplastic elastomers are microphase separated block or graft copolymers and TPUs are not an exception.[128] Many thermoplastic elastomers contain a hard block (either glassy or semicrystalline) and a soft block (rubbery, amorphous). Early polyurethane elastomers consisted of three components: a polyester or polyether macrodiol, a chain extender such as water, a short-chain diol, or a diamine, and a bulky diisocyanate such as naphthalene-1,5-diisocyanate (NDI).[127] The melting temperature of such a material is higher than the decomposition temperature of the urethane linkages, so they are not truly TPUs.[128] Subsequent research led to widespread use of diphenylmethane-4,4'-diisocyanate (MDI) instead of NDI, resulting in a variety of commercially available TPUs in the 1960's, such as Goodrich's Mobay Texin® in the United States and Bayer AG's Desmopan® in Europe.[128]

Early research into the structure-property relationships of TPUs established that their elastomeric properties are due to the microphase separated nature of their domain structure.[128] A hard segment is formed by addition of a chain extender to a diisocyanate, such as the addition of butanediol to MDI. A soft segment is formed by a long flexible polyether or polyester chain that connects subsequent hard segments.[127] At room temperature, the low melting soft segments and the polar, high melting point hard segments are microphase separated. Phase separation is sometimes due in part to the crystallization of the hard block.[127] A highly immiscible hard and soft segment may also be used to cause or aid in phase separation. The soft segments form an elastomer matrix that gives the TPU its elastic properties.[128] The hard segments serve as multifunctional tie segments, acting as both physical cross-links and reinforcing fillers.[128] Due to fact that the cross-links can be removed via heating above the hard segment melting temperature or by solvation, TPUs have been described as "virtually cross-linked" (Fig. 1-10). Subsequent cooling or desolvation returns the cross-links and the elastic properties of the network. In order to ensure thermoplasticity, each monomer unit should have two terminal reactive groups to ensure that a high molecular weight linear chain with few or no branch points is formed.[128] Increasing hard segment content results in an increase in hardness and a higher glass transition temperature.

Segmental mobility is lowered and free volume in the soft segment is decreased by the increased concentration of physical cross-links as the hard segment content increases, leading to this increase in $T_g$.  Once hard segment levels reach 60 to 70 % w/w, a phase transition from an elastomeric polymer to a brittle, high-modulus plastic occurs.[128]
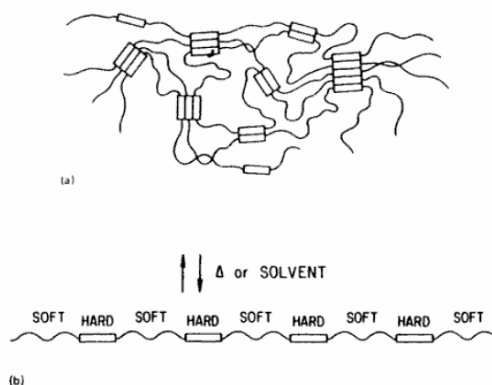


Figure 1-10. Schematic of the structure of a TPU.  At room temperature, the network is "virtually cross-linked" by the crystalline hard segments (a.), while solvation or heating removes these cross-links and results in a homogeneous viscous melt (b.). [Source: Bhowmick, *Handbook of Elastomers*, 1988.]

Polyurethanes are formed via a simple exothermic polyaddition reaction involving an isocyanate end group and an alcohol end group:[129]

$$RNCO + R'OH \leftrightarrow RNHCOOR' + \Delta H \qquad (1\text{-}5)$$

TPUs are generally made from long-chain diols, chain extenders, and short diisocyanate units.[129] Despite the large number of possible starting materials, only a few are of practical interest.[128] The wide variety of properties seen in TPUs, from soft, flexible elastomers to brittle, high-modulus plastics is largely due to the wide range of combinations possible with this relatively small number of relevant diols and diisocyanates.[128]

The long flexible diol is responsible for the low-temperature flexibility of the sample, the resistance to solvents, and the weather-resistant properties of TPUs.[128]  The diol is typically a high  molar mass polymer of 500-4000 g/mol (usually 1000-2000 g/mol).[129]  This segment comprises the majority of the TPU, around 50-80 % w/w.[129]  Two primary flexible segment types include hydroxyl-terminated polyesters and hydroxyl-terminated polyethers.[128]  It is also possible to use hydroxyl-terminated hydrocarbons, but these have found few applications.[128]  The polyester diol is typically made from adipic acid and an excess of a diol such as ethylene glycol, 1,4-butanediol, 1,6-hexanediol, neopentyl glycol, or mixtures thereof.[127]  Azelaic acid or ortho- or terephthalic acid may also be used, though the presence of aromatic or cycloaliphatic rings tends to increase the polyester's glass transition temperature.[127]  After reaction at temperatures up to

200 °C, the resulting polyester is a semicrystalline solid at room temperature with a melting temperature up to about 60 °C. Two special classes of polyesters used in TPUs are polycaprolactones and aliphatic polycarbonates. Polycaprolactones are synthesized using ε-caprolactone and a bifunctional initiator such as 1,6-hexanediol.[128] Aliphatic polycarbonates are useful for their exemplary hydrolytic stability and are synthesized from either a diol and phosgene or via transesterifaction with a low molecular weight carbonate, such as diethyl or diphenyl carbonate.[128] Polyether diols of relevance include the poly(oxypropylene) diols and the poly(oxytetramethylene) diols.[128] Poly(oxypropylene) diols are synthesized by the base catalyzed addition of propylene oxide in bifunctional initators, such as propylene glycol or water. Poly(oxytetramethylene) diols are made using the cationic polymerization of tetrahydrofuran.[128] In order to achieve specific TPU properties, mixtures of polyethers and polyesters are often employed.[128]

Table 1-1 shows the general trends in properties due to the predominant soft segment materials. Although the melting points of most of the listed polyols are above room temperature, they tend to be amorphous in the TPU. Only at very low concentrations of hard segments or after prolonged cooling is any soft segment crystallization observed, due to increased hardness of the sample.[128] However, elongation of the TPU can induce crystallization of the soft segment, leading to a self-reinforcing effect, which is seen in the higher modulus compared to elastomers with noncrystallizable soft segments.[128] Note that this effect disappears above the melting temperature of the soft segment. As such, the soft segment must be carefully chosen for the desired application of the material.

Table 1-1. Important polyols and properties of their corresponding TPUs. $T_e$ is the temperature at the lower end of the glass transition range and $T_m$ is the melting temperature. [Source: Holden, *Thermoplastic Elastomers* 2004].

| Polyol nomenclature | Polyols | | Elastomers | Hydrolytic stability |
| --- | --- | --- | --- | --- |
| | $T_e$ (°C) | $T_m$ (°C) | $T_e$ (°C) | |
| Poly(ethylene adipate) diol | −46 | 52 | −25 | Fair |
| Poly(butylene-1,4 adipate) diol | −71 | 56 | −40 | Good |
| Poly(ethylene butylene-1,4 adipate) diol | −60 | 17 | −30 | Fair/good |
| Poly(hexamethylene 2,2-dimethylpropylene adipate) diol | −57 | 27 | −30 | Good |
| Polycaprolactone diol | −72 | 59 | −40 | Good |
| Poly(diethylene glycol adipate) diol | −53 | / | −30 | Poor |
| Poly(1,6-hexanediol carbonate) diol | −62 | 49 | −30 | Very good |
| Poly(oxytetramethylene) diol | −100 | 32 | −80 | Very good |

Because TPUs often have a glass transition that takes place over a broad range of temperatures, quoting a single value for $T_g$ can be misleading. As such, $T_e$ is defined as the temperature at the onset of the glass transition region. Low to medium hardness TPUs have a glass transition range which starts around 20 to 30 °C above the corresponding temperature of pure soft segment due to the loss of segmental mobility.[128] The breadth of the glass transition range in the final TPU depends on the amount of hard segment present. Higher hard segment concentration leads to a higher breadth of the transition region. Too much hard segment leads to poor low temperature properties. As such, greater low temperature flexibility is achieved by creating a TPU with $T_e$ well below room temperature along with a narrow glass transition temperature range.[128] Such a TPU is synthesized using soft segments that are less compatible with the hard segments, such as polyethers. The immiscible soft and hard segments increase the tendency to phase separate and lower the probability of having hard segments next to soft segments, thus minimizing the variation of soft segment $T_g$. Incompatibility can be further increased by increasing the soft segment molecular weight or annealing the elastomer.[128]

The diisocyanate is a relatively small molecule with molar mass approximately 150-250 g/mol.[129] Only a few commercially available diisocyonates are industrially useful for producing TPUs. Most important among them is MDI.[128] Other useful hard segment materials include toluene diisocyanate (which produces TPUs with prohibitively low softening temperatures), hexamethylene diisocyanate, 4,4'-dicyclohexylmethane diisocyanate, 3,3'-dimethyl-4,4'-biphenyl diisocyanate (TODI), and 1,4-benzene diisocyanate.[128] The most useful diisocyanates are those with cyclic, compact, symmetrical structural units that produce hard segments and urethane groups that associate and pack well with one another.[129]

MDI is the most commonly used diisocyanate due to its combination of desirable performance in consumer products with its low cost. Aliphatics such as hexamethylene diisocyanate are used when improved resistance against discoloration by UV radiation is desired. Aromatic diiscyanates such as TODI are used on a very small scale when TPUs with excellent high temperature performance are needed.[128] Increased hard segment content is found to broaden and shift the glass transition of the TPU to higher temperatures.[128] The observed rise in $T_g$ has been explained by an increased amount of hard segments "dissolved" in the soft matrix, which decreases the free volume of the soft segments. The length of the hard segment block determines the upper limit of the size of the hard segment domains, in turn determining the melting point and thermal stability of the TPU.[128] Increasing hard segment length thus tends to increase the observed melting temperature.[128]

In addition to the diisocyanate itself, the chain extender also influences the properties of the hard segment of the TPU. The chain extender is another small difunctional molecule, usually a glycol of molar mass 100-350 g/mol.[129] As with the diisocyanate, chain extenders that encourage good association and packing within the hard segment are the most desirable.[129] The key chain extenders are linear diols such as ethylene glycol, 1,4-butanediol, 1,6-hexanediol, and hydroquinone bis(2-hydroxyethyl ether).[128] Addition of the small diol to the diisocyanate forms a urethane that is crystallizable and melts without decomposition during processing. As such, ethylene glycol is avoided for TPUs with high hard segment content due to its thermal instability at higher temperatures.[128] Properties of the most commonly used chain extenders are shown in Table 1-2. 1,4-butanediol and hydroquinone bis(2-hydroxyethyl) ether are the most frequently used chain extenders for TPUs. Nonlinear chain extenders are rarely used as the resulting urethanes do not form well-crystallized hard segments,[128] but mixtures of straight-chain extenders are used when a lower order hard segment is desired, as is the case when producing TPUs with a broad processing range for extrusion. Diamines are in theory good chain extenders, but they are not used often in TPUs because the resulting urea linkages raise the melting temperature of the hard segments and make processing temperatures prohibitively high.[128]

Table 1-2.  Common diisocyanate and chain extender combinations.  Melting temperatures before and after reaction of these components are indicated, as is the state of crystallinity as studied via x-ray scattering. [Source: Holden, *Thermoplastic Elastomers* 2004.]

| Diisocyanate | $T_m$ (°C) | Chain extender | $T_m$ (°C) | X-ray[a] | Hard segments Melting point determined by | | |
|---|---|---|---|---|---|---|---|
| | | | | | DSC measurement Curve profile | $T_m$ (°C) | Visual evaluation in the melting tube |
| Naphthalene-1,5-diisocyanate (NDI) | 131 | 1,4-butanediol | 19.5 | C | Thermal effects as from 190 °C, no real melting up to 320 °C | | Sintering as from about 260 °C, no melting up to 320 °C |
| Diphenylmethane-4,4′-diisocyanate (MDI) | 42 | 1,4-butanediol | 19.5 | C | | 230 | Initial softening at about 120 °C, melting at 230 °C to 237 °C[b] |
| Hexamethylene diisocyanate (HDI) | 11 | 1,4-butanediol | 19.5 | C | Step at 75 °C to 100 °C | 165 | Initial softening up to about 100 °C and 148 °C, melting at 166 °C to 172 °C |
| 2,4-TDI | 24 | 1,4-butanediol | 19.5 | A | Step at 70 °C to 110 °C | 217[b] | Initial softening at 78 °C to 120 °C, melting at 220 °C[b] |
| NDI | 131 | 1,4-bis($\beta$-hydroxy-ethoxy) benzene | 104 | C | Step at 133 °C and 210 °C | 302 | Brown discolo-ration as from 288 °C, melting at 298 °C to 302 °C |
| MDI | 42 | 1,4-bis($\beta$-hydroxy-ethoxy) benzene | 104 | C | | 252 | Initial softening at 243 °C, melting at 247 °C to 260 °C[b] |
| HDI | 11 | 1,4-bis($\beta$-hydroxy-ethoxy) benzene | 104 | C | | 214 | Initial softening at 140 °C to 150 °C, melting at 212 °C to 226 °C[b] |
| 2,4-TDI | 24 | 1,4-bis($\beta$-hydroxy-ethoxy) benzene | 104 | C | Step at 140° C | 197 | Initial softening at 140 °C, melting at 200 °C to 216 °C, breakdown as from 250 °C |

[a] X-ray wide angle study
[b] Melts with breakdown
C, crystalline; A, amorphous
After Ref. [31], with permission

Reaction of the three key ingredients in the TPU is typically done at temperatures above 80 °C with the ratio of isocyanate groups to hydroxyl groups close to 1.0.  Below a ratio of 0.96, polymers of insufficient molecular weight are produced, while processing becomes difficult for ratios above 1.1 due to cross-linking reactions.[128]  An average number average molar mass of

40,000 g/mol is generally sufficient for the desired TPU applications and should be easily achieved at ratios of 0.98 and up. Care must be taken in the choice of synthesis method, as the polyaddition reaction is exothermic.[128] Either a one-step or a prepolymer method is used in the polymerization of TPUs.[129] In the former, all of the TPU components are mixed together at once, while in the latter the long-chain diol and diisocyanate are mixed to form a low molecular weight isocyanate-termined polymer before the addition of the chain extender.[128,129] Industrially, synthesis is done using either a belt process, where all reactants are mixed and the reacting liquid mixture is poured onto a belt to solidify, or via reaction extrusion.[128] Again, choice of process is very important, as the phase separation of the TPU is determined by the temperature and shear conditions during synthesis.[128] For instance, in belt processing the reacting melt does not experience any shear after leaving the mixing chamber, while significant shear is applied throughout the processing in a reaction extruder. As a general rule, TPUs produced via reactive extrusion show less pronounced phase separation, and thus lower crystallinity.[128] A variety of additives may be mixed into TPUs during synthesis, including mold release agents such as esters or silicones, stabilizers such as aromatic carbodiimides which improve the hydrolytic degradation resistance of polyester-based TPUs, inorganic materials such as calcium carbonate that act as crystallization promoters or surface rougheners, and plasticizers when a soft grade of TPU is desired.[127]

Traditional rubber elastomers are largely amorphous, gum-like masses with low $T_g$ that must be covalently cross-linked at high temperatures in a slow, irreversible process known as vulcanization in order to be useful for mechanical applications.[129] The absence of the need for this vulcanization step in thermoplastic elastomers is a key reason for their commercial prevalence.[130] As opposed to traditional rubbers, thermoplastic elastomers can change from a processible melt to a solid rubbery article quickly and reversibly. The fast processing of thermoplastic elastomers allows processing equipment commonly used in the plastics industry to be applied to produce rubbery products. However, thermoplastic elastomers have not completely displaced traditional rubbers because there are some property trade-offs. For instance, the compression set is not as high as that in conventional vulcanized rubbers, which are thus still used for automobile tires and fan belts.[130] The thermomechanical behavior of TPUs is fundamentally different from that of chemically cross-linked elastomers.[128] The application of mechanical stress to a TPU results in disruption and recombination of hydrogen bonds to an energetically more favorable position, which may explain the high tensile strength, tear strength, and elongation generally observed for TPUs.[128] While soft segments seem to readily orient under applied tension, the hard segments

display a complex behavior of orientation and relaxation that is dependent on the magnitude of applied stress, molecular weight of the soft segment, and crystallinity of the hard segment.[128]

Generally, TPUs are supplied as granules which may be processed via any of the usual means used for thermoplastic materials, such as injection molding, extrusion, blow molding, or calendering.[129] However, not all grades are suitable to every processing operation, so care must be taken on a case by case basis to determine the optimum processing method. Once the TPU is heated above the melting temperature of the hard segments, the polymer forms a homogeneous viscous melt that can be processed.[128] Cooling back to room temperature causes both the re-segregation to hard and soft segments and, as a result, the return of the elastomeric properties.[128] Different varieties of TPU are often blended together during processing in order to achieve, for instance, intermediate hardnesses or improved processing properties.[128]

## 1.4.2 Properties of TPUs

Understanding the structure-property relationship of TPUs has been a difficult challenge, as crystallization, interphase mixing, hydrogen bonding in both segments, thermal history, etc. all affect the morphology.[128] By definition, thermoplastic elastomers are neither conventional rubbers nor typical thermoplastics. As such, there has been some debate as to how they should be characterized. In general, it has been accepted that the majority of physical property tests for vulcanized rubbers are suitable for thermoplastic elastomers.[131] Common sense must be applied, as harder elastomers may require plastics testing methods, while less hard and more elastic samples are more amenable to rubber test methods. The thermoplastic nature of TPUs can often necessitate alterations to standard characterization tests, such as the temperatures used in ageing and compression set tests. As such, a knowledge of the transition temperatures for the thermoplastic elastomer is important when determining characterization parameters.[131]

The mechanical properties of TPUs greatly depend on hard segment content. Soft grades of TPU have molar ratios of polyol to chain extender to diisocyanate starting around 1:0.5:0.5, while the hard grades at the opposite end of the spectrum tend to have as high as 1:20:21.[128] TPUs exhibit high tensile strength and ultimate elongation.[128] Their high resistance to tearing makes them excellent for high durability applications.[128] Young's modulus for a TPU can range from 5-2000 MPa depending on hard segment content.[128] Ester-based TPUs are generally used when favorable mechanical properties are desired, while more expensive ether-based TPUs are reserved

for specialty applications requiring high resistance to hydrolysis or microbial deterioration or improved low temperature flexibility (Table 1-3).[128]

Table 1-3. Qualitative comparison of TPUs prepared from different diol segments. [Source: Holden, *Thermoplastic Elastomers* 2004]

| | Ester (adipate or caprolactone) | Ester with carbodiimide | Ether | Etherester |
|---|---|---|---|---|
| Tensile strength | ++ | ++ | 0 | + |
| Abrasion resistance | ++ | ++ | 0 | + |
| Low swelling in oil, grease, water | + | + | 0 | + |
| Weathering | + | + | 0 | + |
| Stability to highly energetic radiation | + | + | 0 | + |
| Tear strength, Graves | ++ | ++ | 0 | + |
| Rebound resilience | ++ → + | ++ → + | ++ → + | + |
| Microbe and fungus resistance | + → − | 0 → − | ++ | ++ |
| Low-temperature impact resistance | + → 0 | + → − | ++ → + | + |
| Hydrolysis resistance | 0 | +/0 | + | + |

++  excellent, favorable
+   good
0   indifferent
−   poor, unfavorable

Most TPUs are useful over a temperature range of about -40 °C to 80 °C for long- and short-term applications.[128] For short term applications, temperatures as high as 120 °C, and potentially higher depending on the TPU composition, may be tolerated. TPUs with higher hard segment content are in general capable of sustaining higher temperatures.[128] Additionally, TPUs tend to be resistant to attack by microorganisms after long contact with moist conditions, although soft ester-based TPUs can be susceptible to such attacks.[128] UV absorbers are a beneficial additive in TPUs containing aromatic isocyanates to minimize yellowing due to oxidation, though the mechanical properties are minimally affected by this oxidation.[128] The ease of adding such additives to TPUs, as well as their ability to be heavily loaded with pigments, make them further desirable as commercial products.[129]

**1.4.3 Applications**

TPUs are used in a large number of applications. Typically, TPUs are chosen due to the wide range in hardness that can be achieved via changes in composition, combined with excellent mechanical properties and wear resistance.[128] Other applications may call for specific characteristics, such as transparency, adhesion, or paintability.[128] The most commonly leveraged properties of TPUs, depending on formulation and additives, are abrasion resistance, clarity, cut resistance, flexibility, heat sealability, load bearing capacity, low-temperature flexibility, non-marking, oil resistant, toughness, and vibration damping.[127] For example, thin films of between 20 μm and several mm can be produced via extrusion or calendering.[128] The hardness and melting range of the films can be varied via composition. Such films can be used for scratch resistance on windows, adhesive layers in laminated safety glass, or in special grades containing poly(ethylene glycol) soft segments for breathable films in textiles.[128] Extrusion can also be used to produce hoses of varying size and design for applications such as pneumatic tubes, suction hoses for transport of abrasive goods, or liners for irrigation and fire hoses.[128] Compared to conventional rubber hoses, TPUs allow for a thinner wall thickness to be used as an inner lining due to their high tensile strength, which in turn allows for production of lighter hoses.[128] Due to their mechanical properties and grease resistance, polyester TPUs are used as seals and bearing bushes in the front axle constructions of vehicles.[128] Aliphatic diisocyanate TPUs are used for parts requiring light stability and transparency, such as instrument panels in vehicles.[128] Due to their good adhesion to hard, polar plastics such as polycarbonate or ABS, TPUs are often used as a soft outer grip coating on top of the more structural hard polymer for tool grips, sports equipment, or car interiors.[128] Very prominently, TPUs are the material of choice for shoe soles.[128] Finally, their hemocompatibility allows TPUs to be used in medical applications, such as for catheters and hoses.[128] However, there are exposure limits in some cases, such as for MDI-based materials that should not be in contact with human tissue for more than 28 days.[128] Many more common applications of TPUs can be listed, such as golf ball covers, soccer balls, skateboard wheels, cattle ear tags, upholstery, gas masks, chemical storage tank vapor barriers, and tarpaulins, to name just a few.[129]

## 1.5 Liquid Crystalline Elastomers

### 1.5.1 Introduction

Liquid crystalline polymers (LCP) are a class of polymers that possess limited orientation or positional ordering of segments yet retain liquid-like mobility at the segment level. LCP are generally identified as containing a combination of both rigid units, called mesogens, and flexible spacer units. When mesogens are present within the polymer backbone, the polymer is referred to as a main-chain LCP, while if mesogens are present as pendant groups, the polymer is referred to as a side-chain LCP (Fig. 1-11). Side-chain LCP were among the earliest studied, as their synthesis is more straightforward.[132-135] Additionally, main-chain LCP were difficult to research due to their tendency to have high transition temperatures and poor solubility in common organic solvents.[136] However, interest in main-chain LCP has grown due to the increased constraints on ordering inherent in having the rigid mesogens incorporated into the main chain.[136-138] LCP can be further sub-divided by their liquid crystalline phases. Though many phases exist, two particularly common examples are nematic and smectic (Fig. 1-12). Nematic LCP are found to possess some degree of orientational order; that is to say, the rigid mesogens are approximately oriented in a common direction within a given domain. The vector describing this shared orientation is termed the director. In smectic LCP, mesogens not only share orientational order at a local length scale but also share a limited degree of positional ordering, resulting in segment-level layering. The relative orientations of the mesogens within each layer give rise to a large number of smectic phases, such as smectic A and smectic C. These phases, though distinct, are nonetheless characteristically smectic with respect to their orientational ordering and the presence of layering. The phase of a particular LCP sample can be determined using a combination of polarized light optical microscopy and x-ray diffraction.
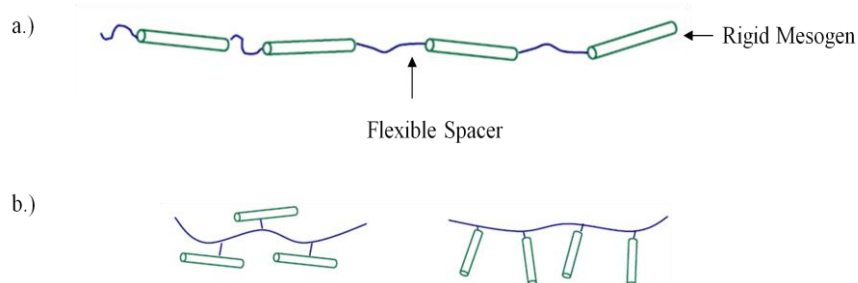


Figure 1-11. Schematic of the structure of (a.) main chain and (b.) side chain LCPs.
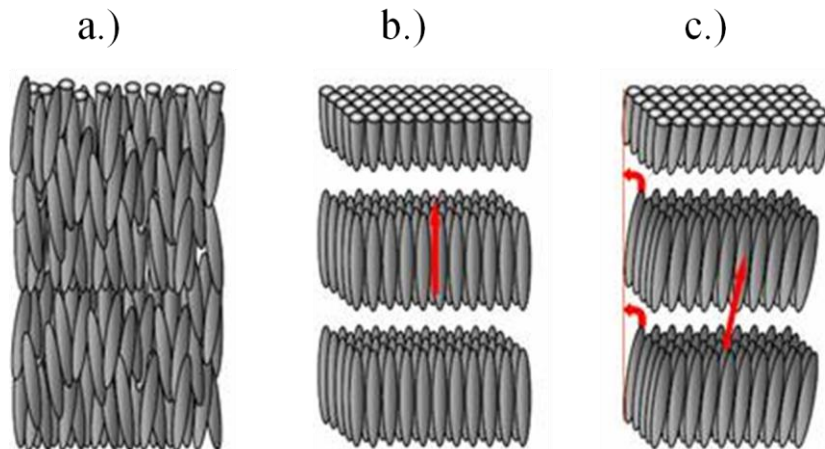
Figure 1-12. Diagram depicting the alignment of the rigid mesogens in three common liquid crystalline phases. (a.) Nematic, which possesses only net orientation of the mesogens. Smectic phases add in a layering constraint, and are defined by the angle of the mesogens within the layers, as can be seen in comparing (b.) smectic A and (c.) smectic C. [Source: www.laynetworks.com/Molecular-Orientation-in-Liquid-Crystal-Phases.htm 02/12/10]

LCP can be slightly cross-linked in order to form a liquid crystalline elastomer (LCE). These LCE tend to have low glass transition temperatures and exhibit rubber-like mechanical properties, despite the presence of liquid crystalline ordering.[133] The same LC phases exhibited by linear LCP are still identifiable in LCE. Furthermore, LCE tend to have low Young's moduli (E~0.5 MPa).[133] Finkelmann et al. reported the first synthesis of LCE and LCP in 1981.[139] These early experiments focused on synthesis and structural characterization of side-chain LCE.[134,140] The first main-chain LCE was synthesized in 1997 by Finkelmann's group, motivated in part by De Gennes' prediction of exceptional mechanical and optical properties due to the direct coupling of mesogenic units with the backbone.[136,137] Moving forward, a less difficult method of producing main-chain LCE by a single step, non-linear polymerization was reported in 2000.[136] As a deeper understanding of synthetic methods developed, LCE research shifted towards their behavior and possible uses.[140] LCE have potential applications as vibration-damping coatings, due to their broad mechanical loss spectrum.[141] Smectic C LCE may also have applications in soft actuation, where "artificial muscles" could be synthesized to leverage the change in orientation of LCE under an applied field, called the electroclinic effect.[140,142-146] Light-driven actuation has also been demonstrated in liquid crystalline polymer networks containing azobenzene units.[147] The cis-trans isomerization of the azobenzene units can be driven via high wavelength light and leveraged to produce bending of the thin film sample.[147,148]

**1.5.2 Polydomain to Monodomain Transition**

Provided that cross-linking is not performed during or after flow alignment, LCE are found to be in a polydomain state at equilibrium (Fig. 1-13). The domains in such a material are differentiated by continuous changes in the director orientation over some distance. These domains are typically found to be on the order of one micrometer in size or smaller. The spatial variation of the director results in the birefringent textures seen when an LCE is viewed under crossed polarizers.[138] Of particular importance is the so-called Schlieren texture, which results from the isotropic polydomain nature of LCE (Fig. 1-14). This texture, most often associated with nematic LCE, consists of dark brushes, which begin at line defects called disclinations.[138] These disclinations result from abrupt discontinuities in the director field.[133] The brushes are visible where the director is oriented along either the polarizer axis or the analyzer axis.[133] Some smectic LCE can also exhibit this texture; thus it is important to be able to differentiate these textures. For example, smectic C LCE will only have 4 brush disclinations. Meanwhile, nematic LCE will seldom have 6 or 8 brush disclinations due to the fact that the number of brushes scales with the energy of the defect. Specifically, defect energy scales as $s^2$, where s is the strength of the singularity, equal to ¼·(number of brushes).[149] Measuring the distance between disclinations allows for a rough estimate of the domain size of the sample.[133]
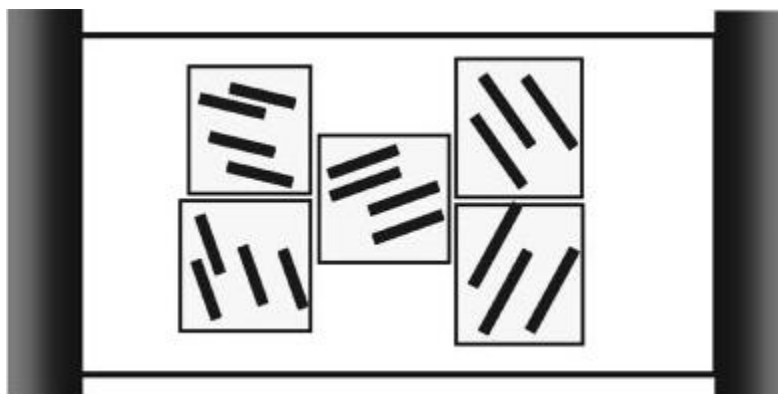


Figure 1-13. Liquid crystals that are cross-linked in the absence of any aligning force, such as flow or tension, are found in a polydomain state. Dark black lines represent the mesogens within each domain. [Source: Fridrikh, *Phys Rev E* 1999]
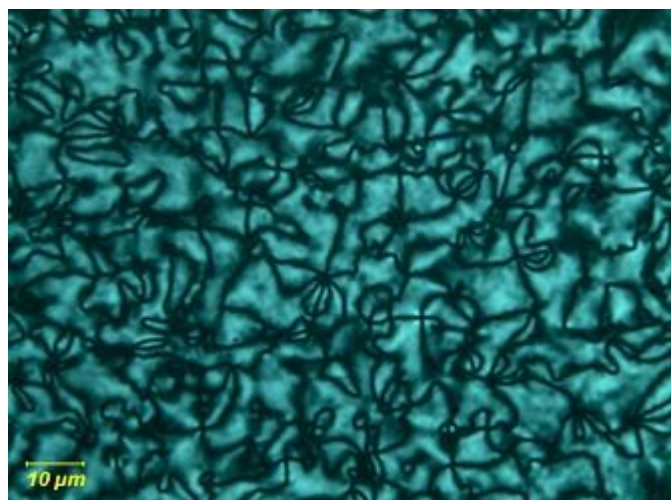
Figure 1-14. Smectic $C_A$ Schlieren texture with two, four, six, and eight brush disclinations. [Source: Patil, *Macromolecules* 2007]

If larger domains having diameter on the order of the wavelength of visible light or higherare present,[150] these polydomain LCE scatter light sufficiently to appear opaque when viewed with the naked eye. In the nascent stages of LCE research, Finkelmann et al. noted that when a tensile force was applied to a polydomain LCE sample, it became transparent (Fig. 1-15).[132,135] Later on, it was noticed that this transparency begins in the center of the sample and moves out towards the grips of the tensile testing apparatus as strain is increased.[133] This change is due to a transition from a randomly oriented polydomain state to a globally oriented "monodomain." That is to say, the mesogens throughout the sample become aligned uniformly along the direction of the tensile force. There are independent refractive indices parallel and perpendicular to the director in these birefringent materials. Therefore in the polydomain state, light passes through numerous randomly oriented domains of different refractive index and is scattered. When the sample is stretched into a monodomain state, these refractive index changes are no longer present, and the sample becomes transparent. This polydomain to monodomain (P-M) transition was first observed by Finkelmann et al. in side-chain nematic LCE, identifiable due to the visible transition from opaque to transparent, as well as a plateau in the stress-strain curve during the transition (Fig. 1-16).[135] Additionally, a plot of segmental orientational order parameter versus stress will exhibit a sharp increase at the P-M transition, as opposed to the linear relation observed in conventional elastomers (Fig. 1-17).[133] The first main-chain LCE also demonstrated this transition, accompanied by an even larger change in sample dimensions than had previously been observed.[137] Since then, the P-M transition has been observed in main-chain and side-chain, smectic and nematic elastomers of a variety of chemical compositions.[151] For

instance, main-chain smectics exhibit the P-M transition with minimal loss of strain after unloading.[133]  Due to the direct coupling of the mesogen orientation to the backbone in main-chain LCE, it has been found to be advantageous to study the P-M transition with such samples, rather than with side-chain LCE, where the mesogens can behave somewhat independently of the backbone.[133,152]  The plateau region has been found to be significantly more pronounced in main chain elastomers than in side chain elastomers.[153]  It must be noted that some confusion can be caused by the terminology "polydomain" and "monodomain."  A polydomain is not a sample with discrete domains of different director orientation.  Rather, the director changes its local orientation in a continuous fashion, eventually losing memory of its previous orientation over a distance that we deem to be the domain size.  Similarly, "monodomain" is a slight misnomer because the orientation of the mesogens is not perfectly uniform throughout the sample, and some defects are present.[154]  The order parameter, S, within the monodomain is typically between 0.5 and 0.6.[133]
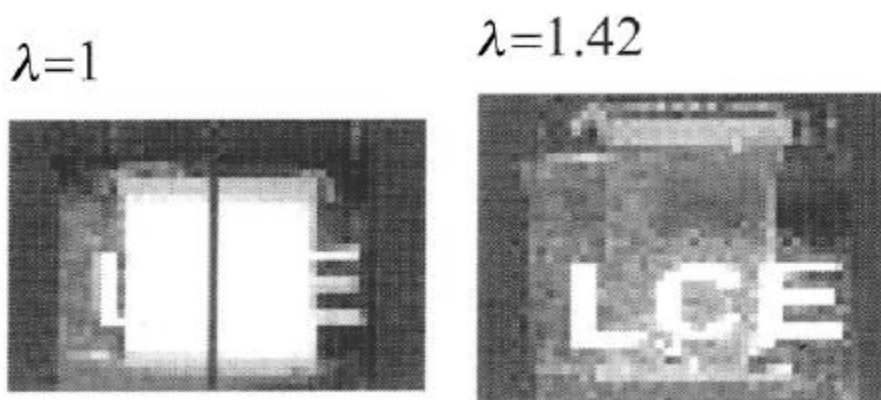


Figure 1-15. Demonstration of the change in opacity before (left) and after (right) the P-M transition, induced by applying a uniaxial tension to a nematic LCE sample.  [Source:  Clarke, *Faraday Discuss.* 1999]
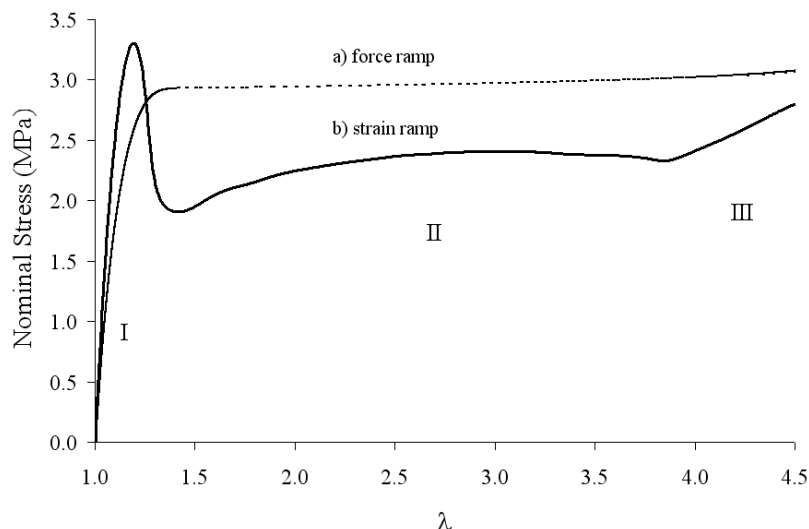
Figure 1-16. Stress-strain curves showing the P-M transition.  The plateau is seen when stress is increased linearly, while the maximum and subsequent valley is seen when the force needed to linearly increase strain is measured. [Source: Patil, *Macromolecules* 2009.]
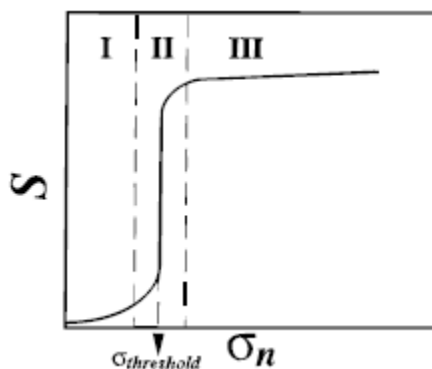


Figure 1-17. Orientation parameter versus nominal stress plot for a polydomain LCE.  Region II is the P-M transition.  [Source:  Ortiz, *Macromolecules* 1998.]

Numerous attempts have been made to model the behavior seen in the P-M transition.[155,156]  According to the models proposed by Terentjev et al., a director rotation will take place within some of the domains in the sample upon the application of uniaxial tension.[155]  The director will rotate within each domain toward the direction of the applied tension.  The result is a region of "soft elasticity."  As the strain increases, there is no entropic restoring force exerted by a soft elastic solid, because the deformation is accommodated by internal rotations of the mesogens.[157]  This accommodation causes the plateau seen in the stress ramp stress-strain curve during the transition.  Though soft elasticity, attributed to this director rotation, is seen in nematic LCE, the effect is diminished for smectic LCE.[141]  In the theory of soft elasticity, director

rotations do not result in a loss of configurational entropy, in direct contrast to the behavior seen in an ordinary amorphous polymer. When such an amorphous sample is stretched, the chains extend, and the number of possible configurations of the chains decreases, thus decreasing entropy. By Terentjev's model, the LCE chains are not being extended at all, only rotated.[155] As a result, there should be no elastic restoring force on the monodomain sample; it should not need to be held under uniaxial tension to keep it from returning to a polydomain state, as the two are entropically equivalent. It is important to note that the domains do not deform in an affine manner. The increase in end-to-end distance of a random individual chain is not necessarily proportional to the strain seen in the bulk sample.[133]

In Terentjev's model of a nematic elastomer, each polymer chain can be modeled as having an ellipsoidal shape, with the long axis aligned along the director.[155] When a stress is applied, the long axes of the ellipsoids rotate toward the axis of extension such that the director gradually becomes aligned with the axis of extension. The result is a macroscopic elongation with no change to the ellipsoidal shapes or domain size. During the transition, the configurational entropy is unchanged. However, the picture becomes less simple when the continuous nature of the director field throughout the polydomain is considered. A domain oriented in one direction cannot rotate freely to respond to the applied tension due to its connectivity to domains oriented in other directions, which are also attempting to rotate.[155] As a consequence, the gradients in mesogen orientation between domains become localized into narrow domain walls between the rotating domains (Fig. 1-18).[155] For instance, the disclinations viewable in the optical microscope become localized to sharp defects within the domain walls following the application of uniaxial tension.[133] Once the domains are oriented more closely with the applied force, the tensile force will be seen locally as a shear on each domain, having opposite character to the shear on the other side of the domain walls.[155] In this way, the shear forces throughout the sample balance, resulting in no global shear. Thus, we see why the so-called "monodomain" state is not truly one domain: there are still many domains, separated by finite walls, although they now have a significantly higher orientational correlation with respect to the axis of extension.
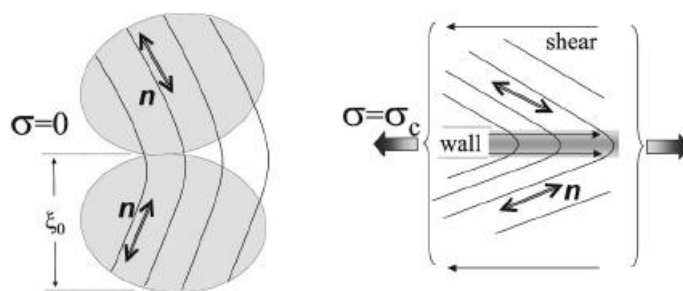
Figure 1-18. At left, the continuous change of the director in an unstressed LCE sample. When stress is applied (right), the domain walls are formed by the localization of the gradient in the director to a narrow domain wall. [Source: Fridrikh, *Phys Rev E* 1999]

Based on the preceding ideas, Terentjev et al. have shown that the "plateau" region in the stress-strain curves for nematic LCE can be explained entirely in terms of director rotations, without invoking any other deformation mechanisms.[155] However, nematic elastomers are not truly soft solids and still exhibit elastic restoring force following stretching, as Finkelmann, Clarke, and Terentjev have demonstrated with side-chain nematic samples.[150,158] Smectics, on the other hand, do not return to their previous size and chain orientation once the load is removed, in spite of a significant stress relaxation.[151] In addition, the ideas of soft elasticity are not readily applicable to smectic LCE, which also show a prominent plateau in the nominal stress under uniaxial tension. Adams and Warner have shown that smectic A elastomers cannot have any soft response, while smectic C elastomers can exhibit a limited soft response in one direction via twisting of the C-director around the layer normal, due to their lower point symmetry.[159] A question then remains regarding why we see this plateau in stress associated with the P-M transition as a universal phenomenon in LCE. Adams and Warner may have provided an explanation.[160] Director rotations are not the only possible source of a plateau in the stress-strain curve of a LCE. Main-chain LC polymers, both smectic and nematic, can contain hairpins: segments at which the chain folds back on itself in a parallel but oppositely directed fashion (Fig. 1-19).[160] These hairpins exist as a means of increasing configurational entropy.[160] Hairpins are somewhat analogous to the chain-folding characteristic of polymer crystallization. Although the hairpinned LCP chains lack the level of structure and long-range order of polymer crystallites, chain-folding is also a means of increasing entropy. Adams and Warner modeled the uniaxial extension of a main-chain nematic LCE along the director and showed that a region of increasing strain with constant stress is observed due to the pulling out of hairpins.[160] That is, a plateau in nominal stress was predicted due to the fact that the number of configurations of the system, and

thus the entropy, were found to depend on the number of hairpins and not the end-to-end length of the chains.[160] Thus, the uniaxial extension of the sample could proceed up to a point with no change in entropy due to a lengthening of the distance between hairpins. Eventually, cross-links and potentially trapped entanglements will necessitate that the number of hairpins decreases, due to loss of hairpins by unfolding, up to the end of the stress-strain plateau. The number of hairpins in a chain can be investigated via SANS measurements, allowing for an experimental analysis of this model.[160] More recently, Watanabe et al. have attributed the P-M transition in smectic $C_A$ main chain elastomers to a transition in the elastic backbone conformation from hairpinned to extended.[161]
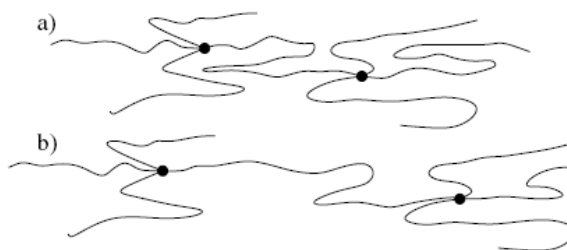


Figure 1-19. Schematic of hairpins in an LCE. Note how in (b.) the strain is accomodated by the pulling out of the hairpins in the central chain, without changing the number of hairpins from the unperturbed state in (a.). [Source: Adams, *Macromolecules* 2005.]

In summary, while theoretical models have shown that the P-M transition can take place entirely via director rotation in nematic main-chain LCE, director rotations cannot be the sole cause of the P-M transition in smectic A or smectic C LCE, in which soft elasticity is not present in its purest sense. The pulling out of hairpins can equally account for the entirety of this plateau in main-chain LCE models. Therefore, the degree to which these mechanisms work together to produce the P-M transition in main chain LCE remains a matter of future discussion.

### 1.5.3 Necking Transition in Liquid Crystalline Elastomers

Necking is a mechanical instability that manifests itself as a local contraction that propagates through a material during uniaxial elongation, eventually consuming the entire sample as it extends to the clamps of the testing apparatus.[153] Once necking begins, the draw ratio ($\lambda_m$) of the sample becomes inhomogeneous, with $\lambda_m$ within the neck always being higher than $\lambda_m$ in the wider, non-necked portion of the sample. Necking during cold-drawing of non-crosslinked linear polymers is a well known phenomenon, the mechanism of which has been studied at length.[162]

Necking has been observed in amorphous polymers at temperatures below $T_g$, as well as in crystalline polymers at some point between $T_g$ and $T_m$.[163] Additionally, strain rate has been noted to have an effect on neck formation, as some polymers will yield homogeneously at low enough strain rates while forming a neck at higher strain rates. As such, the effects of strain rate and/or temperature on necking and yield stress have been studied for a variety of polymers over several decades.[164,165] Earlier papers report the phenomenon in a variety of materials and propose theories for its mechanism, such as polycarbonate and poly(vinyl chloride),[166] high density polyethylene,[163] poly(methyl methacrylate),[167,168] and polyethylene.[169] More recent reports focus on refining these theories and associated mathematical models for polymers such as high density polyethylene[170] and isotactic polypropylene.[171,172] Necking instabilities have not often been reported in LCE, even though the yield stress in the strain ramp stress-strain curve for uniaxial elongation is consistently observed (Fig. 1-16).[133,173-176] However, neck formation was noted in a recent publication by our group during the uniaxial deformation of a smectic MCLCE.[153] The necking transition was shown to be a discrete, localized manifestation of the P-M transition, separating the necked (thinner) portion(s) of the sample, which have essentially reached the monodomain state, from the non-necked (thicker) portions of the sample, which remain in the polydomain state until passing through the necking transition.

Uniaxial elongation of smectic polydomain MCLCE can be described by three regions of deformation (Fig. 1-16). Region I of the stress-strain curve was found to correspond to elastic deformation of the network. If the sample was not stretched beyond this region, it did not return to its original shape.[153] Region II began when the sample yielded, and the neck formed as some of the polydomain sample was converted to a monodomain in a localized fashion. Hairpins are lost at the neck as the P-M transition proceeds. If the sample was held at some constant elongation in Region II, some relaxation was observed as the neck grew slightly, due to the conversion of more material to a monodomain state. By the end of Region II, the entire sample was converted to a monodomain, and further increases in strain resulted in a rapid increase of the required stress. This observation is similar to the strain hardening seen in conventional amorphous elastomers due to the finite extensibility of the network chains.[153] WAXD analysis reveals some degree of layer-buckling during Region III, in which the oriented and layered mesogens in the chains collapse to a layering at some angle oblique to the axis of elongation in an attempt to accommodate the stress on the already elongated chains (Fig. 1-20).[153] In addition, very slow stress relaxation was observed in our smectic MCLCEs, with no loss of the neck to the unaided eye at room temperature (above the sample's $T_g$) for over 1 year.[153] This property is

likely evidence of the formation of new smectic domains within the necked "monodomain" portion of the LCE, such that an energy barrier must be overcome to disrupt the new smectic layering and return to the original non-necked polydomain state. In fact, heating the sample to just below its clearing temperature "resets" the elastomer, returning it to its original dimensions within a few minutes.
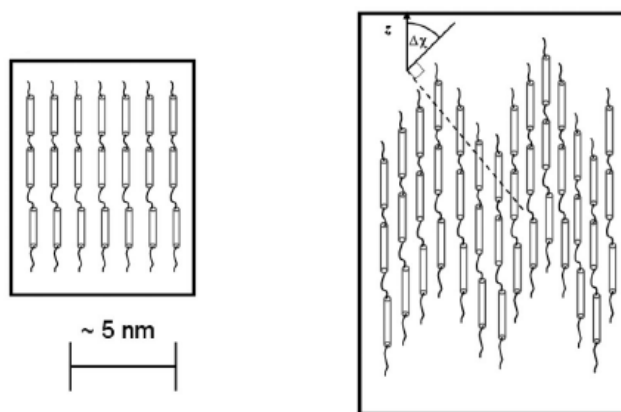


Figure 1-20. Schematic of smectic MCLCE with chains aligned and elongated (left) at the beginning of Region III, and of the subsequent layer buckling as strain continues to increase (right). [Source: Patil, *Macromolecules* 2009.]

MCLCP and MCLCE made with mesogens connected by highly flexible oligodimethylsiloxane units are widely studied for their easily accessible, low temperature mesophases.[136,177-183] Thus, it is plausible that the large gap between $T_g$ and $T_{si}$ of our materials have aided in neck formation, while conventional testing parameters have not been suitable for its formation in other LCE systems. Though it is possible that a clearly defined neck is observed only under certain conditions of temperature and strain rate in some LCE, it is also possible that some LCE do not exhibit a necking transition or a drop in the nominal stress during elongation at any temperature or strain rate. A thorough study of the yield behavior and necking transition is needed in order to understand how and to what degree the temperature and strain rate influence these characteristics of smectic MCLCEs.

A further potential for practical applications exists in leveraging the change in alignment at the P-M transition. The addition of a rod-like guest molecule could take advantage of the change in order to produce a change in the optical properties of the material.[184-187] Anisotropic distributions of nanoparticles could also be created via the stretching of an LCE/nanoparticle composite to produce a similarly dichroic optical material. For instance, dichroism has been demonstrated with PVA/gold nanocomposites, in which the gold nanoparticles align following uniaxial elongation of the sample.[29]

# Chapter 2

## Nanoinfusion Processing of Noble Metal/ Polymer Nanocomposites

The creation of nanoparticles in engineering thermoplastics using AURA® color infusion technology (AURA) is presented as proof of concept for the production of a polymer/metal nanocomposite via infusion into a finished polymer article. The process is broadly applicable to a variety of transition metals such as gold, silver, iron, copper, and nickel. A metal salt was first infused into various pre-processed thermoplastic polymers including thermoplastic polyurethane elastomers (TPUs), a copolymer-coated poly(methyl methacrylate) sheet (acrylic), and a polycarbonate (PC). Due to the presence of solvent in a shallow surface layer of the polymer, the salt became soluble in the plasticized polymer and was able to diffuse into the surface. A second infusion of triethylamine (TEA), followed by a baking/drying step, reduces the metal salt to elemental metal nanoparticles.

For systematic study, gold was chosen for a variety of reasons. Gold nanoparticles have been studied quite frequently and their properties are well known. Gold nanoparticles possess brilliant colors dependent on the size, shape, and dispersity of the particles. Therefore, the success of infusions could be initially evaluated with the unaided eye. Further, gold nanoparticles are chemically stable and will not oxidize. The gold precursor salt used, $HAuCl_4$, was found to be soluble in a variety of polymers. Gold has a high reduction potential, lending itself to the infusion-reduction method described herein. Finally, characterization with SAXS and TEM was aided by the high electron density of the gold nanoparticles, which provides good contrast with the polymer matrix.

### 2.1 Experimental

#### 2.1.1 Materials

Thermoplastic polyurethane elastomers Texin® 245, Texin® 255, Texin® 285, and Texin® DP7-1199 (henceforth referred to as T245, T255, T285, and TDP7-1199, respectively)

were obtained from Bayer MaterialScience (Pittsburgh, PA). Each TPU was injection molded to produce flat slabs of approximate dimensions (7.5 cm x 15 cm). The thickness of the T245, T255, and TDP7-1199 samples was 3.5 mm, whereas the thickness of the T285 samples was 2.0 or 3.2 mm. T245, T255, and T285 are copolymers formed via a polycondensation of butylene adipate polyester, methylene diphenyl diisocyanate, and 1,4 butanediol. The differing glass transition temperatures of the TPUs, shown in Table 2-1, are due to different ratios in the formulations. TDP7-1199 is produced via a similar reaction; however, the specific components are proprietary. Cast acrylic sheet (Plaskolite® abrasion resistant (AR) acrylic) of 2.3 mm thickness was obtained from Plaskolite, Inc. and used as received. The acrylic sheet was coated with a copolymer of pentaerythritol triacrylate (80 % w/w) and 1-ethenyl-2-pyrrolidinone (20 % w/w). This material is marketed as Gafgard® 233 (G233) by International Specialty Products. The abrasion-resistant copolymer layer was approximately 15 μm thick and contained a small volume fraction of a silicate nanofiller. An uncoated acrylic sheet with otherwise identical properties and thermal history was obtained by grinding off the abrasion-resistant coating with sandpaper. Makrolon® 2608 PC was obtained from Bayer MaterialScience as injection molded flat slabs of approximate dimensions (5 cm x 7.5 cm) with 2.6 mm thickness. Glass transition temperatures for all samples, quoted by the supplier, are shown in Table 2-1. The glass transition temperature for G233 was determined using differential scanning calorimetry at a heating rate of 10 °C/min., and the $T_g$ was taken from the midpoint of the usual inflection. Hydrogen tetrachloroaurate trihydrate (99.99 %, Alfa Aesar), triethylamine (99 %, Alfa Aesar), ethylene glycol monobutyl ether (butyl cellosolve) (99 %, Alfa Aesar) and diethylene glycol (99 %, Alfa Aesar) were used as received.

Table 2-1. Glass transition temperatures for unmodified plastic samples.

| Plastic | $T_g$(°C) |
| --- | --- |
| T245 | -46 |
| T255 | -26 |
| T285 | -42 |
| TDP7-1199 | -23 |
| Acrylic | 102 |
| G233 | 238 |
| PC | 145 |

**2.1.2 Metal Salt Infusion and Reduction**

Thermoplastic samples were infused with $HAuCl_4$ using AURA.[1-3,6,7]  $HAuCl_4$ infusion was accomplished by exposure to a dilute solution ($7.00 \cdot 10^{-3}$ M) of $HAuCl_4$ in a mixture of three solvents (70 % distilled water, 20 % butyl cellosolve, 10 % diethylene glycol, by volume) at 60 °C.  $HAuCl_4$ infusion times for individual samples are summarized in Table 2-2.  $HAuCl_4$-infused thermoplastics were subjected to a second processing step where triethylamine was infused to reduce the metal salt precursor to $Au^0$ nanoparticles.  Reductions were performed at either 23 °C (coated acrylic only) or 60 °C (all TPUs) by immersing $HAuCl_4$-infused plastic samples in a stirred solution of 0.072 M TEA in distilled water.  Samples were allowed to air dry at 80 °C for three days prior to further characterization to encourage evaporation of volatiles, during which time the growth of $Au^0$ nanoparticles proceeded, while the distinct pink, purple, or gray color indicative of such nanoparticles stabilized.  Little or no change in color was noted with longer baking times, suggesting that the rate of particle growth had slowed dramatically or ceased.

Table 2-2. Processing conditions employed to prepare Au$^0$-infused thermoplastic samples.

| Sample Name | HAuCl$_4$ infusion time (min.) | TEA reduction time (min.) | Appearance |
|---|---|---|---|
| **T285 TPU** | | | |
| T285-A | 15 | 5 | Pink-Lavender |
| T285-B | 25 | 5 | Purple-Gray |
| **T255 TPU** | | | |
| T255-A | 10 | 5 | Gray |
| T255-B | 15 | 5 | Gray |
| T255-C | 25 | 5 | Gray |
| **T245 TPU** | | | |
| T245-A | 25 | 5 | Pink-yellow |
| T245-B | 25 | 10 | Gray |
| T245-C | 25 | 15 | Gray |
| **TDP7-1199 TPU** | | | |
| DP7-A | 10 | 5 | Gray |
| DP7-B | 15 | 5 | Purple-Gray |
| DP7-C | 25 | 5 | Purple-Gray |
| **Copolymer-Coated Acrylic Sheet** | | | |
| Acrylic-A | 10 | 20 | Light red-purple |
| Acrylic-B | 20 | 20 | Red-purple |

In addition to HAuCl$_4$ infusions, AgNO$_3$ infusions were attempted with TPUs, acrylic, and polycarbonate. A solution of 0.7 M silver nitrate in AURA solvent was heated to 60 °C or 95 °C for the TPUs/acrylic and polycarbonate, respectively. Samples are immersed in the solution for 3 minutes. Silver nitrate-containing samples of T245, TDP7-1199, and polycarbonate were subjected to antibacterial testing by Bayer MaterialScience using *Pseudomonas aeruginosa* bacteria.

A variety of other metal salts were tested for their viability for infusion using AURA processing. Samples of TDP7-1199 were soaked in 0.007 M solutions of Cu(II)Cl$_2$·2H$_2$O, Cu(II)(ClO$_4$)·6H$_2$O, Cu(II)(NO$_3$)$_2$·2.5H$_2$O, Fe(III)Cl·6H$_2$O, Ni(II)(CH$_3$CO$_2$)$_2$·4H$_2$O, Ni(II)Cl$_2$·6H$_2$O, Ni(II)(ClO$_4$)$_2$·4H$_2$O, or Ni(II)(NO$_3$)$_2$·6H$_2$O for 20 minutes at 60 °C. Standard

reduction potentials for each metal, including gold and silver, are provided in Table 2-3 for comparison.

Table 2-3. Standard reduction potentials at 25 °C for all infused metals. [Source: Oxtoby, *Principles of Modern Chemistry* 5th ed. 2002]

| Metal | Standard Reduction Potential (V) |
|---|---|
| $Au^{3+} + 3e^- \rightarrow Au(s)$ | 1.42 |
| $Ag^+ + e^- \rightarrow Ag(s)$ | 0.7996 |
| $Fe^{3+} + 1e^- \rightarrow Fe^{2+}$ | 0.770 |
| $Cu^{2+} + 2e^- \rightarrow Cu(s)$ | 0.3402 |
| $Fe^{2+} + 2e^- \rightarrow Fe(s)$ | -0.409 |
| $Ni^{2+} + 2e^- \rightarrow Ni(s)$ | -0.23 |

## 2.1.3 Transmission Electron Microscopy (TEM)

The $Au^0$-infused acrylic sheet and an unmodified acrylic sheet (control sample) were microtomed at room temperature using a Leica Ultracut UCT Microtome to obtain slices of approximate thickness 70 nm. Slices were taken parallel to the original surface of the sample, in order to obtain the largest possible number of $Au^0$ particles in each slice. Embedding of samples in epoxy was not necessary. The depth of the slices taken was approximately 2 to 5 μm beneath the original surface of the sample. TPU samples were cryo-microtomed at -120 °C into slices of approximate thickness 70 nm using the Leica FCS attachment. Glass knives were cut immediately before sectioning. The sample was faced at a low cutting speed and large (~200 nm) sample thickness. Cutting speed was gradually increased for convenience and set thickness gradually decreased until the desired sample thickness was achieved. Care must be taken to constantly monitor both the cutting speed and the anti-static setting, as the TPU sections are prone to rolling up and adjustments to these parameters may aid in collection of flat, complete sections. Following sectioning, all plastic slices were mounted on 400 mesh copper grids from Electron Microscopy Sciences. TEM images were obtained in a JEOL JEM 1200 EXII TEM, equipped with a Tietz F224 camera, at an accelerating voltage of 80 or 100 kV. Particle size distribution in

the TEM images was quantified using the "Measure" capability in ImageJ 1.38x (created by Wayne Rasband, National Institutes of Health).

## 2.1.4 Ultraviolet-Visible Absorption Spectroscopy

UV-Vis spectroscopy was performed on flat slabs of thermoplastics on a Varian/Cary 100 UV-Vis spectrometer in transmission. Slab thickness was kept constant within each series of samples.

## 2.1.5 Optical Microscopy

Samples were sectioned perpendicular to the original surface at a location far from the edge using a razor blade, and the cross-section was observed edge-on to determine the approximate thickness of the infused surface layer. Samples were characterized via orthoscopic observation (in transmission) using an Olympus BX51 microscope with UMPlanFL 5x or 20x objectives. Images were recorded using a 2.0 megapixel Diagnostic Instruments model # 11.2 Color Mosaic digital camera equipped with Spot$^{TM}$ digital imaging software.

## 2.1.6 Elemental Analysis

Energy dispersive x-ray spectroscopy (EDS) was used as a preliminary method to determine the presence of infused metal ions in the polymer surface. An Oxford Inca 200 EDS in conjunction with an FEI Quanta 200 environmental SEM (ESEM) was used for the measurements. Measurements were taken at three random points far from the sample edge on each sample. Herein, the surface layer refers to the top 1 μm of the sample that EDS is able to probe. For a more quantitative analysis, samples of TDP7-1199 were infused with $HAuCl_4$ at 60 °C using AURA, and an electron probe microanalyzer (EPMA) was used to interrogate the surface immediately thereafter. A CAMECA SX-50 EPMA was used to determine the weight fraction of gold in the surface layer of the samples. The system was operated at 10 KeV, 20 nA

with a spot size of 20 μm. Experimental uncertainties quoted are one standard deviation based upon at least 7 independent measurements of atomic composition at different surface locations.

## 2.2 Results and Discussion

Plastic samples were subjected to $HAuCl_4$ infusion at 60 °C, TEA reduction at 23 °C or 60 °C, and post-process drying in air at 80 °C. Processing conditions for individual samples are summarized in Table 2-2.

### 2.2.1 Metal Salt Infusion

The first step in the processing sequence involves immersing the plastic in a metal salt solution in a ternary solvent mixture consisting of water, butyl cellosolve (BCS) and diethylene glycol (DEG).[1-3,6,7] For all infusions discussed in this report, the composition of the solvent mixture was held fixed at 70:20:10 $H_2O$:BCS:DEG (by volume). Each of the solvents plays a well defined role in the infusion process. Water is a thermodynamically poor solvent for the plastics, which discourages dissolution of polymers during infusion and minimizes hazing and surface crazing in the plastics after drying. DEG and BCS serve as plasticizers that lower the glass transition temperature of a thin surface layer of polymer. DEG has also been used as a surface leveling agent (a substance that encourages uniform coloration) in earlier work that examined infusion of organic dyes.[1-3,6,7]

As has been mentioned, gold is a useful metal to serve as a model system for nanoinfusion synthesis due to a variety of reasons, such as its chemical stability, ease of synthesis, and brilliant size-dependent colors. However, other metals may be of greater practical interest, as gold is expensive and its practical applications in polymer nanocomposites are presently largely limited to its non-linear optical. In order to fully appreciate the broader significance of nanoinfusion processing its applicability to other metal salts must be evaluated. Of interest are a variety of properties, including antibacterial properties of silver ions, catalytic properties of platinum and palladium, magnetic properties of iron oxide, and conductivity of copper.

Samples treated with silver nitrate in AURA were subjected to anti-bacterial testing. The resulting samples take on a slight yellow or brown color, indicating uptake of the silver salt. 99.93 % of bacteria applied to the surface of a treated sample were killed, compared to 37.93 % killed on a sample treated with AURA but no silver nitrate, and 25.17 % killed on a completely untreated sample. Thus, it is reasonable to conclude that the silver nitrate was the cause of the antibacterial properties. However, samples were also tested in artificial urine, with the result that the silver treatment seemed to have no effect. Artificial urine typically consists of salts, urea, ammonia, and acid. For example, artificial urine may be prepared by dissolving 14.1 g NaCl, 2.8 g KCl, 17.3 g urea, 1.9 g ammonia water (25 %), 0.60 g $CaCl_2$, and 0.43 g $MgSO_4$ in 1 L of 0.02 M HCl.[188] It seems that, while the samples exhibited antibacterial properties, they were not effective for medically relevant applications.

Silver ions were also reduced to form $Ag^0$ nanoparticles using processing methods similar to the gold infusions. The yellow to deep brown color of the processed TPUs indicates formation of nanoparticles, which was confirmed by UV-vis and TEM analysis (Fig. 2-1). The T285 sample used for the TEM image was soaked in 0.01 M $AgNO_3$ in AURA for 20 min. at 60 °C, followed by reduction for 20 min. at room temperature in 0.033 M aqueous $NaBH_4$. Several irregularly shaped, highly aggregated silver nanoparticles are seen in the image. Particles were found sporadically throughout the observed sections, with large areas containing no particles intervening.
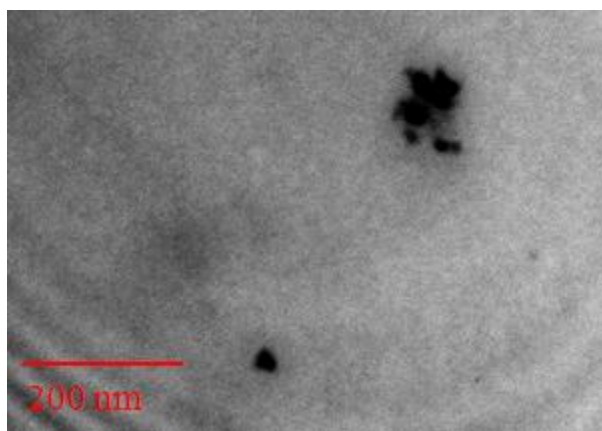


Figure 2-1. Silver nanoparticles observed in T285 via TEM.

Energy dispersive spectroscopy (EDS) was used to test TDP7-1199 samples for measurable amounts of a variety of metal precursor salts within the polymer surface. A control sample of TDP7-1199 soaked in AURA solvent without any metal salt was also tested. The data from this sample was compared to the samples treated with metal salt solutions in order to help

ensure that noise in the intensity versus energy plot were not erroneously identified as peaks. Looking just at the control sample, the EDS software identified 0.24 atomic% copper, -0.17 at.% iron, and 0.01 at.% nickel in the noise. Results from the attempted metal salt infusions are shown in Table 2-4. $Cu(II)Cl_2 \cdot 2H_2O$, $Ni(II)(ClO_4)_2 \cdot 4H_2O$, and $Ni(II)(NO_3)_2 \cdot 6H_2O$ were identified in large enough amounts compared to the control sample and the calculated standard deviation to be safely considered successful infusions. Though the atomic percent of iron detected for $Fe(III)Cl \cdot 6H_2O$ was lower than other infusions deemed succesful, it may also have been infused by this process. The control sample indicates that it is not likely for iron to be erroneously identified in the sample, and the standard deviation of the measurements of $Fe(III)Cl \cdot 6H_2O$ is less than the measured amount of iron. As such, it is reasonable to conclude that $Fe(III)Cl \cdot 6H_2O$ was also successfully infused.

Table 2-4. Metal salts tested for infusion with AURA into TDP7-1199 and characterized using EDS. Average atomic percent is given for each respective metal, based on 3 measurements on each sample, along with the standard deviation.

| Metal Salt | Average Atomic Percent Metal | Standard Deviation |
|---|---|---|
| $Cu(II)Cl_2 \cdot 2H_2O$ | 0.47 | 0.12 |
| $Cu(II)(ClO_4) \cdot 6H_2O$ | 0.07 | 0.06 |
| $Cu(II)(NO_3)_2 \cdot 2.5H_2O$ | 0.06 | 0.11 |
| $Fe(III)Cl_3 \cdot 6H_2O$ | 0.16 | 0.09 |
| $Ni(II)(CH_3CO_2)_2 \cdot 4H_2O$ | 0.02 | 0.04 |
| $Ni(II)Cl_2 \cdot 6H_2O$ | 0.10 | 0.02 |
| $Ni(II)(ClO_4)_2 \cdot 4H_2O$ | 0.28 | 0.07 |
| $Ni(II)(NO_3)_2 \cdot 6H_2O$ | 0.23 | 0.01 |

For the TPUs and the copolymer-coated acrylic sheet, immersion in the $HAuCl_4$ solution at 60 °C produced a bright yellow tint after a few minutes due to absorption of $HAuCl_4$. However, the uncoated acrylic sheet showed little or no absorption of $HAuCl_4$, regardless of infusion time or temperature. Thus, the $HAuCl_4$ was assumed to be absorbed by the copolymer surface coating on the acrylic sheet. Fig. 2-2 presents the UV-Vis absorption profiles of the coated acrylic sheet after different $HAuCl_4$ infusion times (without any further processing). The total amount of infused $HAuCl_4$ in the coating increases continuously with increasing infusion time, judging by the increasingly yellow color and the increase in absorbance in the (400 to

500) nm range (Fig. 2-3). Like the uncoated acrylic, the polycarbonate showed no detectable infusion of $HAuCl_4$, regardless of processing conditions.
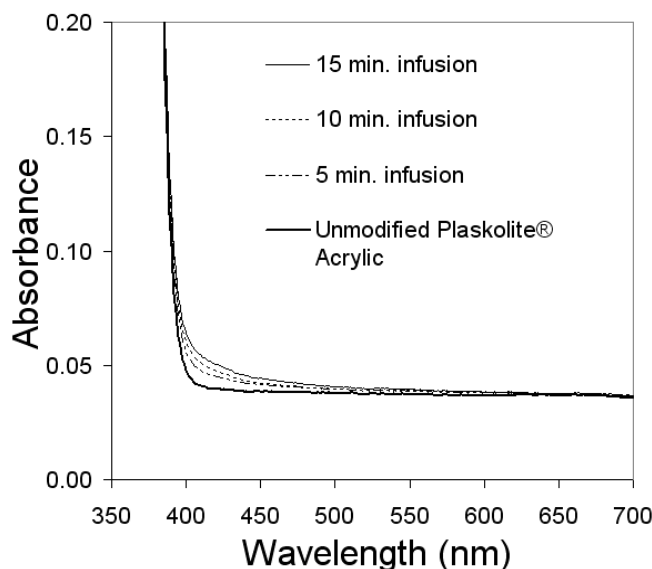


Figure 2-2. UV-vis of Plaskolite® AR acrylic sheet following $HAuCl_4$ infusion at 60 °C for various times.
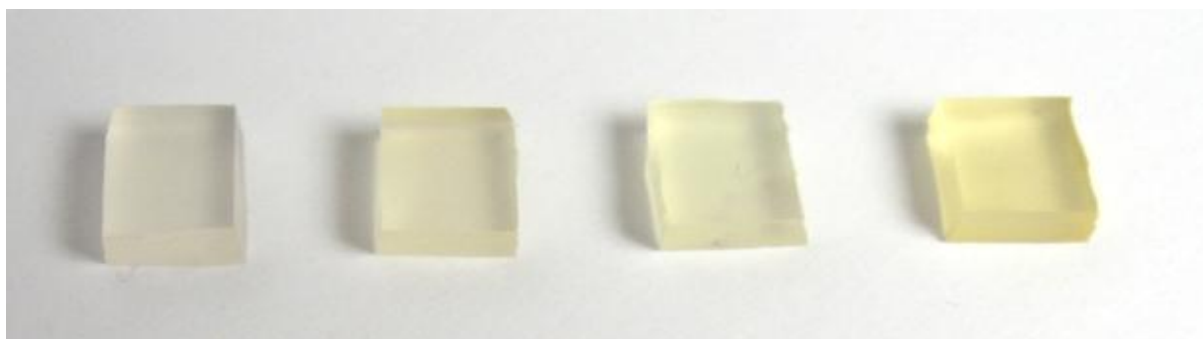


Figure 2-3. T285 infused with $HAuCl_4$ with soak times of (left to right) 5, 10, 15, and 20 min at 60 °C.

For the TPUs, 10 to 25 min. of immersion in the $HAuCl_4$ solution provided sufficient infusion to produce an obvious yellow color. Shorter infusion times may be possible with higher $HAuCl_4$ concentrations and/or higher temperatures. Increasing the external $HAuCl_4$ concentration would be expected to increase the overall flux of $HAuCl_4$ into the thermoplastic surface, assuming that the concentration of $HAuCl_4$ inside the plastic is not already limited by solubility. Increasing the processing temperature with respect to the glass transition temperature of the plastic enhances the rate of infusion of solvents into the article, which would also presumably enhance the rate of infusion of $HAuCl_4$. Previous studies of the infusion of organic

dyes clearly indicated that small increases in the infusion temperature produced dramatic increases in dye sorption rate. EDS was used to confirm the presence of gold, but the error bars on the concentration were too high to determine the quantity with any accuracy. Thus, EPMA data (Fig. 2-4) was used to further confirm the presence of gold in sample TDP7-1199 as well as obtain more quantitative data on the amount of Au in the topmost 1 µm of the sample tested. Au accounts for approximately 0.2 to 0.4 % w/w of the surface layer after 10 minutes or more of infusion. EPMA also reveals some inhomogeneity of the gold concentration on the surface, as seen by the variation in contrast (Fig. 2-5). The bright spots in Fig. 2-5 (higher Au concentration) may indicate local plating of gold on surface contaminants. EPMA measurements in Fig. 2-4 were therefore averaged over 7 locations on the sample surface away from the bright areas.
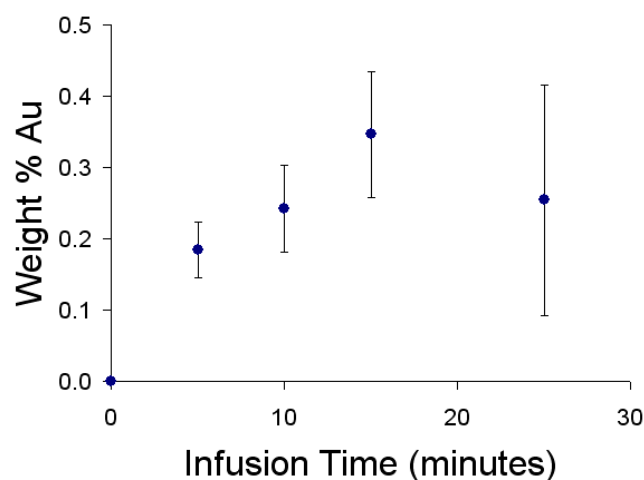


Figure 2-4. Weight % Au in the surface layer of TDP7-1199 determined by EPMA after different infusion times in HAuCl$_4$ solution at 60 °C.
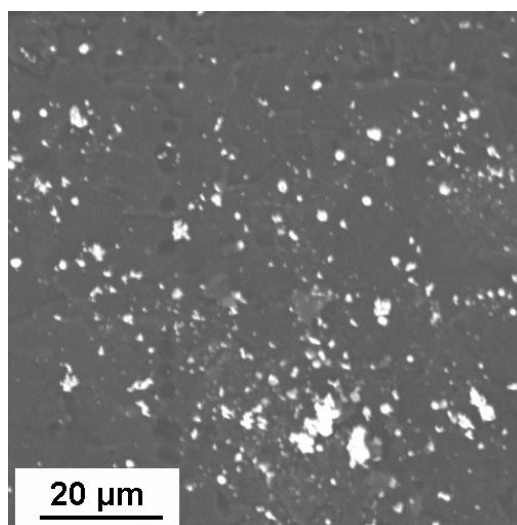
Figure 2-5. EPMA image of the TDP7-1199 sample infused for 15 min. in the HAuCl$_4$ solution. Bright areas indicate higher surface concentration of Au.

When a plastic article is immersed in the AURA solvent system, the rate of infusion of each component depends on its concentration in the external mixture, among other factors. In addition, the thermodynamics of mixing of a solvent with the polymer are affected by the presence of the other solvents (for example, infusion of BCS and DEG may enhance the rate of infusion of H$_2$O). Although we did not attempt to characterize the concentration profiles of the individual solvents in the plastics, it is reasonable to assume that at least DEG and BCS enter all of the plastics to some extent. To support this assertion, the comparative rates of infusion of the individual *pure* solvents were examined at 60 °C for all plastics studied (Table 2-5), by measuring sample mass after 15 minutes of immersion. (Note that thicknesses of samples were not identical; dimensions are quoted in Experimental section). The data in Table 2-5 illustrate that each of the solvents is able to enter each plastic to some extent, except that no significant absorption of water was noted for the acrylic sheet. Thus, during the HAuCl$_4$ infusion step, a mixture of solvents enters a thin surface layer of the plastic. The presence of solvents in the plastic, especially water, may enhance the solubility of the (hydrophilic) HAuCl$_4$, which is assumed to be coordinated by water (HAuCl$_4$·3H$_2$O) and possesses ionic character. The rate of permeation of HAuCl$_4$ into the plastic is likely enhanced as well due to the plasticizing effect of the solvents, which increase the mobility of polymer chain segments.

Table 2-5. Uptake (mass %) of pure solvents at 60 °C after 15 minutes in all plastics studied (determined gravimetrically). Uncertainty is ± 0.1 mass %.

| | TPUs ....................................................... | | | | | |
| | T245 | T255 | T285 | TDP7-1199 | Acrylic | PC |
|---|---|---|---|---|---|---|
| BCS | 4.33% | 2.41% | 5.73% | 14.80% | 3.77% | 0.42% |
| DEG | 1.07% | 0.82% | 1.63% | 1.25% | 0.07% | 0.06% |
| $H_2O$ | 0.56% | 0.37% | 0.81% | 0.51% | -0.01% | 0.13% |

The total mass uptake of mixed solvents at 60 °C was also measured as a function of immersion time (Fig. 2-6). While the TPUs and acrylic absorbed 1 mass % or more of mixed solvents after 15 minutes of infusion, the solvent uptake was significantly lower in the polycarbonate. One might expect that the lower solvent uptake in the polycarbonate might account for the observed lack of $HAuCl_4$ infusion. However, increasing the infusion temperature to 95 °C and/or allowing longer times for infusion increased the uptake of combined solvents to 1.5 mass %, but did not produce a detectable increase in $HAuCl_4$ infusion.
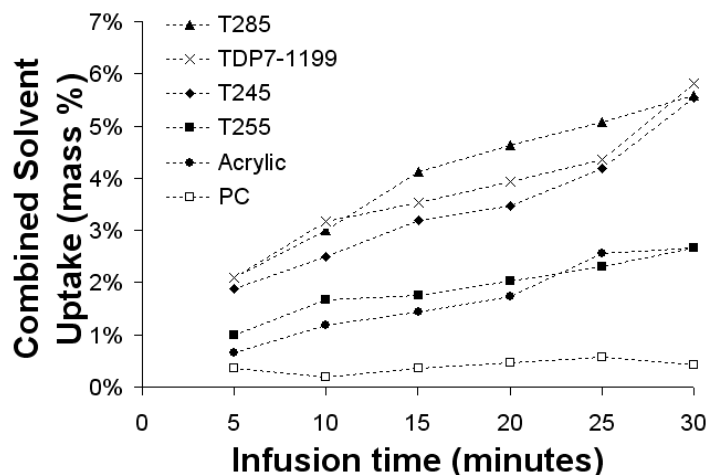


Figure 2-6. Combined solvent uptake as a function of infusion time for AURA with no added solute at 60 °C in all polymers tested.

It is tempting to rationalize the unsuccessful infusions of the polycarbonate and uncoated acrylic in terms of their higher glass transition temperatures compared to the TPUs. However, earlier work clearly demonstrated rapid infusion of organic dyes into both polycarbonate and acrylic under processing conditions similar to those studied here,[1-8] and increasing infusion times and temperatures had little effect on the uptake of $HAuCl_4$ in polycarbonate or uncoated acrylic.

These observations suggest that poor miscibility of the HAuCl$_4$ with these plastics is the underlying cause for the lack of infusion. The poor miscibility likely results in part from the relatively low uptake of water in these plastics, especially given that HAuCl$_4$ is coordinated by water molecules (HAuCl$_4$·3 H$_2$O).

### 2.2.2 HAuCl$_4$ Reduction: Chemical Reduction Method

Following infusion with HAuCl$_4$, the plastic samples are exposed to a dilute (0.072 M) solution of TEA in water to reduce HAuCl$_4$ to Au$^0$, then baked at 80 °C to remove volatiles. The infusion of TEA and subsequent redox reaction between HAuCl$_4$ and TEA are rapid at 60 °C, judging by nearly instantaneous fading of the bright yellow color of HAuCl$_4$ upon immersion in the TEA solution. Newman and Blanchard studied reduction of HAuCl$_4$ in dilute solution by various amine reagents including TEA,[189] and proposed the generic redox reaction:

$$HAuCl_4 + 3\ NR_3 \rightarrow Au^0 + 3\ NR_3\bullet^+ + H^+ + 4Cl^- \tag{2-1}$$
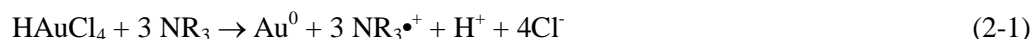
Au$^0$ nanoparticles form by a nucleation and growth mechanism in solution, and the NR$_3$•$^+$ radicals were found to form a polyamine by-product in some instances.[189] In the system herein reported, reduction of HAuCl$_4$ is apparently rapid, but growth of Au$^0$ nanoparticles within the plastic is significantly slower. After reaction with TEA, samples are baked in an oven at 80 °C for a few days (TPU samples) or two weeks (coated acrylic sheet). During baking, the volatile components evaporate, while the characteristic color of the Au$^0$ nanoparticles (generally pink, purple, or gray) appears and stabilizes (Fig. 2-7). Au$^0$ nanoparticles apparently form by arrested precipitation, at a rate which is significantly slower than that of the initial redox reaction between HAuCl$_4$ and TEA. Au$^0$ nanoparticles may grow by diffusion of smaller Au$^0$ clusters through the plasticized polymer, with particle growth slowing greatly when particles become too large to diffuse readily through the matrix. Evaporation of the volatile plasticizers with time is expected to further slow the diffusion of particles by increasing the matrix viscosity.
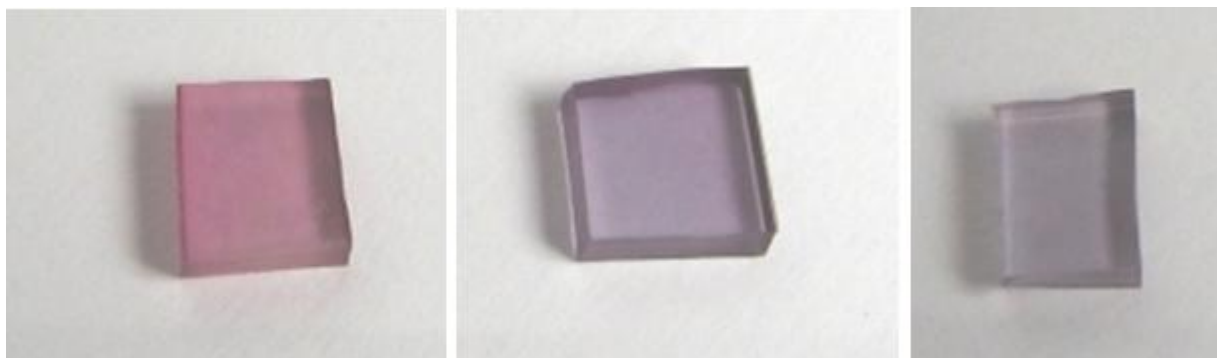
Figure 2-7. T285 samples following 15 min. 0.072 M HAuCl$_4$ infusion and (left to right) 3, 5, and 7 min. soaks in aqueous triethylamine solution.

The depth of infusion of the Au$^0$ nanoparticles into the plastic surface was estimated by optical microscopy after sectioning the samples with a razor blade perpendicular to the original surface, at a location far from the edges. Fig. 2-8 illustrates cross-sections of several TPU samples, where the darker (pink, purple, or gray) surface layer contains the highest concentration of nanoparticles. The Au$^0$ nanocomposite layer is at least 20 to 30 μm thick in the TPU samples. The fading of the color with increasing depth is attributed to the expected gradient in HAuCl$_4$ concentration beneath the surface after infusion. Fig. 2-9 shows a cross-sectional view of the Au$^0$-infused acrylic sheet. The well-defined surface layer of approximate thickness 15 μm is the acrylate-pyrrolidinone copolymer coating. Judging by the reddish brown color of this layer and the sharp cut-off at the interface with the underlying acrylic, the infusion of Au$^0$ particles is confined to the surface coating. The uncoated acrylic control sample showed no significant infusion of gold under similar processing conditions, supporting this assertion.
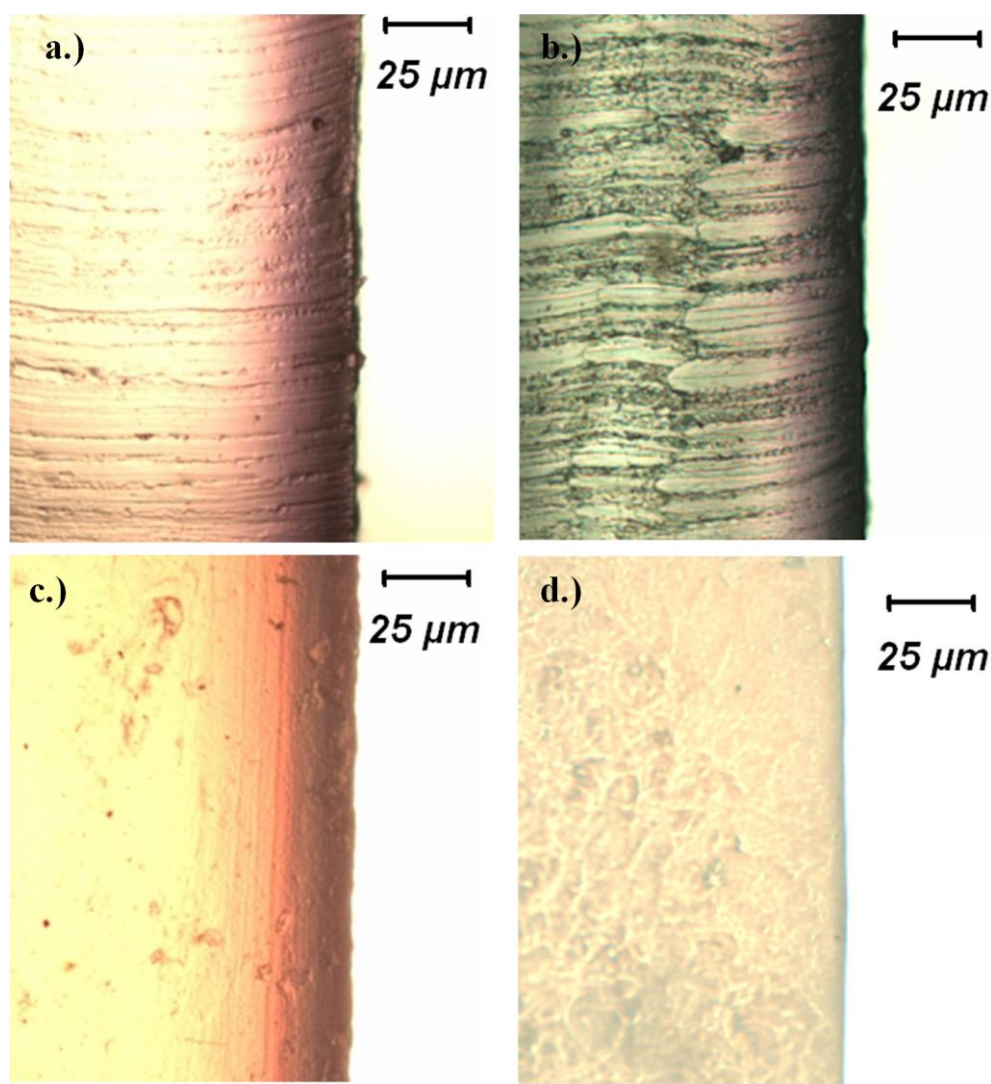
Figure 2-8.  Optical micrographs illustrating infused surface layer of $Au^0$ nanoparticles in (a.) T245-B, (b.) T285-B, and (c.) TDP7-B, while (d.) depicts an unmodified T285 sample.
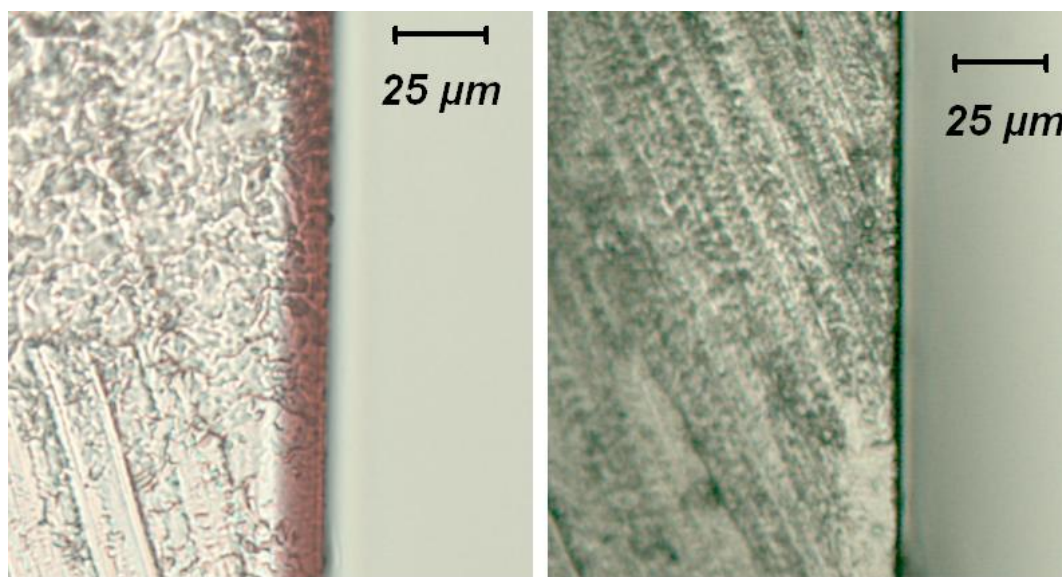
Figure 2-9. Optical micrograph illustrating Au$^0$-containing surface coating on Acrylic-B sample (left), compared with an unmodified piece of coated acrylic (right).

## 2.2.3 Au$^0$ Particle Characterization

UV-Vis spectra (Figs. 2-10 and 2-11) confirm the presence of Au$^0$ nanoparticles in the TPU and coated acrylic samples after TEA reduction. The well-defined absorbance centered in the 530 nm to 570 nm range is assigned to the surface plasmon resonance absorption of Au$^0$.[190] Though the wavelength and bandwidth of the Au$^0$ surface plasmon absorption are known to depend upon the Au$^0$ nanoparticle size,[190-192] the shape and position of the band(s) may also be affected by the breadth of the size distribution, the particle shape,[193-196] and the possible formation of aggregates.[197-199] Therefore, microtomed nanocomposite samples were characterized by TEM to probe the Au$^0$ particle size distribution, particle shape, and quality of dispersion.
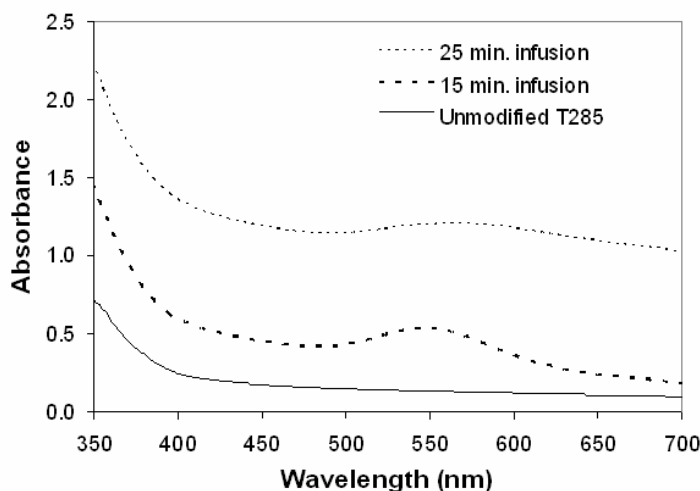
Figure 2-10. UV-vis spectra for $Au^0$-infused T285 samples produced using different $HAuCl_4$ infusion times and a consistent 5 min. reduction step in TEA solution.
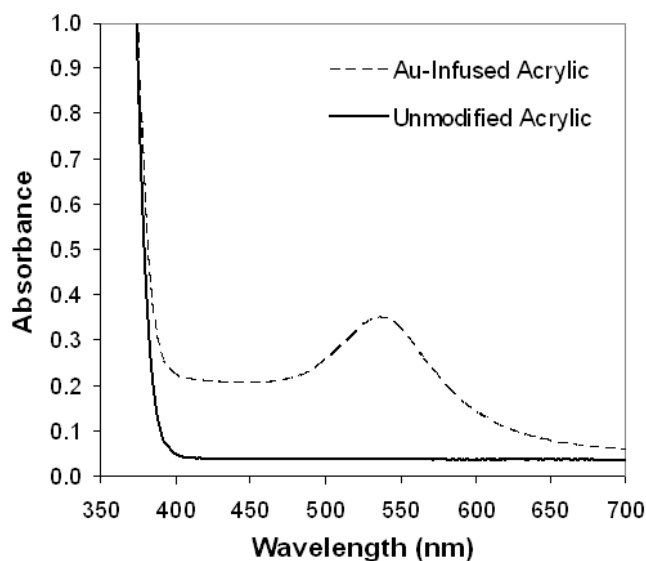


Figure 2-11. UV-vis spectra for both unmodified Plaskolite AR acrylic sheet and Acrylic-B sample infused with $Au^0$ nanoparticles, produced via a 20 min. $HAuCl_4$ infusion and a 20 min. TEA reduction.

For TPU samples, the particle size was found to depend on both the $HAuCl_4$ infusion time and the TEA reduction time. For the T285, gray colors (largest average $Au^0$ particle size) were obtained with longer $HAuCl_4$ infusion times, whereas purple or pink colors characteristic of smaller $Au^0$ particles were produced after shorter infusion times. UV-Vis spectra support the assertion that longer $HAuCl_4$ infusion times generally lead to larger average particle size. Both broadening and redshifting of the surface plasmon absorption are observed with increasing

HAuCl$_4$ infusion time (Fig. 2-10). For Au$^0$ particles having diameter of about 25 nm or larger, both broadening and redshifting of the surface plasmon band are expected with increasing particle size due to extrinsic size effects.[190,200] The HAuCl$_4$ infusion time not only affects the concentration profile and depth of penetration of the HAuCl$_4$, but also affects the surface concentration of solvents in the plastic. Longer infusion times also increase the amount of solvent in the plasticized surface layer, which could enhance aggregate formation by increasing the diffusivity of small Au$^0$ clusters.

The time allowed for reduction in the aqueous TEA solution also affects the Au$^0$ particle size. Short reduction times may lead to smaller Au$^0$ particles due to incomplete reduction of HAuCl$_4$ to Au$^0$. Some evidence for incomplete reduction was seen in the T245 samples in Table 2-2, for example. Gray colors characteristic of comparatively large Au$^0$ particles were obtained for longer TEA reduction times. However, the pink-yellow color of sample T245-A suggests incomplete reduction of HAuCl$_4$ to Au$^0$. Longer TEA reduction times should be required for samples subjected to longer HAuCl$_4$ infusion times because the depth of infusion of the HAuCl$_4$ is greater.

TEM images were obtained for a few T285 samples having significantly different colors (T285-A, pink; and T285-B, purple-gray) (Fig. 2-12, Fig. 2-13). T285-A was found to contain well-dispersed Au$^0$ particles of diameter 10 nm to 50 nm, and approximately spherical shape (Fig. 2-12). A control sample of unmodified T285 did not contain any particles or other inclusions that could be mistaken for Au$^0$ particles. On the other hand, T285-B contained isolated larger aggregates, some with diameter in excess of 100 nm (Fig. 2-14). The irregularly shaped aggregates observed in T285-B suggest that particle growth occurs by diffusion of smaller particles through the plasticized polymer matrix. It should be noted that the sections observed with the TEM were approximately 70 nm thick, so it is possible and even likely that some larger aggregates may have been removed by the glass knife during sectioning, resulting in images that are non-representative of the state of the nanoparticles within the polymer matrix.
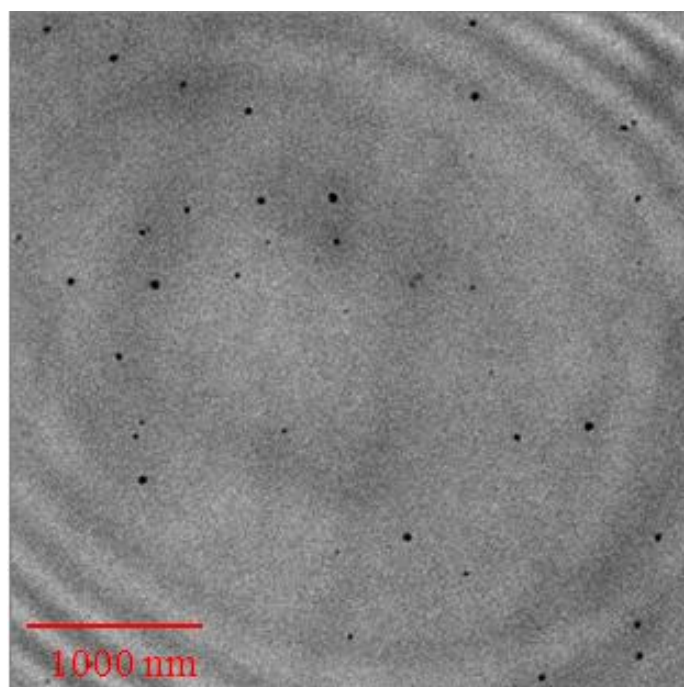
Figure 2-12.  TEM image of $Au^0$-containing sample T285-A.
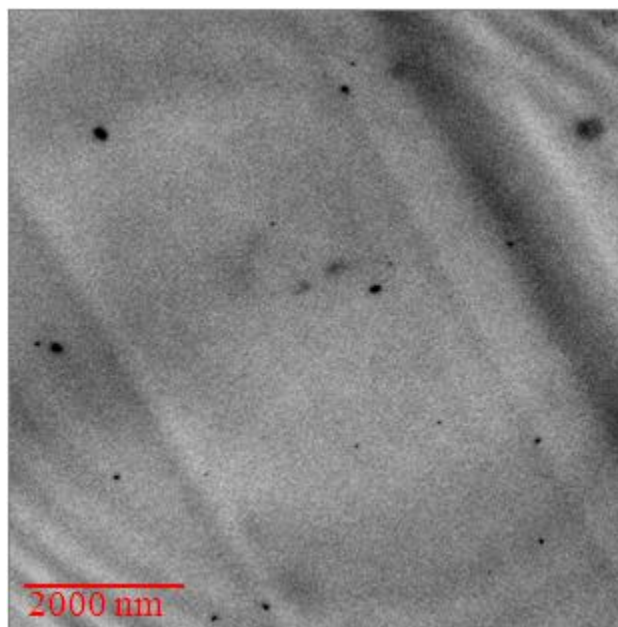


Figure 2-13.  TEM image of $Au^0$ nanoparticles in T285-B.
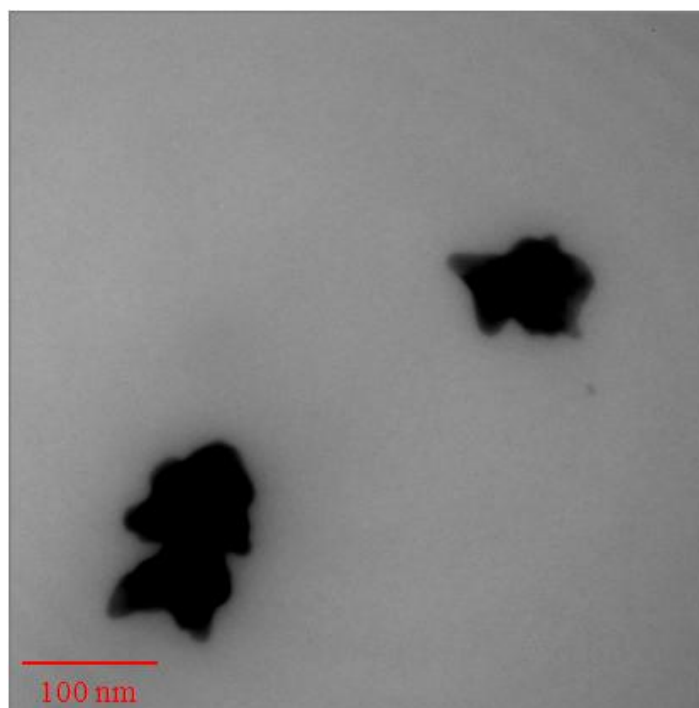
Figure 2-14. TEM image of $Au^0$ nanoparticle aggregates in sample T285-B.

UV-Vis spectra (Fig. 2-11) and TEM images (Fig. 2-15) were also acquired for the sample Acrylic-B, which exhibited a strong red-purple color due to $Au^0$ nanoparticles in the surface coating. The peak of the surface plasmon absorption was observed at $\lambda_{max} = 537 \pm 5$ nm, and the absorption band was narrower than that observed in the TPUs. A similar $\lambda_{max} = 533$ nm has been reported for $Au^0$ colloids of 48 nm diameter in aqueous solution.[190] In Fig. 2-15, $Au^0$ particles appear as small, nearly round black dots, which are well-dispersed. The larger, irregular structures in Fig. 2-15 are the silicate nanofiller that was present in the surface coating. A control sample of the unmodified coated acrylic material contained the silicate nanofiller, but none of the small, highly absorbing particles identified as $Au^0$ (Fig. 2-16). The $Au^0$ particles were estimated to have a mean diameter of 56 nm with a standard deviation of 16 nm (n = 374) (Fig. 2-17). Compared to the TPUs, the coated acrylic sheet showed less evidence of $Au^0$ particle aggregation, at least under the processing conditions used to prepare the single sample studied. Fig. 2-18 shows an enlarged view of a few $Au^0$ particles, revealing that some of the particles are nearly spherical, whereas some polygonal shapes are also observed, perhaps indicating crystalline gold. In addition, some of the particles found appear to have hollow centers (Fig. 2-19). Hollow particles could result if $Au^0$ particles nucleate and grow on the surface of quasi-spherical impurities or voids in the plastic. The lack of $Au^0$ aggregates in the surface coating, which is

cross-linked, suggests that the viscosity of the plasticized surface layer may be higher than that in the TPUs, slowing aggregation.
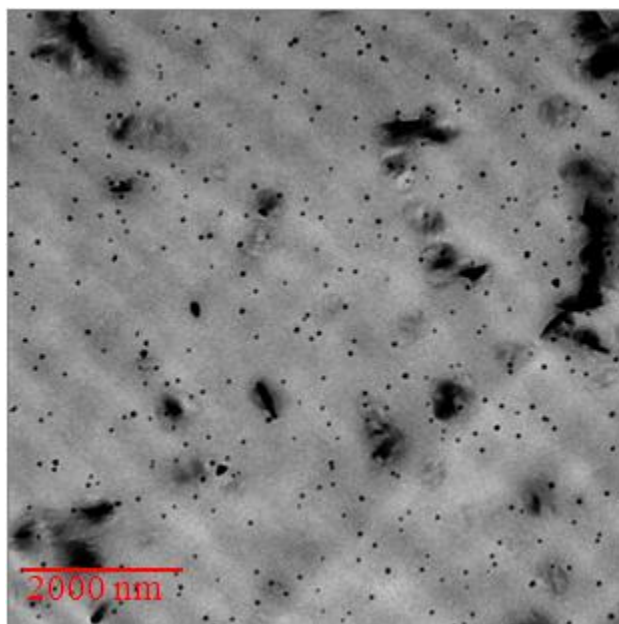


Figure 2-15.  TEM image of $Au^0$ nanoparticles in sample Acrylic-B.
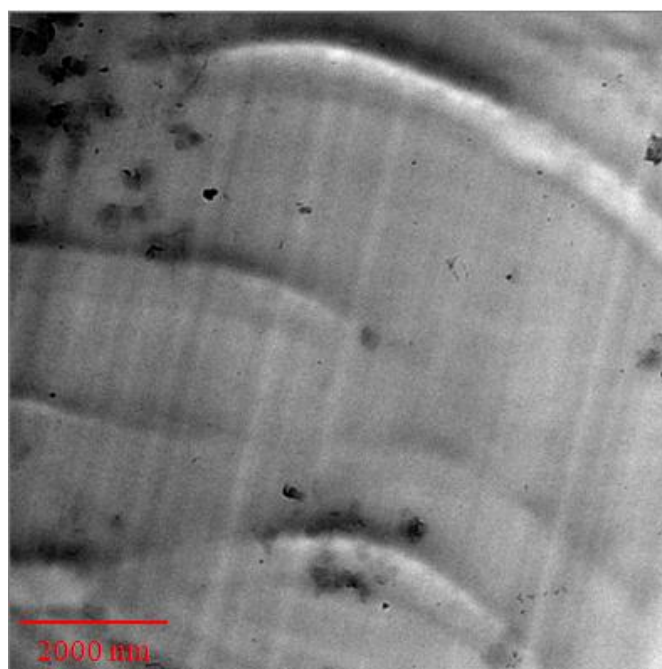


Figure 2-16.  TEM image of an unmodified acrylic sample showing a large amount of the nanofiller present in the surface coating.
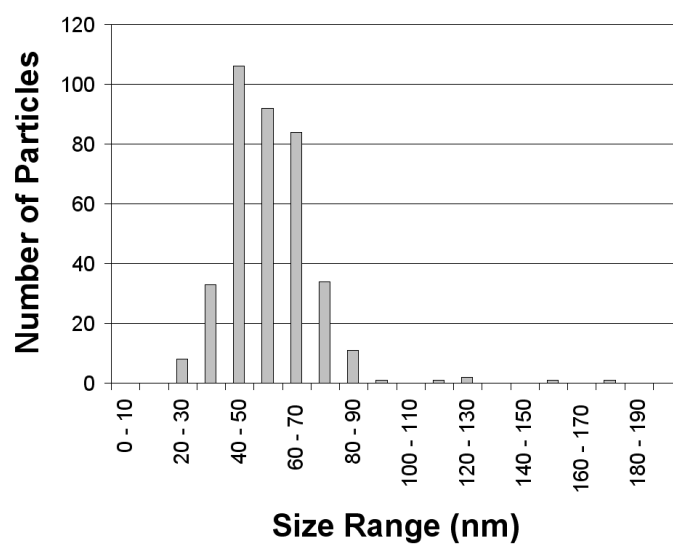
Figure 2-17.  Particle size distribution statistics generated from Figure 2-15.
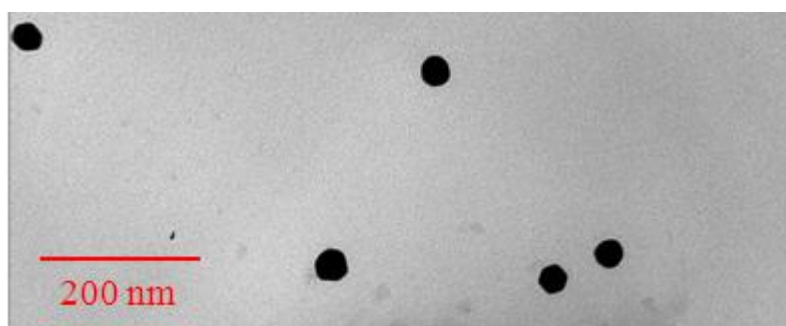


Figure 2-18.  TEM image of polygonal $Au^0$ nanoparticles in sample Acrylic-B.
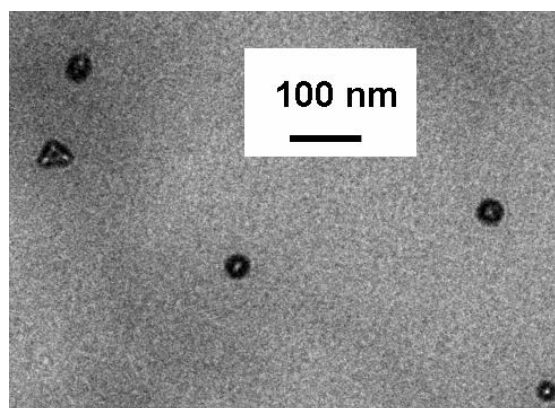


Figure 2-19.  Hollow nanoparticles seen in TEM image of $Au^0$ nanoparticles in sample Acrylic-B.

# Chapter 3

## Gradient Interpenetrating Networks via Surface Infusion Processing of Thermoplastic Polyurethane Elastomers

An interpenetrating polymer network (IPN) is usually defined as a material which consists of a pair of intermeshing networks, one of which at least has been synthesized and/or cross-linked in the presence of the other.[201] Sometimes termed a sequential interpenetrating network, the most common synthetic method is the swelling of a host polymer network with a monomer, along with cross-linking and/or activation agents, such that the monomer can be polymerized within the host polymer.[202] The result is two polymer networks that interpenetrate on a molecular level. Ideally, the interpenetration is entirely physical, with little or no chemical grafting between the two polymer networks.[203] If only one of the polymers is cross-linked, the system is referred to as a semi-IPN; systems where both polymer are cross-linked are full-IPNs.[201,203] IPNs have been extensively studied since the 1970s. Early work focused on synthesis and tuning of IPN mechanical properties,[201,202] while more recent work has also sought to leverage the properties of the IPN for advanced applications such as controlled drug delivery from IPN hydrogels.[204,205] Particularly relevant to the current work, the in situ reduction of $AgNO_3$ to $Ag^0$ has been demonstrated using $NaBH_4$ as a reducing agent within an interpenetrating network, where $COO^-$ groups on the polymer serve as templating cites for the reduction.[206]

Herein, an infusion process is outlined, which consists of the creation of a surface layer semi- or full-IPN of a polymethacrylate in a thermoplastic polyurethane elastomer. Bulk diffusion of the monomer into TPU samples, with no need for AURA solvent, was used to introduce the monomer and an initiator to the host polymer. Following infusion, the monomer was polymerized using a UV light source. This method is most applicable to elastomeric polymer hosts that are able to swell as the monomer diffuses into the polymer. Conversely, a rigid polycarbonate sample was found to crack and haze at the surface in the presence of the monomer, due to its inability to accommodate any swelling. The creation of a surface-layer IPN of a guest polymer within the matrix of a host polymer is interesting due to the potential for enhancement of the surface properties of the TPU. Properties of interest include mechanical properties (such as the energy of failure, Young's modulus, and elongation at break), enhanced barrier properties, or even enhanced conductivity. For instance, a change in surface energy may be achieved or scratch

resistance may be improved via the creation of a surface layer IPN. Further, due to the gradient nature of the infusion, there is a potential for interesting vibration damping properties because of the creation of a gradient in $T_g$ at the surface.

In addition to its use in modifying the barrier and mechanical properties of the host polymer, the IPN method may also be used as a reduction method for the in situ synthesis of metal nanoparticles. Unlike the chemical reduction method described earlier, the IPN process results in the auto-reduction of the salt by pendant amine groups in the IPN layer, eliminating the additional reduction step. The IPN method yields smaller, more concentrated, and less agglomerated particles than the previous chemical reduction method. Transmission electron microscopy (TEM) and small angle x-ray scattering (SAXS) are utilized to examine the particle size distribution and quality of dispersion, while optical microscopy is employed to probe the depth of penetration of the surface layer of $Au^0$ nanoparticles.

## 3.1 Interpenetrating Network Synthesis

### 3.1.1 Initial Work

In order to investigate the possibility of property enhancement using an infused surface layer IPN, several polymerizable unsaturated monomers were infused and polymerized in the surface of TPU samples and characterized in order to evaluate the change in the samples' properties. In early work on this project done in conjunction with Ms. Morgan Iannuzzi, an undergraduate researcher in our group, four monomers were tested for creation of IPN materials: methyl methacrylate (MMA), ethylene glycol dimethacrylate (EGDMA), 1,4-divinylbenzene (DVB), and 2-hydroxyethyl methacrylate (HEMA) (Fig. 3-1). All monomers were purchased from Sigma Aldrich and used as received. EGDMA has previously been studied in semi-IPNs along with poly(HEMA) hydrogels in an effort to improve the mechanical properties of the gels.[207] However, any monomer that is a thermodynamically "good" solvent for the TPU should be amenable to this processing. As long as the monomers were able to sufficiently swell the polymer at room temperature and, in doing so, carry in enough of the radical initiator, in situ polymerization could be conducted using a UV lamp. Fig. 3-2 shows the mass uptake of the monomer solution into the 3.3 mm thick, injection molded TDP7-1199 samples as a function of

time at room temperature. From these measurements, it is possible to estimate the diffusivity of each monomer into the flat polymer slab using the equation:[9]

$$\frac{M_t}{M_\infty} \approx 2\left(\frac{D_{12}^{1/2}}{\pi L^2}\right)t^{1/2}$$

(3-1)

where $M_t$ is the mass of solvent in the slab at time t, $M_\infty$ is the mass of solvent in the slab at equilibrium swelling, $D_{12}$ is the diffusivity of the solvent in the polymer, and L is half the thickness of the slab when not swollen. It is important to note that equation 3-1 is valid for short times, assumes that the diffusivity is concentration-independent, and assumes that the slab thickness is constant.[9] Additionally, the equation assumes one-dimensional diffusion from both sides of the slab, that the concentration of monomer on either side of the slab is the same, and that the diffusion considered is far from any edges.[9] Though not an appropriate model for glassy polymers, it is suitable for use with TPU elastomers above their $T_g$ such as those we are studying. By plotting $M_t/M_\infty$ versus $t^{1/2}$, $D_{12}$ can be determined from the slope. $M_\infty$ was determined by swelling the polymer samples in a monomer until equilibrium swelling was reached, normally over a period of several days. Once the mass of the swollen sample ceased to increase with immersion time, the value was taken as $M_\infty$. Note that this equation is valid for $M_t/M_\infty \ll 0.5$, where the plot is linear. Applying this model to the monomers infused into TDP7-1199, we found diffusivities for MMA, DVB, and EGDMA (Table 3-1).
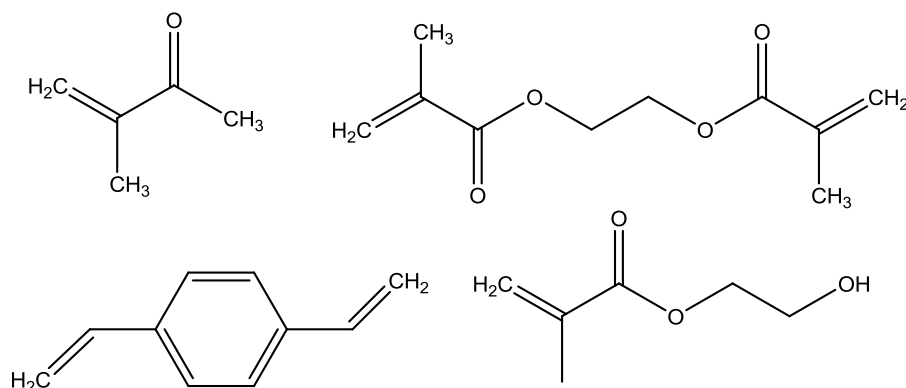


Figure 3-1. Chemical structures of the four methacrylate monomers tested (clockwise from top left): MMA, EGDMA, HEMA, and DVB.
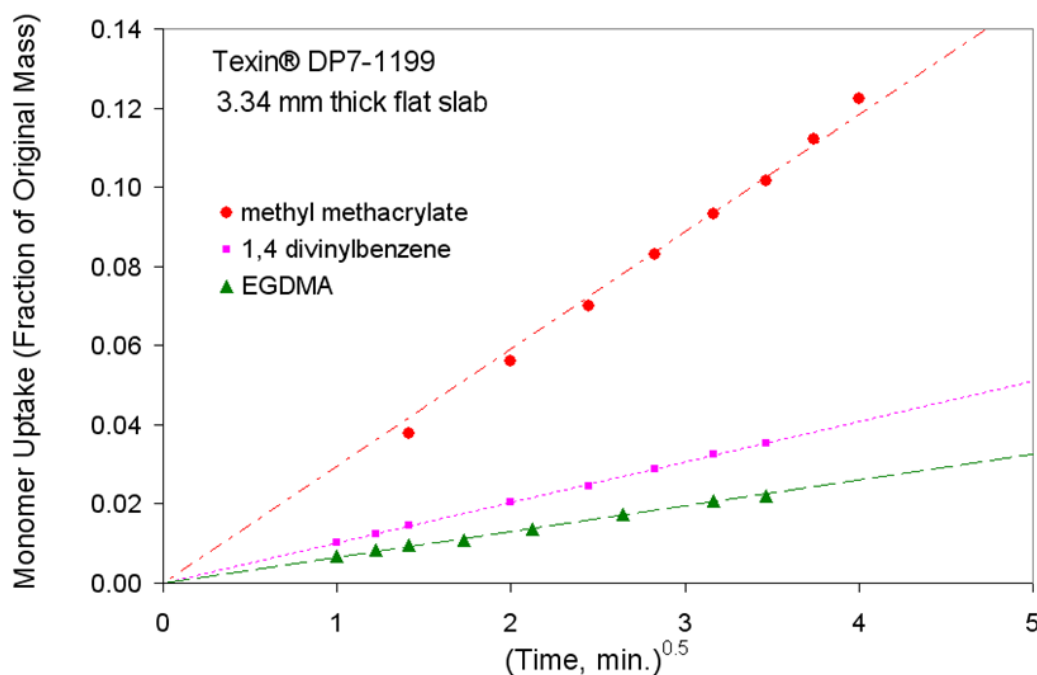
Figure 3-2. Uptake of polymerizable monomers by TDP7-1199 at 22 °C.

Table 3-1. Calculated diffusivities of monomers into TDP7-1199.

| Monomer | $D_{12}$ (22 °C) (cm$^2$/s) | $M_\infty/M_o$ (48 hours) |
|---------|------------------------------|----------------------------|
| MMA | $8.23 \cdot 10^{-5}$ | 3.03 |
| DVB | $6.22 \cdot 10^{-5}$ | 1.93 |
| EGDMA | $4.35 \cdot 10^{-5}$ | 1.85 |

Knowledge of the diffusivity permits modeling of the concentration profile at short times using the following equation:[208]

$$C = (C_s)erfc(\frac{x}{2\sqrt{D_{12}t}})$$

(3-2)

where x is the distance beneath the surface, C is the concentration of monomer within the sample at a given time and distance beneath the surface, and $C_s$ is the external surface concentration. This equation assumes an infinitely thick source and an infinitely thick slab, with diffusion proceeding in one dimension from only one side of the slab.[208] The result of this analysis is a rough idea of the calculated concentration of monomer as a function of depth for a given infusion time, which is shown for DVB in Fig. 3-3. Though we have assumed diffusion from only one side of the slab, diffusion will occur from both sides in reality. As the samples tested are 3.3 mm

thick, the estimated concentration profiles shown would begin to be affected by the monomer entering from the other side before the 1.5 mm of depth depicted in the figure. Another important caveat is that diffusion will continue during polymerization. Nonetheless, this analysis provides an idea of the amounts of infused monomer and their depth dependence. Furthermore, the depth of the surface layer of the eventual IPN is not just limited by diffusion of the polymer. The diffusion of the initiator and the transparency of the sample to UV light will both affect the thickness of the surface-layer IPN. As such, the final polymerized IPN may not have the same concentration profile as the monomer itself.
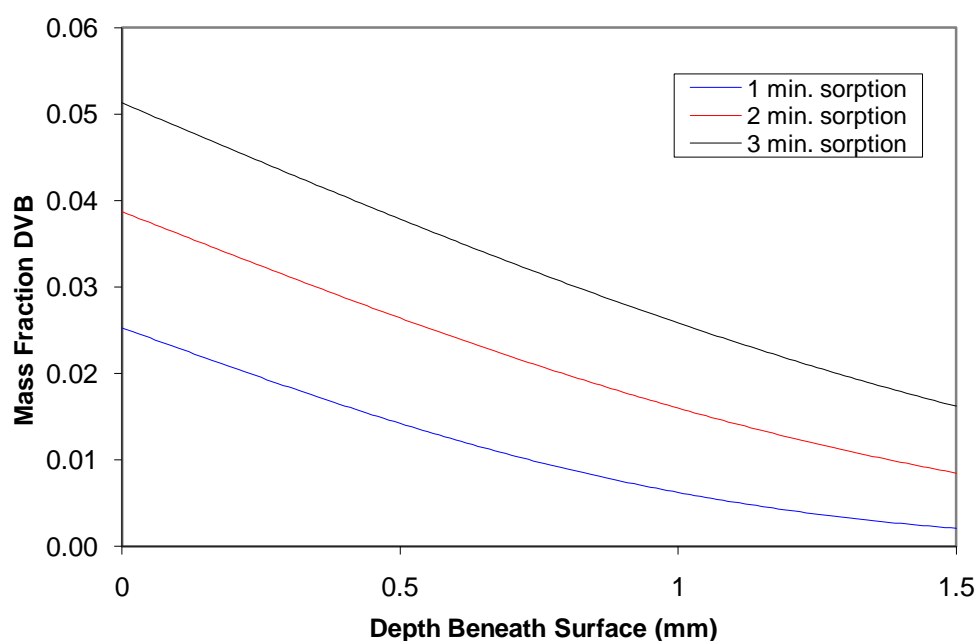


Figure 3-3. Modeled concentration of DVB in TDP7-1199 after 1, 2, and 3 minute soaks at room temperature. Model assumes diffusion in one dimension from one side of the slab.

We tested a variety of initiators for the polymerization of the infused monomers. Thermal initiation was found to be problematic. The monomer was found to completely evaporate from the host polymer at the elevated temperatures needed for initiation. Additionally, using benzoyl peroxide as the thermal initiator resulted in browning of the plastic, likely due to the initiator's reaction with the host polymer rather than the monomer. UV initiators were found to be both successful and advantageous. In addition to their ability to initiate polymerization at room temperature without problems of polymer degradation and rapid monomer evaporation, UV initiators also allowed for the photo-patterned polymerization of the infused monomer. Two initiators in the Irgacure® line produced by Ciba were found to be optimal and readily available. Irgacure® 651 was chosen for use with non-polar solvents and polymers, and Irgacure® 2959 was

chosen for use with polar chemicals and aqueous conditions (Fig. 3-4).  In particular, Irgacure® 651 was chosen as our preferred radical initiator due to its universal solubility in all of the studied monomers and TPUs.
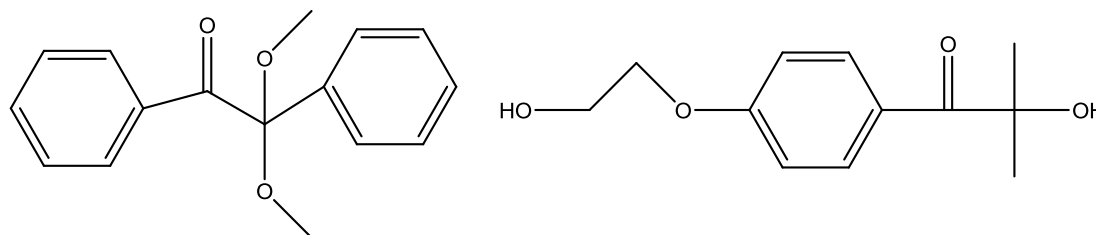


Figure 3-4.  Chemical structure of Irgacure® 651 (2,2-dimethoxy-1,2-diphenylethan-1-one) (left) and of Irgacure® 2959 (1-[4-(2-hydroxyethoxy)-phenyl]-2-hydroxy-2-methyl-1-propane-1-one) (right).

Samples were soaked in a 99 % w/w solution of monomer and 1 % w/w Irgacure® 651, thoroughly dried to remove any uninfused monomer on the surface, and polymerized using a 4 W, 365 nm UV light source at a distance of two inches.  The sample was placed under a quartz plate during polymerization, such that the UV light could reach the sample but monomer evaporation was minimized.  The key to the successful polymerization was found to be the absence of $O_2$.[209-214]  Thus, polymerizations were done under flowing $N_2$ gas.  Photo-patterning was achieved via the same process with the addition of masking of the sample during photopolymerization.  Samples were soaked for 20 min. at room temperature in a 99 % w/w solution of EGDMA and 1 % w/w Irgacure® 651.  A 4 W, 365 nm UV light source at a distance of two inches was used to polymerize the monomer within the sample through a chrome-plated glass mask.  Fig. 3-5 shows an optical microscopy image of the results of this patterned photopolymerization on the surface of an injection molded TDP7-1199 sample.  The sample shown in Fig. 3-5 was sectioned perpendicular to the sample surface at a point far from the edge of the sample.  Note the birefringence of the poly(EGDMA) IPN portion, likely indicating frozen-in stress following the polymerization due to the elongation of the TPU polymer chains while swelled by the guest polymer.  No additional material is seen in the masked region, as unpolymerized monomer is allowed to evaporate in a post-polymerization bake step at 70 °C.  A series of samples was observed in this manner in order to determine the thickness of the IPN layer, with the results shown in Table 3-2.
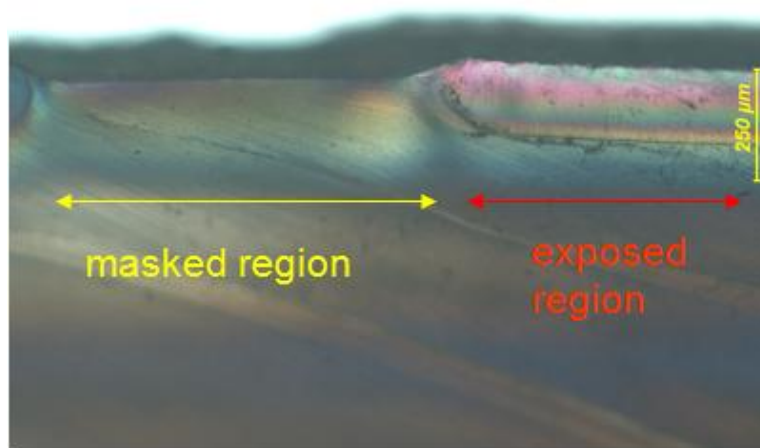
Figure 3-5. Optical microscopy image of the patterned surface of a TDP7-1199 sample infused with EGDMA. The poly(EGDMA) IPN is clearly seen in the exposed region at the right due to the birefringence and the slight bulge at the surface.

Table 3-2. Thickness of poly(EGDMA) IPN layer in TDP7-1199 samples, as determined by optical microscopy.

| Sample | Soak Time/Temp. | UV Cure Time | Layer Thickness (μm) |
|---|---|---|---|
| **TDP7-1199** | 60 min. / 22 °C | 5 min. | (difficult to judge) |
| **(injection molded)** | 60 min. / 22 °C | 10 min. | $155 \pm 10$ |
| | 60 min. / 22 °C | 15 min. | $157 \pm 10$ |
| | 60 min. / 22 °C | 20 min. | $155 \pm 10$ |
| | 60 min. / 22 °C | 25 min. | $177 \pm 10$ |
| | 20 min. / 22 °C | 25 min. | $180 \pm 10$ |
| | 5 min. / 22 °C | 25 min. | $45 \pm 10$ |
| | 20 min. / 60 °C | 25 min. | $400 \pm 10$ |
| **TDP7-1199 (thin film)** | 20 min. / 22 °C | 25 min. | $70 \pm 10$ |

With a better understanding of the diffusion of the monomer and the subsequent polymerized IPN layer, we moved forward to evaluate property changes in the modified polymer samples. Sessile water contact angle was measured for a TDP7-1199 sample containing a poly(EGDMA) surface layer IPN. Before modification, the contact angle was found to be 81.8° +/- 1.9°, while after creation of the poly(EGDMA) IPN, the contact angle was 96.9° +/- 6.5°.

This result demonstrates the potential to change surface hydrophobicity using surface layer IPNs. The tensile behavior of the infused sample was also tested (Fig. 3-6). The addition of a poly(EGDMA) IPN layer was seen to produce a definite increase in the Young's modulus of the TDP7-1199 sample. However, the IPN layer is apparently glassy and soon begins to show visible cracks, corresponding with the decrease in stress seen for the treated samples with increasing strain. The end result is stiffening of the material at the surface but lowering of the energy of failure. It is worth noting that in similar testing of T250, no cracking was seen, nor was any evidence of the IPN layer being glassy observed. In fact, Young's modulus was not necessarily improved in the T250 tests, and stress continues to increase with strain up to 20 % strain. Harder grades of Texin® were found to take up less monomer, so it is plausible that this result is due to a greater swelling of the TDP7-1199 with EGDMA monomer relative to the T250. Thus, the amount of monomer infused is an important parameter in optimizing the improvement to mechanical properties as a result the IPN layer.
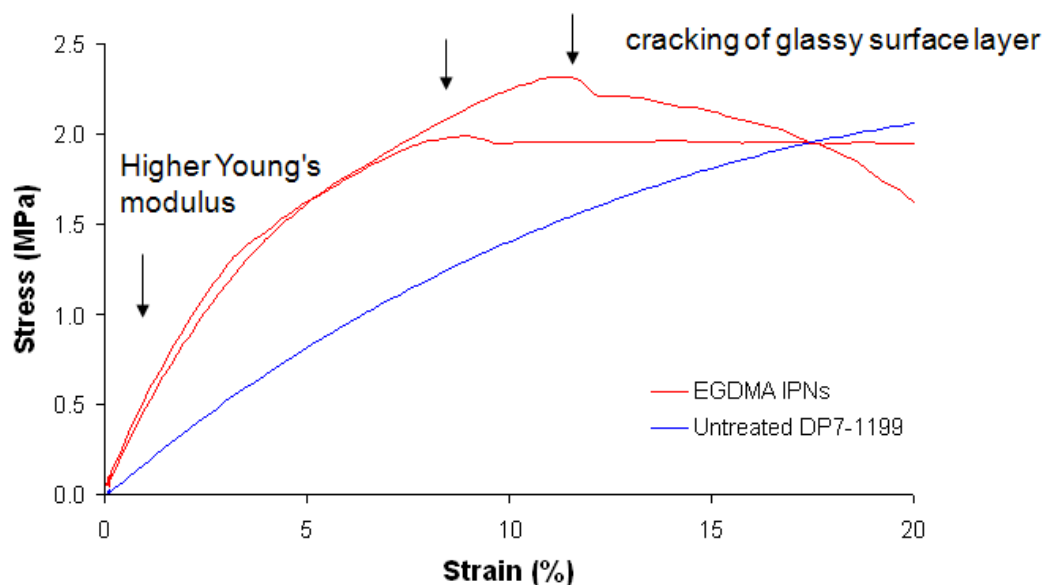


Figure 3-6. Uniaxial tensile testing results of both untreated and EGDMA-modified TDP7-1199.

Finally, the barrier properties of the sample were tested by swelling treated and untreated TDP7-1199 samples in hexanes (Fig. 3-7). The presence of a poly(EGDMA) surface layer has a definite effect on slowing the uptake of the solvent. Further hexane swelling tests were performed on samples of T250 and TDP7-1199 with poly(HEMA) IPN layers, produced using the same method as the poly(EGDMA) IPNs (Fig. 3-8 and Fig. 3-9). While the poly(HEMA) IPN inhibits the swelling of the T250 sample beyond about 0.1% for the time

period tested, the poly(HEMA) IPN in the TDP7-1199 sample initially retards the swelling of the sample in the hexanes. Eventually, however, the treated sample reaches the same level of swelling as the untreated sample. With identical processing conditions used to make these samples, this difference likely comes down to the different structures of the two TPUs. T250 is a harder TPU, which allows less monomer or solvent uptake to begin with. Addition of the small amount of the thin poly(HEMA) monomer which it will accomodate serves to further inhibit swelling. TDP7-1199 is a softer grade of TPU. A large amount of HEMA swells the polymer, likely producing a thicker layer of poly(HEMA) at the surface. Once this layer is permeated by the infused hexanes, the inner TDP7-1199 swells just as it would with no barrier layer.
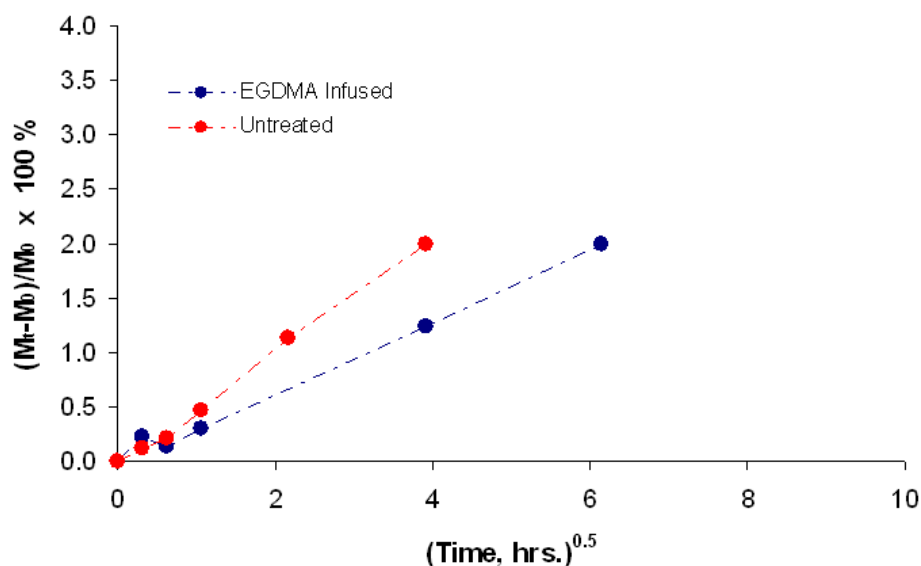


Figure 3-7. Mass uptake of TDP7-1199 samples, both untreated and with a poly(EGDMA) IPN layer, in hexanes at 22 °C. (Data collected by Morgan Iannuzzi)
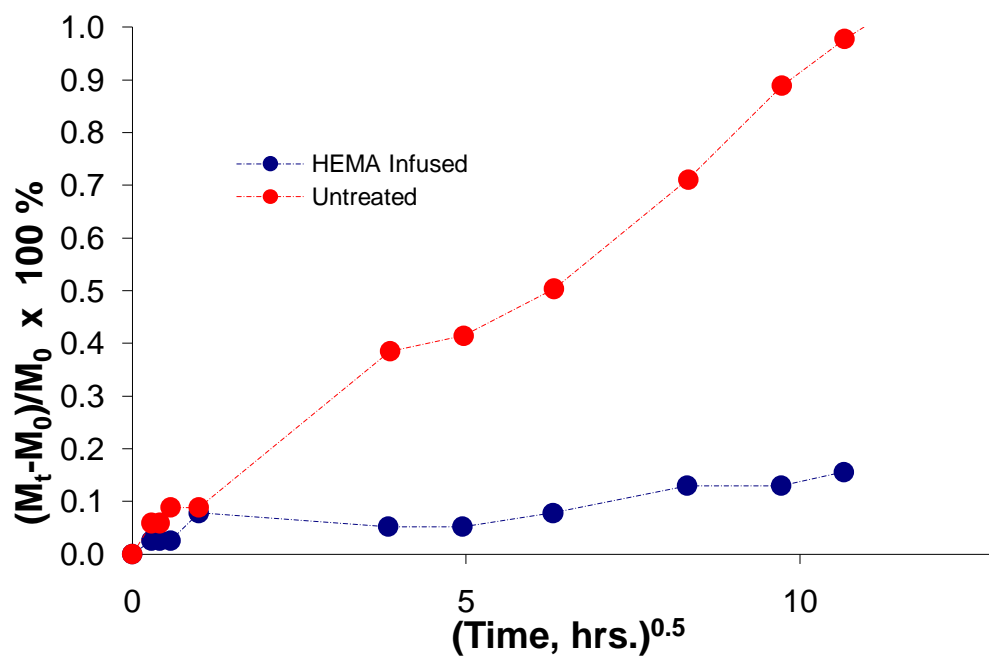
Figure 3-8. Mass uptake of T250 samples, both untreated and with a poly(HEMA) IPN layer, in hexanes at 22 °C. (Data collected by Morgan Iannuzzi)
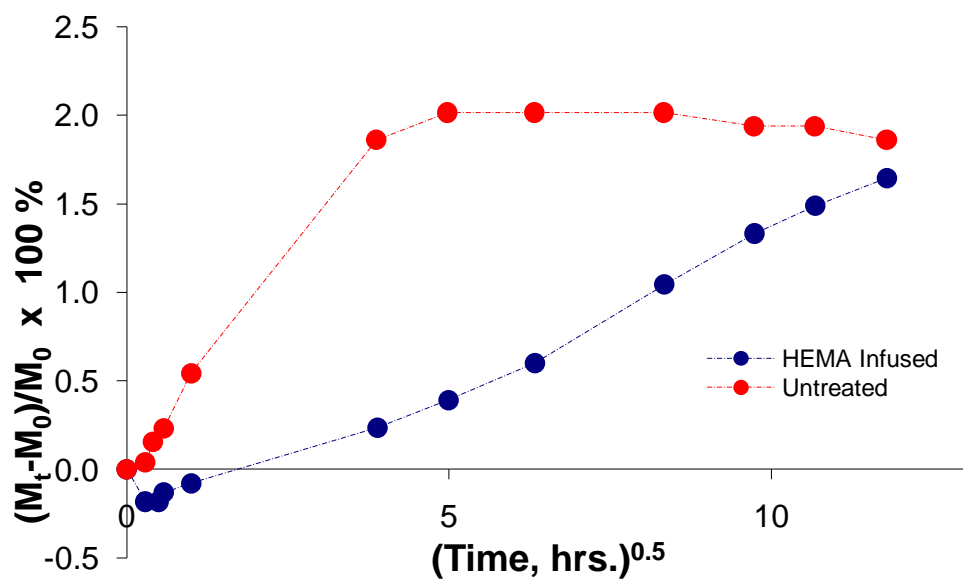


Figure 3-9. Mass uptake of TDP7-1199 samples, both untreated and with a poly(HEMA) IPN layer, in hexanes at 22 °C. (Data collected by Morgan Iannuzzi)

### 3.1.2 Application – Improvement of a Golf Ball Polymer Coating

Knowing that the potential for material improvement was dependent on the optimization of the processing parameters, the addition of a scuff-resistant IPN layer to the TPU surface-coating of a golf ball was attempted. The golf ball coating is a proprietary blend of Texin[®] 920280-7 and Texin[®] 920280-9 in unknown proportions. Each of these materials is an aromatic polyether TPU. Texin[®] DP7-1196 was also tested, due to its similarity to T920280-7, particularly with respect to the hard segment concentration. The primary difference between the two is the lower molecular weight of the polyether polyol used in the synthesis of TDP7-1196, resulting in smaller, better dispersed hard segments than in T920280-7. Samples were used as received from Bayer MaterialScience. TDP7-1196 was supplied as a 0.30 mm thin film, while T920280-x was supplied as a 15 cm square molded plaque of thickness 3.18 mm. As such, the T920280-x samples were sectioned by razor blade to produce thin (0.5-1 mm) sections for infusion and mechanical testing. Also tested was the actual aromatic TPU polymer blend from the surface of a golf ball. Samples were cut off of the golf ball by razor blade, and found to have a thickness of about 1.1 mm, although the dimples in the golf ball surface introduce significant variability.

Initial tests were done using 20 min. soaks in 1 % w/w solution of Irgacure[®] 651 in EGDMA. Significant swelling was found in each of the materials tested (Fig. 3-10). Samples of all three TPUs and the aromatic golf ball polymer blend were subjected to uniaxial elongation using a TA instruments Q800 DMA. Samples of approximately 0.5 mm x 3 mm x 5 mm were stretched at 5 % strain per minute to 70 % strain or fracture, whichever came first (Fig. 3-11). In general, the mechanical properties of the polymers appeared in these preliminary results to be improved by creation of the IPN layer. Additional tests were performed on the aromatic golf ball polymer blend, specifically attempting to determine the effect of infusion time and temperature on the resultant mechanical properties (Fig. 3-12). It was here found that, although the Young's modulus tended to be increased by the presence of the IPN layer, the elongation at break was drastically reduced by the presence of the EGDMA. Stretching by hand was found suitable to break the treated polymer but not the control sample. In the treated polymer, small cracks were plainly apparent as the glassy IPN layer fractured. As a result of these problems, a new monomer system was investigated.
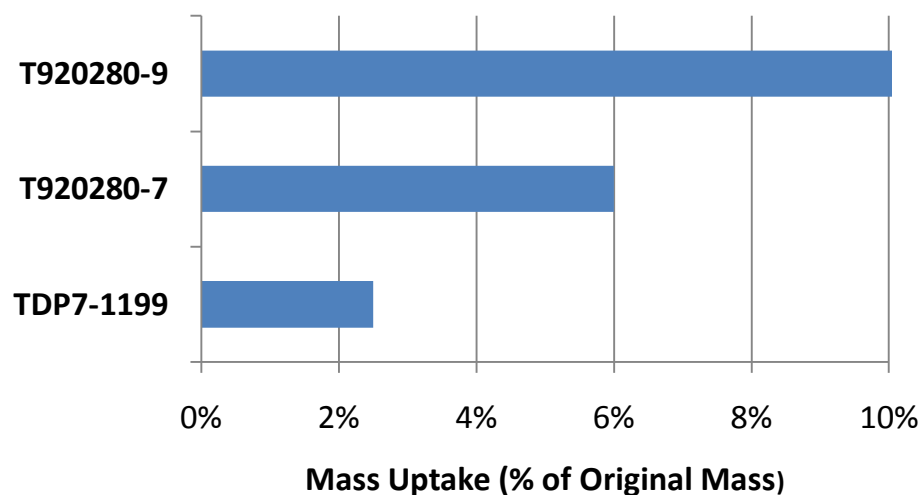
Figure 3-10.  Mass uptake of EGDMA and Irgacure® 651 in TDP7-1196, T920280-7, and T920280-9 following 20 minutes of infusion at room temperature.  Mass increase was determined following UV polymerization and one day in a 60 °C oven to allow evaporation of volatiles.
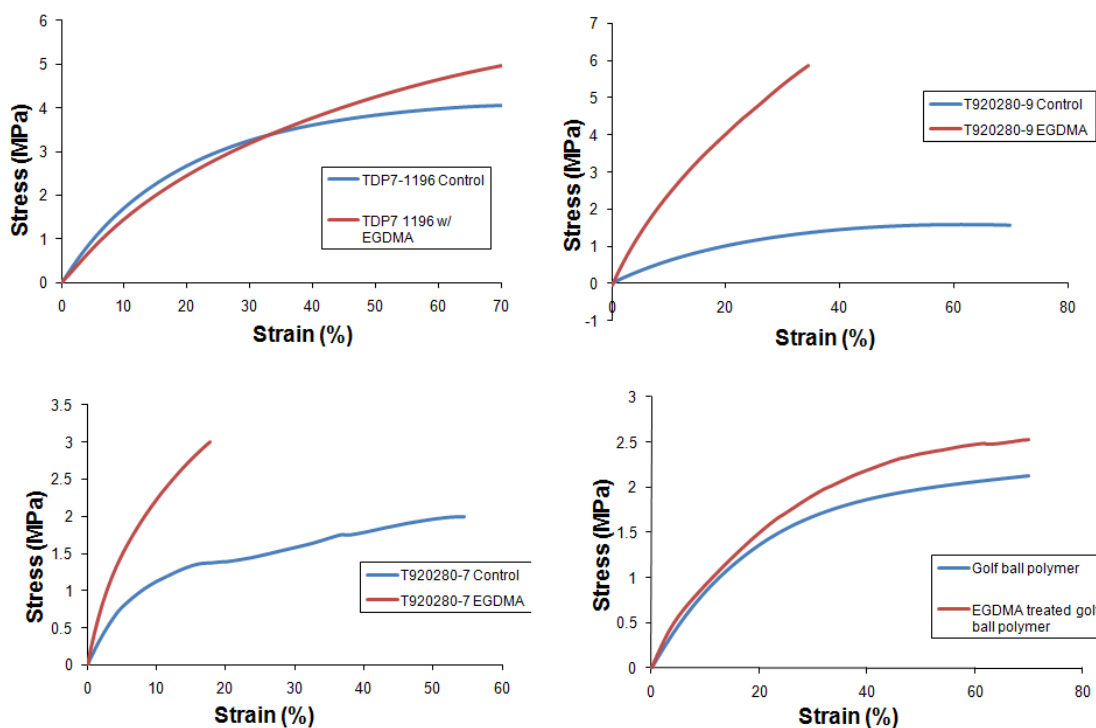


Figure 3-11. Uniaxial elongation of TDP7-1196, T920280-7, T920280-9, and the aromatic golf ball polymer blend.
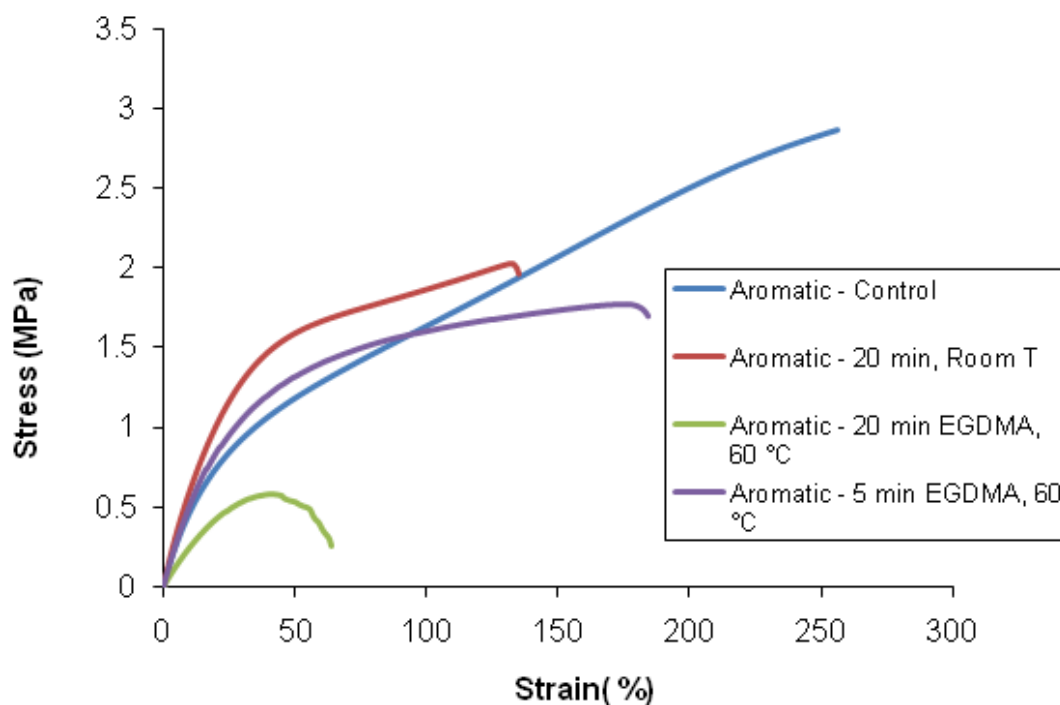
Figure 3-12. Uniaxial elongation of aromatic golf ball polymer blend at a variety of EGDMA infusion conditions.

It is important to make two key notes about the testing done here. First of all, the aim of the project is to improve the scuff resistance of the polymer surface coating. As such, the Young's modulus and elongation at break are not necessarily optimal parameters to measure this improvement. However, they were chosen here for use as preliminary results in order to determine if sufficient change to the properties of the polymer was being made to warrant testing of the scuff resistance by the golf ball manufacturer. Further, it must be mentioned that elongation at break is a particularly fickle measurement. A thorough analysis of this parameter requires multiple tests and rigorous statistical analysis in order to acquire conclusive data. Here, the elongation at break was used as an indication of the glassy nature of the EGDMA IPN layer, which was confirmed by stretching the samples by hand and observing the cracks in the surface with the unaided eye. It is this obvious problem which ultimately led to the decision to try a new monomer for IPN formation.

A monomer mixture consisting of 80 % w/w pentaerythritol triacrylate (PETA) and 20 % w/w 1-ethenyl-2-pyrrolidone (NVP) was made, and 1 % w/w Irgacure® 651 was added. This mixture essentially mimics the formulation of the scratch-resistant surface coating Gafgard® 233 without the addition of nanofillers. The motivation here was to use a similarly scratch-

resistant polymer coating as an IPN for better adhesion than is possible with a material like Gafgard® 233, which is simply deposited on the surface and polymerized. Pieces of the aromatic golf ball polymer blend of approximate dimensions 1.1 mm x 20 mm x 60 mm were infused with this mixture at 60 °C. Significant mass uptake was found for short times (~20 min.), and equilibrium swelling was not reached for much longer times (t > 4 hours) (Fig. 3-13). Swelling for 20 min. at 60 °C was also attempted in each monomer individually, with the result being that PETA caused a 4 % mass increase to the sample with minimal change to sample dimension, while NVP was found to completely dissolve the sample. Initial uniaxial tension tests, analogous to those performed on the EGDMA-modified samples, were used for samples of both the golf ball polymer and T920280-9 infused with the triacrylate monomer mixture for 20 min. at 22 °C (Fig. 3-14). In both instances, increases in both Young's modulus and elongation at break were observed. Additionally, it appears that the toughness of the material, as observed via the area under the stress-strain curve, was significantly increased. In order to optimize the infusion time and temperature, Young's modulus measurements were made for a variety of conditions on T920280-9 samples of 3.2 mm width and 0.9 mm thickness. Young's modulus was chosen primarily for its ease of measurement, compared to the toughness and elongation at break. The results are summarized in Table 3-3. Temperature had the largest influence on the Young's modulus, while soak time had a significantly smaller influence. As such, 20 min. at 60 °C was chosen for testing of the golf ball polymer blend. A number of golf balls were infused using these conditions. UV irradiation was achieved via constant agitation of an $N_2$ filled box containing a golf ball under a Dymax® Lightwelder® PC-2, with wavelength of irradiation over the range 300-500 nm and power output of 20-45 mW/cm$^2$, for 3 min. Over-exposure was found to cause a yellowing of the golf ball polymer.
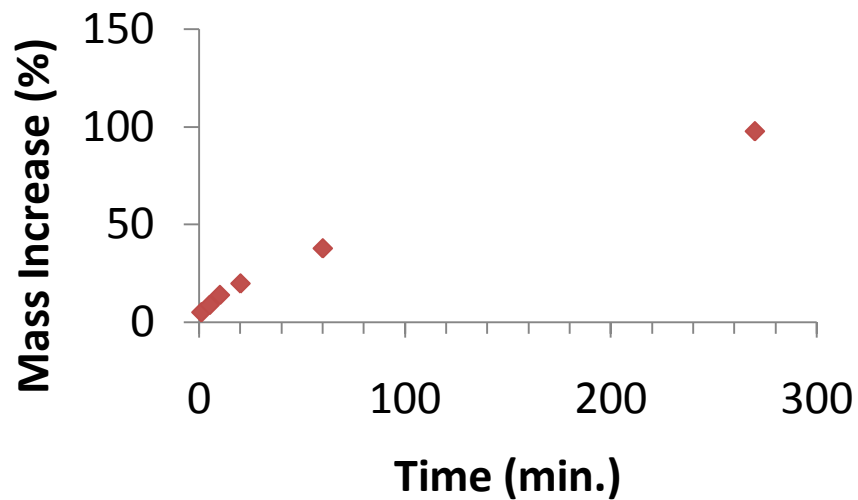
Figure 3-13. Mass uptake as a function of time for infusion of the PETA/NVP monomer mixture into the aromatic golf ball polymer blend at 60 °C.
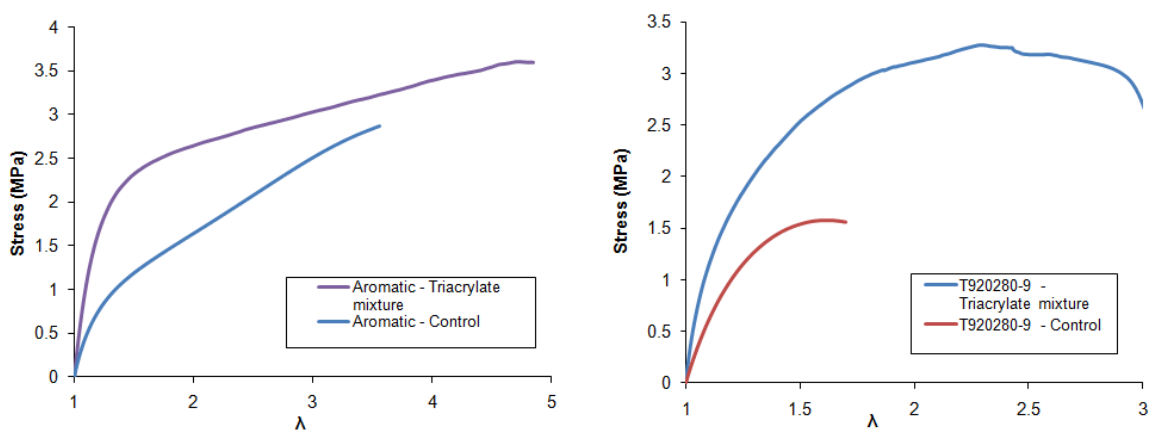


Figure 3-14. Uniaxial elongation results for the aromatic golf ball polymer blend (left) and T920280-9 (right) treated with the triacrylate monomer mixture.

Table 3-3. Young's moduli of aromatic golf ball polymer blend measured for a variety of soak conditions. (Data collected by Dr. Jun Zhao and Dr. Huipeng Chen at Texas Tech University)

| Sample | Soak T (°C) | Soak Time (min.) | Young's Modulus (MPa) |
|---|---|---|---|
| 0 | N/A | N/A | 9.7 |
| 1 | 21 | 5 | 11.7 |
| 2 | 21 | 10 | 15.6 |
| 3 | 21 | 20 | 17.6 |
| 4 | 40 | 5 | 26.2 (questionable) |
| 5 | 40 | 10 | 14.8 |
| 6 | 40 | 20 | 14.5 |
| 7 | 60 | 5 | - |
| 8 | 60 | 10 | 21.4 |
| 9 | 60 | 20 | 41.2 |

The processed golf balls were sent back to Bayer MaterialScience for thorough testing. An important observation made during our drop tests was the equal rebound height of the treated and untreated golf balls, indicating that no deleterious effect had been made to the elastic response of the golf ball as a whole.

### 3.1.3 Synthesis of an Interpenetrating Network for use as a Reducing Agent

The use of a surface layer IPN as an "in situ reduction" method for the production of a polymer/metal nanocomposite was investigated. By choosing an IPN monomer with the proper functionality, such as pendant amine groups, an immobilized, cross-linked reducing agent can be synthesized. Subsequent infusion of metal precursor salts results in auto-reduction to elemental metal by the IPN, with no further processing step needed.

TDP7-1199 was supplied by Bayer MaterialScience (Pittsburgh, PA). Large extruded sheets, of thickness 0.5 mm were used as received from the supplier. $T_g$ of the material is -23 °C, as quoted by the supplier. The synthetic scheme of TDP7-1199 is proprietary. Irgacure® 651 (Ciba) and 2-(diethylamino)ethyl methacrylate (DEAMA) (99 %, Aldrich) were used as received.

Chemical structures of DEAMA and Irgacure[®] 651 (2,2-dimethoxy-1,2-diphenylethan-1-one) are shown in Fig. 3-15 and Fig. 3-4, respectively.
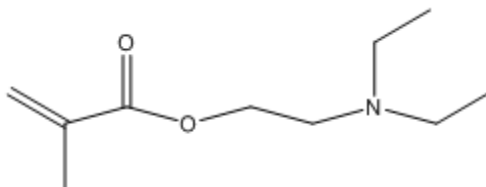
Figure 3-15.  Chemical structure of 2-(diethylamino) ethyl methacrylate (DEAMA).

TPU samples were allowed to soak in a 0.036 M solution of Irgacure[®] 651 in DEAMA for 20 min. at room temperature.  The samples were then wiped well to remove any excess monomer on the surface and exposed to 2 min. of irradiation under a Dymax[®] Lightwelder[®] PC-2, with wavelength of irradiation over the range 300-500 nm and power output of 20-45 mW/cm$^2$.

The key step in this particular process was the creation of a functionalized IPN layer on the surface of the TPU.  It was found that no solvent mixture was needed to swell the TPU with the DEAMA; rather, the polymer absorbed DEAMA via immersion in the pure chemical (Fig. 3-16).  In order to successfully photopolymerize the methacrylate monomer, Irgacure[®] 651 was added at a low concentration as a radical initiator.  The swelling of the network with monomer was sufficient to carry in this initiator, as evidenced by the success of the photopolymerization using a high-power UV light source.  As before, it was of critical importance that this photopolymerization step not be done in the presence of oxygen.  The present work was done under flowing $N_2$ gas, which proved to be successful at sufficiently removing the oxygen so as to allow the polymerization to proceed.  Optical microscopy revealed the poly(DEAMA) layer to be approximately 50 µm thick, with a gradient in concentration appearing to trail off over the next 50 µm (Fig. 3-17).
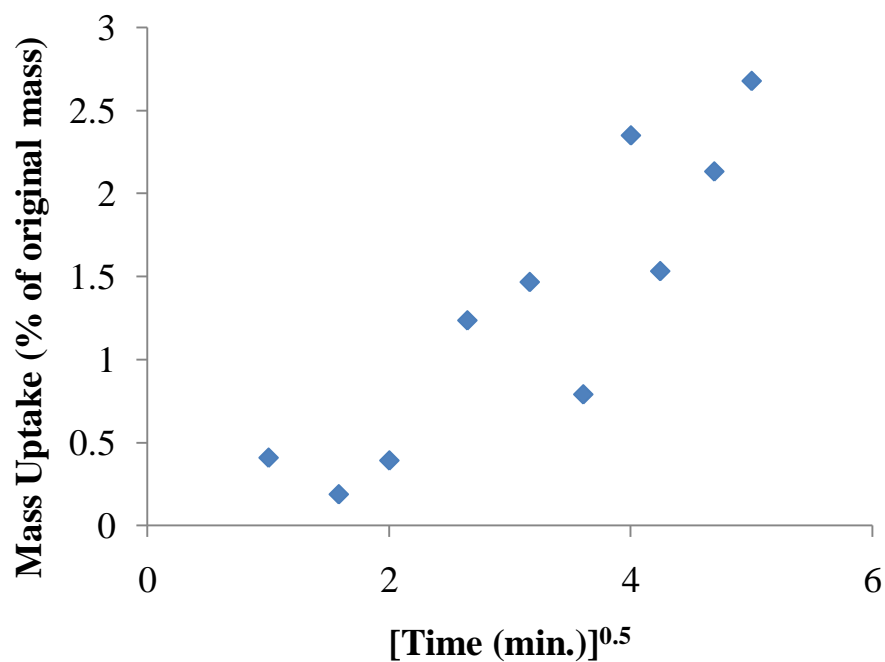
Figure 3-16.  Uptake of DEAMA, containing 0.036 M Irgacure® 651, into TDP7-1199 thin films as a function of time at room temperature.  Polymer samples were 1 cm x 1 cm x 0.5 mm, and masses were taken after wiping excess monomer off thoroughly but before photopolymerization.
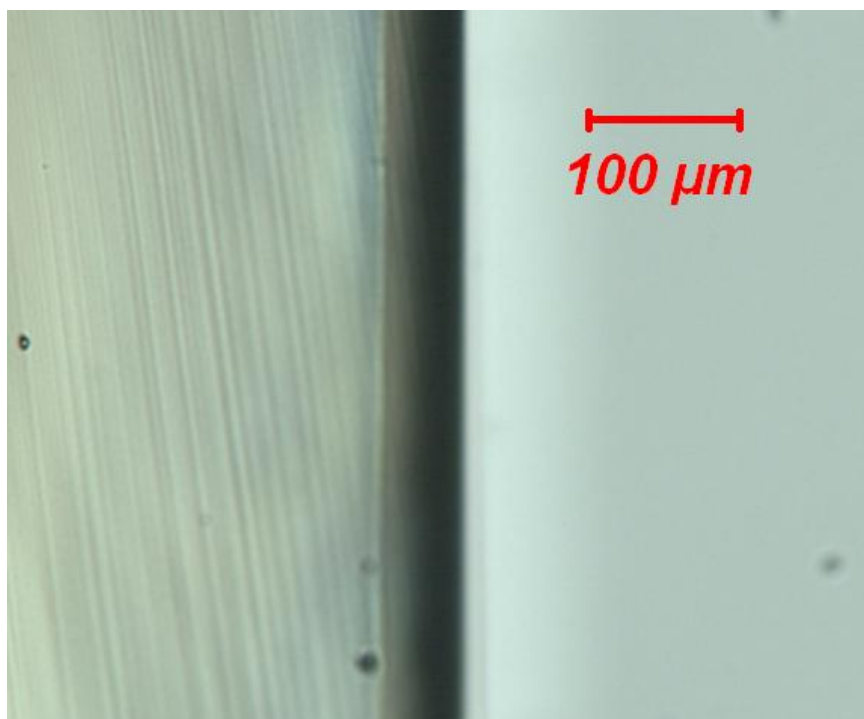


Figure 3-17. Optical microscope image of the poly(DEAMA) layer on the surface of TDP7-1196.

## 3.2 Interpenetrating Network Reduction of Metal Precursors

Once the poly(DEAMA) IPN layer had been synthesized, the TPU samples were immersed in a 0.007 M solution of $HAuCl_4$ in a 70:20:10 (by volume) mixture of water, BCS, and DEG for 3 min. at 60 °C. Hydrogen tetrachloroaurate trihydrate (99.99 %, Alfa Aesar), ethylene glycol monobutyl ether [butyl cellosolve (BCS)] (99 %, Alfa Aesar), and diethylene glycol (DEG) (99 %, Alfa Aesar) were used as received from the suppliers. Following the gold infusion, samples were placed in an 80° C oven and left for at least 24 hours. Each solvent in this solution has a specific role, as has been previously discussed. It is observed that the sample turns brick red rapidly upon being immersed in the $HAuCl_4$ solution (Fig. 3-18). This observation is in contrast to the previous chemical reduction method, where the polymer article turns a bright yellow during the initial $HAuCl_4$ soak and subsequently loses this color during the reduction soak step. The final color of the sample in the prior process only develops when the polymer is left in an oven for at least a day to allow the evaporation of solvent and the diffusion of $Au^0$ through the sample to form larger particles and aggregates. It would appear that there is not as much growth and aggregation of the $Au^0$ over time in the currently considered IPN process, as the brick red color forms during the $HAuCl_4$ infusion and remains essentially unchanged both during and beyond the subsequent baking step. Thus, it seems that the particle size does not change significantly throughout these events. However, this is not to say that there is little or no diffusion of the $Au^0$ through the TPU sample. In fact, it appears to be quite unlikely, due to the fact that particles are found throughout the thin film, even beyond where the DEAMA layer appears to extend, as is discussed below.
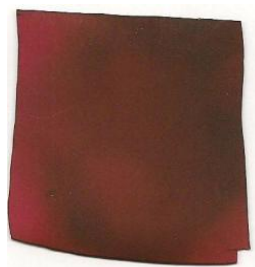


Figure 3-18.  Photograph of IPN-reduced gold nanocomposite sample.

## 3.3 Sample Characterization

### 3.3.1 Optical Microscopy

Samples were sectioned perpendicular to the original surface at a location far from the edge using a razor blade, and the cross-section was observed edge-on to determine the approximate thickness of both the poly(DEAMA) IPN before the $HAuCl_4$ soak and the infused surface layer of gold following said soak. Samples were characterized via orthoscopic observation (in transmission) using an Olympus BX51 microscope with a UMPlanFL 10x objective. Images were recorded using a 2.0 megapixel Diagnostic Instruments model # 11.2 Color Mosaic digital camera equipped with Spot$^{TM}$ digital imaging software.

### 3.3.2 Transmission Electron Microscopy

TPU samples were microtomed following $HAuCl_4$ infusion and the post-processing bake step using a Leica EM UC6 Microtome with Leica EM FC6 Cryo-attachment at -100° C to take 90 nm thick sections. Sections were taken perpendicular to the surface of the sheet, such that the entire thickness could be examined in a given section. In contrast to the samples prepared using the chemical reduction method, the gold nanoparticles were present in high enough amount and at small enough sizes that a large number of particles could be seen on a single section. The collected sections were placed on 400 mesh copper grids and examined using a JEOL JEM 1200 EXII TEM, equipped with a Tietz F224 camera, at an accelerating voltage of 80 kV. Images were taken such that successive images could be overlapped to create a continuous image from surface to surface, other than at the copper grid lines. Particle sizes were measured over a 1 μm × 1 μm box every 50 μm in the TEM images using the "Measure" capability in ImageJ 1.38x (created by Wayne Rasband, National Institutes of Health). The particle size distribution, number, and volume fraction were calculated for each box and examined as a function of depth from the surface.

### 3.3.3 Small Angle X-ray Scattering

Small angle x-ray scattering (SAXS) was performed on $Au^0$-containing samples of TPU and on unprocessed TPU samples for background subtraction. A Rigaku pinhole SAXS system utilizing a Cu $K_\alpha$ ($\lambda$= 1.54 Å) sealed microfocus tube and a 120 mm multi wire area detector was used. Beam diameter at the sample was approximately 1 mm, and the sample to detector distance was 1.5 m. All measurements were made at 25 °C, with counts being recorded for two hours per sample. Background was subtracted as

$$I = I_s - I_b(\frac{T_s t_s}{T_b t_b})$$

(3-3)

where I is the scattered intensity, $I_s$ and $I_b$ are the sample and background scattered intensity, $T_s$ and $T_b$ are the transmission intensity of sample and background, and $t_s$ and $t_b$ are the scattering times for sample and background.[215] Error shown in all SAXS plots is 10 % of the corrected scattered intensity.

Two particle size distributions were considered. The first was a Gaussian size distribution, and the second was a Schulz distribution. The Gaussian distribution is calculated using:[216]

$$f(R) = \frac{1}{\sigma\sqrt{2\pi}} exp\left[-\frac{1}{2\sigma^2}(R - \bar{R})^2\right]$$

(3-4)

where R is the particle radius, $\bar{R}$ is the average particle radius, and $\sigma$ is the standard deviation. The polydispersity of this distribution is defined as:[216]

$$\rho = \sigma/\bar{R}$$

(3-5)

The Schulz distribution is described by the equation:[217,218]

$$f(R) = \left[\frac{z+1}{\bar{R}}\right]^{z+1} R^z exp\left[-\left(\frac{z+1}{\bar{R}}R\right)\right]\frac{1}{\Gamma(z+1)}$$

(3-6)

where R is the particle radius, $\bar{R}$ is the average particle radius, and z is the Schulz "width factor," which must be greater than -1.[217,218] A z value of $10^4$ corresponds to an essentially monodisperse sample.[218] Note that the final term of the Schulz distribution equation makes use of the gamma distribution. The polydispersity index of the Schulz distribution can be calculated as:[217]

$$\rho = \sigma_R/\bar{R} = \frac{1}{\sqrt{z+1}}$$

(3-7)

where $\sigma_R$ is the root-mean-square deviation from the mean size in the distribution, given by:[217]

$$\sigma_R = \bar{R}/(z+1)^{1/2}$$

(3-8)

The polydispersity is physically limited to have a value between zero and one such that negative particle radii are not considered.

IGOR Pro version 6.0.4.0 with the NIST NCNR analysis and reduction package was used to model the scattering.[216] Using the Gaussian distribution, a Gaussian spheres model for scattering was attempted. This model calculates scattering from a polydisperse population of non-interacting spheres with uniform scattering length density.[216] The input variables into the NIST NCNR software package for the Gaussian spheres model are particle radius, polydispersity, volume fraction of particles, scattering length density of the spherical particles, scattering length density of the polymer matrix, and a background correction.[216] The Gaussian spheres model calculates scattering intensity as:[216]

$$I(q) = \left[\frac{4\pi}{3}\right]^2 np^2 \int_0^\infty f(R)R^6 F^2(qR)dR \tag{3-9}$$

where n is the total particle number density, q is the modulus of the wave vector ($q = 4\pi \sin(\theta)/\lambda$ with scattering angle, $2\theta$, and wavelength, $\lambda$), p is the numerical difference in the scattering length densities of sphere and medium, and f(R) is the Gaussian distribution, given in equation 3-4.[216] F(x) is the scattering amplitude for a sphere and is calculated as:[216]

$$F(x) = \frac{[\sin(x) - x\cos(x)]}{x^3} \tag{3-10}$$

As particle interactions are not considered, there is no structure factor contribution to this model.[216]

A polydisperse hard sphere model, wherein scattering from interacting hard spheres is modeled for any degree of size polydispersity that is describable by the above Schulz distribution, was also used to model the measured scattering.[218] The input variables into the NIST NCNR software package for the polydisperse hard sphere model are particle radius, polydispersity, volume fraction of particles, scattering length density of the spherical particles, scattering length density of the polymer matrix, and a background correction.[216] Scattering intensity is calculated for a continuous distribution of particles of radius $R_i$ and scattering amplitude $F_i(q)$ using the equation:[218]

$$I(q) = n \int_0^\infty F_i^2(q)f(R_i)dR_i + n \int_0^\infty \int_0^\infty F_i(q)F_j(q)H_{ij}(q)f_i(R_i)f_j(R_j)dR_i dR_j \tag{3-11}$$

where

$$H_{ij}(q) = S_{ij}(q)\text{-}1 \tag{3-12}$$

are the partial structure functions, related to the partial structure factors, $S_{ij}(q)$.[218] n is the total particle number density, q is the modulus of the wave vector ($q = 4\pi \sin(\theta)/\lambda$ with scattering angle, $2\theta$, and wavelength, $\lambda$), and $f_i(R_i)$ is the Schulz distribution, given in equation 3-6.[218] The

scattering amplitude for spheres with uniform scattering length density and a given diameter is calculated as:[218]

$$F_i(q) = 4\pi p \left[ \sin\left(\frac{qR_i}{2}\right) - \frac{1}{2} qR_i \cos\left(\frac{qR_i}{2}\right) \right] \qquad (3\text{-}13)$$

where p is the contrast between the particle and the surrounding medium.[218]  In modeling the scattering data with the polydisperse hard sphere model, it must be kept in mind that the volume fraction and the scattering contrast are correlated.[216]

### 3.3.4 Discussion

In order to achieve an accurate depiction of the particle size distribution within the nanocomposite sample and determine how it varies with depth, sections were microtomed far from the sample edge in a manner such that the full thickness of the sheet was intact.  Such samples allowed for overlapping TEM images to be taken and subsequently concatenated into a series of continuous images from surface to surface (Fig. 3-19), with the exception of gaps of 23 μm thickness due to the grid lines of the copper TEM grids.  Fig. 3-20 shows the locations of the TEM image series, as well as the approximate locations where particles were measured and counted, as discussed below.
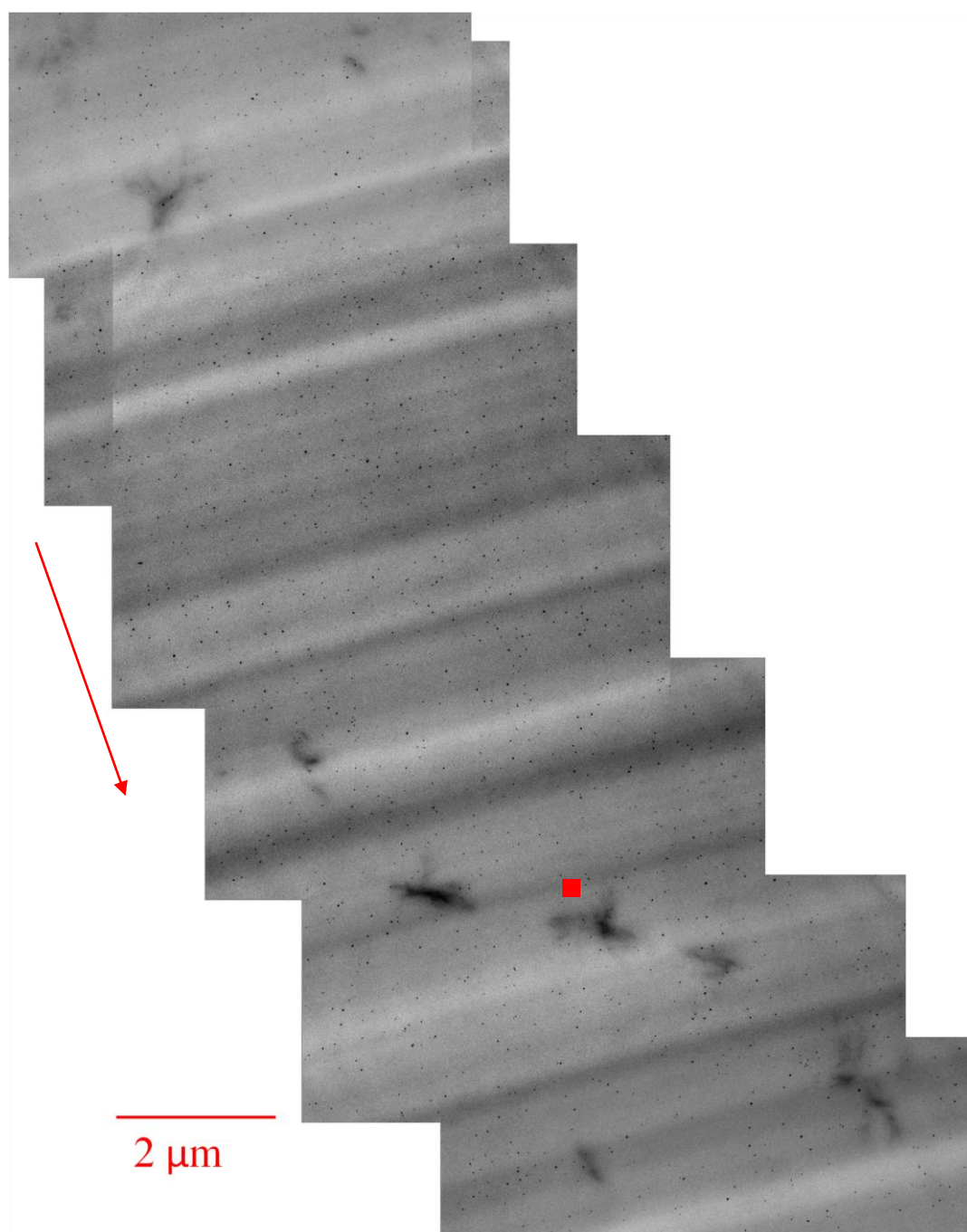
Figure 3-19. An example of the continuous TEM images constructed for the IPN-reduced gold nanocomposite sample. The arrow added indicates the direction of the surface, and the red square represents a point 200 μm from said surface.
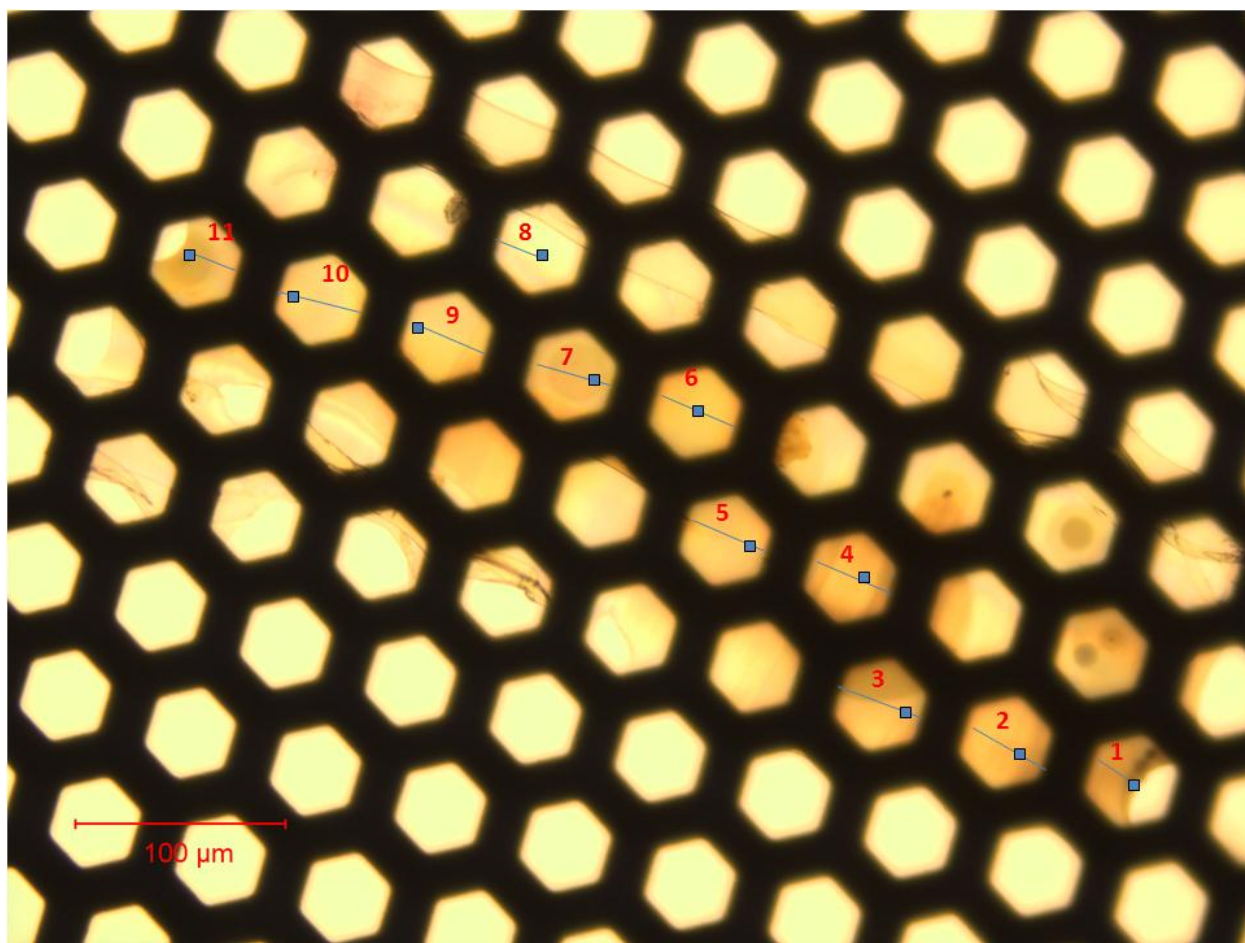
Figure 3-20. Optical microscope image of IPN and gold infused TDP7-1199 sample on a copper TEM grid. Blue lines indicate areas where TEM images were taken. Boxes indicate approximately where particles were counted, every 50 μm throughout the sample. Wrinkling observed at the section edges are due to beam damage during TEM imaging.

The first feature of note from the TEM images was the first several micrometers on each surface of the sheet, in which no nanoparticles were found (Fig. 3-21). This result was counterintuitive, as the highest particle size and concentration was expected immediately next to the surface. We believe that this surface "dead zone" is a result of the use of a water rinse following the $HAuCl_4$ infusion step. The gold precursor was able to diffuse out of the still-plasticized polymer into the aqueous rinse. Alternatively, DEAMA monomer at the surface may evaporate during the UV curing step, before it is able to polymerize.
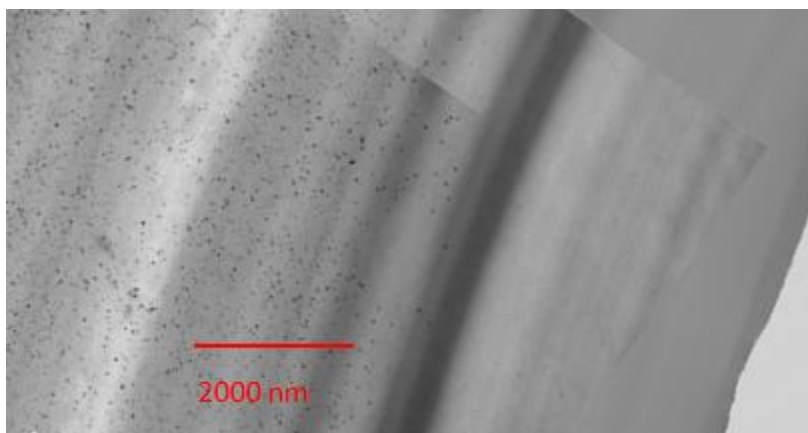
Figure 3-21. TEM image depicting, from right to left, empty space, the surface layer of the sample devoid of any particles, and the beginning of the presence of gold nanoparticles approximately 3 μm beneath the surface.

In order to get accurate statistics on the size of the nanoparticles depicted in the TEM without the need to count every particle from surface to surface, 1 μm$^2$ boxes of particles were counted and measured every 50 μm, traveling perpendicular to the surface. As expected, the bulk of the particles are within the first 50 μm from the surface (Fig. 3-22). An image of the density of particles near the surface can be seen at the left of Fig 3-21. However, there is still a noticeable concentration of particles within the central part of the sample (Fig. 3-23 and Fig. 3-24). Although not visible by optical microscopy, it is apparent that the gold salt is able to migrate a significant distance during infusion and nucleate the growth of nanoparticles deep into the plastic. Interestingly, the average particle diameter does not change throughout the thickness of the sample, despite the large change in particle number density beyond the initial surface layer (Fig. 3-25). The final results of the measurement of all particles considered are shown in Table 3-4.
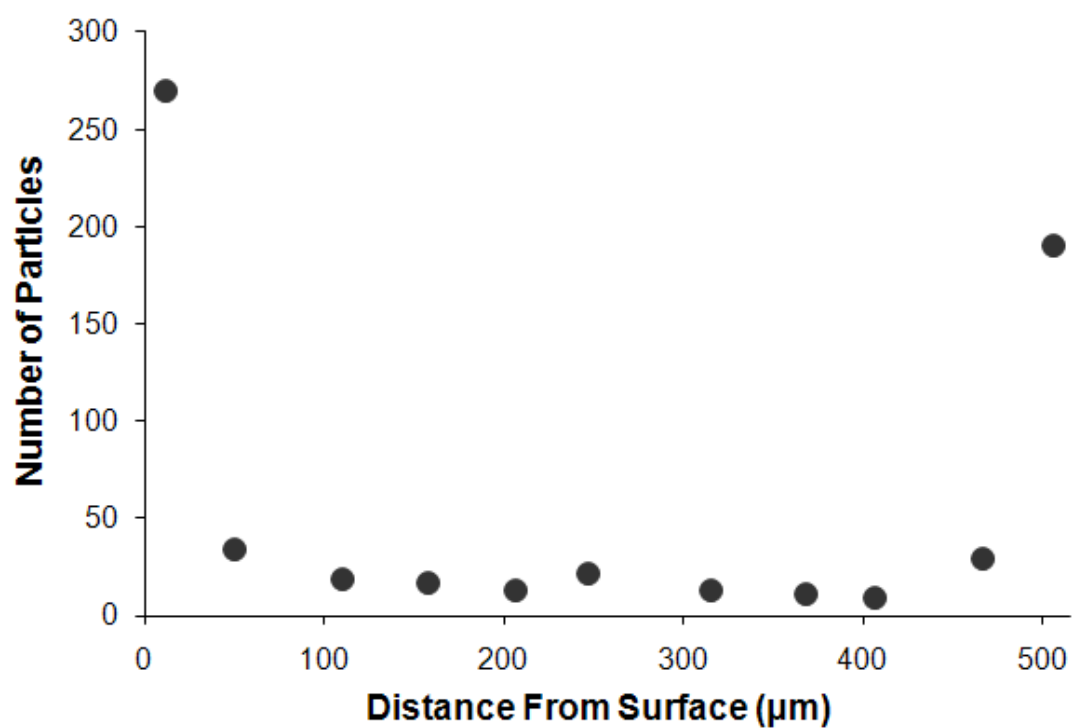
Figure 3-22. Number of particles in a 1 µm square box every 50 µm based on measuring particles in TEM images. The sample was approximately 500 µm thick, so the middle of the sample is approximately the 250 µm point.
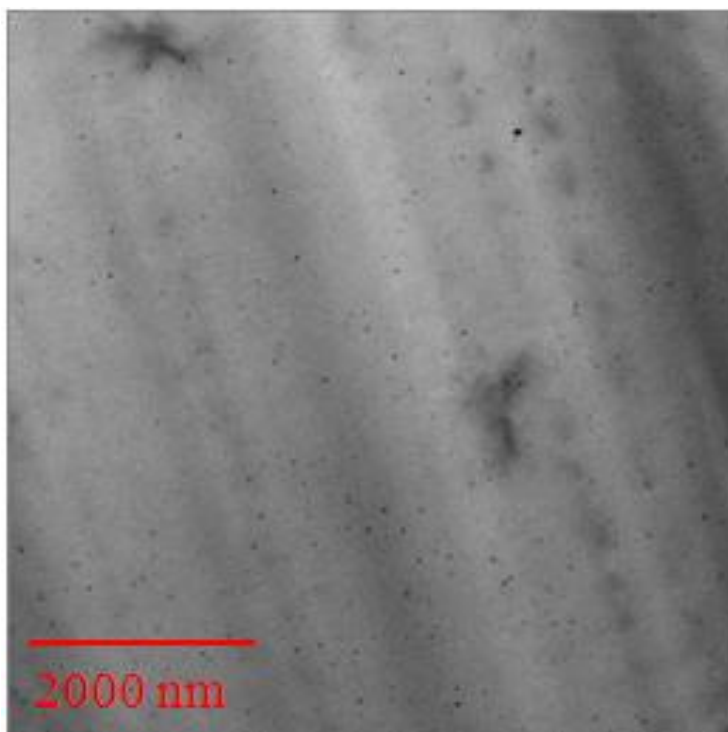
Figure 3-23.  Example TEM image, 100 μm beneath the surface of the polymer.
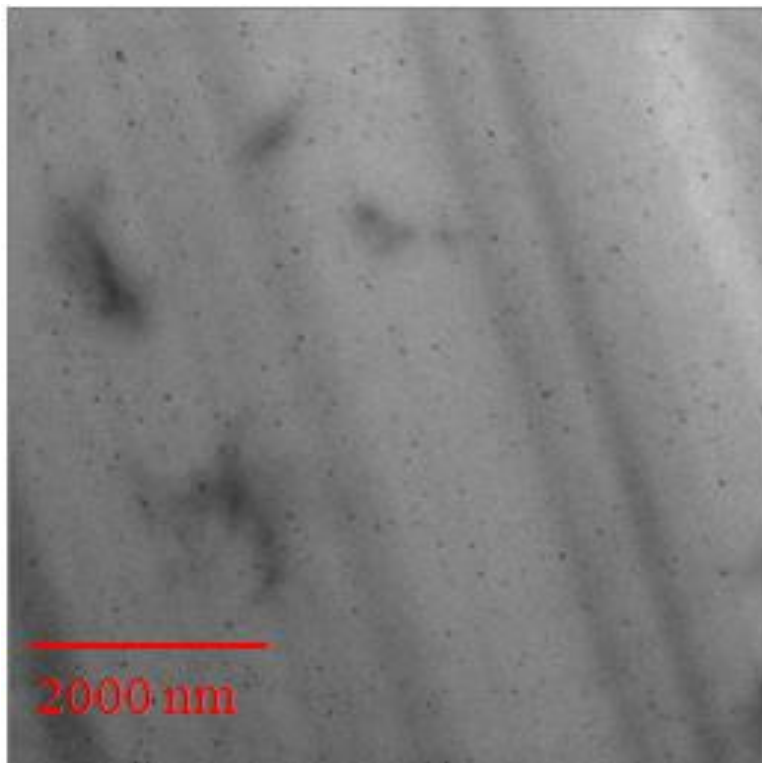


Figure 3-24.  Example TEM image at the center of the sample, 250 μm from either surface.
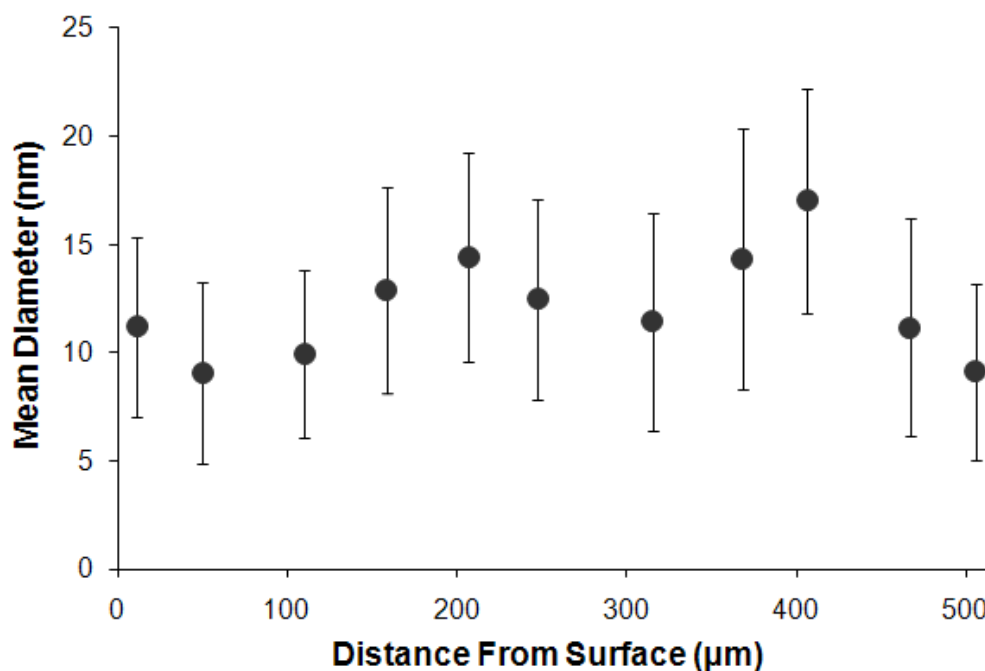
Figure 3-25.  Mean diameter based on measuring particles as a function of depth from the surface. Note that the sample was approximately 500 µm thick, so the middle of the sample is approximately the 250 µm point.  Error bars are one standard deviation for the diameters of the particles counted within each respective 1 µm$^2$ box.

Table 3-4. Counting statistics for all particles measured in TEM images.

| Number of Particles | 626 |
|---|---|
| Total Volume | $1.10 \cdot 10^7$ nm$^2$ |
| Number Density | $5.68 \cdot 10^{-5}$ particles/nm$^2$ |
| Volumetric Density | $6.31 \cdot 10^{-7}$ particles/nm$^3$, assuming 90 nm thick sections |
| Volume Fraction | $6.50 \cdot 10^{-4}$, assuming spherical particles and 90 nm thick sections |
| Mean Diameter | 10.7 nm |
| Standard Deviation of Diameter | 4.52 nm |

Despite the quantity of information yielded by the TEM, it would be advantageous to have a faster method of characterizing the particle size for a given sample.  As such, SAXS was employed as a high throughput, beam based characterization technique.  In order to quantify particle size and polydispersity by SAXS, an appropriate scattering model must be assumed.  The

statistics from the TEM data were used as initial guesses for the fitting algorithm (Fig. 3-26). Both Gaussian and Schulz distributions were attempted as fits for the TEM-determined particle size distribution. Use of these models assumes that the particles throughout the sample are spherical. In each case, the measured average radius of 5.35 nm was used to minimize the sum of squares difference between the modeled distribution and the measured distribution by altering the width factor and standard deviation, respectively. The sum of squared differences was 0.05 for the Schulz distribution with a polydispersity of 0.607 and was 0.04 for a Gaussian model with a polydispersity of 0.701. Both models fit the data relatively well, particularly considering the error in the radii of the measured particles. However, the Gaussian distribution must consider unphysical negative particle radii (not shown in Fig. 3-26) in order to fit the data, indicating its use is likely not desirable.
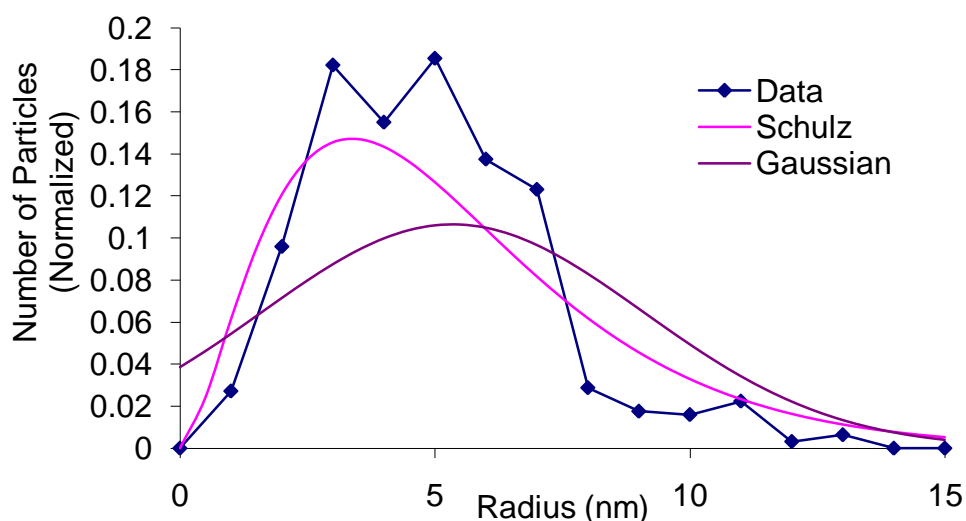


Figure 3-26. Fit of the particle distribution throughout the sample containing poly(DEAMA)-reduced gold nanoparticles using both a Gaussian and a Schulz distribution. Note that the average radius used here is that measured with the TEM analysis. (Line added to data as a guide to the eye.)

Both a Gaussian sphere model and a polydisperse hard sphere model of the measured scattering were considered. The primary differences between the two are the size distributions (Gaussian and Schulz, respectively) and whether interactions between spheres are considered (no and yes, respectively). The TEM measurements were particularly important as initial guesses, considering the large number of adjustable parameters required by the two scattering models. It is important to note the intensity units of our SAXS data are arbitrary and not absolute, and the scattering length density and volume fraction of the fits are coupled and therefore non-

quantitative. However, the shape of the plot was determined by the polydispersity and average radius of the particles. The fit shown in Figure 3-27 for the polydisperse hard sphere model corresponds to an average radius of 4.82 nm and a polydispersity of 0.62. The fit shown in Figure 3-28 for the Gaussian spheres model corresponds to an average radius of 2.1 nm and a polydispersity of 1.79. Comparing Figures 3-27 and 3-28, it is apparent that that Gaussian spheres model does not fit the measured data well at low q. Furthermore, the calculated values for radius and polydispersity based on the polydisperse hard sphere model are in better agreement with the values determined via TEM than those using the Gaussian sphere model. As such, the polydisperse hard sphere model will be considered for the remainder of this work.
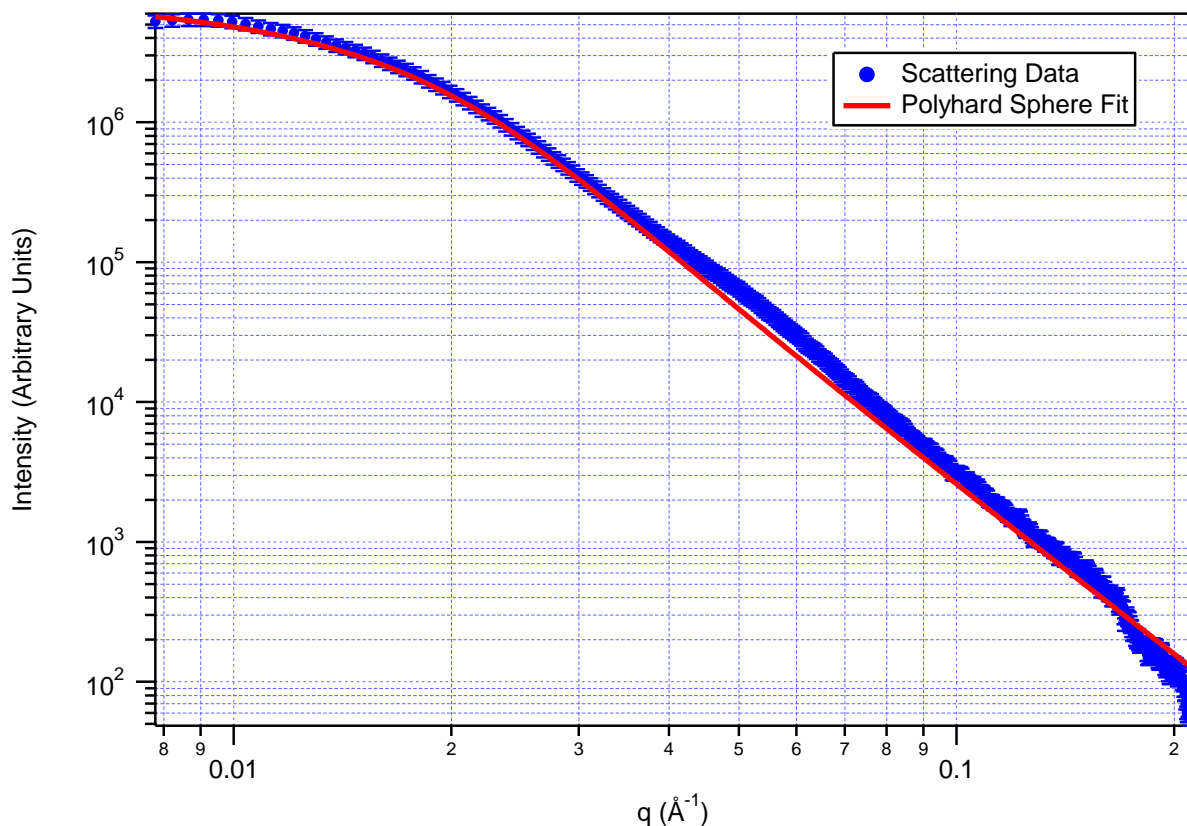


Figure 3-27. SAXS data for the same IPN-reduced gold nanoparticle sample that was tested via TEM, along with the fit done using the polydisperse hard sphere model.
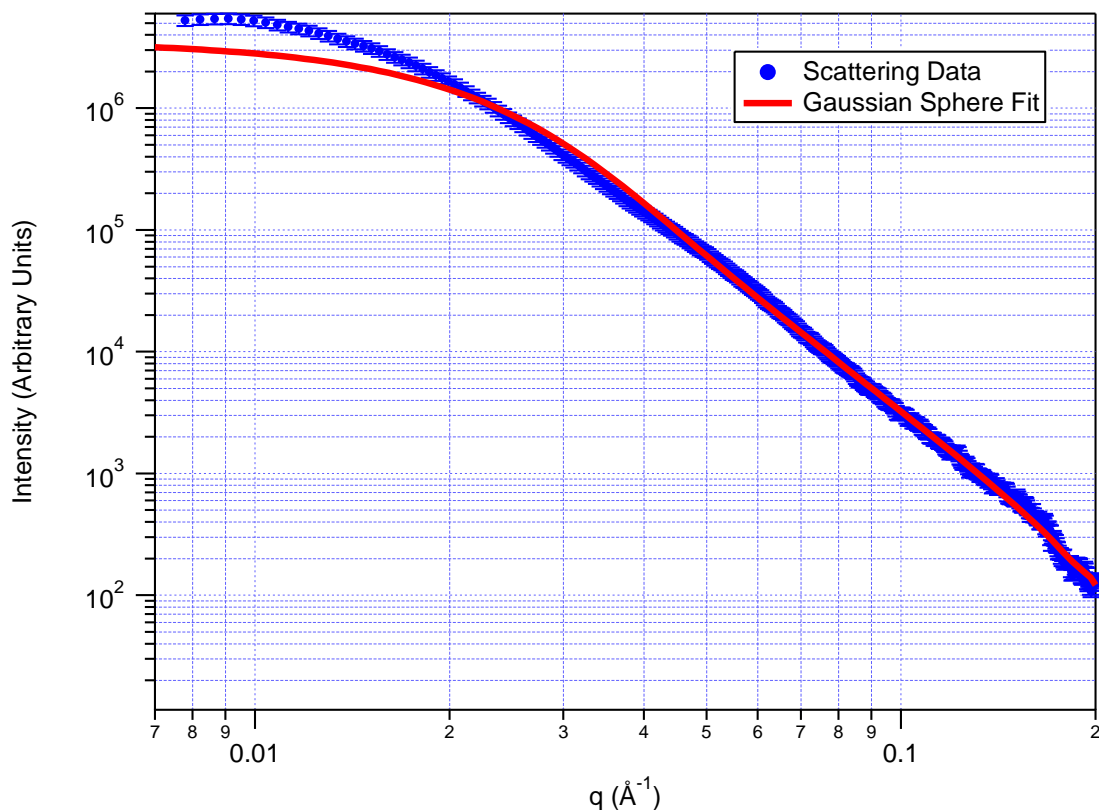
Figure 3-28.  SAXS data for the same IPN-reduced gold nanoparticle sample that was tested via TEM, along with the fit done using the Gaussian sphere model.

## 3.4 Combinatorial Optimization of Interpenetrating Network Method

Combinatorial samples were synthesized by creating a gradient in the DEAMA infusion time in one direction along with an orthogonal gradient in $HAuCl_4$ soak time (Fig. 3-29). Samples are slowly lowered into the monomer bath, removed, and polymerized via UV irradiation.  Samples were subsequently immersed in the metal salt infusion solution, producing a combinatorial library where the "x coordinate" corresponds to monomer soak time and the "y coordinate" corresponds to metal salt infusion time.  A BPI® Advanced Computer Gradient III™ system set to the parabolic gradient setting was used to immerse the 5 mm square pieces of TPU into the respective solutions in a controlled manner.  The parabolic gradient protocol produces a gradient in soak time as shown in Fig. 3-30.  Samples are lowered into the solution at an increasing rate with time.  This program was chosen as the simplest gradient available on our

dipping apparatus. 5 cm x 5 cm squares of 0.5 mm thick TDP7-1199 were used, with 20 min. gradient dips along each axis.
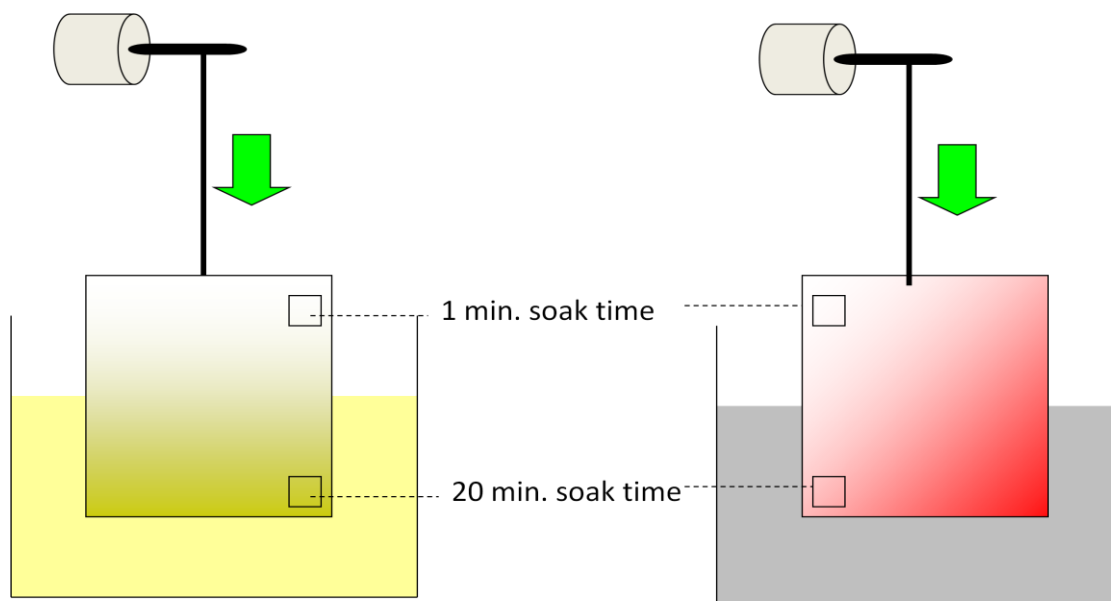


Figure 3-29. Schematic of combinatorial infusion. Samples are lowered into the infusion solution at a known rate, producing a gradient in the infused species within the polymer. Successive orthogonal immersions in the two processing solutions results in a combinatorial library.
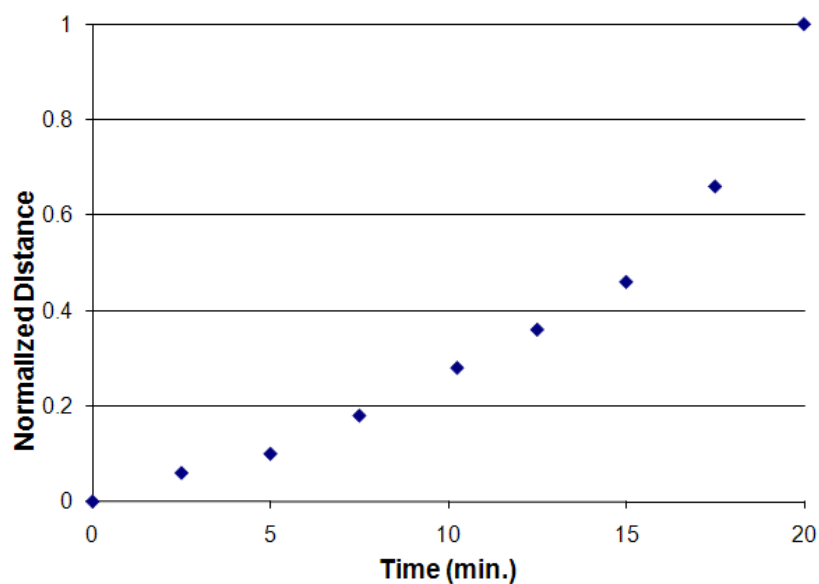


Figure 3-30. Normalized distance of the solution level from the bottom edge of the surface as a function of immersion time using the parabolic gradient dipping protocol.

With an efficient method for particle characterization in place, a combinatorial sample, with one axis having varying soak time in DEAMA and the other axis having a varying soak time in the gold precursor solution, was produced in order to understand how particle size and polydispersity varies with these processing conditions (Fig. 3-31). Although the combinatorial sample appears to be splotchy and uneven, the pictured pattern was found to be repeatable through the production of several such combinatorial samples. Four points were analyzed using SAXS (Table 3-5, labeled in Fig. 3-31). The parameters pulled from the polydisperse hard sphere model, again used to fit the SAXS data, are concomitant with both the visual observation of the combinatorial sample, as well as with the analysis of the original, non-combinatorial sample discussed up to this point. Scattering data for the four points on the combinatorial sample are shown in Fig. 3-32. The fit of the model to one tested point on the sample is shown in Fig. 3-33, while the results are summarized in Table 3-5. Fig. 3-34 shows the Schulz distributions for the points studied, as determined by the average particle radius and polydispersity given using the polydisperse hard sphere model to fit the SAXS data. The original sample does not necessarily fall in line with the trend in particle sizes of the combinatorial sample, as the $HAuCl_4$ solution temperature in the original sample tended to overshoot the 60 °C target by 2-3 °C, while the temperature in the combinatorial sample was more carefully regulated. Also, note that the polydispersity of point D is at its maximum value of 1. The blue band at this point is narrow enough that the beam, of diameter 1 mm, is scattering off of smaller, red particles as well as the larger blue particles observed by the eye. Thus, the average radius is increased by the presence of the blue particles as expected, but the polydispersity is likely inflated by the area interrogated during SAXS.
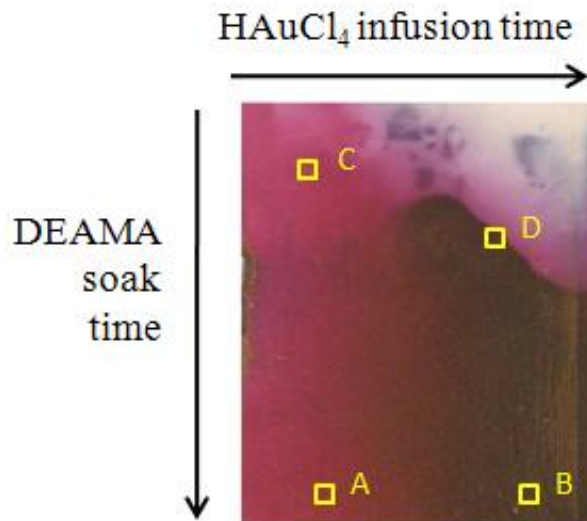
Figure 3-31. Photograph of the combinatorial IPN-reduced gold nanocomposite sample. Axes of infusions are indicated, as are the four points interrogated by SAXS.
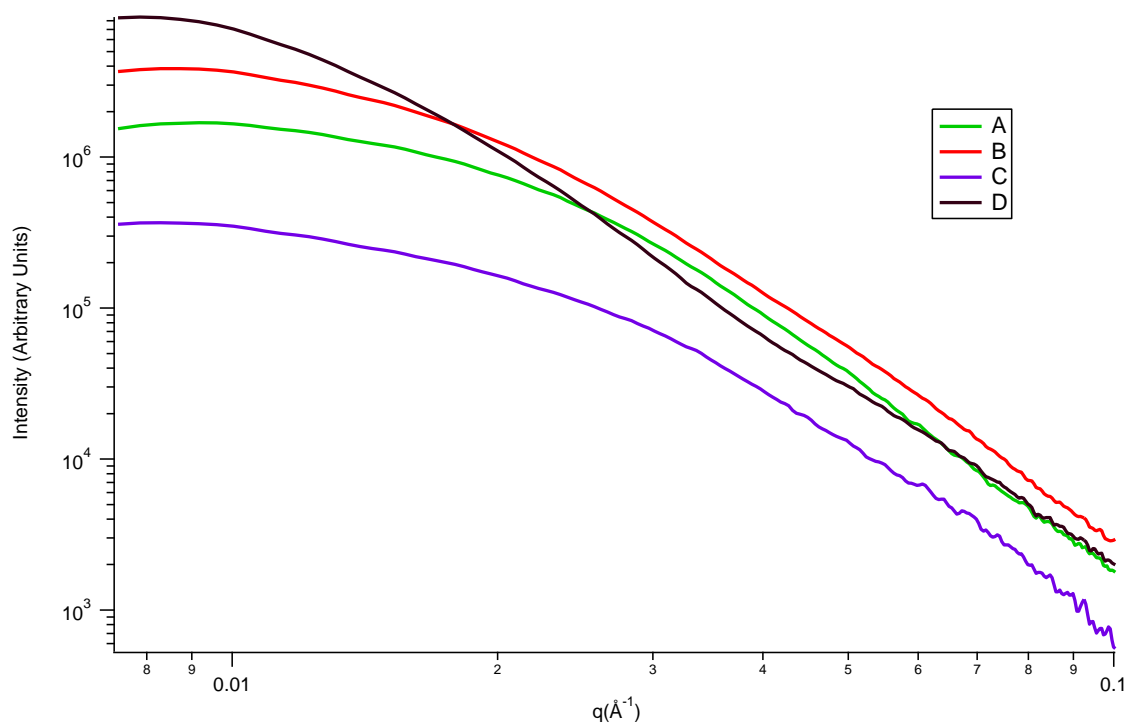


Figure 3-32. SAXS data for the all points studied on the IPN-reduced combinatorial sample.
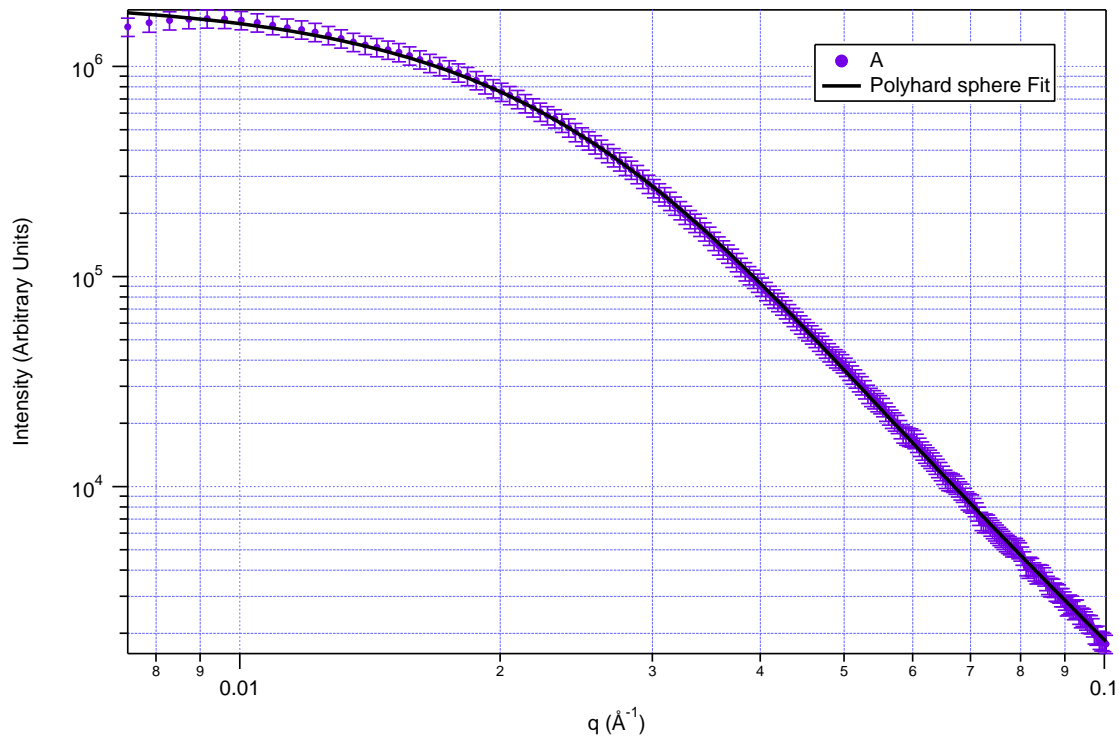
Figure 3-33. SAXS data for the point 'A' on the IPN-reduced combinatorial sample and its best fit using the polydisperse hard sphere model.

Table 3-5. Processing times and fitting results for SAXS data from the four points tested on the combinatorial sample, in addition to the original, previously discussed sample for comparison.

| Sample | DEAMA Soak Time (min.) | Gold Soak Time (min.) | Particle Radius from SAXS (Å) | Polydispersity from SAXS |
|---|---|---|---|---|
| Original | 20 | 3 | 48.2 | 0.62 |
| A | 20 | 10.25 | 45.2 | 0.54 |
| B | 20 | 18.5 | 32.0 | 0.83 |
| C | 8.5 | 9.75 | 25.0 | 0.75 |
| D | 13 | 17.5 | 35.8 | 1 |
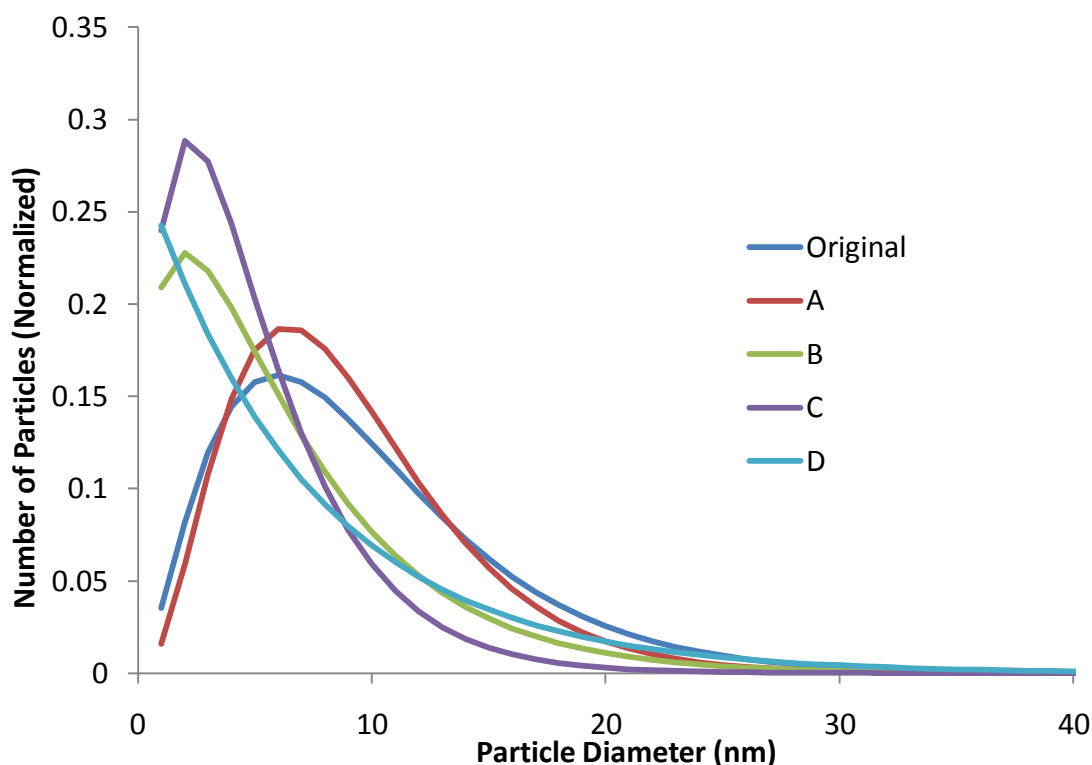
Figure 3-34. Schulz particle size distributions for the original IPN sample and the four points studied on the IPN combinatorial sample based on the average radii and polydispersities determined using the polydisperse hard sphere fit to the SAXS data.

The effect of DEAMA and gold soak times can be analyzed by comparing the Schulz distributions of the points tested. Comparing point A to point B, it is seen that an increase in gold soak time ($t_{Au}$) at constant DEAMA soak time ($t_D$) produces smaller particles of a significantly higher polydispersity. In a somewhat contradictory result, the original IPN-reduced sample and point A also have equal $t_D$ and different $t_{Au}$ (again, taking into account the slightly higher gold soak temperature in the original sample), with the result here that a somewhat narrower distribution of smaller particles is observed for the longer $t_{Au}$. Looking into the effect of $t_D$, samples A and C have similar enough $t_{Au}$ to observe that increased $t_D$ yields larger particles with a smaller polydispersity. However, this seems to be directly contradicted by the consideration of points B and D. Here, an increase in $t_D$ at roughly constant $t_{Au}$ leads to slightly smaller particles with a smaller polydispersity.

In order to rectify these conflicts and fully understand the particle size distribution trends seen in the investigated points, recent work in our group by Dr. Huipeng Chen (Texas Tech University) must be considered. Dr. Chen produced linear poly(DEAMA) in pure BCS at a concentration of 3.5 g polymer per 100 mL of solvent. $HAuCl_4$ was subsequently added at a

variety of loading ratios relative to the polymer. It was found that there is an optimum ratio between moles of $HAuCl_4$ and moles of amine-functionalized monomer units (*l*) to produce a large number of small particles, at l~0.15. Moving slightly off of this ratio in either direction, the production of small, red particles is still observed by the unaided eye. Further increasing or decreasing the loading ratio resulted in the production of larger navy blue particles, represented on the combinatorial sample at point D. At very low molar ratios of $HAuCl_4$:DEAMA (*l*~0.01), particles were large enough to precipitate out in solution. Conversely, at a ratio of *l*=1, no particles were produced and the solution remained the color of $HAuCl_4$, corresponding to the upper right corner of the pictured combinatorial sample (Fig. 3-31). Although the exact chemical mechanism of the gold reduction is not known, it is likely that multiple amine groups are necessary to reduce one molecule of $HAuCl_4$. Therefore, there is a limit to the number of gold molecules a poly(DEAMA) network of a given size can reduce, and the IPN must not be overloaded with $HAuCl_4$. Additionally, HCl is produced by the reduction, which may react with amine groups, further increasing the apparent consumption of reducing agents by the reaction. From this, we conclude that a key parameter in determining the particle size distribution for a given $t_D$ and $t_{Au}$ is the molar ratio of the two species that results within the host polymer. Thus, for a given soak time of one chemical, trends in the particle size distribution as a function of the soak time in the other chemical are not linear. Rather, the average particle size is minimized at a molar ratio of *l*~0.15, and moving off of this ratio produces larger particles. Further analysis would be useful in order to produce a plot of the molar ratio of $HAuCl_4$:DEAMA as a function of soak time in each solution for the given processing temperatures. Such a plot, in conjunction with the scattering results herein, would allow for relatively accurate prediction of average particle size and polydispersity for any combination of soak times.

### 3.5 Combinatorial Optimization of Nanoinfusion Method

In addition to combinatorial samples produced using the IPN reduction method, samples were produced using the initial chemical reduction method. Large extruded sheets of thickness 0.5 mm of both TDP7-1199 and T250 were cut into 5 cm x 5 cm squares. 20 min. parabolic gradient dips were done into $7.00 \cdot 10^{-3}$ M solutions of $HAuCl_4$ in the ternary AURA solvent at 60 °C. Following a water rinse, the samples were subjected to 20 min. parabolic gradient dips

into 0.072 M TEA in distilled water at 60 °C.  Samples were left in an 80 °C oven for at least one day following reduction, consistent with the non-combinatorial processing method.

SAXS was run on 8 points on the T250 sample, as well as on one point on a TDP7-1199 sample, using the equipment and methodology described above.  In addition, SAXS was taken on two samples of T250 that were processed in a non-combinatorial fashion with matching times to two of the combinatorial points tested.  This redundancy was used to validate the combinatorial methodology.  Table 3-6 summarizes all points tested via SAXS.

Table 3-6.  Conditions of chemical reduction method samples measured with SAXS.

| Sample | Infusion Time (min.) | Reduction Time (min.) |
|---|---|---|
| **Combinatorial T250** | | |
| A | 8 | 10 |
| B | 15 | 18 |
| C | 20 | 19 |
| D | 18 | 10 |
| E | 14.2 | 13.2 |
| F | 14.2 | 18.4 |
| G | 19.4 | 13.0 |
| H | 19.8 | 18.0 |
| | | |
| **TDP7-1199** | | |
| I | 19 | 14 |
| | | |
| **T250** | | |
| A1 | 8 | 10 |
| D1 | 18 | 10 |

The scattering for these gold nanoparticle samples are shown in Fig. 3-35 and Fig. 3-36. The non-combinatorial points tested (A1, D1) were found to have nearly identical scattering to the corresponding combinatorial points (A,D), validating the use of a continuous gradient with the spot size of 1 mm provided by the SAXS beam.  The "hump" observed at a q value of approximately 0.065 Å$^{-1}$ was not present in the scattering of the IPN-reduced samples and

presented a significant amount of difficulty in achieving a good fit of the polydisperse hard sphere model to the data. No "hump" was observed in samples B, D, or D1. Rather, a sharp drop off at q lower than the "hump" was seen in these samples. Regardless, no physically possible fitting parameters resulted in a good fit using the polydisperse hard sphere model. The "hump" was nonetheless present in samples produced with both T250 and TDP7-1199, so it was not due to use of a different TPU formulation than in the IPN-reduced samples. The maximum was shifted slightly to a q of approximately 0.05 $\text{Å}^{-1}$ in the TDP7-1199 sample. The Gaussian sphere model was tested as well, with no good fit found for either model to the chemical reduction method samples' scattering.

Recall that aggregates were observed in the TEM images of the chemical reduction method samples, and more aggregates were likely lost when the samples were microtomed. As such, it appears quite probable that the local maximum is a correlation peak due to the proximity of the nanoparticles within the sample. Such a peak is very difficult to model given the information available on our samples and would explain the difficulty in achieving good model fits of the data. However, $2\pi/q$ can be used to calculate the average distance between particles for a correlation peak. Using the q value at the maximum of the "hump," the average distance between particles was found to be 9.7 nm for the T250 samples and 12.6 nm for the TDP7-1199 sample.
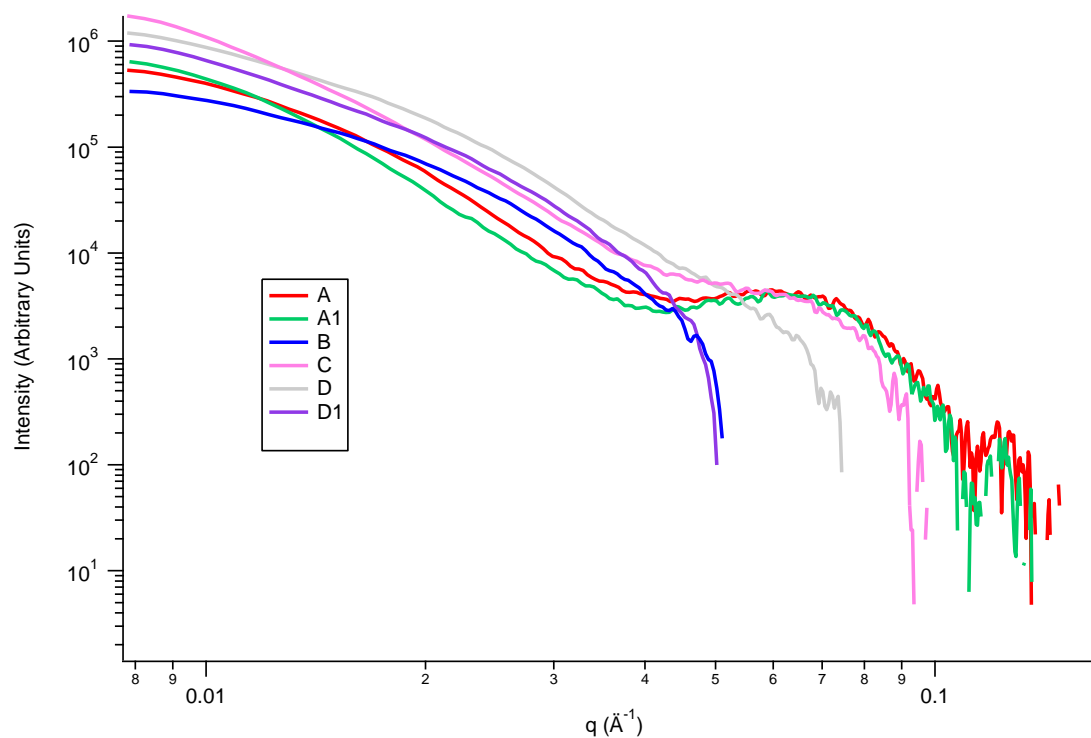
Figure 3-35. SAXS data for the points A through D on the chemical reduction method combinatorial sample. Note the maximum at q ~ 0.065 $\text{Å}^{-1}$ for points A, A1, and C.
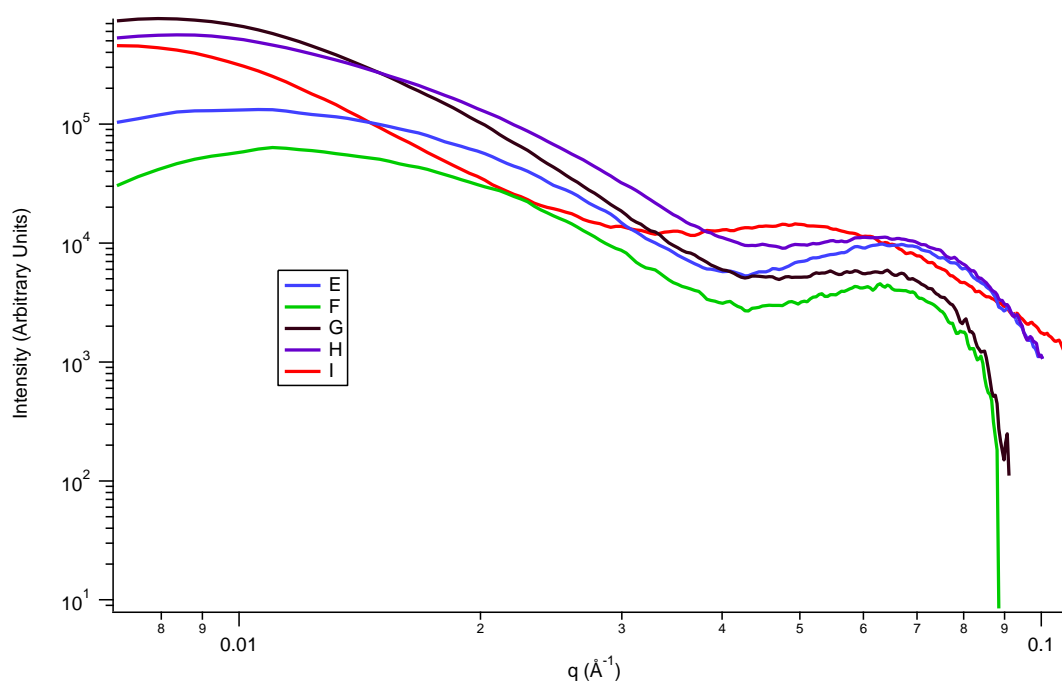


Figure 3-36. SAXS data for the points E through I on the chemical reduction method combinatorial sample. Note the maximum at q ~ 0.065 $\text{Å}^{-1}$ for points E through H and its shift to 0.05 $\text{Å}^{-1}$ for point I.

UV-vis spectra were also taken for the points A through D using a Perkin-Elmer Lambda 950 UV-vis-NIR spectrophotometer in transmission. Point A, which appears pink to the unaided eye, had the smallest absorbance (Fig. 3-37). Point B appears blue, indicating larger particles than point A. As expected, the absorbance peak at point B is significantly broadened and red-shifted relative to point A. Points C and D, which appear as increasingly darker shades of purple, were only slightly red-shifted from A, indicating that the particle size at these points was likely closer to that observed at point A than at point B, though slightly larger. The primary change between point A and points C and D, as seen with the UV-vis, was the increased absorbance at points C and D, likely indicating a higher number density of particles. This observation is congruous with the longer infusion and reduction times at points C and D relative to point A. Note that the UV-vis data is insufficient to make more than qualitative comparisons between points, due to the fact that the surface plasmon resonance absorbance can change due to not only particle size, but also particle shape and agglomeration. As such, particle radii cannot be determined directly from this data, as the shape and level of agglomeration are not constant from one point to another.
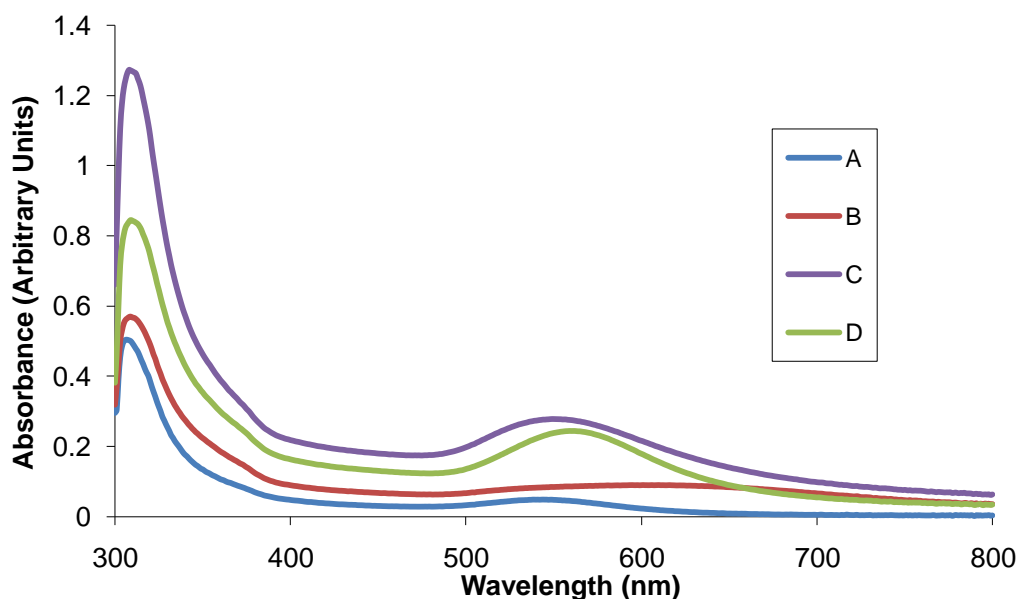


Figure 3-37. UV-vis spectra of points A through D on the combinatorial T250 sample.

### 3.6 Electrical Characterization of Interpenetrating Network Samples

Physical properties of TPU elastomers such as elasticity, high elongation at break, impact resistance, light fastness, oxidation and hydrolysis resistance, and low-temperature flexibility have facilitated their widespread commercial production and use in consumer products, medical applications, and military applications. However, due to their electrically insulating nature, electric charge that builds up, most often triboelectrically, may not easily move across the surface of the article to recombine. As such, some method of conduction is needed to allow this migration in cases where surface charge may be detrimental. When surface resistivity falls in the range $10^4$ - $10^{11}$ Ω/square, the material may be referred to as possessing electrostatic discharge (ESD) properties. Polymers with ESD properties are used in a wide variety of applications, notably for the prevention of explosions due to charge build up in engines and turbines[219,220] and for the protection of electronics.[221-224]

ESD properties have been conferred to polymer articles in a variety of ways. Inherently conductive polymers can serve as an ESD medium. For example, an acid-cured, solvented resole can be synthesized with no additional additives to possess sufficient conductive properties for ESD applications.[225] Other examples include the synthesis of a poly(urea-urethane) based on PDMS, which exhibits sufficient conductivity at high humidity for ESD applications.[226] Addition of moieties capable of conduction within the polymer backbone can also be a successful strategy for ESD. For instance, a method has been developed for achieving ESD in a transparent polymer material, made from conductive polymer, cross-linkable polymer, and cross-linking agent, for use as a thin film for packaging materials.[227] Addition of metallocene moieties to the polymer backbone has also been found to confer ESD properties.[228]

In another class of ESD polymers, a chemical additive can be either applied to the surface or incorporated beneath the surface of the article. Note that surface coatings are subject to wear and thus may not be permanent. As such, additives introduced beneath the surface may potentially be more resilient. For example, ESD properties may be achieved in a shaped resin without damaging physical properties or causing discoloration.[229] A nitrogen-containing compound is added during molding, followed with corona discharge treatment to the surface of the shaped article.

Fillers, such as metal particles or carbon fibers, can also be added to a polymer article in order to achieve sufficient conductivity for ESD. Carbon black has been demonstrated for this purpose, as have carbon nanotubes and metal nanocomposites. A plethora of examples of these

methods exist. ESD can be achieved through a dispersion of non-insulating particles, such as gold or carbon black, and an inherently dissipative polymer within a thermosetting resin.[230] A polymer composition consisting of a poly(aryl ether ketone), a poly(biphenyl ether sulfone), and a fibrous carbon nanofiller has been demonstrated to have sufficient conductivity for ESD applications.[231] One particularly relevant demonstration of ESD polymers describes a high temperature, high strength polymer which uses a metal oxide to achieve ESD for read/write heads in magnetic media.[232] These polymers may be dyed via a pigment while maintaining their conductive properties, which may be useful in consideration of ESD materials produced via AURA processing. Still further examples of ESD-capable polymer systems include the use of non-carbonaceous fillers, such as metal oxide particles, within thermoplastic polymers,[233] the polymerization of a thermoplastic in the presence of a lithium salt,[234] graphite-filled polymer composites,[235] oriented nanotubes within a polymer matrix ESD-capable material,[236,237] and degradable polymers with metal flakes, fibers or powders.[238]

Preliminary testing done by Bayer MaterialScience indicated the potential for conductivity sufficient for ESD properties in the IPN-reduced gold nanoparticle samples described in section 3.2. Gold nanoparticle composites prepared via the chemical reduction method did not exhibit a change in conductivity from the unmodified polymer. We performed a more thorough characterization of the surface resistivity of a variety of samples using a Keithley 6517b ultra high-resistance electrometer with surface Model 8009 resistivity test fixture. Samples were injection molded slabs of thickness 3.3 mm, and dimensions 3 in. x 3 in. square. The surface resistivity of unmodified TDP7-1199 was found to be $(7.06 +/- 0.33) \cdot 10^{13}$ $\Omega$/square over ten measurements. The quoted uncertainty is one standard deviation. A poly(DEAMA) IPN sample of TDP7-1199 was prepared via 25 min. soak in DEAMA and 1 % w/w Irgacure® 651, followed by a 5 min. UV cure on each side of the sample using a 100 W long wavelength UV lamp. Curing was done under in a nitrogen atmosphere at a distance of 5 inches. Without gold, the sample was found to have a surface resistivity of $(2.98 +/- 0.27) \cdot 10^{13}$ $\Omega$/square (n=10). A second piece, processed identically, had surface resistivity $(2.89 +/- 0.13) \cdot 10^{13}$ $\Omega$/square (n=7). Finally, an identically prepared poly(DEAMA) sample was produced and immersed in a solution of 0.025 M solution of $HAuCl_4$ in AURA at room temperature for 43 min. The sample was baked overnight at 75 °C to ensure gold reduction and solvent evaporation, resulting in the typical dark red color. The surface resistivity of this gold-containing sample was found to be $(2.55 +/- 0.24) \cdot 10^{12}$ $\Omega$/square (n=5).

The above samples show an increase in surface resistivity by about 27 times after the introduction of gold nanoparticles. However, we know from TEM images in the previous sample that percolation is unlikely in this system given the current processing conditions. It is unlikely that a large increase in conductivity is due to the presence of a large number of non-contacting conductive particles. As such, we believe that the increase in surface conductivity is due to the reaction of the HCl produced by the addition of $HAuCl_4$ to the poly(DEAMA) IPN layer, essentially creating an ionomer, where mobile ions can move along the polymer backbone in response to an applied electric field. To test this hypothesis, Dr. Huipeng Chen (Texas Tech University) prepared a poly(DEAMA) IPN layer after the TDP7-1199 was soaked in a 0.2 N solution of HCl in AURA at 60 °C. Increasing soak times in the HCl resulted in lower surface resistivity values. Dr. Chen has produced samples with surface resistivity as low as $10^{10}$ Ω/square, well into the range needed for ESD properties. Thus, while the IPN-reduction method yielded a large number of nanoparticles in the TPU, the use of gold nanoparticles is both unnecessary and prohibitively expensive for the production of an ESD material.

Several applications of a surface layer IPN have been discussed, including enhancement to mechanical properties, barrier properties, electrical properties, surface hydrophilicity, and optical properties. Using infusions of polymerizable monomers, IPNs can be produced that are otherwise not possible, such as IPNs of thermosets that could not be prepared via melt processing. A thin surface layer IPN can be produced which alters the barrier properties or surface energy of the host polymer without affecting its mechanical properties. The production of nanoparticles within the host polymer using a functionalized IPN has also been demonstrated, with a significant decrease in agglomeration of particles relative to that seen in other similar methods.

# Chapter 4

## Smectic Main Chain Liquid Crystalline Elastomers

The polydomain to monodomain transition (P-M) of smectic main chain liquid crystalline elastomers (MCLCE) was studied through a variety of methods.  In working towards the study of the P-M transition at the molecular level via small angle neutron scattering (SANS) of a deuterated LCE sample, the synthesis of an end-linked LCE was attempted.  Though a network was produced, improvements still need to be made before synthesis of a deuterated end-linked sample can be realized.  The P-M transition was also interrogated via the uniaxial elongation of LCE samples at varied temperatures and strain rates, yielding insight into the origin of an observed necking instability.

Materials used for the syntheses detailed herein are as follows.  4-dimethylaminopyridine, allyl alcohol, 1,1,1,2-tetrachloroethane, and terephthalic acid were purchased from Alfa Aesar.  1-ethyl-3-(3-dimethylaminopropyl)-carbodiimide, tert-butoxystyrene, Pt(0)-1,3-divinyl-1,1,3,3-tetramethyldisiloxane, and cis-dichlorobis(diethyl sulfide)Pt(II) were acquired from Sigma Aldrich.  Dichloromethane, hexane, toluene, and dimethyl sulfoxide were purchased from BDH.  Hydroquinone, terephthaloyl chloride, and trimethylsilyliodide were purchased from TCI America, and pyridine was acquired from J.T. Baker.  Tetrakis(dimethylsiloxysilane) (A4), 1,1,3,3,5,5,7,7-octamethyltetrasiloxane (90 %) (F4) and 1,1,3,3,5,5 hexamethyltrisiloxane (99 %)  (F3) were purchased from Gelest, Inc.  All reagents were used as received, unless noted otherwise.

### 4.1 End-Linked Liquid Crystalline Elastomers

An end-functionalized liquid crystalline polymer has been synthesized, as shown in the reaction schematic in Fig. 4-1.  Great care was taken to ensure that the product of each reaction was highly purified, primarily through column chromatography following each step.  To begin the synthesis, a 20 % molar excess of tert-butoxystyrene was added to F4 in toluene and stirred at 45 °C.  20 μL of $6.0 \cdot 10^{-3}$ M Pt(0)-1,3-divinyl-1,1,3,3-tetramethyldisiloxane in toluene was added

to catalyze the reaction. A 1:2 mixture, by volume, of dichloromethane and hexane was used to test the product via thin layer chromatography (TLC) and identify any unreacted chemicals or undesired side products. A silica gel column, in conjunction with TLC, was used to isolate the product of the reaction. In reaction II, the product of reaction I was added to a 10 % molar excess of trimethylsilyliodide in dichloromethane. 10 mL of dichloromethane were utilized for every gram of the reaction I product. The reaction was allowed to proceed for 2 days at room temperature under anhydrous conditions. The product of reaction II was cleaned with a saturated solution of sodium bicarbonate, washed with dichloromethane and water in a separatory funnel, and vacuum-filtered. A silica gel column was again used in conjunction with TLC to further isolate the desired product of the synthesis. In a glove box under anhydrous conditions, a 5 % molar excess of terephthaloyl chloride was added to the product of reaction II via a saturated solution of terephthaloyl chloride in toluene. Pyridine was also added as an acid scavenger. The product was again purified via separatory funnel, using toluene and water, and with vacuum-filtration. Finally, the product of reaction III was dissolved in dichloromethane, to which was added 0.3834 g 1-ethyl-3-(3-dimethylaminopropyl)-carbodiimide, 0.1189 g 4-dimethylaminopyridine, and 0.6615 g allyl alcohol for each gram of polymer, as determined by previous work.[239] The mixture was allowed to react for at two days at room temperature. The product was dissolved in toluene and fractionated via the addition of small quantities of methanol over several days.
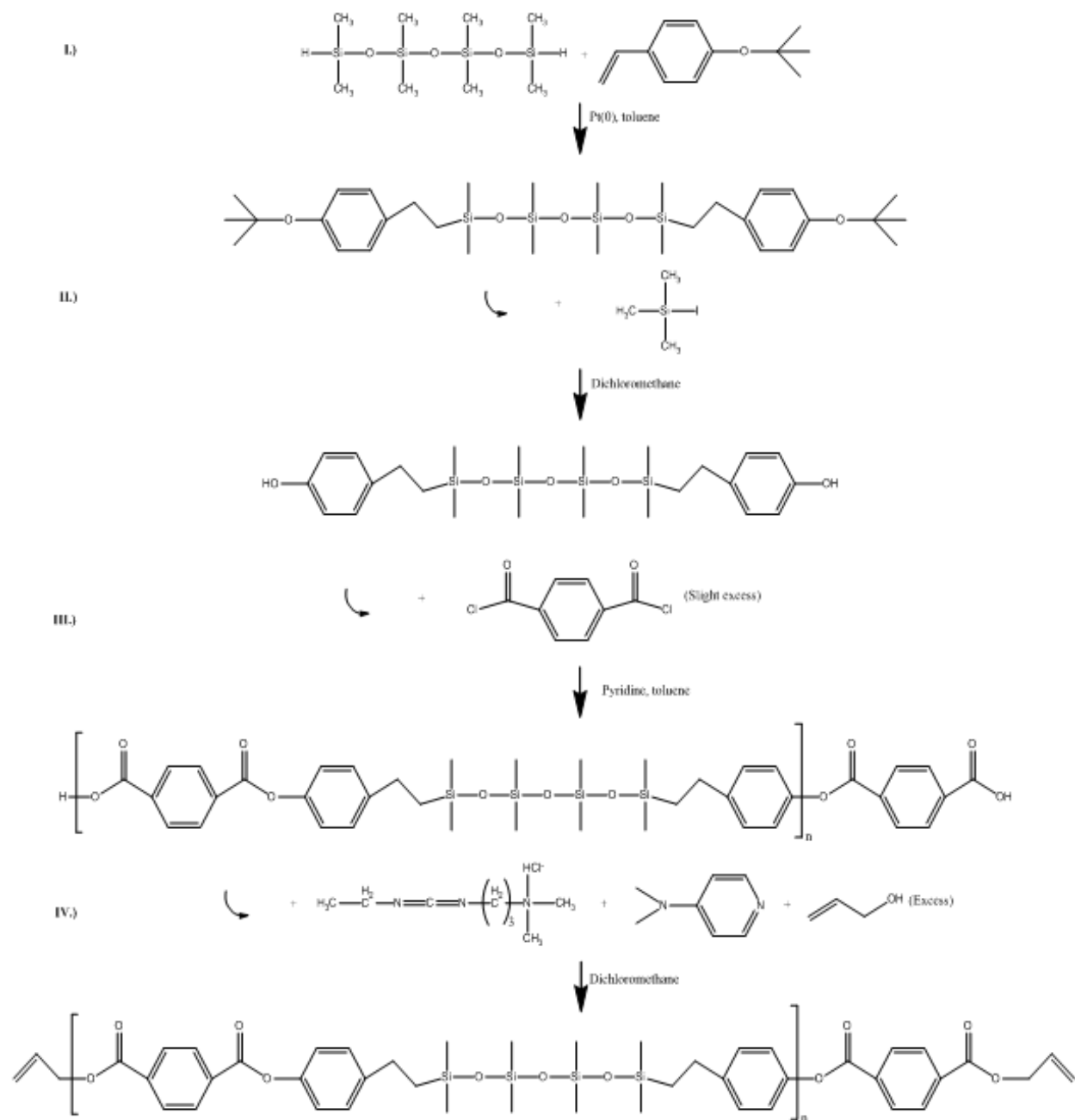
Figure 4-1. Schematic of the synthesis of the vinyl-terminated polymer used in the end-linking reaction.

The resulting polymer was characterized using nuclear magnetic resonance spectroscopy (NMR), gel permeation chromatography (GPC), and x-ray diffraction (XRD). $^1$H NMR was performed on a Bruker DRX-400 NMR using deuterated chloroform as the solvent. A Waters Alliance GPC/V2000 with refractive index, light scattering, and intrinsic viscosity detectors was used for GPC. Measurements were taken at 40 °C using tetrahydrofuran (THF) as a solvent, with

a flow rate of 1 mL/min. Samples were dissolved at 1 mg/mL in THF and 20 µL injected to the GPC for testing. XRD was done using a Rigaku DMAX-Rapid Microdiffractometer with a copper tube.

NMR data indicate that the polymer is end-functionalized with the desired allyl groups, as indicated by the peaks found between about 5 and 7 ppm (Fig. 4-2). Number average molecular weight ($M_N$) of the polymer, following fractionation, was determined using NMR. This calculation was done by comparing the integrated area of the peak corresponding to the aromatic protons ($A_{Ar}$) of the rigid mesogen portion to that for the allyl protons of the end groups ($A_{Al}$). The large peak at approximately 7.2 ppm is due to the 12 mesogen protons per repeat unit (plus four aromatic protons on one end group, when viewed as shown in the final product of Fig. 4-1), while the three peaks at 4.9, 5.4, and 6.1 ppm correspond to the 5 end group protons per side. The ratios of the peak areas can be compared to the ratio of the number of corresponding protons using the equation

$$\frac{A_{Ar}}{A_{Al}} = \frac{12DP_n + 4}{10} \qquad (4\text{-}1)$$

from which the degree of polymerization, $DP_n$, can be calculated. With $DP_n$, $M_N$ can be easily calculated, knowing that the molar mass of the repeat units is 653.04 g/mol and the combined molar mass of the two end groups is 246.26 g/mol. In order to help confirm this calculation, GPC was also used to determine the weight average molecular weight ($M_W$) of fraction 3. The value for $M_W$ from GPC agreed within 10 % with the NMR-determined $M_N$ value (Table 4-1).
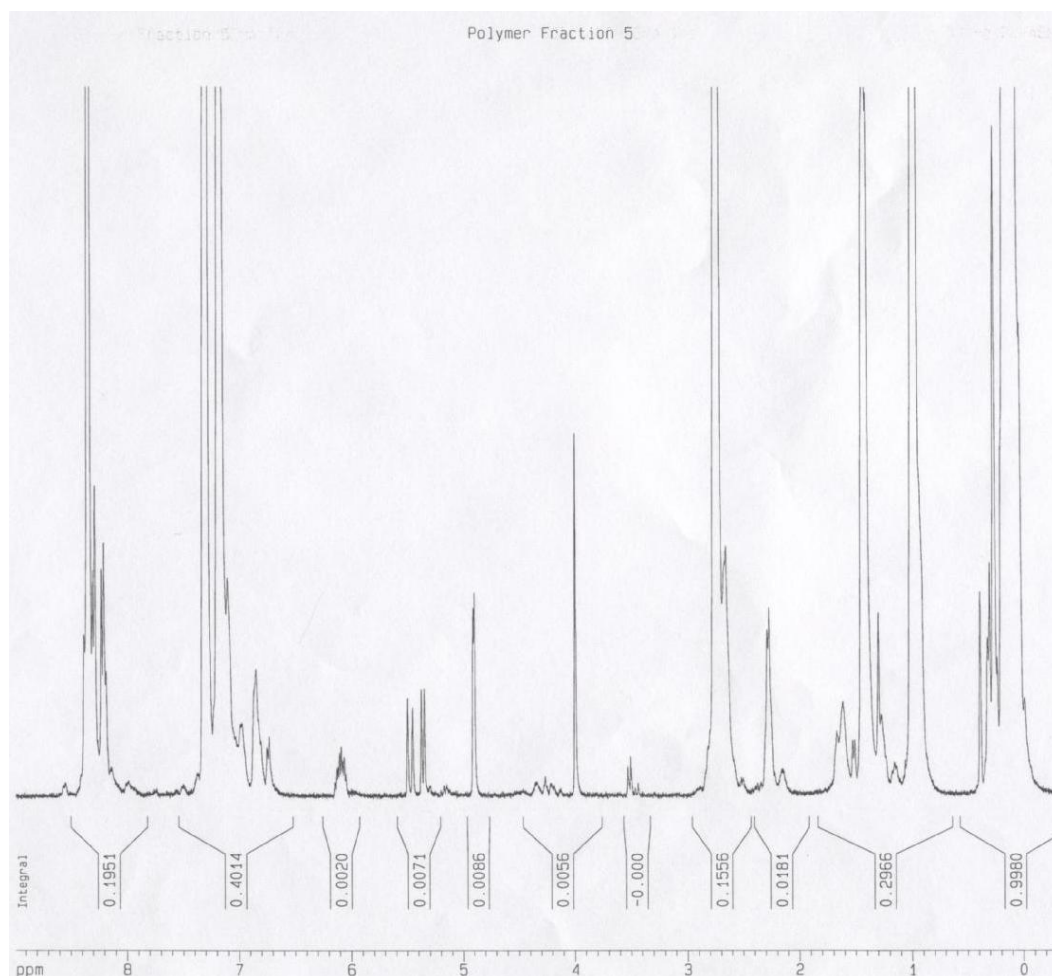
Figure 4-2. $^1$H NMR of a 12,400 g/mol fraction of synthesized LCP. Peaks at 4.9, 5.4, and 6.1 ppm confirm the presence of the desired allyl end-groups.

Table 4-1. Molecular weights of fractionated LCP, as determined by $^1$H NMR and GPC.

| Fraction | 3 | 4 | 5 | 6 | 7 |
|---|---|---|---|---|---|
| NMR | 12,300 g/mol | 12,200 g/mol | 12,400 g/mol | 11,900 g/mol | 10,200 g/mol |
| GPC | 13,300 g/mol | | | | |

In order to identify the phase of the LCP, optical microscopy and XRD were performed. Optical microscopy did not produce any identifiable texture, but XRD yielded the intensity versus $2\Theta$ data shown in Fig. 4-3. A nematic LCP would exhibit little or no peak in intensity at low angles, due to the lack of any sort of long-range ordering, while smectic LCP should have a high intensity peak at low angles due to the added degree of positional ordering found in the phase. Here, however, we see a peak of moderate intensity. This discrepancy is explained by the NMR

data.  Assigning the peaks found in the NMR to their appropriate hydrogens and considering their relative amounts, we see that reaction I yields about 60 % of the desired product and 40 % of an isomeric side product, shown in Fig. 4-4.  As a result, the LCP cannot fully align into the smectic phase that it seeks to attain, and is left in a "frustrated" smectic state.
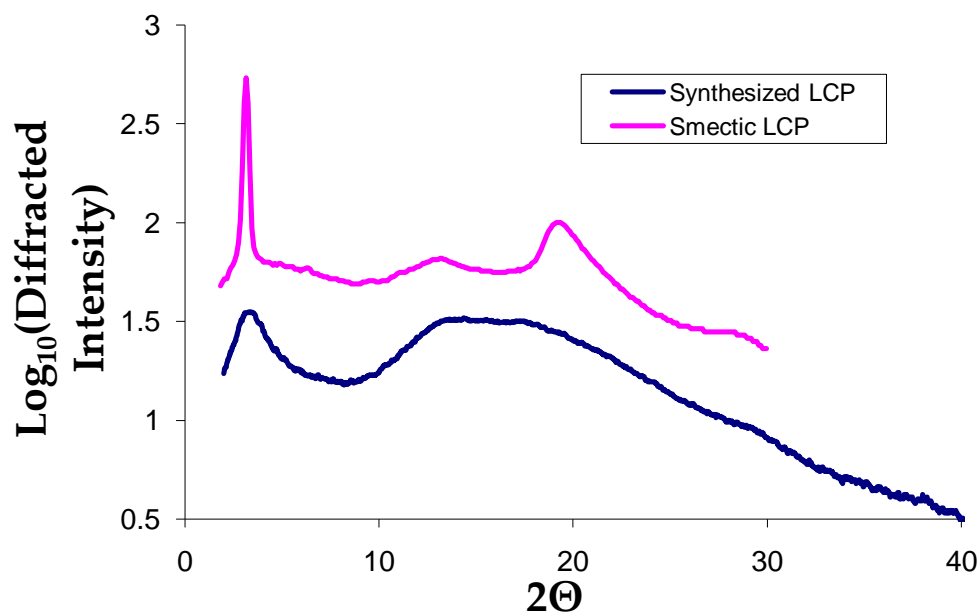


Figure 4-3.  XRD data for the synthesized polymer, as well as a known smectic LCP for comparison.
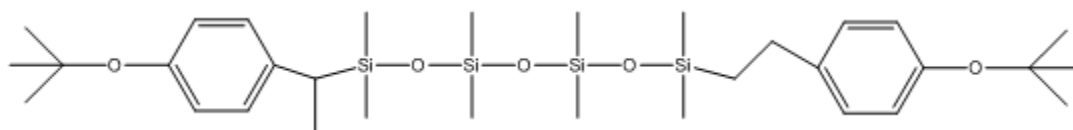


Figure 4-4.  Side product of reaction I in Fig. 4-1.  This side product was found by NMR to account for 40 % of the yield of this reaction.

Cross-linking of the LCP was performed via the reaction shown in Fig. 4-5. Stoichiometric amounts of LCP and A4 were added, based on the molecular weight of a given fraction as determined by NMR.  20 μL of $5.2 \cdot 10^{-3}$ M cis-dichlorobis(diethylsulfide)Pt(II) in toluene was added for every gram of polymer present.  Following addition of the cross-linker, samples were stirred vigorously by hand for 3-5 minutes before catalyst addition.  After 3-5 minutes more stirring, samples were placed in a 35 °C oven for one day.  Note that a solvent is needed for this reaction due to the fact that the tetra-functional cross-linker is not miscible with our LCP.  Further, the viscosity of the polymer is very high at room temperature.  Increasing the temperature is not an option, as this change would lead to an increased number of side products in

the hydrosilation reaction. As such, the effect of solvent on the cross-linking reaction was studied using polydimethylsiloxane (PDMS).
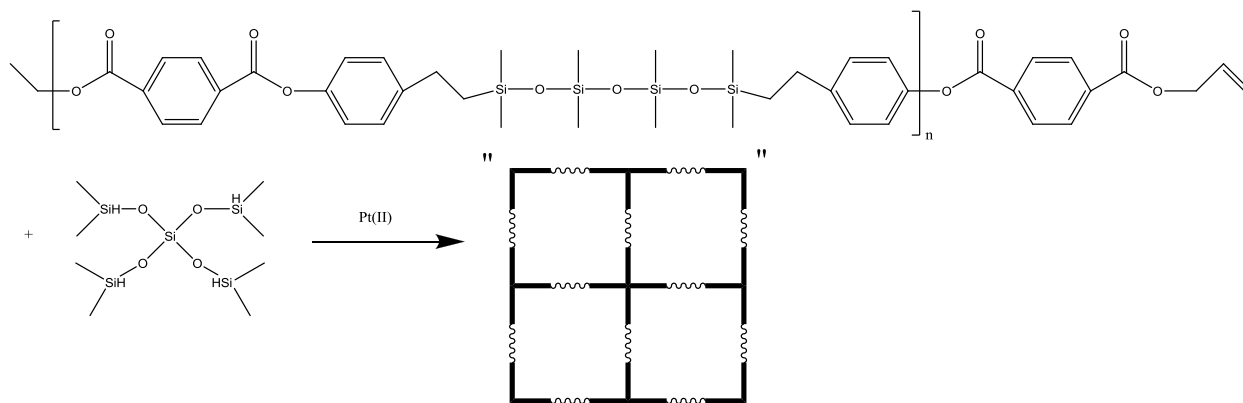


Figure 4-5. Cross-linking reaction used to form an LCE from the above synthesized LCP.

PDMS can be cross-linked using the same reaction shown in Fig. 4-5 without the need for solvent. Key parameters of interest here are $r$, the ratio of the number of end groups on the cross-linker to the number of end groups on the polymer; $w_{sol}$, the fraction of the mass of the network which is washed out when the system is swollen and then deswollen with toluene; and $Q$, the swelling ratio, which is the ratio of the volume when swollen with toluene at equilibrium to the volume of the network following deswelling. $r$ is determined by the chosen ratio of LCP to A4 during the synthesis reaction and sets the values for $w_{sol}$ and $Q$. Minimum values of $w_{sol}$ and $Q$ indicate a tighter network, with fewer dangling bonds and entanglements. Fig. 4-6 shows a comparison of these variables for a range of $r$ values in PDMS networks formed both with and without 1,1,1,2-tetrachloroethane as a solvent. We have found that the optimal $r$ value for the system increases from about 1.5 to about 2.3 when solvent is used in the production of the network. Note that these minima are rather broad due to the use of unfractionated 20,000 g/mol PDMS. Fractionated PDMS networks, with a narrower molecular weight distribution, result in a sharper minimum of soluble fraction at 1.5.[240] Interestingly, though the $r$ value needed increases, the minimum soluble fraction is about 5 % in both cases. $Q$, however, is changed due to the use of solvent, increasing from a minimum of about 4 to a minimum of 6. We would expect such a change, due to the fact that the PDMS in solvent will have fewer entanglements. When the network is formed, less trapped entanglements will therefore be present, which in turn increases the average molecular weight between effective cross-links in the network and allows for swelling to take place to a greater degree.

**Soluble Fraction without Solvent**

**Swelling Ratio without Solvent**

**Soluble Fraction with Solvent**

**Swelling Ratio with Solvent**
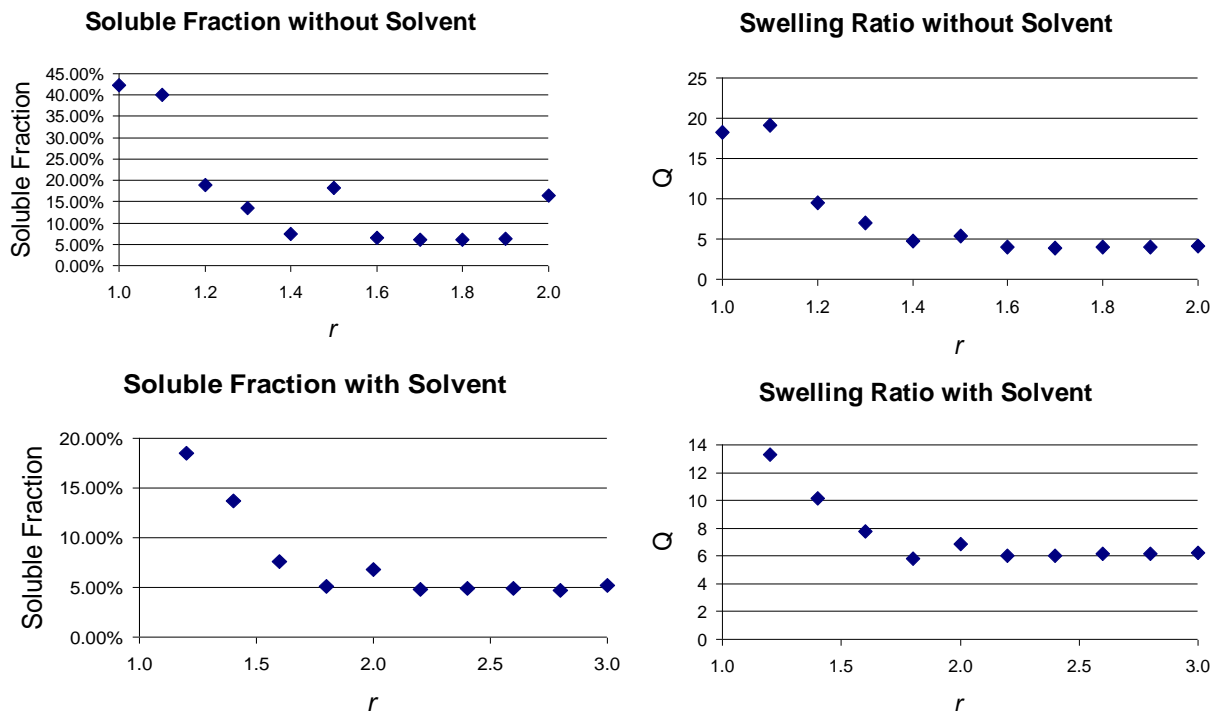


Figure 4-6.  Soluble fractions and swelling ratios found at various r values for PDMS networks. While the minimum soluble fraction does not change, the r value at which it is attained increases with the addition of solvent to the system, as does the minimum swelling ratio achieved.

Using the knowledge gained from the PDMS networks, end-linked networks of the synthesized LCP have been attempted in 1,1,1,2-tetrachloroethane, based upon the earlier success of Patil et al. with cross-linking in $CH_2Cl_2$.[239]  Despite the apparent purity of the starting LCP and the care taken in all reaction steps, no visually transparent networks were ever produced.  All networks synthesized were cloudy and opaque, likely due to the presence of some impurity or unwanted side product.  As such, work is needed to further clean up the synthesis of the end-linked networks before this avenue of research can be continued.

**4.2 Smectic Liquid Crystalline Elastomer Synthesis**

A previously utilized synthetic scheme for producing smectic MCLCEs of a similar structure to the end-linked LCP was used in order to make samples for mechanical testing (Fig. 4-7).[239] MCLCE samples were synthesized via nonlinear polymerization of allyloxy-terminated mesogens, siloxane spacers, and a cross-linker using a Pt(0)-catalyzed hydrosilylation

reaction. The mole ratio of Si-H to allyloxy end groups ($r$) was set to 1.5, while the mole fraction of SiH groups belonging to cross-linkers ($\rho$) was set to 0.06. The elastomer studied here is similar to those described in earlier work by our group,[149,153] except cross-linking was conducted in toluene at 80 °C. Cross-linking occurred in the isotropic state due to the presence of the solvent. Following cross-linking, the LCE was swollen and extracted in excess toluene for 7 d to remove solubles, during which time the toluene was replaced with fresh solvent daily. The MCLCE was de-swollen by slow addition of methanol (a poor solvent) to the toluene over a period of a few days in order to avoid cracking from rapid evaporation of solvent. Networks were air and vacuum dried at 50 °C. All mechanical experiments were performed on the dry, extracted elastomer. Domains were found to be 30-100 nm long.[149,153] Due to this relatively small domain size, the samples were always transparent and the opaque to translucent transition at the P-M transition was not observed.[239]
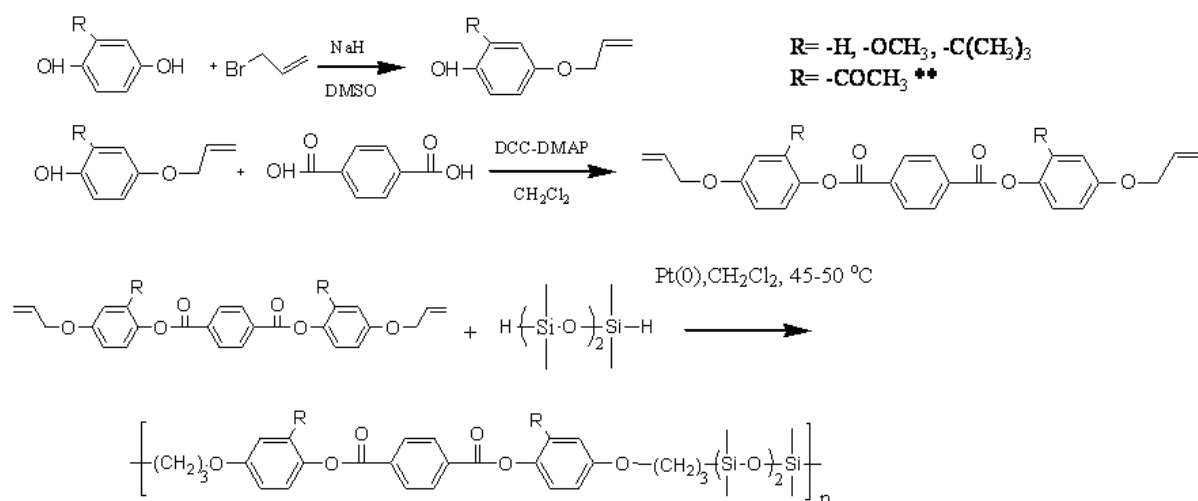


Figure 4-7. An alternate LCP synthesis scheme. Note that in the current work, all samples tested have R = -H.

## 4.3 Necking Phenomenon in Smectic Liquid Crystalline Elastomers

Necking has rarely been reported in the LCE literature, though it has been observed to depend on both the temperature and the rate of elongation in mechanical testing of a variety of other polymers, as was discussed in Chapter 1. The influence of both temperature and strain rate

on the mechanical response of a smectic polydomain MCLCE which can develop an obvious neck upon uniaxial elongation was examined. Necking is observed in unaxial elongation at a constant strain rate as a maximum at the yield point, followed by a significant drop in the nominal stress[153] to a local minimum value, $\sigma_N$, which will here be referred to as the post-necking stress. The value of $\sigma_N$ can be significantly lower than the yield stress, $\sigma_y$, which may be determined by construction of a Considére tangent if the true stress and strain values are known.[153] While Griffin et al. reported similar yielding behavior in a smectic elastomer having "transverse rod" mesogens in the main chain,[175] other studies only reported a plateau during uniaxial elongation, without any neck formation or any measurable decrease in the nominal stress in the plateau region.[133,155] In order to determine under what conditions neck formation may be observed in our smectic MCLCE, constant strain rate uniaxial deformations were performed at a variety of temperatures between the glass transition temperature, $T_g$, and the smectic to isotropic clearing temperature, $T_{si}$, as well as at a variety of strain rates at a constant temperature within this range.

## 4.3.1 Mechanical Testing

Stress-strain behavior was characterized in uniaxial elongation using a TA Instruments Q800 DMA. Standard dogbone-shaped samples were prepared, having initial length of 7 mm, width of 1.15 mm, and thickness of approximately 0.4 mm. Prior to mechanical testing, samples were subjected to a thermal pre-treatment that was found to produce a repeatable mechanical response. Samples were heated to 100 °C for 5 min. (slightly above the smectic-isotropic clearing temperature), then cooled quickly to room temperature and allowed to equilibrate overnight. Strain ramp measurements were obtained by allowing the sample to pre-heat at the desired temperature for 15 min., followed by the application of strain at a given rate, up to an overall draw ratio of $\lambda=2.5$, where $\lambda=(L/L_0)$ is calculated from L and $L_0$, the final and initial sample lengths between the clamps, respectively. The compliance of the machine was assumed to be negligible in calculating the yield stress. Variation of strain rates was performed at a constant temperature of 35 °C, while variation of temperature was performed with a constant strain rate of $2.08\times10^{-3}$ s$^{-1}$. For optical microscopy experiments, samples were allowed to relax at an overall draw ratio of $\lambda=2.5$ for at least one hour before being removed from the DMA clamps. The local or mesoscopic draw ratio ($\lambda_m$) was measured at the center of the necked portion immediately after removal from the DMA, using an "ink dot" technique (Fig. 4-8). Small dots of

black ink were placed throughout the necked portion of the elongated sample. The distances between five pairs of points were measured. The sample was then "reset" by heating to 100 °C for 5 min., after which the distance between the same five pairs of points was again measured. $\lambda_m$ is the ratio of the elongated distance to the reset distance for a given pair of points. An average of all points measured for a given sample was used for the values reported herein.

$$\lambda_m = d_2 / d_1$$
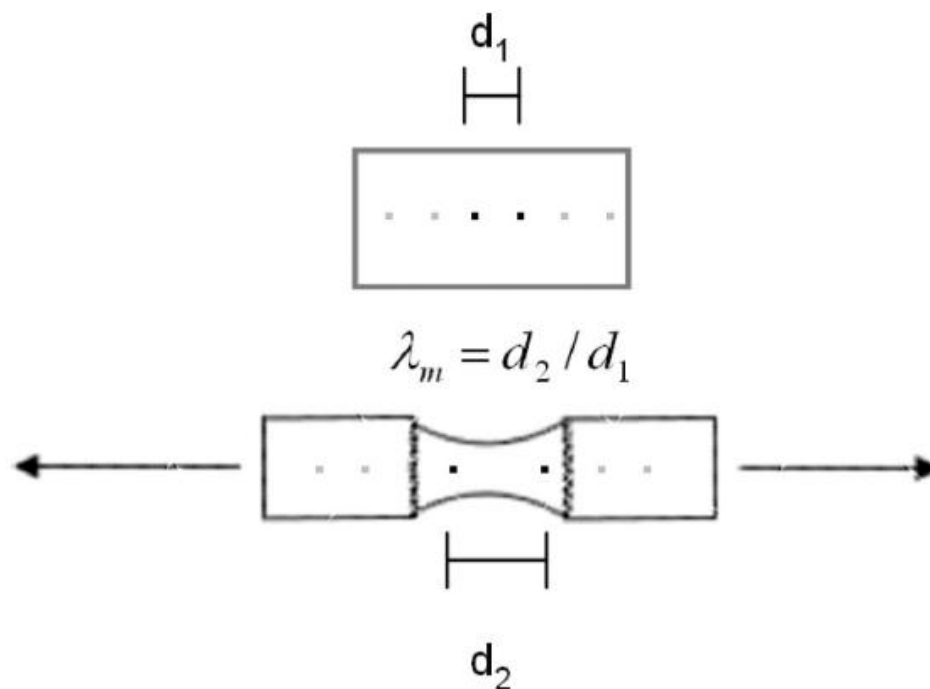
Figure 4-8. Schematic of "ink dot" technique for measurement of the mesoscopic draw ratio ($\lambda_m$), given by the ratio of the distance between ink dots on the surface of the sample after and before deformation, respectively.

Samples were stretched in the Q800 DMA, allowed to relax for 1 h, and then removed from the clamps at room temperature (22 °C). The residual stress in the sample was negligible after 1 h, allowing samples to be removed from the clamps and observed in the microscope immediately after stretching without any observable relaxation of the neck. Samples were characterized via orthoscopic observation between crossed polarizers in an Olympus BX51 microscope with UMPlanFL 5× objective. Images were recorded between crossed polarizers using an Olympus DP25 Color Digital Camera.

**4.3.2 Results**

*Strain Rate Variation*

The MCLCE studied has $T_g$ of about 8 °C, and the $T_{si}$ occurs near 95 °C. Under uniaxial tension, the MCLCE proceeds through three distinct regions of stress-strain behavior (Fig. 4-9).[153] Region I (deformation of the polydomain) is characterized by the increase of the nominal stress ($\sigma_n$) until yielding/necking is observed. Region II involves the growth of the necked region, at the expense of the polydomain regions, producing either a local minimum or a plateau in the $\sigma_n$ versus strain curve. The necked region was previously determined to be a monodomain via XRD.[153] Finally, Region III is characterized by a strong upturn in $\sigma_n$, which is observed at overall draw ratios ($\lambda$) above 4.0 for this particular elastomer.
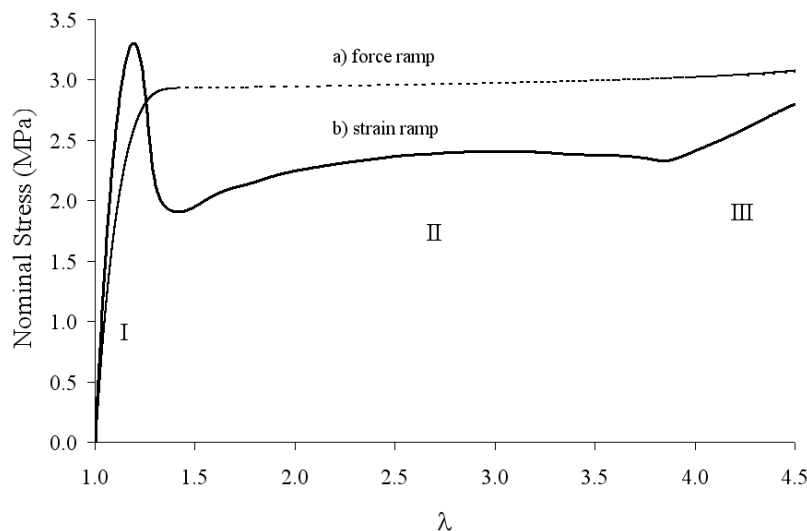


Figure 4-9. The result of uniaxial elongation on our LCE samples using (a.) increasing stress and (b.) increasing strain. Region I is the initial increase in stress with strain, up to the yield point in (b.), while Region II includes the subsequent minimum and slow increase in stress over a wide range of strain.

Fig. 4-10 shows stress versus strain curves for the MCLCE obtained at extensional strain rates ($\dot{\varepsilon}$) ranging from $1.67\times10^{-5}$ s$^{-1}$ to $8.33\times10^{-3}$ s$^{-1}$, for uniaxial elongation to a final $\lambda$ of 2.5 at 35 °C. (Note that values of $\dot{\varepsilon}$ quoted are overall or nominal strain rates, and significant local variations in $\dot{\varepsilon}$ occur once necking begins.) The Young's modulus (E) of the network in the polydomain state ($\lambda<1.17$, Region I) is essentially independent of $\dot{\varepsilon}$ (Fig. 4-11). Within the range

of $\dot{\varepsilon}$ values examined, the polydomain MCLCE behaves like a stiff rubber at low strains, and any elongation to $\lambda<1.17$ is recovered completely upon release of the tension.
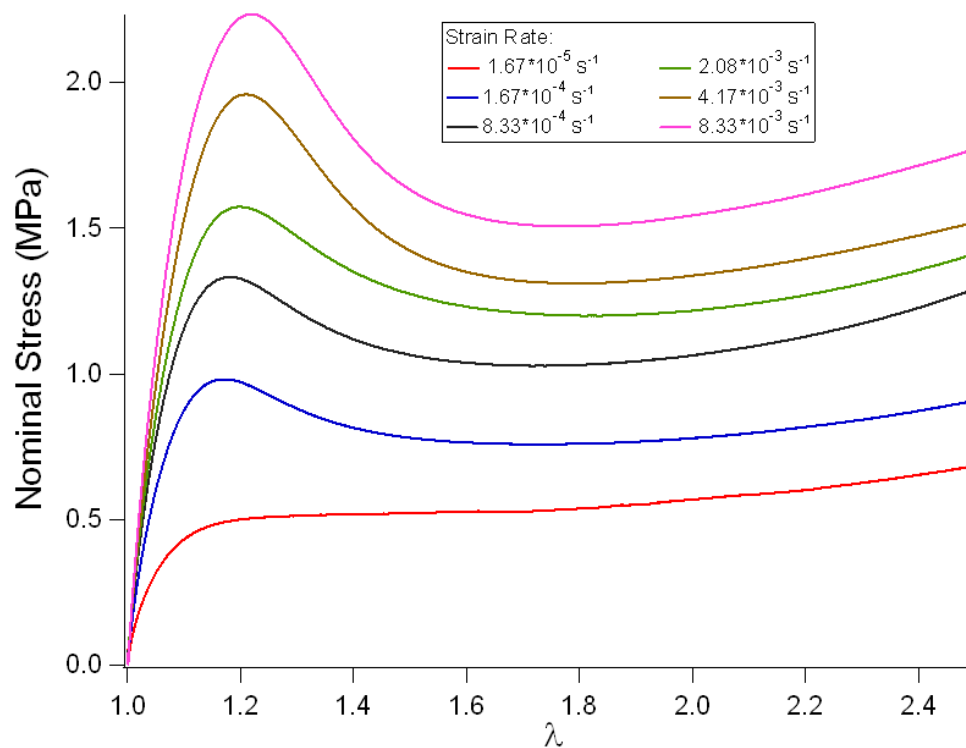


Figure 4-10. Dependence of nominal stress on macroscopic draw ratio for smectic LCE at different strain rates (35 °C).
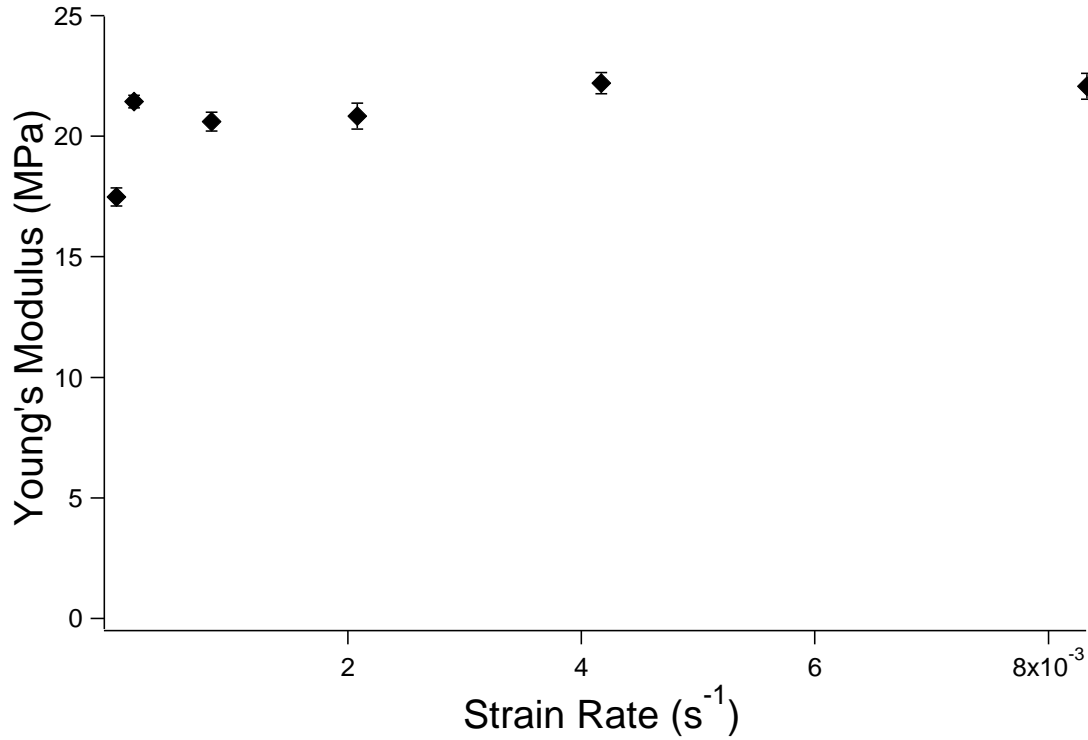
Figure 4-11. Young's modulus (Region I, polydomain state) determined at different strain rates (35 °C). Error bars represent the standard error of the slope from a linear least squares fit to the data at 1.0<λ<1.04.

At 35 °C, a yield stress ($\sigma_y$) is observed for $\dot{\varepsilon}$ greater than or equal to about $1.67 \times 10^{-4}$ s$^{-1}$. The nominal stress sometimes drops to a local minimum value ($\sigma_N$) after yielding. However, for the lowest value of $\dot{\varepsilon}$ studied ($1.67 \times 10^{-5}$ s$^{-1}$), $\sigma_n$ increases continually with strain, with only a decrease in slope noted above λ=1.17. For simplicity, $\sigma_y$ was taken to be approximately equal to the maximum value of $\sigma_n$ at the yield point (though it is more accurate to apply the Considére construction,[241] true stress and strain cannot here be measured reliably). Fig. 4-12 compares $\sigma_y$ to $\sigma_N$, determined as the lowest nominal stress observed after yielding. $\sigma_N$ is undefined for the lowest strain rate tested. The ratio ($\sigma_y/\sigma_N$) increases steadily as $\dot{\varepsilon}$ increases, reaching a value of about 1.5 at the highest $\dot{\varepsilon}$ tested. The drop in $\sigma_n$ after yielding most likely results from geometrical effects due to contraction at the neck boundaries, though it is possible that viscous heating at the neck may also contribute to the drop in the nominal stress.[242]
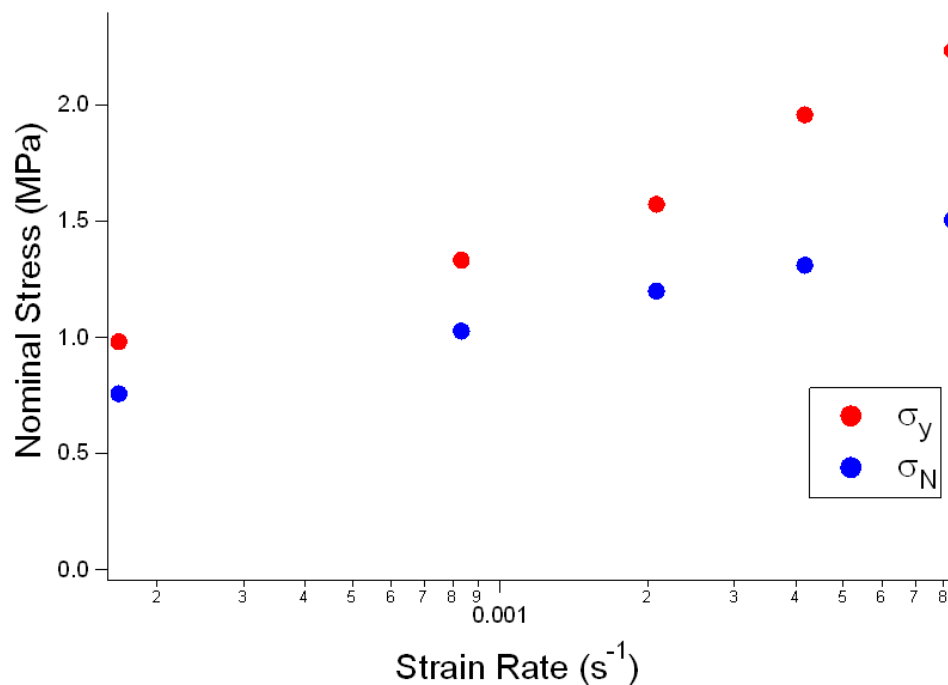
Figure 4-12. Yield stress and necking stress for different strain rates (35 °C).

Though $\sigma_y$ depends upon $\dot{\varepsilon}$, the critical draw ratio for yielding ($\lambda_c$=1.17±0.03) was essentially independent of $\dot{\varepsilon}$ (Fig. 4-13) over the range of $\dot{\varepsilon}$ studied. It is possible that a different value of $\lambda_c$ might be observed at very high strain rates beyond those accessible with our instrumentation, however. The local or mesoscopic draw ratio ($\lambda_m$) was measured within the necked portion of the sample after stretching to $\lambda$=2.5 at 35 °C. A value of $\lambda_m \approx 2.7$ was observed within the necked portion (Fig. 4-14), independent of $\dot{\varepsilon}$. No significant difference in $\lambda_m$ within the neck was observed between runs at both 35 °C and 55 °C (Fig. 4-14), but $\lambda_m$ within the neck does depend on the overall draw ratio ($\lambda$), as values of $\lambda_m$ up to 5.0 can be observed after stretching the MCLCE to higher $\lambda$.[153]
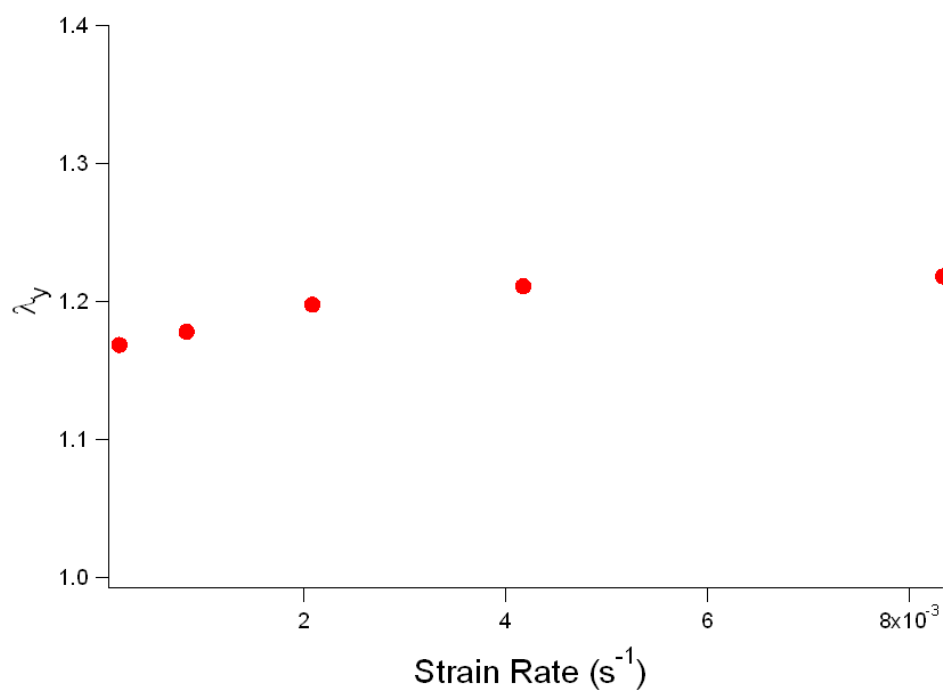
Figure 4-13.  Yield strain at different strain rates (35 °C).
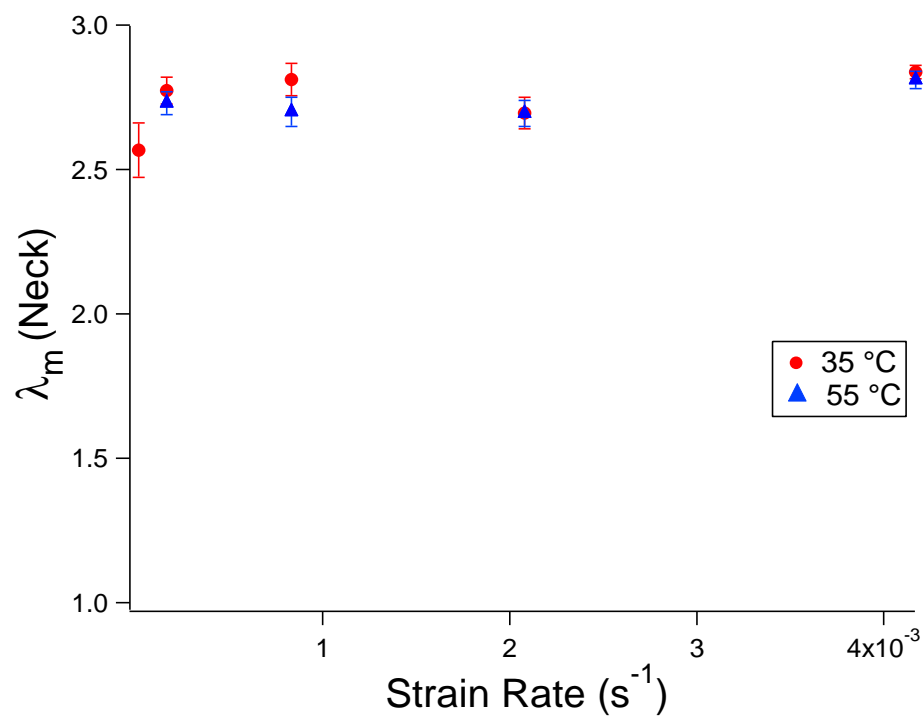


Figure 4-14.  Measured mesoscopic draw ratios ($\lambda_m$) in the center of the necked region after elongation to $\lambda=2.5$ at different strain rates and temperatures.  Values are averages based on five measurements, and error bars represent one standard deviation.

*Temperature Variation*

Additional elongation experiments were conducted at temperatures between $T_g$ and $T_{si}$ at $\dot{\varepsilon} = 2.08 \cdot 10^{-3}$ s$^{-1}$.   Fig. 4-15 shows the mechanical response of the MCLCE at different temperatures, and Fig. 4-16 illustrates the values of $\sigma_y$ and $\sigma_N$ observed as a function of T.  The effects of increasing T at constant $\dot{\varepsilon}$ are qualitatively similar to the effects of decreasing $\dot{\varepsilon}$ at constant T, in that $\sigma_N$ approaches $\sigma_y$ (compare Figs. 4-12 and 4-16).  Fig. 4-17 shows the Young's moduli (E) determined from the slope of the stress-strain curves at low strain.  A decrease in E is observed in the polydomain state as temperature increases, in contrast to the behavior of conventional (amorphous) elastomers above $T_g$, which stiffen as temperature increases.[243]  The Young's modulus of the smectic MCLCE is not set by the free energy cost for elongating elastic chains, as in an unordered rubbery network.  Rather, the modulus is significantly enhanced by the resistance of the polydomain microstructure to deformation at relatively low temperatures, due to the elastic free energy cost associated with disrupting smectic ordering by rotation, elongation, and other deformations of domains.  As T increases toward $T_{si}$, the energy cost for deforming the polydomain structure appears to lessen significantly.
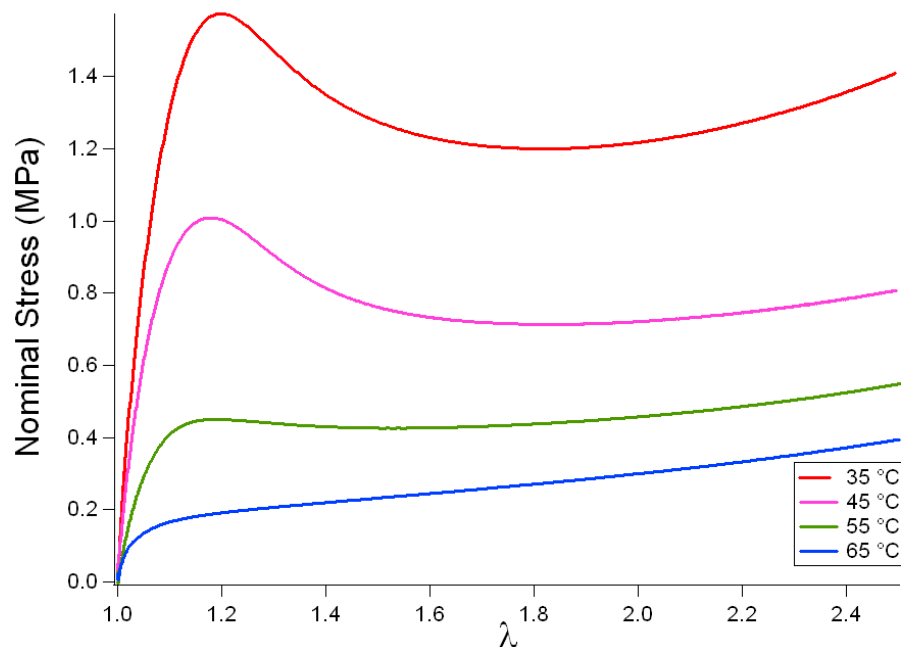


Figure 4-15.  Dependence of nominal stress on macroscopic draw ratio at different temperatures for smectic LCE.   All data were acquired with $\dot{\varepsilon} = 2.08 \cdot 10^{-3}$ s$^{-1}$.
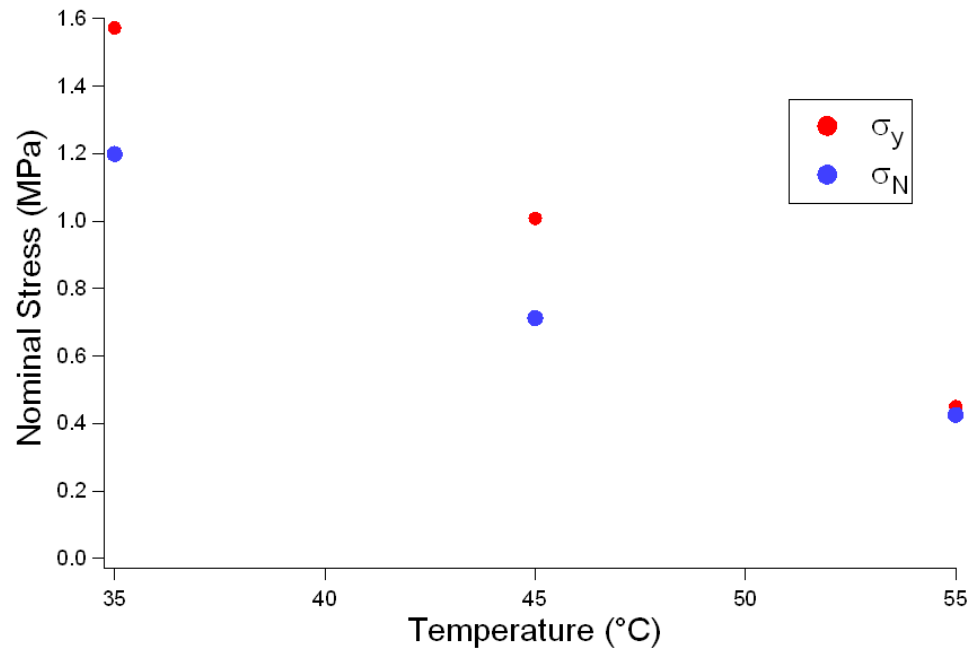
Figure 4-16.  Yield stress and necking stress at different temperatures ($\dot{\varepsilon}= 2.08 \cdot 10^{-3}$ s$^{-1}$).
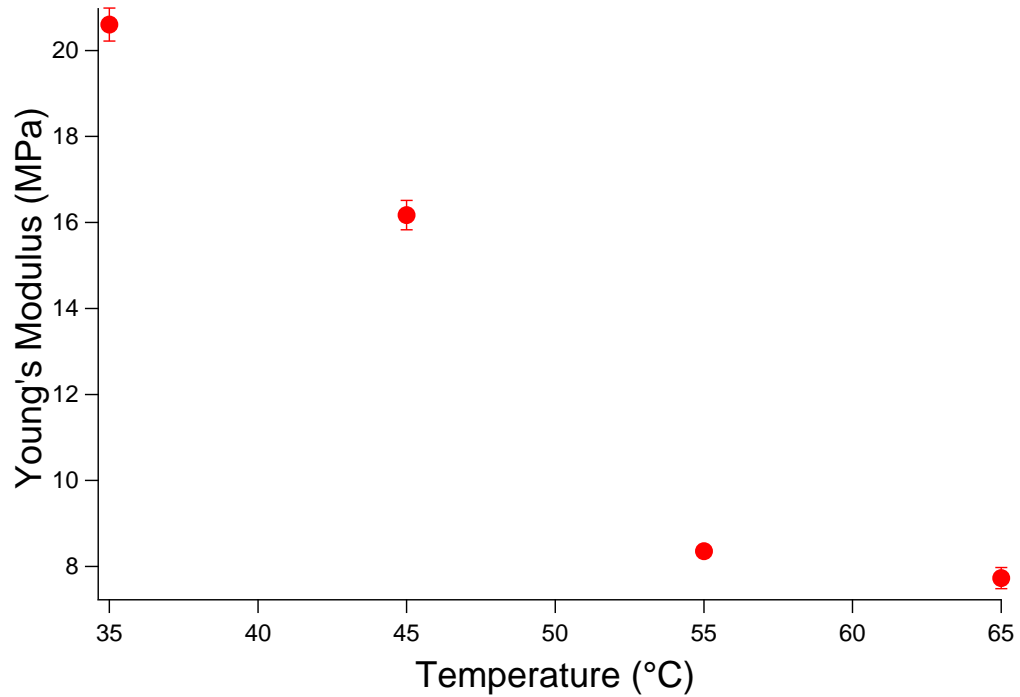


Figure 4-17.  Dependence of Young's modulus (Region I, polydomain state) on temperature. Error bars represent the standard error of the slope from a linear least squares fit to the data at $1.0 < \lambda < 1.04$.

At a fixed strain rate of $\dot{\varepsilon} = 2.08 \cdot 10^{-3}$ s$^{-1}$, the critical strain for yielding was again reached at $\lambda_c$=1.17±0.03 at all temperatures examined (Fig. 4-18). Thus, no dependence of $\lambda_c$ on either temperature or strain rate could be discerned for this elastomer. This observation suggests that yielding occurs once the sample can no longer elongate by simple rotations of the director within smectic microdomains. At low strains, local director rotations allow anisotropically shaped smectic microdomains to align with the axis of elongation. Once most of the domains are aligned, this mechanism of strain accommodation is depleted, and yielding occurs. Fast director rotations in the polydomain state may account for the constant value of $\lambda_c$ observed in this sample. Prior to yielding, if local director rotations are relatively fast compared to the overall time scale of the deformation, then no dependence of $\lambda_c$ on $\dot{\varepsilon}$ would be expected. The polydomain sample would appear to respond essentially instantaneously to the applied load by elongating through local director rotations, until further rotations become energetically unfavorable. If so, then it is possible that lower values of $\lambda_c$ may be observed at very high rates of deformation beyond those accessible to our instrumentation.
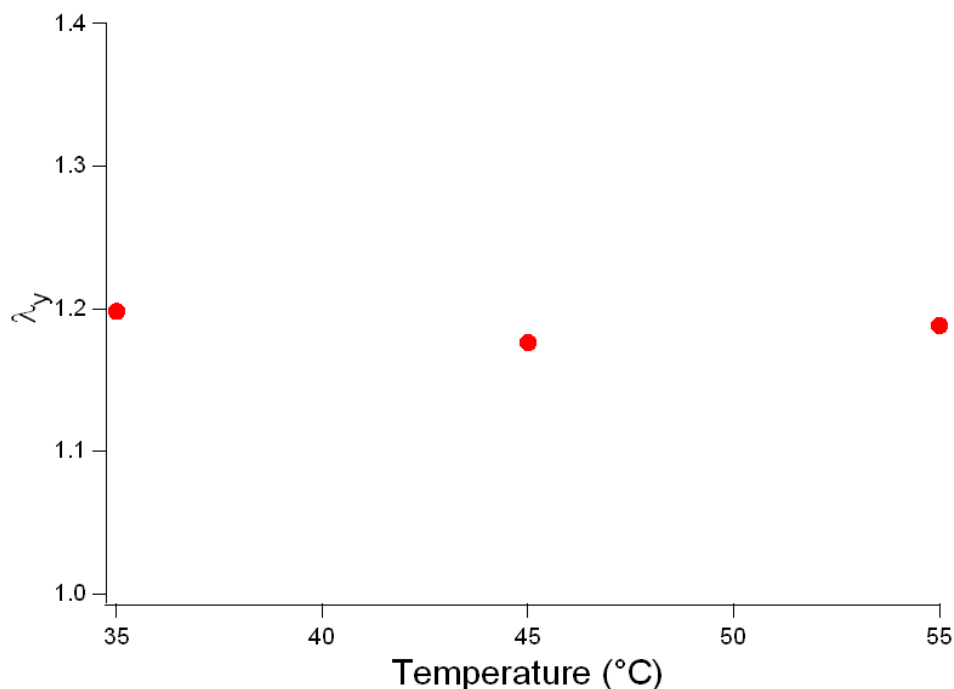


Figure 4-18. Yield strain determined at different temperatures ($\dot{\varepsilon}$= 2.08·10$^{-3}$ s$^{-1}$).

*Interpretation*

The appearance of the necking transition is dependent upon both T and $\dot{\varepsilon}$. Fig. 4-19 shows the appearance of the neck after drawing to $\lambda=1.35$ at different T and $\dot{\varepsilon}$, as observed in a light microscope between partially crossed polarizers. At $\dot{\varepsilon}=2.08\times10^{-3}$ s$^{-1}$ and T slightly above T$_g$, a sharply defined boundary between polydomain and monodomain regions is observed (Fig. 4-19a). If $\dot{\varepsilon}$ is reduced substantially (Fig. 4-19c) or T is increased much above T$_g$ (Fig. 4-19b), the necking instability becomes less localized, occurring gradually over a larger portion of the sample's length. Although the contraction is more difficult to observe with the unaided eye, the elongation is still quite inhomogeneous, judging by the birefringence isochromatics in Fig. 4-19. The geometry of the neck may depend on the rate of stress relaxation in the material, with slow stress relaxation favoring the formation of a more localized, sharply-defined neck. By comparison of the optical micrographs to the results in Figs. 4-12 and 4-16, formation of a localized neck results in $\sigma_N/\sigma_y <1.0$. The drop in the nominal stress from $\sigma_y$ to $\sigma_N$ after necking begins is likely attributed to the sudden reduction in cross-sectional area.

Necking was more clearly defined at temperatures slightly above T$_g$ and at comparatively high elongation rate. The less localized neck observed at temperatures approaching the smectic-isotropic clearing transition may explain why necking was not always reported in previous studies of polydomain smectic MCLCE. The necking process involves the breakdown of the original polydomain structure in a localized fashion, which is followed by cold-drawing or propagation of the neck. Neck formation may be favored under conditions where stress relaxation is slow compared to the rate of deformation. Despite the differences in neck geometry observed under different conditions, it is interesting that the neck appeared at approximately the same value of $\lambda$ at all temperatures and elongation rates studied, and the mesoscopic draw ratio within the neck was essentially constant given a fixed final overall strain. The neck geometry appears to have little influence on the final strain within the neck.
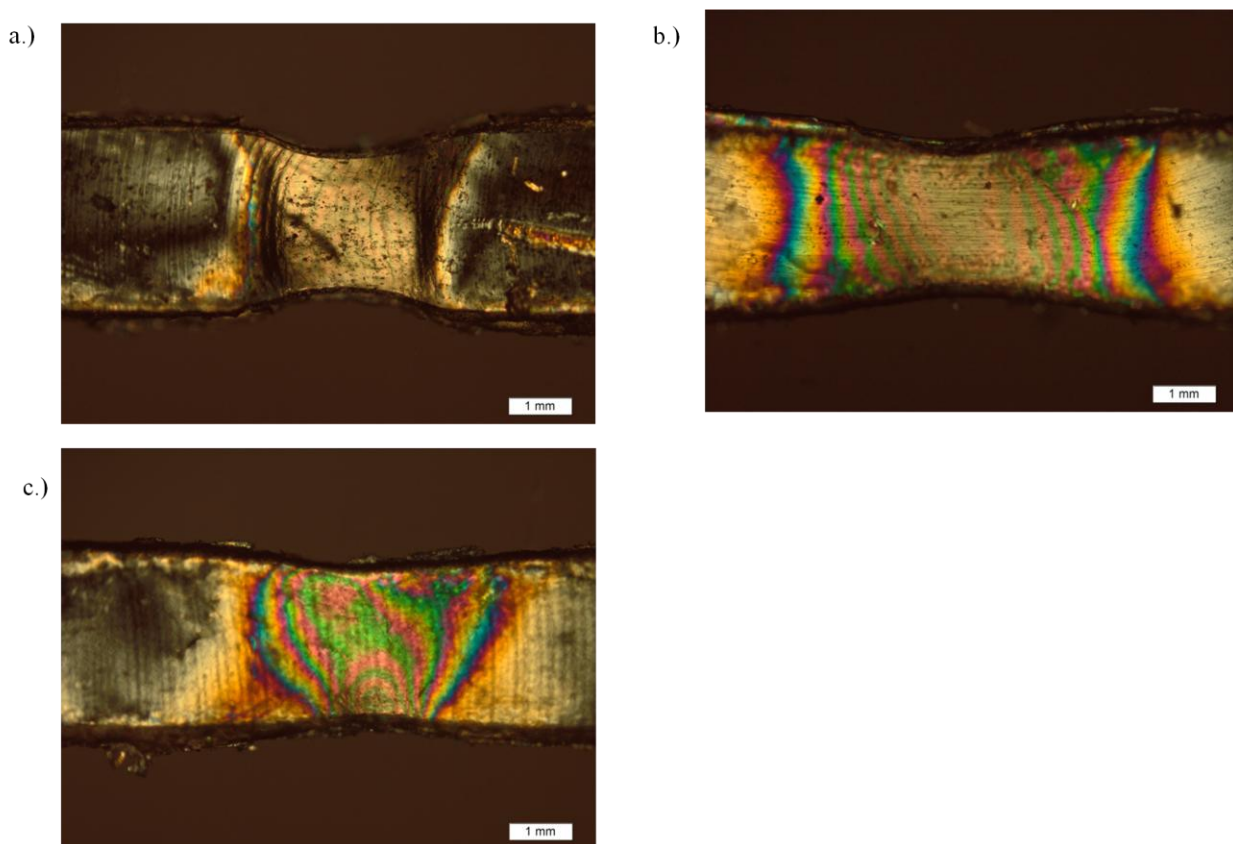
Figure 4-19. Polarized optical microscopy images of the MCLCE sample after elongation to $\lambda = 1.35$ at (a.) $\dot{\varepsilon}=2.08\times10^{-3}$ s$^{-1}$ at 30 °C, (b.) $\dot{\varepsilon}=2.08\times10^{-3}$ s$^{-1}$ at 65 °C, and (c.) $\dot{\varepsilon}=1.67\times10^{-6}$ s$^{-1}$ at 30 °C. (Images taken by Dr. Huipeng Chen at Texas Tech University)

## 4.4 Infusion Attempts with Liquid Crystalline Elastomers

With the success of the nanoinfusion processing of TPU elastomers along with the synthetic and mechanical investigation of our smectic MCLCE samples, it was a logical step to interrogate the possibility of using AURA to introduce nanofillers to the LCEs. In situ synthesis of gold nanoparticles within an LCE sample could, for instance, have applications as a non-linear optical material due to the lack of restoring force observed once the LCE is stretched into Region II. By elongation of the LCE with gold nanoparticles present, an anisotropic distribution of the nanoparticles would be produced that could be reverted to the original isotropic distribution via heating the sample to 100 °C for several minutes.

Gold nanocomposites with various liquid crystal moieties have been previously demonstrated. The synthesis of gold nanoplates of controlled shape has been reported using the

synthesis of lyotropic liquid crystals in aqueous solutions of $HAuCl_4$.[27] The lamellar structure of the liquid crystal restricts the growth of the plates, with variability in nanoplate size found when reaction conditions were varied. Gold nanoparticles coated with discotic liquid crystals have been dispersed in a matrix of similar LCs.[244,245] The resulting material combines the self-assembling properties of a discotic LC, unperturbed by the presence of the gold nanoparticles, with enhanced electrical conductivity. Similar ordering with liquid crystals has been attempted with other LC systems.[246] Precedent is also found for the benefits of nanoparticle synthesis within a polymer network. Batra et al. have demonstrated a polymer gel which, when deswollen, contains chains of gold nanoparticles within the lamellar structure of the polymer.[58] Upon swelling with ethanol, the particles are found to separate into isolated particles. In another study, it was noted that, following uniaxial elongation, nanocomposites of gold and PVA exhibited dichroic behavoir.[29]

Another possibility for an infusable substance is a dichroic dye. Dichroic dyes are long rod-like compounds that are optically active and possess the property of absorbing plane polarized light more along one molecular axis than the other.[187] A great deal of attention has been given to the so-called guest-host effect, which refers to the tendency of the dichroic dye to align itself with the molecular orientation of the matrix into which it is introduced.[186] When dichroic dyes are dissolved in liquid crystalline media, they line up their long axis preferentially with the liquid crystalline director.[185] Dichroic dyes have been added to liquid crystalline matrices for a variety of reasons, including studying the electronic spectra of the dyes and studying the interactions of the guest and host molecules.[184,185] Dichroic dyes are used in liquid crystal displays, both passive and active, to improve color contrast, brightness, and viewing angles.[184,185] A wide variety of dichroic dyes have been used with liquid crystals, such as derivatives of 4-amino-(N-ethylnaphthalimide), or azo dyes that have a cylindrical shape.[184,185] Disperse red 1 and disperse yellow 7 have both been used to probe the orientational order of the mesogen layers in smectic A liquid crystals that do not exhibit a layer contraction when going through the smectic A to smectic C transition (which normally involves such a change of dimension, due to the change in thickness as the angle of the mesogens relative to the layers changes from perpendicular to oblique).[247] Disperse red 1 is also a useful dichroic dye in that the hydroxyl group on one end can serve as a hydrogen bond donor for applications where hydrogen bonding to the liquid crystal may be useful, as in some liquid crystalline displays.[187]

Azo dyes are generally found in the more stable trans conformation at ambient temperatures, giving them a largely linear structure. However, the molecules can be induced to a

cis conformation via thermal or photochemical means.[248] This cis-trans isomerization is reversible[248] and has potential applications, such as in optical storage due to the reversible, photoinduced dichroism and birefringence of the dye molecules.[249] Information can be "written" by applying plane polarized irradiation and "erased" by applying circularly polarized light or heating the polymer matrix above its glass transition temperature.[250] Disperse red 1 (DR1), for instance, has been investigated in polymer matrices for this purpose, largely due to its familiarity in the literature as a dye with a well-known cis-trans isomerization behavior.[248,251,252] Generally, polymer films containing DR1 are cast from solution. Though these investigations have utilized non-covalently bound dyes, the bonding of the dye to the polymer matrix has been shown to produce a larger reversible effect.[251,252]

Camacho-Lopez et al. introduced a dichroic dye to a nematic side chain LCE via solution.[253] The LCE was soaked in a toluene solution of disperse orange 1, an azo dye. The dye was infused into the LCE, where it aligned with the nematic director. By illuminating the dye-infused samples with 514 nm irradiation from an $Ar^+$ ion laser, the samples were found to rapidly bend at angles greater than 45°. The bending is caused by a contraction along the nematic director, which is likely due to some combination of laser heating and the reduction of orientational ordering due to photoisomerization of the dichroic dye.[253] Beyond the bending, the paper also demonstrated that, when floated on water, the bending of the dye-infused sample could be leveraged to make the sample "swim" away from the laser irradiation.

## 4.4.1 Gold Nanoparticles in Smectic MCLCEs

Gold infusion was attempted using both the chemical reduction and the IPN method. The chemical reduction method was unsuccessful, but the IPN method succeeded in creating colored samples concomitant with the TPU samples previously tested. Samples were immersed in a solution of 1 % w/w Irgacure® 651 and DEAMA for 20 min. at room temperature, polymerized with the Dymax® Lightwelder® PC-2, and soaked in a 0.007 M $HAuCl_4$ AURA solution for 5 min. at 60 °C. The observed color was only visible in the stretched LCE samples, while the unstretched LCE samples appeared to be solidly gold-plated. Only upon inspection in a microscope was it apparent that a large number of small islands of gold plating were causing this appearance (Fig. 4-20). In the microscope, the purple color associated with the surface plasmon resonance of the gold nanoparticles is plainly apparent in the unstretched sample. Once

elongated, the islands of gold plating were moved sufficiently far from one another to allow the color of the nanoparticles in the LCE to be observed by the unaided eye. Wide angle x-ray diffraction (WAXD) was also employed in an attempt to observe any ordering or periodicity of the gold nanoparticles along the stretching direction in a uniaxially deformed sample. The sample was deformed at 5 %/min. up to 150 % strain on the TA Q800 DMA and WAXD was done using a Rigaku DMAX-Rapid Microdiffractometer with a copper tube. The observed scattering (Fig. 4-21) was no different than that seen for the same LCE without gold particles present. It appears that the current processing conditions and elongation protocol does not produce any unique features in the distribution of the gold nanoparticles. Further, it is possible that the gold nanoparticle concentration is too low within the sample to produce a strong pattern, particularly in light of the plating out of the gold on the sample surface.
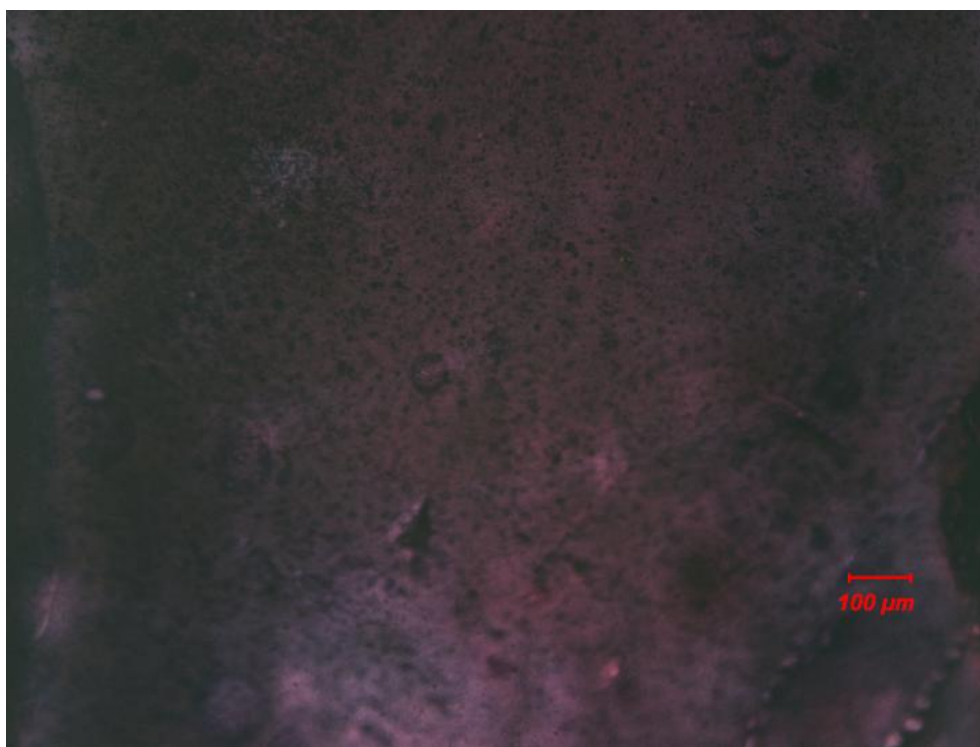


Figure 4-20. Optical microscopy image of IPN-reduced nanoparticles within the smectic MCLCE sample. Although the sample appears gold-plated to the unaided eye, the color associated with the surface plasmon resonance of the gold nanoparticles is clear in this image. The small black dots are islands of gold plating on the sample surface, which result in the macroscopically-viewed metallic appearance.
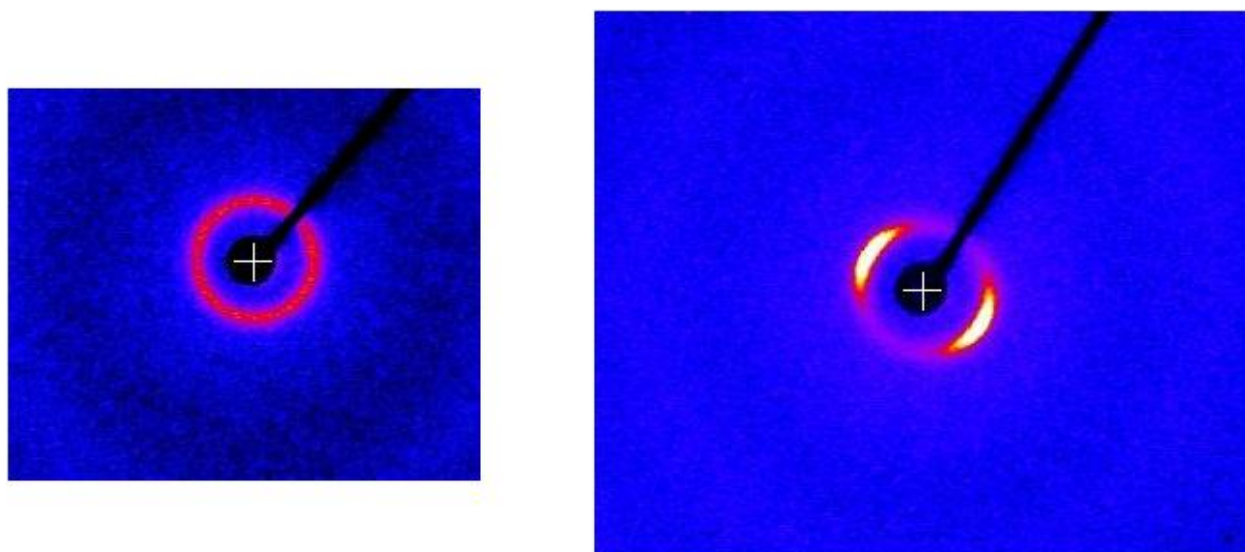
Figure 4-21.  WAXD of IPN-reduced gold nanoparticles in MCLCE before (left) and after (right) stretching to 150 % strain at 5 %/min. using the DMA.

### 4.4.2 Dichroic Dye Infusions

Two dichroic dyes were tested using AURA infusion with the LCE samples.  Disperse red 1 (DR1) and disperse yellow 7 (DY7) were infused from a solution of $5.0 \cdot 10^{-4}$ M dye at 60 °C for 20 minutes (Fig. 4-22).  Both infusions were successful (Fig. 4-23), and the red dye was chosen to move forward with characterization due to the difficulty of seeing the difference between the innate LCE color and the yellow dye.  In order to investigate the dichroic nature of the infused dyes, attenuated total reflectance Fourier transform infrared spectroscopy (ATR-FTIR) and ultraviolet-visible spectroscopy (UV-vis) were performed.  ATR-FTIR was done on a Bruker IFS 66/S FTIR spectrometer with a Pike VeeMax II variable angle attenuated total reflectance accessory.   UV-vis was done with a Perkin-Elmer Lambda 950 UV-vis-NIR spectrophotometer.
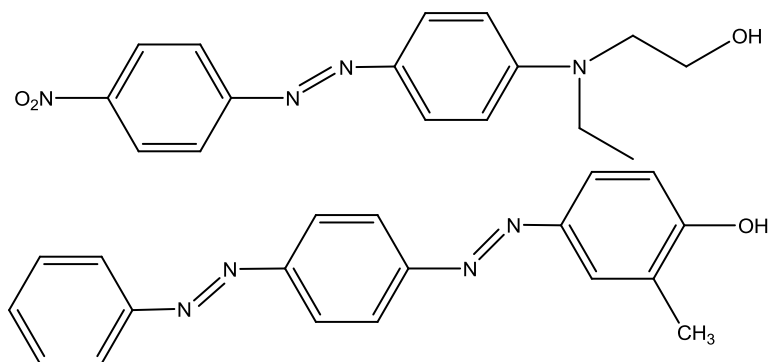
Figure 4-22.  Chemical structure of disperse red 1 (top) and disperse yellow 7 (bottom).



Figure 4-23.  LCE infused at various conditions with dichroic dyes.  Left to right:  unaltered LCE sample;  LCE infused with 0.010 M DR1 for 2 hours at 60 °C; LCE sample infused with 0.010 M DR1 for 2 min. at 60 °C, and stretched by hand to approximately 200 % strain; LCE sample infused with 0.00050 M DY7 for 20 min. at 60 °C.

ATR-FTIR measurements were found to require a high concentration of dye within the LCE.  As such, a two hour infusion of the LCE in a 0.010 M DR1 AURA solution at 60 °C was used to produce a deep red color (Fig. 4-23, second from left).  Samples were uniaxial elongated by hand using a metal stretching apparatus to approximately 200 % strain.  Spectra were taken on stretched and unstretched samples of both dyed and undyed LCEs.  In order to try to observe the dichroic behavior of the dye, spectra were taken with the beam parallel, perpendicular, and at 45 ° angles to the stretching direction (Fig. 4-24).  The presence of DR1 within the dyed sample was identifiable compared to the undyed samples, particularly in the symmetric stretch of the $-NO_2$ group of DR1.  This peak was seen in the bulk dye at ~1338 cm$^{-1}$ and resulted in a slight increase of the reflectance of the dyed sample over the control.  It appears that the dye does align along the stretching direction of the sample, due to the larger increase in reflectance for the sample stretched perpendicular to the beam than parallel to the beam, with the 45 ° sample demonstrating an intermediate value.  This result seems counter-intuitive, but the symmetric stretch of the $-NO_2$ group is perpendicular to the long dimension of the rod-like DR1

dye, resulting in its strong presence when the stretching direction is perpendicular to the beam. In this case, the symmetric stretch is actually parallel to the beam.
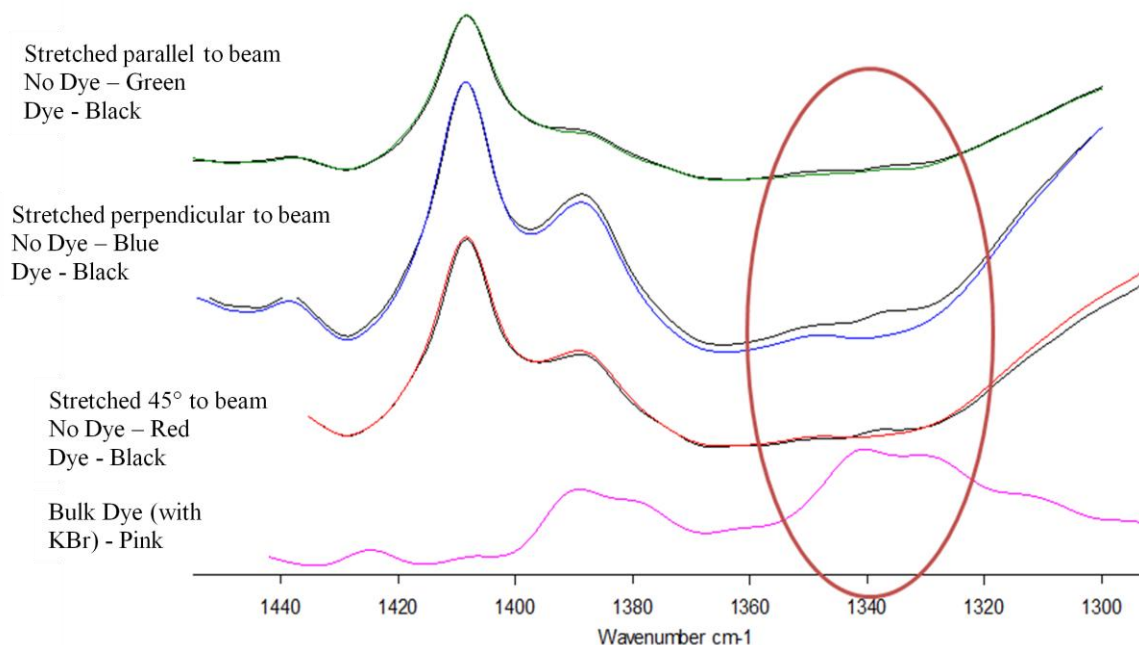


Figure 4-24. ATR-FTIR of smectic MCLCE sample containing a high concentration of DR1 dye. The y axis is reflectance in arbitrary units. Orientation of stretching direction relative to the beam direction is indicated at left. The circled area indicates the symmetric stretch of the -NO$_2$ group of DR1.

In spite of the evidence of the dye's alignment with the stretching direction and confirmation of its dichroism, there are definite caveats to these measurements. The difference in the peaks of the dyed and control samples at the symmetric –NO$_2$ stretch are negligible, and noise is apparent in the data. Further, the asymmetric –NO$_2$ stretch, which should be at approximately 1514 cm$^{-1}$, is not discernable due to the polymer's own spectra in this region. The lack of a clear spectra of the assymmetric stretch presents a major challenge to quantitative measurements of the DR1 dichroism, as a ratio of the symmetric and asymmetric stretches is needed for a dichroic ratio analysis. As a result of these problems, UV-vis was investigated as an alternative characterization technique.

Contrary to the ATR-FTIR, UV-vis was found to require a low concentration of the dye within the LCE. A 2 min. infusion from a 0.010 M DR1 AURA solution at 60 °C was used to produce samples (Fig. 4-23, third from left). Samples were again stretched by hand to 200 % strain, and tests were performed on stretched and unstretched, dyed and undyed samples. In spite

of its relative ease compared to the ATR-FTIR measurements and the low concentration of dye in the samples, the results clearly show the dichroic behavior in a quantifiable fashion (Fig. 4-25). With the stretching direction both parallel and perpendicular to the beam polarization but no dye in the sample, no absorbance was observed. The absorbance was identical for an unstretched dyed sample with no beam polarization, for unstretched dyed samples with parallel beam polarization, and for unstretched dyed samples with perpendicular beam polarization. Finally, a repeatable difference was found between stretched and dyed samples interrogated with beam polarization parallel to the elongation direction and perpendicular to the elongation direction. An absorbance approximately two times higher is seen in the parallel direction than in the perpendicular, again indicating alignment of the dye with the stretching direction. An unusual feature of the parallel beam polarization absorbance for the stretched samples is a shoulder on the absorbance peak at ~460 nm. A blue-shift of the UV-vis absorption of DR1 has been noted in cases where the molecules aggregate in an anti-parallel fashion, such that the dipole moment influences the optical response of neighboring dye molecules.[249] Thus, this shoulder may be due to aggregation of the dye molecules into aligned bundles once they are oriented along the stretching direction of the sample.
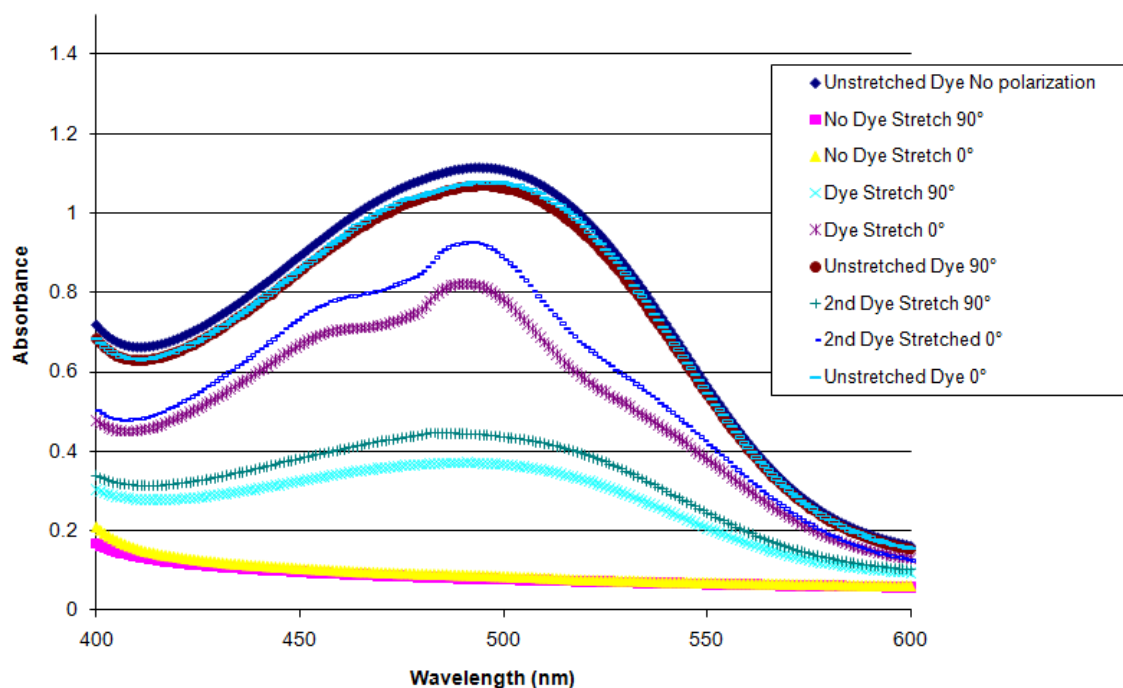


Figure 4-25. UV-vis data of smectic MCLCE sample containing DR1, both stretched and unstretched, as well as an unmodified LCE sample.

# Chapter 5

# Conclusions and Suggested Future Work

Two infusion-based methods for producing polymer/metal nanocomposites have been considered. In spite of their different reduction methods, each synthesis scheme hinges on the introduction of a metal precursor salt to a polymer article via a plasticizing solution, with subsequent reduction by an agent introduced either before or after the metal salt. Larger, more aggregated particles are produced when reduction is achieved via aqueous solution of triethylamine, while less agglomerated particles of smaller radius can be created using an amine-functionalized interpenetrating network layer as a reducing agent. Each method has some degree of tunability in particle size and distribution based on the infusion times and temperatures of each step. Future work needs to test the in situ reduction of a wider variety of metals, including those already deemed successfully infused. A combinatorial synthetic method has been set forth, along with high throughput characterization via SAXS, which will facilitate the expansion of the infusion/reduction methods to other metals, as well as help understand and leverage the tunability in size and shape control of the particles. Further, gaseous reactants should be considered for use in the synthetic schemes. For instance, a gaseous amine may be able to reduce the infused metal salt following evaporation of the AURA solvent in the chemical reduction method. The polymer matrix, no longer plasticized during reduction, would further restrict particle growth and agglomeration, possibly resulting in smaller, less agglomerated particles more akin to those produced via the IPN reduction method.

The research of our group on the synthesis and characterization of liquid crystalline elastomers has also been furthered. An end-linking synthesis scheme was investigated at length, with improvements made to both the reactions and the purification protocols in order to ensure the purity and predictability of the resulting product. However, despite spectroscopic evidence indicating synthesis of the desired product, the cloudy nature of the produced elastomer samples indicates that further improvements to the precision of the synthesis are needed in order to achieve the desired end-linked networks. Once these improvements are made, deuterated LCE can be produced and subjected to small angle neutron scattering in order to more directly observe the molecular behavior during the polydomain to monodomain transition.

Nonetheless, our understanding of the P-M transition has been improved via the mechanical investigation of similar smectic MCLCE samples produced by a known synthetic method. The effect of temperature and strain rate on the necking behavior of these samples demonstrates that there is a relationship between the time scale required for the polydomain sample to transition to a monodomain within the neck. Fast director rotations may account for the observed constant critical yield strain, while the subsequent neck formation is caused by the necessity of other mechanisms to accommodate the strain beyond this point. High temperatures and low strain rates produced no distinct neck, while a clear necking instability was observed at lower temperatures and higher strain rates. Further research is needed to clarify these insights. Stress relaxation experiments would provide clearer detail of this time scale, allowing for a more accurate picture of the molecular behavior to be produced. Characterization was done on only one elastomer variety. Future work needs to investigate the mechanical behavior of samples of variable cross-link density and different thermal histories in order to gain further insight into the molecular basis for the observed necking instability.

Finally, AURA infusion was tested with LCE samples using both gold nanoparticle and dichroic dyes. In order for metal infusions into LCE samples to be useful, synthetic schemes must be determined which do not result in plating out of the metal on the sample surface. A new LCE chemistry, with better solubility of the metal salt within the LCE, may be necessary in order to accomplish this goal. Dichroic dye infusions, though found to be quite successful, have yet to produce any novel results. The reversible isomerization of the dyes should be tested in order to determine if the samples are viable for any applications such as actuation, which has been previously demonstrated in a similar system.[253]

Putting together some of these ideas, a logical next step is the investigation of an LCE that will allow for infusions of metal nanoparticles. A key requirement of a new LCE chemistry is the solubility of several common metal precursor salts within the sample. Introduction of DEAMA directly into the polymer is one possibility, as the metal salts tested herein are known to be soluble in it, and its use presents the potential for auto-reduction of the metal salt by the LCE. The DEAMA could be incorporated as a side chain unit, pendant to the flexible siloxane portion of the polymer. A platinum-catalyzed reaction, similar to that described by Finkelmann et al., would be used to bond the DEAMA to a methyl group of the siloxane.[139] Appropriate reaction stoichiometry would have to be investigated in order to ensure metal salt solubility while retaining the liquid crystalline nature of the material. This latter point is of particular importance,

and full characterization of the liquid crystalline phases of the new polymer would need to be performed.

Once an appropriate LCE is synthesized, the combinatorial method could be used to investigate the metal infusions and ensure solubility of the metal salts. Two applications of this system are of particular interest. In the first, shape-controlled metal nanoparticles should be attempted. Modification of the method used by Stamplecoskie et al. may allow for such a synthesis to be accomplished within the polymer using discrete wavelengths of light for polymerization.[73] Of particular interest is the synthesis of nanorods, which has been reported for citrate-stabilized silver using Irgacure® 2959 as a reducing agent with 720 nm irradiation.[73] The production of metal nanorods within an LCE would create a material which can be uniaxially deformed to produce an array of aligned nanorods.[32,74] The result would be a material with optically and electrically anisotropic properties that could be turned on and off via stretching and resetting (via mild heating) of the sample.

A second approach would be the tuning of the metal nanoparticle surface plasmon resonance, via use of the combinatorial optimization method to control particle size. The purpose of this approach is to produce an LCE sample which could be exposed to a low power laser at the surface plasmon resonance wavelength of the particles, resulting in a local heating of the elastomer in the vicinity of the exposed nanoparticles. If the sample were stretched beyond the P-M transition prior to illumination and not cross-linked as a monodomain, the local heating would melt the smectic phase, "resetting" that region and resulting in internal stresses and deformation of the sample. This deformation may lead to actuation similar to that observed by Camacho-Lopez et al. using dichroic dyes.[253] Should this approach be successful, the potential also exists to use multiple sizes or elements of metal nanoparticles within one sample in order to produce a sample that deforms in different ways based on the wavelength of the incident laser. For instance, a gradient in one dimension in metal salt soak time may produce particles of a very different average size at one end of the sample than the other. A laser of one wavelength would produce a strong deformation at one end of the sample, while a different wavelength laser would produce a strong deformation at the other end. These possibilities need to be investigated, not only to take full advantage of the flexibility of the nanoinfusion method, but also to make use of the great potential for useful applications that leverage the coupling of LCE order with nanoparticle dispersion.

# References

1.      Pyles RA, Archey RL. U.S. Patent 6,749,646.

2.      Pyles RA, Archey RL. U.S. Patent 6,733,543.

3.      Pyles RA, Archey RL. U.S. Patent 6,949,127.

4.      Pyles RA, Archey RL. U.S. Patent 6,929,666.

5.      Pyles RA, Archey RL. U.S. Patent 7,094,263.

6.      Pyles RA, Archey RL, Derikart DM, Nikolakopolous M. U.S. Patent 6,994,735.

7.      Pyles RA, Archey RL, Derikart DM. U.S. Patent 7,175,675.

8.      Pyles RA, Archey RL, Derikart DM. U.S. Patent 7,504,054.

9.      Crank J .*Mathematics of Diffusion*. London: Oxford University Press, 1956. pp. 41-61.

10.     Krishnamoorti R, Vaia RA. *Journal of Polymer Science Part B-Polymer Physics* 2007;45(24):3252-3256.

11.     Okada A, Usuki A. *Macromolecular Materials and Engineering* 2006;291(12):1449-1476.

12.     Balmer JA, Schmid A, Armes SP. *Journal of Materials Chemistry* 2008;18(47):5722-5730.

13.     Vaia RA, Maguire JF. *Chemistry of Materials* 2007;19(11):2736-2751.

14.     Harrats C, Groeninckx G. *Macromolecular Rapid Communications* 2008;29(1):14-26.

15.     Paul DR, Robeson LM. *Polymer* 2008;49(15):3187-3204.

16.     Darder M, Aranda P, Ruiz-Hitzky E. *Advanced Materials* 2007;19(10):1309-1319.

17.     Hussain SM, Braydich-Stolle LK, Schrand AM, Murdock RC, Yu KO, Mattie DM, Schlager JJ, Terrones M. *Advanced Materials* 2009;21(16):1549-1559.

18.     Ciardelli F, Coiai S, Passaglia E, Pucci A, Ruggeri G. *Polymer International* 2008;57(6):805-836.

19.     Leszczynska A, Njuguna J, Pielichowski K, Banerjee JR. *Thermochimica Acta* 2007;453(2):75-96.

20.     Strawhecker KE, Manias E. *Chemistry of Materials* 2000;12(10):2943-2949.

21. Bredeau S, Peeterbroeck S, Bonduel D, Alexandre M, Dubois P. *Polymer International* 2008;57(4):547-553.

22. Moniruzzaman M, Winey KI. *Macromolecules* 2006;39(16):5194-5205.

23. Jang BZ, Zhamu A. *Journal of Materials Science* 2008;43(15):5092-5101.

24. Link S, El-Sayed MA. *Journal of Physical Chemistry B* 1999;103(40):8410-8426.

25. Lin T, Ho RM, Ho JC. *Macromolecules* 2009;42(3):742-751.

26. Adachi H, Taki K, Nagamine S, Yusa A, Ohshima M. *Journal of Supercritical Fluids* 2009;49(2):265-270.

27. Sun ZW, Chen X, Wang LY, Zhang GD, Jing B. *Colloids and Surfaces A-Physicochemical and Engineering Aspects* 2008;326(1-2):23-28.

28. Abecassis B, Testard F, Spalla O, Barboux P. *Nano Letters* 2007;7(6):1723-1727.

29. Ramesh GV, Porel S, Radhakrishnan TP. *Chemical Society Reviews* 2009;38(9):2646-2656.

30. Hasell T, Lagonigro L, Peacock AC, Yoda S, Brown PD, Sazio PJA, Howdle SM. *Advanced Functional Materials* 2008;18(8):1265-1271.

31. Link S, El-Sayed MA. *Journal of Physical Chemistry B* 1999;103(21):4212-4217.

32. Perez-Juste J, Rodriguez-Gonzalez B, Mulvaney P, Liz-Marzan LM. *Advanced Functional Materials* 2005;15(7):1065-1071.

33. Bhargava SK, Booth JM, Agrawal S, Coloe P, Kar G. *Langmuir* 2005;21(13):5949-5956.

34. Yu J, Liu RYF, Poon B, Nazarenko S, Koloski T, Vargo T, Hiltner A, Baer E. *Journal of Applied Polymer Science* 2004;92(2):749-756.

35. Oates TWH, Christalle E. *Journal of Physical Chemistry C* 2007;111(1):182-187.

36. Huang KC, Ehrman SH. *Langmuir* 2007;23(3):1419-1426.

37. Huber DL. *Small* 2005;1(5):482-501.

38. Grohn F, Bauer BJ, Akpalu YA, Jackson CL, Amis EJ. *Macromolecules* 2000;33(16):6042-6050.

39. Brust M, Walker M, Bethell D, Schiffrin DJ, Whyman R. *Journal of the Chemical Society* 1994;801-802.

40. Newman JDS, Blanchard GJ. *Langmuir* 2006;22(13):5882-5887.

41. Pastoriza-Santos I, Liz-Marzan LM. *Pure and Applied Chemistry* 2000;72(1-2):83-90.

42. Porter LA, Ji D, Westcott SL, Graupe M, Czernuszewicz RS, Halas NJ, Lee TR. *Langmuir* 1998;14(26):7378-7386.

43. Sarathy KV, Raina G, Yadav RT, Kulkarni GU, Rao CNR. *Journal of Physical Chemistry B* 1997;101(48):9876-9880.

44. Leff DV, Ohara PC, Heath JR, Gelbart WM. *Journal of Physical Chemistry* 1995;99(18):7036-7041.

45. Tzhayik O, Sawant P, Efrima S, Kovalev E, Klug JT. *Langmuir* 2002;18(8):3364-3369.

46. Schwartzberg AM, Grant CD, van Buuren T, Zhang JZ. *Journal of Physical Chemistry C* 2007;111(25):8892-8901.

47. Hsu SLC, Wu RT. *Materials Letters* 2007;61(17):3719-3722.

48. Kobayashi Y, Katakami H, Mine E, Nagao D, Konno M, Liz-Marzan LM. *Journal of Colloid and Interface Science* 2005;283(2):392-396.

49. Van Hyning DL, Klemperer WG, Zukoski CF. *Langmuir* 2001;17(11):3128-3135.

50. McGilvray KL, Decan MR, Wang DS, Scaiano JC. *Journal of the American Chemical Society* 2006;128(50):15980-15981.

51. Qi LM, Ma JM, Shen JL. *Journal of Colloid and Interface Science* 1997;186(2):498-500.

52. Guo L, Huang QJ, Li XY, Yang SH. *Physical Chemistry Chemical Physics* 2001;3(9):1661-1665.

53. Chen DH, Hsieh CH. *Journal of Materials Chemistry* 2002;12(8):2412-2415.

54. Saunders AE, Sigman MB, Korgel BA. *Journal of Physical Chemistry B* 2004;108(1):193-199.

55. Hussain F, Hojjati M, Okamoto M, Gorga RE. *Journal of Composite Materials* 2006;40(17):1511-1575.

56. Costanzo PJ, Beyer FL. *Macromolecules* 2007;40(11):3996-4001.

57. Yakimovich NO, Ezhevskii AA, Guseinov DV, Smirnova LA, Gracheva TA, Klychkov KS. *Russian Chemical Bulletin* 2008;57(3):520-523.

58. Batra D, Seifert S, Varela LM, Liu ACY, Firestone MA. *Advanced Functional Materials* 2007;17(8):1279-1287.

59. Porel S, Singh S, Radhakrishnan TP. *Chemical Communications* 2005;(18):2387-2389.

60. Mallick K, Witcomb MJ, Scurrell MS. *Journal of Materials Science* 2004;39(14):4459-4463.

61.    Mallick K, Witcomb MJ, Scurrell MS. *European Physical Journal-Applied Physics* 2005;29(1):45-49.

62.    Tanahashi I, Kanno H. *Applied Physics Letters* 2000;77(21):3358-3360.

63.    Gaddy GA, Mclain JL, Steigerwalt ES, Broughton R, Slaten BL, Mills G. *Journal of Cluster Science* 2001;12(3):457-471.

64.    Sohn BH, Seo BW, Yoo SI. *Journal of Materials Chemistry* 2002;12(6):1730-1734.

65.    Korchev AS, Bozack MJ, Slaten BL, Mills G. *Journal of the American Chemical Society* 2004;126(1):10-11.

66.    Lagonigro L, Peacock AC, Rohrmoser S, Hasell T, Howdle SM, Sazio PJA, Lagoudakis PG. *Applied Physics Letters* 2008;93(26)

67.    Zhang Y, Erkey C. *Journal of Supercritical Fluids* 2006;38(2):252-267.

68.    Rosolovsky J, Boggess RK, Rubira AF, Taylor LT, Stoakley DM, StClair AK. *Journal of Materials Research* 1997;12(11):3127-3133.

69.    Berens AR, Huvard GS, Korsmeyer RW. U.S. Patent 4,820,752.

70.    Sand ML. U.S. Patent 4,598,006.

71.    Zhou Y, Wang CY, Zhu YR, Chen ZY. *Chemistry of Materials* 1999;11(9):2310-+.

72.    Callegari A, Tonti D, Chergui M. *Nano Letters* 2003;3(11):1565-1568.

73.    Stamplecoskie K, Scaiano J. *Journal of the American Chemical Society* 2010;132:1825-1827.

74.    Kaneko K, Sun HB, Duan XM, Kawata S. *Applied Physics Letters* 2003;83(7):1426-1428.

75.    Buffat P, Borel JP. *Physical Review A* 1976;13(6):2287-2298.

76.    Luo WH, Hu WY, Xiao SF. *Journal of Physical Chemistry C* 2008;112(7):2359-2369.

77.    Moon KS, Dong H, Maric R, Pothukuchi S, Hunt A, Li Y, Wong CP. *Journal of Electronic Materials* 2005;34(2):168-175.

78.    Murugaraj P, Mainwaring DE, Chen LG, Sawant P, Al Kobaisi M, Yek WM. *Journal of Applied Polymer Science* 2010;115(2):1054-1061.

79.    Huang XY, Brittain WJ. *Macromolecules* 2001;34(10):3255-3260.

80.    McNally T, Murphy WR, Lew CY, Turner RJ, Brennan GP. *Polymer* 2003;44(9):2761-2772.

81.    Ray SS, Okamoto M. *Progress in Polymer Science* 2003;28(11):1539-1641.

82. Calandra P, Giordano C, Longo A, Liveri VT. *Materials Chemistry and Physics* 2006;98(2-3):494-499.

83. Awad WH, Beyer G, Benderly D, Ijdo WL, Songtipya P, Jimenez-Gasco MD, Manias E, Wilkie CA. *Polymer* 2009;50(8):1857-1867.

84. Turhan Y, Dogan M, Alkan M. *Industrial & Engineering Chemistry Research* 2010;49(4):1503-1513.

85. Mori Y, Furukawa M, Hayashi T, Nakamura K. *Particulate Science and Technology* 2006;24(1):97-103.

86. Nakamura K, Kawabata T, Mori Y. *Powder Technology* 2003;131(2-3):120-128.

87. Radlinski AP, Mastalerz M, Hinde AL, Hainbuchner M, Rauch H, Baron M, Lin JS, Fan L, Thiyagarajan P. *International Journal of Coal Geology* 2004;59(3-4):245-271.

88. Shibayama M, Karino T, Miyazaki S, Okabe S, Takehisa T, Haraguchi K. *Macromolecules* 2005;38(26):10772-10781.

89. Singh PS, Aswal VK. *Pramana-Journal of Physics* 2008;71(5):947-952.

90. Hermes HE, Frielinghaus H, Pyckhout-Hintzen W, Richter D. *Polymer* 2006;47(6):2147-2155.

91. Utracki LA, Sepehr M, Boccaleri E. *Polymers for Advanced Technologies* 2007;18:1-37.

92. Abecassis B, Testard F, Zemb T. *Soft Matter* 2009;5(5):974-978.

93. Maye MM, Lim IIS, Luo J, Rab Z, Rabinovich D, Liu TB, Zhong CJ. *Journal of the American Chemical Society* 2005;127(5):1519-1529.

94. Srivastava S, Frankamp BL, Rotello VM. *Chemistry of Materials* 2005;17(3):487-490.

95. Zhang F, Skoda MWA, Jacobs RMJ, Dressen DG, Martin RA, Martin CM, Clark GF, Lamkemeyer T, Schreiber F. *Journal of Physical Chemistry C* 2009;113(12):4839-4847.

96. Zucchi IA, Hoppe CE, Galante MJ, Williams RJJ, Lopez-Quintela MA, Matejka L, Slouf M, Plestil J. *Macromolecules* 2008;41(13):4895-4903.

97. Jorgensen JM, Erlacher K, Pedersen JS, Gothelf KV. *Langmuir* 2005;21(23):10320-10323.

98. Carroll JB, Frankamp BL, Srivastava S, Rotello VM. *Journal of Materials Chemistry* 2004;14(4):690-694.

99. Korgel BA, Fullam S, Connolly S, Fitzmaurice D. *Journal of Physical Chemistry B* 1998;102(43):8379-8388.

100. Park MJ, Park J, Hyeon T, Char K. *Journal of Polymer Science Part B-Polymer Physics* 2006;44(24):3571-3579.

101. Benetatos NM, Smith BW, Heiney PA, Winey KI. *Macromolecules* 2005;38(22):9251-9257.

102. Schaefer DW, Justice RS. *Macromolecules* 2007;40(24):8501-8517.

103. Takeuchi I, Lauterbach J, Fasolka MJ. *Materials Today* 2005;(10):18-26.

104. Meredith JC, Karim A, Amis EJ. *Macromolecules* 2000;33(16):5760-5762.

105. Meredith JC, Smith AP, Karim A, Amis EJ. *Macromolecules* 2000;33(26):9747-9756.

106. Julthongpiput D, Wenhua Z, Douglas JF, Karim A, Fasolka MJ. *Soft Matter* 2007;3:613-618.

107. Epps TH, DeLongchamp DM, Fasolka MJ. *Langmuir* 2007;23:3355-3362.

108. Karim A, Amis EJ, Meredith JC .In: Cawse, J. N., editor. *Experimental Design for Combinatorial and High Throughput Materials Science*. Hoboken: John Wiley & Sons Ltd., 2003. pp. 73-88.

109. Smith AP, Douglas JF, Meredith JC, Amis EJ, Karim A. *Physical Review Letters* 2001;87(1):5503-5504.

110. Meredith JC, Karim A, Amis EJ. *MRS Bulletin* 2002;27(4):330-335.

111. Meredith JC, Smith AP, Crosby AJ, Amis EJ, Karim A .*Encyclopedia of Polymer Science and Technology*. New York: John Wiley & Sons, 2002. pp.

112. Walker ML, Smith AP, Karim A. *Langmuir* 2003;19(17):6582-6585.

113. Yurekli K, Karim A, Amis EJ, Krishnamoorti R. *Macromolecules* 2004;37:507-515.

114. Stafford CM, Roskov KE, Epps TH, Fasolka MJ. *Review of Scientific Instruments* 2006;77:1-7.

115. Senkan S, Kahn M, Duan S, Ly A, Leidhom C. *Catalysis Today* 2006;117(1-3):291-296.

116. Yanase I, Ohtaki T, Watanabe M. *Solid State Ionics* 2002;154:419-424.

117. Chen L, Bao J, Gao C. *Journal of Combinatorial Chemistry* 2004;6(5):699-702.

118. Baeck SH, Jaramillo TF, Kleiman-Shwarsctein A, McFarland EW. *Measurement Science and Technology* 2005;16(1):54-59.

119. Norman AI, Cabral JT, Karim A, Amis EJ. *Macromolecular Rapid Communications* 2004;25(1):307-311.

120. Wang JS, Yoo Y, Gao C, Takeuchi I, Sun XD, Chang HY, Xiang XD, Schultz PG. *Science* 1998;279(5357):1712-1714.

121. Noda S, Sugime H, Osawa T, Tsuji Y, Chiashi S, Murakami Y, Maruyama S. *Carbon* 2006;44:1414-1419.

122. Karim A, Yurekli K, Meredith JC, Amis EJ, Krishnamoorti R. *Polymer Engineering and Science* 2002;42(9):1836-1840.

123. Sljukic B, Baron R, Salter C, Crossley A, Compton RG. *Analytica Chimica Acta* 2007;590(1):67-73.

124. Dai X, Wildgoose GG, Compton RG. *Analyst* 2006;131(11):1241-1247.

125. Bhat RR, Genzer J. *Applied Surface Science* 2006;252(7):2549-2554.

126. Roth SV, Walter H, Burghammer M, Riekel C, Lengeler B, Schroer C, Kuhlmann M, Walther T, Sehrbrock A, Domnick R, Muller-Buschbaum P. *Applied Physics Letters* 2006;88(2):1-3.

127. Drobny JG .*Handbook of Thermoplastic Elastomers*. Norwich, NY: William Andrew Publishing, 2007. pp. 215-300.

128. Meckel W, Goyert W, Wieder W, Wussow HG .In: Holden, G., Kricheldorf, H. R., Quirk, R. P., editors. *Thermoplastic Elastomers*. Cincinatti, OH: Hanser, 2004. pp. 15-44.

129. Schollenberger CS .*Handbook of Elastomers*. New York: Marcel Decker, Inc., 1988. pp. 375-409.

130. Holden G, Hansen DR .In: Holden, G., Kricheldorf, H. R., Quirk, R. P., editors. *Thermoplastic Elastomers*. Cincinatti, OH: Hanser, 2004. pp. 493-518.

131. Brown R . *Physical Testing of Rubber*, 4th edition. New York: Springer, 2006.

132. Finkelmann H, Rehage G. *Advances in Polymer Science* 1984;60/61:97-172.

133. Ortiz C, Wagner M, Bhargava N, Ober CK, Kramer EJ. *Macromolecules* 1998;31(24):8531-8539.

134. Finkelmann H, Kock HJ, Gleim W, Rehage G. *Makromolekulare Chemie-Rapid Communications* 1984;5(5):287-293.

135. Schatzle J, Kaufhold W, Finkelmann H. *Makromolekulare Chemie-Macromolecular Chemistry and Physics* 1989;190(12):3269-3284.

136. Donnio B, Wermter H, Finkelmann H. *Macromolecules* 2000;33(21):7724-7729.

137. Bergmann GHF, Finkelmann H, Percec V, Zhao MY. *Macromolecular Rapid Communications* 1997;18(5):353-360.

138. Elias F, Clarke SM, Peck R, Terentjev EM. *Europhysics Letters* 1999;47(4):442-448.

139. Finkelmann H, Kock HJ, Rehage G. *Makromolekulare Chemie-Rapid Communications* 1981;2(4):317-322.

140. Terentjev EM. *Current Opinion in Colloid & Interface Science* 1999;4(2):101-107.

141. Clarke SM, Tajbakhsh AR, Terentjev EM, Remillat C, Tomlinson GR, House JR. *Journal of Applied Physics* 2001;89(11):6530-6535.

142. Spillmann CM, Naciri J, Chen MS, Srinivasan A, Ratna BR. *Liquid Crystals* 2006;33(4):373-380.

143. Spillmann CM, Ratna BR, Naciri J. *Applied Physics Letters* 2007;90(2)

144. Lehmann W, Skupin H, Tolksdorf C, Gebhard E, Zentel R, Kruger P, Losche M, Kremer F. *Nature* 2001;410(6827):447-450.

145. Gebhard E, Zentel R. *Macromolecular Chemistry and Physics* 2000;201(8):902-910.

146. Gebhard E, Zentel R. *Macromolecular Chemistry and Physics* 2000;201(8):911-922.

147. Serak S, Tabiryan N, Vergara R, White TJ, Vaia RA, Bunning TJ. *Soft Matter* 2010;6(4):779-783.

148. White TJ, Serak SV, Tabiryan NV, Vaia RA, Bunning TJ. *Journal of Materials Chemistry* 2009;19:1080-1085.

149. Patil HP, Liao J, Hedden RC. *Macromolecules* 2007;40(17):6206-6216.

150. Clarke SM, Terentjev EM, Kundler I, Finkelmann H. *Macromolecules* 1998;31(15):4862-4872.

151. Ortiz C, Ober CK, Kramer EJ. *Polymer* 1998;39(16):3713-3718.

152. Patil HP, Hedden RC. *Journal of Polymer Science Part B-Polymer Physics* 2007;45(24):3267-3276.

153. Patil HP, Lentz DM, Hedden RC. *Macromolecules* 2009;42(10):3525-3531.

154. Beyer P, Terentjev EM, Zentel R. *Macromolecular Rapid Communications* 2007;28(14):1485-1490.

155. Fridrikh SV, Terentjev EM. *Physical Review e* 1999;60(2):1847-1857.

156. Tenbosch A, Varichon L. *Macromolecular Theory and Simulations* 1994;3(3):533-542.

157. Warner M, Bladon P, Terentjev EM. *Journal de Physique Ii* 1994;4(1):93-102.

158. Kupfer J, Finkelmann H. *Macromolecular Chemistry and Physics* 1994;195(4):1353-1367.

159. Adams JM, Warner M. *Physical Review e* 2005;71(2):021708-1-021708-15.

160. Adams JM, Warner M. *European Physical Journal e* 2005;16(1):97-107.

161. Ishige R, Osada K, Tagawa H, Niwano H, Tokita M, Watanabe J. *Macromolecules* 2008;41:7566-7570.

162. Leonov AI. *International Journal of Solids and Structures* 2002;39(24):5913-5926.

163. Wada Y, Nakayama A. *Journal of Applied Polymer Science* 1971;15(1):183-&.

164. Allison SW, Andrews RD. *Journal of Applied Physics* 1967;38(11):4164-4168.

165. Boyce MC, Montagut EL, Argon AS. *Polym Eng Sci* 1992;32:1073-1085.

166. Bauwens C, Bauwens JC, Homes G. *Journal of Polymer Science Part A-2-Polymer Physics* 1969;7(4PA2):735-&.

167. Allison SW, Andrews RD. *Journal of Applied Physics* 1967;38(11):4164-&.

168. Roetling JA. *Polymer* 1965;6(6):311-317.

169. Strella S, Newman S. *Polymer* 1964;5(3):107-123.

170. Dasari A, Duncan SJ, Misra RDK. *Materials Science and Technology* 2003;19(2):244-252.

171. Dasari A, Sarang S, Misra RDK. *Materials Science and Engineering A-Structural Materials Properties Microstructure and Processing* 2004;368(1-2):191-204.

172. Drozdov AD, Christiansen JD. *Polymer* 2003;44(4):1211-1228.

173. Hedden RC, Saxena H, Cohen C. *Macromolecules* 2000;33(23):8676-8684.

174. Hedden RC, Tachibana H, Duncan TM, Cohen C. *Macromolecules* 2001;34(16):5540-5546.

175. Ren W, McMullan PJ, Guo H, Kumar S, Griffin AC. *Macromolecular Chemistry and Physics* 2008;209(3):272-278.

176. Warner M, Terentjev EM . *Liquid Crystal Elastomers*, Oxford: Clarendon Press, 2003.

177. Hiraoka K, Uematsu Y, Stein P, Finkelmann H. *Macromolecular Chemistry and Physics* 2002;203(15):2205-2210.

178. Nishikawa E, Finkelmann H. *Macromolecular Chemistry and Physics* 1999;200(2):312-322.

179. Diaz F, Tagle LH, Valdebenito N, Aguilera C. *Polymer* 1993;34(2):418-422.

180. Horn M, Hepuzer Y, Yagci Y, Bilgin-Eran B, Cernenco U, Harabagiu V, Pinteala M, Simionescu BC. *European Polymer Journal* 2002;38(11):2197-2205.

181. Aguilera C, Bartulin J, Hisgen B, Ringsdorf H. *Die Makromolekulare Chemie* 2003;184(2):253-262.

182. Aguilera C, Ringsdorf H. *Polymer Bulletin* 1984;12(1):93-98.

183. Braun F, Willner L, Hess M, Kosfeld R. *Makromolekulare Chemie* 2003;191(8):1775-1785.

184. Bauman D, Martynski T, Mykowska E. *Liquid Crystals* 1995;18(4):607-613.

185. Bauman D, Moryson H. *Journal of Molecular Structure* 1997;404(1-2):113-120.

186. Heilmeier GH, Zanoni LA. *Applied Physics Letters* 1968;13:91-92.

187. Thote A, Gupta RB. *Fluid Phase Equilibria* 2004;220(1):47-55.

188. Tanaka T, Hayashi Y. *Clinica Chimica Acta* 1986;156(1):109-113.

189. Newman JDS, Blanchard GJ. *Langmuir* 2006;22(13):5882-5887.

190. Link S, El-Sayed MA. *Journal of Physical Chemistry B* 1999;103(40):8410-8426.

191. Kreibig U, Genzel L. *Surface Science* 1985;156:678-700.

192. Kreibig U, Zacharia P. *Zeitschrift fur Physik* 1970;231(2):128-

193. Papavassiliou GC. *Progress in Solid State Chemistry* 1979;12(3-4):185-271.

194. Kreibig U, Vollmer M . *Optical Properties of Metal Clusters*, Berlin: Springer, 1995.

195. Link S, Mohamed MB, El-Sayed MA. *Journal of Physical Chemistry B* 1999;103(16):3073-3077.

196. Yu YY, Chang SS, Lee CL, Wang CRC. *Journal of Physical Chemistry B* 1997;101(34):6661-6664.

197. Quinten M, Schonauer D, Kreibig U. *Zeitschrift fur Physik D-Atoms Molecules and Clusters* 1989;12(1-4):521-525.

198. Quinten M, Kreibig U. *Surface Science* 1986;172(3):557-577.

199. Kreibig U, Althoff A, Pressmann H. *Surface Science* 1981;106(1-3):308-317.

200. Link S, El-Sayed MA. *Journal of Physical Chemistry B* 1999;103(21):4212-4217.

201. Hourston DJ, Zia Y. *Journal of Applied Polymer Science* 1984;29(10):2951-2961.

202. Siegfried DL, Thomas DA, Sperling LH. *Macromolecules* 1979;12(4):586-589.

203. Kong XH, Tan SS, Narine SS. *Journal of Applied Polymer Science* 2009;114(1):139-148.

204. Liu CH, Chen YQ, Chen JG. *Carbohydrate Polymers* 2010;79(3):500-506.

205. Fu Y, Kao WJ. *Pharmaceutical Research* 2009;26(9):2115-2124.

206. Thatiparti TR, Kano A, Maruyama A, Takahara A. *Journal of Polymer Science Part A-Polymer Chemistry* 2009;47(19):4950-4962.

207. Han YA, Lee EM, Ji BC. *Fibers and Polymers* 2008;9(4):393-399.

208. Crank J .*Mathematics of Diffusion*. London: Oxford University Press, 1956. pp. 11-13.

209. Murayama S, Kuroda S, Osawa Z. *Polymer* 1993;34(18):3893-3898.

210. Murayama S, Kuroda S, Osawa ZJ. *Polymer* 1993;34(13):2845-2852.

211. Lee TY, Guymon CA, Jonsson ES, Hoyle CE. *Polymer* 2004;45(18):6155-6162.

212. Ramis X, Morancho JM, Cadenato A, Salla JM, Fernandez-Francos X. *Thermochimica Acta* 2007;463(1-2):81-86.

213. Vallittu PK. *Journal of Materials Science-Materials in Medicine* 1997;8(8):489-492.

214. Biernat M, Rokicki G. *Polimery* 2005;50(9):633-645.

215. Dou, S. "Synthesis and characterization of ion containing polymers." Ph.D. Dissertation. Penn State University, 2007.

216. Kline SR. *Journal of Applied Crystallography* 2006;39:895-900.

217. Kotlarchyk M, Stephens RB, Huang JS. *Journal of Physical Chemistry* 1988;92(6):1533-1538.

218. Griffith WL, Triolo R, Compere AL. *Physical Review A* 1987;35(5):2200-2206.

219. Vasquez JA, Ekstrom EJ, Stallings R, Velasquez R. U.S. Patent Application 20080237527.

220. Crary LF. U.S. Patent Appliation 20060219318.

221. Anderson NC, Ahmann RD. U.S. Patent 6687097.

222. Ichikawa S, Mekdhanasarn B, Ahmed AR. U.S. Patent 6344412.

223. Ichikawa S, Mekdhanasern B, Ahmed AR. U.S. Patent 6534422.

224. Dodsworth RS. U.S. Patent 6459043.

225. Murray GS. U.S. Patent Application 20090186254.

226. Yang J, Ma CM, Chen H, Chen C. U.S. Patent Application 20040097683.

227. Ibar JP. U.S. Patent 6586041.

228. Nelson GL, Najafi-Mohajeri N. U.S. Patent 7041374.

229. Shiraiwa T. U.S. Patent 5571472.

230. Hong M, Liu S, King J. U.S. Patent Application 20090236132.

231. Stern BA, El-Hibri MJ, Ireland DJ. U.S. Patent Application 20090281227.

232. Extrand CW. U.S. Patent Application 20040126521.

233. Czubarow P, Swei G, Kwon O. U.S. Patent 7476339.

234. Suh C, Lee T, Kim D. U.S. Patent Application 20050194572.

235. Hayward TP, Roemmler MG. U.S. Patent 6746626.

236. Barrera EV, Rodriguez-Macias FJ, Lozano K, Chibante LPF, Stewart DH. U.S. Patent Application 20060047052.

237. Barrera EV, Rodriguez-Macias FJ, Lozano K, Chibante LPF, Stewart DH. U.S. Patent Application 20090104386.

238. Rivas VA. U.S. Patent 5904980.

239. Patil, H. P. "Dynamic Mechanical Response of Main-Chain Smectic Elastomers." Ph.D. Dissertation. Penn State University, 2008.

240. Patel SK, Malone S, Cohen C, Gillmor JR, Colby RH. *Macromolecules* 1992;25(20):5241-5251.

241. Ward IM, Sweeney J .*An Introduction to the Mechanical Properties of Solid Polymers, Second Edition*. Chichester, West Sussex: Ch. 11, 245-249.  Wiley, 2004. pp. 245-249.

242. Robertson RE. *Journal of Applied Polymer Science* 1963;7:443-450.

243. Flory PJ . *Principles of Polymer Chemistry*, Ithaca, NY: Cornell University Press, 1953.

244. Kumar S, Pal SK, Kumar PS, Lakshminarayanan V. *Soft Matter* 2007;3(7):896-900.

245. Kumar PS, Pal SK, Kumar S, Lakshminarayanan V. *Langmuir* 2007;23(6):3445-3449.

246. Qi H, Lepp A, Heiney PA, Hegmann T. *Journal of Materials Chemistry* 2007;17(20):2139-2144.

247. Collings PJ, Ratna BR, Shashidhar R. *Physical Review e* 2003;67(2)

248. Bohm N, Materny A, Kiefer W, Steins H, Muller MM, Schottner G. *Macromolecules* 1996;29(7):2599-2604.

249. Marino LG, Raschella R, Lottici PP, Bersani D. *Journal of Non-Crystalline Solids* 2008;354(2-9):688-692.

250. Iftime G, Fisher L, Natansohn A, Rochon P. *Canadian Journal of Chemistry* 2000;78:409-414.

251. Bohm N, Materny A, Steins H, Muller MM, Schottner G. *Macromolecules* 1998;31(13):4265-4271.

252. Chaput F, Riehl D, Levy Y, Boilot JP. *Chemistry of Materials* 1993;5(5):589-591.

253. Camacho-Lopez M, Finkelmann H, Palffy-Muhoray P, Shelley M. *Nature Materials* 2004;3(5):307-310.

# VITA

## Daniel M. Lentz

Daniel M. Lentz was born on March 9th, 1984 in Kingsport Tennessee, where, despite three years spent living in northern England, he graduated from high school 18 years later. Daniel matriculated to Cornell University, where he received a B.S. degree, Magna Cum Laude with Honors, in Materials Science and Engineering in 2006. His coursework emphasized polymer science and engineering management. Following this, he began graduate work at the Pennsylvania State University. Here he was awarded the 3M Graduate Fellowship in Materials Science and Engineering, the University Graduate Fellowship award, and the Anne C. Wilson Graduate Student Research Award. Working under Dr. Ronald C. Hedden and Dr. Evangelos Manias, Daniel researched polymer science and chemistry, specifically focusing on liquid crystalline elastomers and polymer-metal nanocomposites. He is seeking to complete his Ph.D. in May 2010 and has accepted a position to work with 3M beginning in June 2010.

Publications

Harshad P. Patil, Daniel M. Lentz, and Ronald C. Hedden, "Necking instability during polydomain-monodomain transition in a smectic main-chain elastomer," *Macromolecules* 42(10), April 2009, 3525-3531.

Daniel M. Lentz, Robert A. Pyles, and Ronald C. Hedden, "Surface Infusion of Gold Nanoparticles into Processed Thermoplastics," *Polymer Engineering and Science* 50(1), January 2010, 120-127.

Robert A. Pyles, Ronald C. Hedden, and Daniel M. Lentz, "Process for Incorporating Metal Nanoparticles in a Polymeric Article and Articles Made Therewith," United States Patent Application 20090297829, December 2009.

Morgan A. Iannuzzi, Roderick Reber III, Daniel M. Lentz, Jun Zhao, Lan Ma, and Ronald C. Hedden, "USANS study of porosity and water content in sponge-like hydrogels," *Polymer*, In press March 2010.

Daniel M. Lentz, Huipeng Chen, Harshad P. Patil, Ziniu Yu, and Ronald C. Hedden, "Influence of strain rate and temperature on necking transition in a smectic main-chain elastomer," submitted to *Macromolecules* April 2010.

Daniel M. Lentz, Alicyn M. Rhoades, and Ronald C. Hedden, "Synthesis of nanoparticles via Infusion into an amine-functionalized surface layer interpenetrating network," In preparation April 2010.